Instituut voor Materiaalonderzoek

Faculteit Wetenschappen

Study by means of photothermal deflection methods of the opto-electronic properties of CVD diamond in relation to the defect population

Proefschrift voorgelegd tot het behalen van de graad van

Doctor in de Wetenschappen, richting Natuurkunde

aan het Limburgs Universitair Centrum, te verdedigen door

Kristien Meykens

Op 23 mei 2000 te 16.00

Promotor :	Prof. Dr. L.M. Stals
Co-promotor :	Dr. M. Nesládek

2000

Chairman	Prof. Dr. F. Dumortier
	Vice-rector
Promotor:	Prof. Dr. L.M. Stals
Copromotor:	Dr. M. Nesládek
Members of the jury:	Dr. M. Vanecek
	Prof. Dr. G. Adriaenssens
	Prof. Dr. C. Van Haesendonck
	Prof. Dr. L. De Schepper
	Prof. Dr. G. Knuyt

Dankwoord

Ook dit proefschrift kon alleen tot stand komen dankzij de medewerking van velen. Mijn oprechte dank gaat daarom ook uit naar alle mensen die op de één of andere manier hun steentje hebben bijgedragen aan het welslagen van dit werk. In het bijzonder dank ik:

mijn promotor, Prof dr. Lambert Stals, voor het vertrouwen dat hij mij zes jaar geleden gegeven heeft om aan dit werk te beginnen. Zijn grote interesse in ons diamantonderzoek heeft me erg gestimuleerd. De boeiende gedachtewisselingen, zijn vele waardevolle suggesties en positieve kritiek hebben zeker geholpen bij de realisatie van dit proefschrift.

mijn co-promotor en directe begeleider dr. Milos Nesladek, degene die me alle facetten van het diamantonderzoek en de diamanten zelf heeft leren kennen. Zijn stimulerende en originele ideeën hebben in belangrijke mate bijgedragen tot de kwaliteit van dit werk.

de andere leden van de doctoraatscommissie Prof dr. Gilbert Knuyt en prof. Dr. Herman Janssen, voor hun oprechte belangstelling voor de vorderingen van dit onderzoekswerk.

Especially I would like to thank Dr. Milan Vanecek, for all the elucidating discussions and in particular for the critical reading of this manuscript. This is an appropriate place to thank once more him and his colleagues for their kind hospitality during my interesting stay at the Institute of Physics in Prague.

De mensen die ik vervolgens wil bedanken zijn de technische medewerkers. Omdat we een compleet nieuwe opstelling hebben opgebouwd, was de technische ondersteuning van enorm belang. Bedankt Johnny, Christel en Johan.

Mijn grote dank voor Jean Claude die tot het bittere einde klaar stond met advies en praktische hulp betreffende computers. Zonder zijn hulp zou dit proefschrift er gewoon niet geweest zijn.

Ook een woordje van dank voor al de didactiek collega’s van de afgelopen jaren met wie het zeer prettig werken was.

Tenslotte wil ik iedereen bedanken voor de fijne en stimulerende sfeer waarin ik heb mogen werken, in het bijzonder mijn collega ‘diamantonderzoeker‘ Ken en Els voor de ondersteuning in de laatste fase.

Natuurlijk was dit werk nooit tot stand gekomen zonder de inbreng van de mensen in mijn persoonlijke omgeving in de afgelopen jaren. Ik wil afsluiten met mijn vrienden, mijn familie en mijn ouders te bedanken voor hun steun, interesse en betrokkenheid.

Kristien Meykens , mei 2000

Table of contents

6. STUDY OF ACTIVE IMPURITIES: SUBSTITUTIONAL NITROGEN, LITHIUM AND PHOSPHORUS

Samenvatting

Inleiding

In dit proefschrift zijn we nagegaan of de fotothermische deflectie (PDS) techniek, tot hier toe gebruikt voor andere doeleinden, kon aangepast worden om defecten in CVD diamantfilms te bestuderen. In een eerste fase werden met behulp van de PDS techniek de intrinsieke defecten en onzuiverheden aanwezig in ongedopeerde CVD diamantfilms onderzocht. Vervolgens werd de eerste aanzet gegeven om ook stikstof-, lithium- en fosfor-gedopeerde diamantfilms te karakteriseren.

CVD diamantfilms

Diamant - een covalent halfgeleidend materiaal – vertoont een combinatie van unieke eigenschappen: optisch transparant van infrarood tot ultraviolet, een grote bandgap (5.45 eV), een hoge elektronen- en gaten-mobiliteit (2200 – 1600 $m^2\ V^{-1}\ s^{-1}$), grootste diëlektrische constante (5.66), hoogste thermische geleidbaarheid bij kamertemperatuur (2000 $W\ m^{-1}\ K^{-1}$), grootste hardheid en chemisch inert. Theoretisch kunnen deze buitengewone eigenschappen leiden tot een reeks unieke en belangrijke toepassingen zoals optische vensters voor lasertoepassingen, hoge-temperatuur hoog-vermogen elektronica, heat-sinks, koude elektronen emitters (voor beeldschermen), deeltjesdetectoren, enz. Niettegenstaande het enorme potentieel van diamant vormen zowel de hoge kostprijs en de relatief kleine afmetingen van natuurlijke en hoge druk hoge temperatuur (HDHT) synthetisch diamant, als de technische problemen met n-doperen een serieuze hinderpaal bij de commercialisering.

Sinds het begin van de jaren ‘80 is de studie van diamant sterk in de belangstelling gekomen omwille van het ter beschikking komen van diamantfilms bereid met de Chemical Vapour Deposition (CVD) methode. Met deze techniek werd het mogelijk om dunne diamantfilms variërend van enkele micron tot enkele millimeter dik, meerdere vierkante centimeters in oppervlakte en met een hoge optische kwaliteit te groeien. Niettemin bevatten alle CVD diamantfilms, in meerdere of mindere mate, defecten zoals amorf koolstof, grafiet, stikstof, enz. Deze defecten worden tijdens de groei in de film geïntroduceerd. Samen met het feit dat het merendeel van de CVD diamantfilms polykristallijn is, zijn deze defecten de beperkende factor voor elektronische en optische

toepassingen.

Wil men diamant gebruiken in allerhande elektronische toepassingen, dan is niet enkel een zo klein mogelijke defectconcentratie in de film noodzakelijk, maar ook het beschikken over zowel n- als p-type diamant is van cruciaal belang. Alhoewel p-type diamant bestaat, zowel in natuurlijke (IIb) als in CVD (boor-gedopeerde films) vorm, vormt n-type doperen van diamant een fundamenteel probleem. De aanwezigheid van hoge concentraties van andere defecten en onzuiverheden (niet-diamant koolstof, stikstof, etc.) kan immers de actieve dopering sterk bemoeilijken door compensatie of neutralisatie. Voor n-type doperen zijn er verschillende kandidaat doperingselementen: N, P en Li. In 1997 werd door de groep op het NIRIM (Japan) een eerste doorbraak gerealiseerd wat betreft n-type doperen met fosfor van homoepitaxiale diamantfilms door toevoeging van fosfine aan de reactiegassen. Hallmetingen bevestigden de elektrongeleiding. Karakterisaties met spectroscopische technieken toonden een nieuw optisch actief defect aan in de bandgap (0.56 eV beneden de conductieband). Vele pogingen werden ondernomen om diamantfilms te doperen met Li, maar tot vandaag leverde geen enkele methode elektrische actieve n-type defecten.

Vandaar, één van de hoofdthema's in het diamantonderzoek is de aanmaak van hoge kwaliteit CVD diamant met vermindering van het aantal defecten, resulterend in films equivalent aan type IIa (zuiverste kwaliteit) natuurlijke diamant. Om dit doel te kunnen realiseren, is de kwantificatie en een beter begrip van deze defecten, gelokaliseerd in de bandgap, één van de belangrijkste taken. Feedback van de (spectroscopische) karakterisatietechnieken naar het depositieproces kan zo leiden tot hogere kwaliteit diamantfilms. In een tweede stap kan dan, vertrekkend met hoge kwaliteit diamant, overgegaan worden tot dopering van de films. Ook voor deze gedopeerde films is een uitgebreide karakterisatie noodzakelijk om fundamentele kennis over de elektronische structuur van de defecten, de mobiliteiten en geleidingsmechanismen te verkrijgen.

Om zowel ongedopeerde als gedopeerde (N, Li) polykristallijne CVD diamantfilms aan te maken beschikt het Instituut voor Materiaalonderzoek (IMO) over twee microgolf plasma CVD depositie installaties: ASTeX PDS17 (zie Fig. 2.2) en AX6500 (zie Fig. 2.3). Bij deze techniek worden bij lage druk (~10000 Pa) en temperatuur (~850 °C) diamantfilms afgezet op (Si-)substraten. De depositiegassen, (H_2, een koolstof bevattend gas b.v. CH_4, eventueel N_2, O_2 en andere doperingsprecursors) worden in de reactiekamer gebracht. De gassen worden met behulp van de microgolven in het plasma geactiveerd (radicalen, ionen,…) en diffunderen vanuit het plasma naar het substraat waar een

diamantdeklaag gevormd wordt.

Polykristallijne CVD diamantfilms bestaan hoofdzakelijk uit sp^3 gebonden koolstof. CVD diamant wordt gesynthetiseerd onder metastabiele druk en temperatuur omstandigheden waaronder grafiet de stabiele vorm van koolstof is (zie Fig. 2.1). Hierdoor worden ook grafiet en amorf koolstof (a-C) defecten opgenomen in de diamantstructuur. Vermoedelijk zijn deze grafiet en a-C insluitsels terug te vinden in de korrelgrenzen en op andere defectlocaties in de film.

Afhankelijk van de gebruikte procesparameters (druk, temperatuur, concentraties van de verschillende procesgassen, microgolfvermogen) kunnen films met volledig andere morfologie, oriëntatie, kleur, korrelgrootte en kwaliteit (sp^2/sp^3 verhouding) bereid worden (zie Fig. 2.6). De dikte, net als de ruwheid van het groeioppervlak (piramidaal, vlakken) worden mede bepaald door de depositiecondities. Onder optimale condities is de groeisnelheid van de orde van 5-10 µm/h.

Na het aanmaken van de diamantfilms worden de substraten verwijderd tijdens een chemisch etsproces. Eventueel kunnen de vrijstaande diamantfilms nog een polijstbehandeling ondergaan.

Fotothermische deflectie spectroscopie (PDS)

De PDS techniek, ontwikkeld in het begin van de jaren '80, is gebaseerd op de zwakke absorptie van (periodisch) invallend licht door de defecten aanwezig in de halfgeleidende film. De eruit voortvloeiende kleine temperatuurstijging in de film wordt gemeten door de registratie van de afbuiging van een langs het filmoppervlak scherende invallende laser test-bundel. Elke temperatuurstijging in de film of de vloeistof rondom resulteert op zijn beurt in een verandering van brekingsindex. De afbuiging van de laser test-bundel wordt veroorzaakt door de verandering van de brekingsindex van een vloeistof in contact met het filmoppervlak (transverse configuratie t-PDS). Alternatief kan de minieme temperatuurstijging in de film ook rechtstreeks opgemeten worden door een laser test-bundel quasi parallel met de invallende lichtbundel door het sample te sturen (collineaire configuratie c-PDS). In dit geval wordt de bundel afgebogen door de brekingsindexgradiënt in het meetmonster zelf.

In vergelijking met ‘klassiek’ optische transmissiemetingen blijkt PDS, omwille van een kleinere invloed van lichtverstrooiing, veel gevoeliger te zijn en wordt het met PDS

mogelijk om defectconcentraties beneden ppm niveau te bepalen. De PDS techniek meet al de mogelijke optische transities in de bandgap: zowel overgangen tussen gelokaliseerde toestanden in de gap als de overgangen naar de conductie- en valentieband die aanleiding geven tot het ontstaan van vrije ladingsdragers. Fotostroommetingen detecteren enkel deze laatste overgangen en leveren dus informatie, complementair aan PDS, over welke de elektrisch actieve transities zijn.

De PDS techniek wordt al uitgebreid toegepast om de optische absorptie in andere halfgeleiders zoals a-Si, GaN, enz. te bestuderen. We hebben voor het eerst deze techniek gebruikt om ook defecten in de zwak absorberende polykristallijne CVD diamantfilms te karakteriseren. Er moet wel de aandacht getrokken worden op enkele belangrijke verschillen tussen Si en diamant: diamant is transparant over een erg breed gebied van IR tot UV (brede indirecte bandgap van 5.45 eV), bezit de hoogste thermische geleidbaarheid bij kamertemperatuur (KT) en verder, een 'as-grown' polykristallijne diamantfilm bezit een ruw gefaceteerd oppervlak dat, samen met korrelgrenzen, oorzaak is van sterke lichtverstrooiing in de film. Daarom vraagt de toepassing van PDS op diamant een gedetailleerd onderzoek van deze feiten, zowel vanuit theoretisch als experimenteel oogpunt.

Een hoofddoel van dit proefschrift was de aanpassing en het op punt stellen van een PDS opstelling voor CVD diamantfilms. Een nieuwe geautomatiseerde experimentele t-PDS opstelling (Fig. 3.1(a) en Fig. 3.3), aangepast aan de specifieke vereisten van diamant, werd opgebouwd in het IMO. De keuze van de optische componenten zoals lichtbronnen, monochromator, roosters, filters, spiegels, cuvette en deflectie-vloeistof was zodanig dat het volledige bandgap gebied van 230 nm tot 2480 nm (0.5 - 5.4 eV) kon overbrugd worden. De modulatiefrequentie (~ 8 Hz) werd gekozen in functie van de thermische diffusielengte in diamant. In een tweede fase werd ook een PDS opstelling in collineaire geometrie opgebouwd. Met deze opstelling kan een (x,y)-scan uitgevoerd worden. Er werd gebruik gemaakt van een CO_2 laser als lichtbron (constante λ = 10.6 µm). De afmetingen van het onderzochte gebied en de resolutie van de metingen zijn afhankelijk van de bundelgeometrie. Beide laserbundels, de ‘pump’ bundel en de 'probe' bundel, zijn gefocusseerd tot spots met een straal van respectievelijk 100 µm en 40 µm (Fig. 3.1(b) en Fig. 3.6). Dit laat toe om lokaal optische absorptiemetingen uit te voeren met een ruimtelijke resolutie van de orde van 100 µm. Hierdoor is deze techniek uiterst geschikt voor het in beeld brengen (imaging - spatial profiling) van zwak absorberende onzuiverheden en defecten in de films. De 1D en 2D afbeeldingen van de optische

absorptie coëfficiënt kunnen een indicatie geven over de positie van de onzuiverheden en defecten.

Theoretische beschouwingen wezen uit dat, voor beide configuraties, de optische absorptiecoëfficiënt α berekend kan worden uit het opgemeten PDS-signaal S met behulp van volgende uitdrukking: $\alpha(E) = -1/d \ln(1 - S(E)/S_{sat})$. Hierbij is S_{sat} de saturatie waarde van het PDS-signaal en d de dikte van het diamant sample. Deze uitdrukking is enkel geldig in de incoherente limiet en wanneer verstrooiing verwaarloosbaar is.

In het algemeen is het erg moeilijk om absolute optische absorptiewaarden te bepalen uit t-PDS en c-PDS metingen (opgemeten in relatieve waarden), in het bijzonder voor CVD diamantfilms.

Verschillende schalingsprocedures om absolute waarden te verkrijgen uit t-PDS metingen worden vergeleken. De S_{sat}-schaling procedure (zie Fig. 3.15) is enkel toepasbaar op CVD diamantfilms die een grote hoeveelheid sp^2-gebonden koolstof bevatten en waarvan het t-PDS signaal satureert in het onderzochte energiegebied. Deze methode kan niet gebruikt worden voor matig tot hoge kwaliteit CVD diamantfilms, omdat voor deze films geen volledige absorptie wordt bereikt. De T-schaling procedure (zie Fig. 3.16) om t-PDS spectra in absolute waarden te bekomen, bestaat er uit de PDS optische absorptie spectra te fitten aan de absolute absorptie waarden bepaald met transmissiemetingen. Beide spectra worden gematched op het grensgebied van hoge en lage absorptiegebieden (4.0 - 4.5 eV). Omdat integrerende sfeer transmissiemetingen het minst leiden onder verstrooiingsverliezen, worden deze gebruikt om de PDS metingen te schalen.

Collineaire PDS metingen worden geschaald aan de hand van absolute laser calorimetriemetingen. Een referentiesample wordt opgemeten met behulp van beide methoden, waaruit een schalingsconstante bepaald wordt. Deze constante wordt vervolgens gebruikt om de c-PDS absorptie waarden van de andere samples te schalen. c-PDS metingen kunnen enkel uitgevoerd worden op hoge kwaliteit diamantfilms.

Lichtverstrooiing: vergelijking tussen PDS en transmissiemetingen

De invloed van lichtverstrooiing aan de ruwe oppervlakken van de diamantfilms (zie Fig. 4.3) op t-PDS en transmissie- en reflectiemetingen in relatie met de ruwheid van het oppervlak werd onderzocht.

Oppervlakte verstrooiing heeft een grote invloed op speculaire transmissie-metingen (Fig.

4.6). Integrerende sfeer transmissiemetingen daarentegen worden minder beïnvloed door de lichtverstrooiing aan ruwe oppervlakken, maar niettemin blijven de verschillen tussen gepolijste en ongepolijste samples duidelijk zichtbaar (Fig. 4.8).

Het PDS-signaal, tenslotte, is kunstmatig verhoogd door een toename van de effectieve optische dikte omwille van verstrooiing (oppervlak en bulk) en licht 'trapping' in de CVD diamantfilms (Fig. 4.2 en Fig. 4.12). In het lage absorptiegebied, $\alpha d < 1$, is deze toename spectraal onafhankelijk en bijgevolg wordt de vorm van het spectrum niet vervormt. Eigenlijk kan men de invloed van verstrooiing vertalen naar een toename van de fysische dikte d tot een effectieve dikte d_{eff} van het sample. Dit leidt zelfs tot een verhoging van de gevoeligheid van de PDS techniek. Omwille van de spectraalonafhankelijkheid van d_{eff} , is het effect van lichtverstrooiing op PDS niet relevant en kunnen de PDS data van de ongepolijste samples gematched worden aan de correcte absorptiewaarden opgemeten aan het (gepolijste) sample (met behulp van PDS of transmissie). Het is duidelijk dat in de uiteindelijke absolute spectra de grootte van de effectieve dikte van geen belang is. In het hoge absorptiegebied, $\alpha d > 1$, wordt het licht snel geabsorbeerd, vooraleer het een afstand d_{eff} heeft afgelegd en gaat scattering wel een rol spelen. Dit resulteert in echte (α_a) en schijnbare absorptiespectra ($\alpha_a + \alpha_s$) waarbij de afstand tussen beide spectra afneemt met toenemende energie.

Uit deze studie kunnen we besluiten dat de methode om optische absorptiemetingen uit te voeren moet aangepast worden aan de ruwheid van het diamantoppervlak. Gepolijste films ondervinden quasi geen hinder van lichtverstrooiing en de optische absorptie kan eenvoudig bepaald worden uit zowel PDS als transmissiemetingen. Wat betreft de ongepolijste films, de categorie waartoe het merendeel van de onderzochte samples behoort, moeten we voor transmissiemetingen twee klassen beschouwen. Enerzijds, wanneer de oppervlakteruwheid relatief klein is, kunnen de theoretische modellen van Filinski en Yin gebruikt worden om de invloed van verstrooiing op speculaire transmissiemetingen te modelleren. Met behulp hiervan kunnen dan correcte absorptie-coëfficiënten bepaald worden. Anderzijds, wanneer de ruwheid van het oppervlak groter wordt (groter dan de golflengte van het invallend licht) zijn deze theorieën niet meer toepasbaar en falen speculaire transmissiemetingen als karakterisatietechniek. Voor beide klassen geldt dat in het lage absorptiegebied lichtverstrooiing en licht 'trapping' geen directe invloed op PDS spectra hebben. Vandaar dat PDS in dit gebied de meest geschikte techniek is om de spectraalafhankelijkheid van de optische absorptiecoëfficiënt

α in CVD diamantfilms te bepalen. De gevoeligheid van PDS is voldoende hoog om de lage absorpties in hoge kwaliteit CVD diamantfilms te meten. Bijkomend voordeel van PDS is dat een vlak oppervlak geen absolute vereiste is. Ze moeten dus geen tijdrovend polijstproces ondergaan alvorens ze onderzocht kunnen worden. Voor het hoge absorptiegebied zijn geen PDS data voorhanden maar in dit gebied geven integrerende sfeer transmissiemetingen absolute absorptiewaarden. Om de PDS data naar absolute waarden te herschalen wordt de T-schaling procedure gebruikt.

Tot hiertoe kunnen we besluiten dat PDS een geschikte techniek is om de optische absorptie in polykristallijne CVD diamantfilms op te meten. In een volgend onderdeel van dit proefschrift gaan we deze techniek uittesten om ongedopeerde en gedopeerde films te karakteriseren.

Ongedopeerde CVD diamantfilms

Met behulp van de t-PDS techniek werd de defectgeïnduceerde sub-bandgap absorptie in ongedopeerde diamantfilms opgemeten als functie van de depositieparameters. De bestudeerde films varieerden van hoge kwaliteit diamantfilms tot nanokristallijne films. Uit de t-PDS metingen kunnen de concentratie en distributie van de diepe gelokaliseerde defecten bepaald worden. De defecttoestanden zijn aanwezig in de bandgap van diamant tengevolge van de aanwezigheid van kristallijne defecten en onzuiverheden in de diamantstructuur.

Uit de experimentele data blijkt dat de absorptiespectra van al de onderzochte CVD diamantfilms een karakteristieke vorm vertonen in het IR en in het zichtbaar spectraal gebied (Fig. 5.8 - Fig. 5.10). De opgemeten absorptiespectra zijn sterk gelijkend op die van amorf koolstof (a-C) films. De absorptie in a-C films wordt toegeschreven aan π-π^* optische overgangen. Er wordt aangenomen dat de karakteristieke absorptie in diamant ook overeenstemt met optische transities tussen π-π^* subgap toestanden. Een morfologiestudie toonde aan dat de films met de grootste subgap absorptie nanokristallijn zijn met een toenemende oppervlakte aan korrelgrenzen (en dus sp^2 gebonden grafiet en a-C insluitsels). Raman spectroscopie detecteerde eveneens een stijgende hoeveelheid van sp^2 gebonden koolstof in deze films. De films waren optisch vlak (kleine verstrooiingsverliezen). De optische transmissiemetingen toonden aan dat de typische indirecte overgang, te wijten aan de lange-afstandsorde van de diamantstructuur, was

verloren gegaan (Fig. 5.6 - Fig. 5.7). De hoogste kwaliteit CVD diamant, anderzijds, behoud het karakter van de fundamentele absorptiekant, maar de optische absorptie in dit gebied vertoont verbreding. Uit vergelijking met synthetische Ib diamant, werd aangetoond dat de karakteristieke absorptie niet kan verklaard worden door de aanwezigheid van substitutioneel stikstof of door andere onzuiverheden.

Een theoretisch model werd ontwikkeld om de subgap absorptie, aanwezig in de polykristallijne CVD diamantfilms, te verklaren (Fig. 5.1). Een numerieke deconvolutieprocedure overeenkomstig het theoretisch model werd gebruikt om de experimentele data te fitten (bv. Fig. 5.8). De modellering van de t-PDS metingen leidde tot de eerste identificatie van een van de belangrijkste defectstructuren in CVD diamantfilms. De optische absorptie in het gebied van 0.5 eV tot 4.0 eV wordt toegeschreven aan optische transities van bezette π toestanden naar onbezette π^* toestanden in de bandgap van diamant. Deze toestanden in de bandgap worden veroorzaakt door de aanwezigheid van amorf koolstof en sp^2 gebonden koolstof in de diamantfilms (talrijke publicaties melden de aanwezigheid van amorf koolstof en sp^2 gebonden koolstof aan korrelgrenzen en als intrinsieke defecten). Dit motiveerde de aanname van 2 gaussische banden van gelokaliseerde π- en π^*-toestanden in de bandgap van diamant.

Raman en PDS-metingen werden beide toegepast op dezelfde CVD diamantfilms (Fig. 5.12 - Fig. 5.15). Er werd aangetoond dat bij benadering een één-één correlatie bestaat tussen de niet-diamant koolstof fractie (bepaald via Raman spectroscopy), en de waarde van de optische absorptiecoëfficiënt α bij een fotonenergie van 2.41 eV(bepaald via t-PDS) (Fig. 5.16). Omwille van de hoge gevoeligheid van PDS, kunnen grafietinclusies (sp^2 gebonden koolstof) getraceerd worden in CVD diamantfilms met een karakteristieke sub-bandgap absorptie beneden ppm niveau. Metingen op een uitgebreider set van samples zouden moeten helpen om de betrouwbaarheid van de afgeleidde relatie te vergroten en om een meer precieze kwantificering toe te laten. Verdere pogingen om de grootte van de Raman cross-secties van al de niet-diamant componenten te schatten zijn nodig.

De c-PDS methode werd voor het eerst succesvol toegepast om de optische absorptie van hoge kwaliteit ongedopeerde CVD diamantfilms te bepalen bij de CO_2 laser golflengte (10.6µm). De toepasbaarheid van deze techniek op hoge kwaliteit CVD diamantfilms metingen werd aangetoond aan de hand van metingen uitgevoerd op een set samples van verschillende kwaliteit. De c-PDS metingen uitgevoerd met een ruimtelijke resolutie van

100 µm, bepaald door de focusseringsoptica, leverden optische absorptiebeelden ('images') voor de verschillende samples (Fig. 5.17 - Fig. 5.21). Er werd aangetoond dat het optisch absorptiemechanisme hoofdzakelijk beïnvloed werd door de zwarte spots, die -in meerdere of mindere mate- aanwezig zijn in alle CVD diamantfilms. Het optische kwaliteit materiaal bevat praktisch geen van deze kenmerken. Wiskundige modellering werd uitgevoerd om na te gaan of het temperatuur- (warmtediffusie) profiel in diamant met de theoretische voorspellingen beschreven kon worden. Een erg goede overeenkomst tussen experiment en theorie werd vastgesteld. Tot slot, de relatieve c-PDS waarden werden gecalibreerd met behulp van een sample met gekende absorptie (bepaald met LC) en de c-PDS en caloriemetrische waarden werden bepaald.

Gedopeerde diamantfilms

Het laatste onderdeel van dit proefschrift is gewijd aan de eerste PDS metingen op gedopeerde CVD diamantfilms. Karakterisatie van defecten vormt al gedurende vele jaren een belangrijke topic in het diamantonderzoek. Met het oog op elektronische toepassingen is, zoals al eerder vermeld, n-type dopering van de diamantfilms onontbeerlijk.

Stikstof-gedopeerde diamantfilms

Zowel homoepitaxiaal vlamgegroeide CVD diamantfilms (KUN, Nijmegen, Nederland) als microgolf plasma geassisteerde CVD diamantfilms (IMO) werden met behulp van t-PDS bestudeerd. Voor het eerst werd duidelijk de aanwezigheid van substitutioneel stikstof in CVD diamantfilms aangetoond. Substitutioneel stikstof is een diepe donor met een optische aktivatie-energie van 2.2 eV.

De spectraalafhankelijkheid van de optische absorptiecoëfficiënt α in stikstof-gedopeerde homoepitaxiale CVD diamantfilms werd bestudeerd. De opgemeten absorptiespectra werden vergeleken met de spectra van type Ib en IIa diamant. De diamantfilm afgezet op een {110} georiënteerd substraat vertoont een spectraal absorptiegedrag zoals een type Ib diamant (bevat stikstof in substitutionele positie). Gebruikmakend van de omrekeningsfactor van Woods et al. en Nazaré et al. schatten we een N concentratie van 15 ppm in dit sample. Voor de diamantlaag afgezet op een {001} georiënteerd substraat, kon geen N-gerelateerde absorptie gedetecteerd worden. De resultaten van de oriëntatieafhankelijke stikstofincorporatie stemmen goed overeen met de cathodoluminescentie data. Verder, vertonen al deze N-gedopeerde CVD films een

karakteristieke continuüm subgap absorptie, vergelijkbaar met deze in de polykristallijne ongedopeerde CVD diamantfilms, waar deze toegeschreven werd aan π-π* overgangen (zie 'ongedopeerde samples'). Mogelijke posities voor a-C op het oppervlak van de onderzochte homoepitaxiale diamant éénkristallen zijn de groeistappen op de {001} georiënteerde lagen en de microfacetten op de {110} georiënteerde lagen.

N-gedopeerde polykrystallijne CVD diamantfilms werden in-situ gedopeerd door toevoeging van een stikstof precursor. Het N-gedopeerde sample, dat geprepareerd was met 100 ppm N_2 in de gasfase, toonde dezelfde spectraalafhankelijkheid als de optische absorptiecoëfficiënt van Ib diamant. Dit suggereert de aanwezigheid van N in substitutionele positie. De optische absorptiespectra van de N-gedopeerde diamantfilms zijn duidelijk gesuperponeerd op de typische continuüm absorptie horend bij π - π* optische overgangen.

Lithium-gedopeerde diamantfilms

Li-gedopeerde CVD diamantfilms werden gegroeid door toevoeging van butyllithium in hexaan aan de standaard precursorgassen. SIMS diepteprofilering bevestigde de succesvolle incorporatie van Li in de CVD diamantfilms. Een nieuwe defectband bij 1.5-1.6 eV werd gedetecteerd met behulp van t-PDS. Onafhankelijk werd, aan Li-gedopeerde samples afkomstig van een andere bron, een zelfde band opgemeten bij fotostroommetingen. De verklaring voor deze absorptieband is niet eenduidig. De invloed van een vacature, Li, H en Si op de aanwezigheid van deze defectband is onduidelijk en verder onderzoek is nodig.

Fosfor-gedopeerde diamantfilms

De eerste preliminaire resultaten van t-PDS metingen op P-gedopeerde diamantfilms, gegroeid op het NIRIM door toevoeging van fosfine, worden voorgesteld. De absorptiespectra vertonen drie absorptiebanden. De defectstructuur bij 0.56 eV wordt toegewezen aan het P-niveau. Deze waarde stemt goed overeen met de resultaten bekomen uit andere karakterisatietechnieken. Een tweede absorptieband met een fotoionisatie-energie rond 1.35 eV wordt waargenomen, maar tot op heden, is the oorsprong van deze band onbekend. De absorptieband bij hogere energie is te wijten aan de substraatabsorptie. Verder onderzoek is noodzakelijk om een duidelijker beeld over de elektronische structuur van P te verkrijgen.

List of symbols and abbreviations

A	absorptance
AC	alternating current
A_{ref}^{LC} , A_{ref}^{PDS}	absorptance of the reference sample as measured by LC and collinear PTD respectively.
α_e	total attenuation coefficient
α_s	scattering coefficient
α, α_a	optical absorption coefficient
a_p	radius of the pump beam
a_s	radius of the probe beam
a-C	amorphous carbon
BEN	bias enhanced nucleation
B_2H_6	diborane
B_2O_3	boron trioxide
b	sample width
χ	angle between the pump beam and the surface normal
C	specific heat of the deflecting medium ($C_{diamond}$ = 6.195 J/mol.K)
C_f ,C_s	specific heat of fluid and sample respectively
CaF_2	calcium fluoride
CH_4	methane
CCl_4	carbon tetrachloride
CH_3OH	methyl alcohol
CH_4	methane

C_6H_{14}	hexane
C_4H_9Li	butyllithium
CPM	constant photocurrent method
CVD	chemical vapour deposition
CrO_3	chroom oxide
c-PDS	collinear photothermal deflection spectroscopy
D	clear aperture
D	detector transducing factor
DLC	diamond like carbon
DOS	density of states
d, d_{eff}	(effective) thickness of the sample
d	distance of the substrate from the inner flame cone
d**s**	the change of the unit tangent vector **s** along the beam path
ds	length of the infinitesimal propagation-measured along the path
E	energy
ΔE	energy interval
EPR	electron paramagnetic resonance
ERD	elastic recoil detection
ϕ	crossing angle of the pump and the probe beam
FC72	fluorinert
FTIR	fourier transform infrared spectroscopy
FWHM	full width at half maximum
f	focal length
f_{ox}	absolute oxygen flow
HC source	hydrocarbon source

HF	hydrogen fluoride
HNO_3	nitric acid
HPHT	high pressure high temperature
H_2SO_4	sulphuric acid
I	intensity
I_0	intensity of the pump beam in the focus spot
IMO	Instituut voor Materiaalonderzoek, Diepenbeek, Belgium
IR	infrared
κ , κ_f , κ_s	thermal conductivity of the probed medium, surrounding fluid and sample
KUN	Katholieke Universiteit Nijmegen, Nijmegen, the Netherlands
k, k_f , k_s	thermal diffusivity of the probed medium, surrounding fluid and sample
λ	wavelength
L	interaction length between the probe beam and the sample (transverse PDS), interaction length of the pump and probe laser beams (collinear PTD)
L(x,y,z)	equi-phase surfaces of the beam
LC	standard laser calorimetry
Lz	z-component of interaction length of the two laser beams (collinear PTD)
l	thickness of the sample
μ	thermal diffusion length
$\mu_{i,\ i=f,s}$	thermal diffusion length of the fluid, sample respectively
MW	microwave
MWP	microwave power
MWPE	microwave plasma enhanced
η	quantum efficiency at which the absorbed light is converted to heat by the nonradiative deexcitation processes

N	unit vector normal to the equi-phase surfaces
NEP	noise equivalent power
NIRIM	National Institute for Research in Inorganic Materials, Tsukuba, Japan.
NH_3	ammonia
n, n_0	index of refraction ($n_{diamond}$ = 2.4)
dn/dT	index of refraction gradient ($(1/n*dn/dT)_{diamond} = 4.04*10^{-6}$ K^{-1})
P_0	power of the pump beam
PC	photocurrent
PDS	photothermal deflection spectroscopy
PE	plasma enhanced
PH_3	phosphine
PSD	position sensitive detector
ρ	density of the deflecting medium ($\rho_{diamond} = 3.51*10^3$ kg/m^3)
$\rho_{i,\ i=f,s}$	density of the surrounding fluid, sample respectively
P	pressure
P_0	power of the pump beam
θ	integrated deflection angle, PTD deflection signal
θ_k	critical angle of incidence
$d\theta$	change in the direction of propagation
Q_{in}	influx
Q_{out}	efflux, the rate at which heat diffuses out of the illuminated volume
Q(z)	heat deposited per unit length along the z-axis (depth) and per unit time in the sample
ρ	radius of curvature
R	point of the beam path

R	reflectance
RT	room temperature
R_A	surface roughness
r	relative distance between the probe beam and the pump beam
r_D	deposition rate
σ	rms surface roughness of the growth surface
$\mathbf{s}_\perp$	the unit vector normal to **s**
S	normalized PDS-signal (PDS-signal from position sensitive detector / signal of pyrodetector)
S	scattering
S_{ac}	acetylene supersaturation
S_{ext}, S_{int}, S_t	scattering correction factors
S_0	illuminated surface area of the sample
S_{sat}	saturation signal
SEM	scanning electron microscope
SIMS	secondary ion mass spectroscopy
sccm	cubic centimetre per minute at standard temperature and pressure
τ	a correlation length of the surface roughness and inhomogeneities.
T	transmittance or temperature
$T_{i,\ i=f,s}$	the temperature rise above the ambient temperature in medium i, with i = s, f for respectively the sample and fluid
ΔT_1, ΔT_2	temperature increase and decrease
T_R	ambient temperature
T_S	substrate temperature
$T_s(0)$	complex amplitude of sample temperature at y = 0, i.e. at the illuminated area.

T_{so} T_{0s}	sample surface temperature
TM_{01}	transversal magnetic mode 01.
t	time
t_D	deposition time
t-PDS	transverse photothermal deflection spectroscopy
UV	ultra violet
υ	modulation frequency
ω	circular frequency
WTOCD	Wetenschappelijk en Technisch Onderzoekscentrum Diamant (Lier, Belgium)
x_0	relative position of the probe beam to the pump beam
z_0	minimal distance between the probe beam and the sample surface

Preface

Because of its unique properties diamond has attracted the attention of scientists for ages. Its extreme hardness, transparency over a very wide wavelength range, high thermal conductivity, wide bandgap, high carrier mobility and breakdown voltage are very promising for a myriad of applications varying from cutting tools, heat sinks, optical windows, to particle detectors and surface acoustic wave devices etc. The full exploitation of diamond for electronic and optical applications was hindered due to problems with the preparation of high quality material. First of all, as is well known, natural diamond is extremely rare and moreover its cost price is astronomically high. On the other hand, synthetic diamond grown by high pressure high temperature (HPHT) methods forms since the fifties an alternative, but the HPHT diamond crystals are very small and include a lot of substitutional nitrogen and metallic impurities. Therefore the practical use is mainly limited to industrial applications such as cutting tools and abrasion-resistant materials.

The discovery of the chemical vapour deposition (CVD) technique at the beginning of the eighties, created high expectations of utility. The CVD technique allows to deposit diamond thin films on top of (non)-diamond substrates, over a relatively large area, at relatively low temperatures and pressures. However, up till now, CVD diamond films contain, to a greater or lesser extent, defects (e.g. amorphous carbon and graphite, nitrogen) introduced during growth. In combination with the fact that most of the CVD diamonds are polycrystalline and contain a lot of grain boundaries, the presence of these defects is a limiting factor for future electronic and optical applications.

The use of diamond in electronic applications demands not only low extrinsic/intrinsic defect concentrations but also a high incorporation of n- and/or p-type dopants. Within these limitations, the use of the CVD technique for diamond thin film preparation was expected to be very promising because of the possibility of in-situ doping from the gas phase. In general, except the p-type doping, in-situ doping during CVD did not yield significant success in the past, in spite of theoretical studies which indicate P, Li and Na as possible n-dopants. The main reason is that the (intrinsic) defects in CVD diamond act as compensation and neutralisation centres for the donor levels.

Therefore, a key issue in the diamond field is the preparation of high quality CVD diamond films with reduction of the number of defects resulting in films equivalent to

type IIa (purest quality) natural diamond. To achieve this goal, one of the main tasks is the quantification of these defects. A deeper understanding of their localised defect states in the bandgap is needed for further progress in the CVD diamond-application area. In a second stage, doping experiments can be carried out to search for a suitable dopant.

To deposit diamond films of the required quality and doping-level, optimisation of the deposition conditions is very important. In addition, sensitive characterisation tools, which can detect very low levels of defect and dopant concentrations, are needed to investigate the quality of the diamond films and to obtain spectroscopic information about the dopant levels in the bandgap. Feedback has to be given to adapt the deposition process in such a way that it results in the synthesis of higher quality CVD diamond films.

To get a deeper understanding about the defects present in CVD diamond films (in relation with the deposition conditions), we have studied the defect related subgap absorption. Conventional optical transmission measurements are not sensitive enough to detect low absorption values. Moreover, they are strongly influenced by elastic light scattering (in the free-standing polycrystalline CVD diamond films). Hence, special techniques have to be used. Photothermal deflection spectroscopy (PDS) is a very sensitive technique, which has been used in the past to study the spectral dependence of the optical absorption coefficient in e.g. amorphous Si. With this technique absorptance αd down to 10^{-5} can be measured, compared to 10^{-2} for conventional spectrophotometers. This investigation yields information about optically active defects and impurities in the diamond films and gives indications about the structure and the optical excitation energies of the defects.

In this thesis we will describe how the PDS technique is adapted to investigate the spectral dependence and the spatial distribution of defects and impurities in CVD diamond films. The PDS method is applied to a variety of undoped and doped diamond films of different quality.

Chapter 1 summarises briefly the main properties and applications of diamond. The shortcomings of CVD diamond to be candidate for a variety of applications are discussed. It is pointed out that defects play the leading role in many properties of CVD diamond films. We motivate why we have chosen PDS techniques to study the defect-related optical absorption in CVD diamond.

Chapter 2 describes the synthesis of undoped and doped CVD diamond thin films. The

chapter starts with an historical overview of diamond synthesis and focuses on the low pressure deposition. The main principles of the microwave plasma enhanced chemical vapour deposition are enlightened. The nucleation and growth stages are discussed. A short remark about polishing is made.

In Chapter 3, we continue the experimental part with an extensive description of the two PDS techniques used: the transverse PDS (t-PDS) technique, used to study the spectral dependence of the optical absorption coefficient, and the collinear PDS (c-PDS) method, which allows 1D and 2D mapping of the optical absorption coefficient with a spatial resolution of 100µm. For both configurations (transverse and collinear), the experimental set-ups and the theoretical models are discussed. Emphasis is put on the specific adaptations for the study of CVD diamond and much attention is devoted to the scaling on absolute values. Finally, in Chapter 4 the influence of scattering and light trapping on transverse PDS measurements is investigated.

The study of native defects and impurities in undoped CVD diamond is the topic of Chapter 5. Firstly, lower quality material is studied using t-PDS measurements. For the first time, one of the most important defect structures in the CVD diamond films (π-π^* optical transitions) is identified. A theoretical model to describe these transitions is developed. Comparison of PDS absorption spectra with Raman spectra took place and a good agreement between the intensities of the π-π^*absorption band (t-PDS) and the graphite Raman band can be observed. Secondly, the local optical absorption coefficient α of high quality CVD diamond films at the CO_2 laser wavelength of 10.6 µm is investigated by means of c-PDS measurements. It is suggested that the absorption mechanism is greatly affected by the black features present in all CVD diamond films.

Chapter 6 is devoted to the study of doped CVD diamond films. To investigate the spectral dependence of the optical absorption coefficient related to the presence of nitrogen, lithium and phosphorus in CVD diamond films, the t-PDS technique is used. N-doped diamond films show absorption spectra similar to type Ib HPHT diamonds, indicating the presence of substitutional nitrogen in the films. In the Li-doped films a new Li- related defect at 1.5 eV was detected, but up till now the exact electronic picture is not clear. Finally, we have investigated for the first time P-doped diamond films by t-PDS and the measurements point to a donor level at about 0.56 eV.

1. CVD Diamond – a new optical and semiconducting material?

1.1. Diamond and CVD diamond thin films

1.1.1. The structure of diamond

Diamond is one of the many forms of solid carbon. Besides a range of non-crystalline and/or semi-crystalline forms as amorphous carbon, diamond-like-carbon, nanotubes, bucky balls, crystalline forms as graphite and hexagonal diamond (lonsdaleite) and cubic diamond are well known. Cubic diamond crystals have a face-centred cubic structure consisting of two interpenetrating lattices whereby one lattice is shifted one quarter of a cube diagonal with respect to the other (see Fig. 1.1).

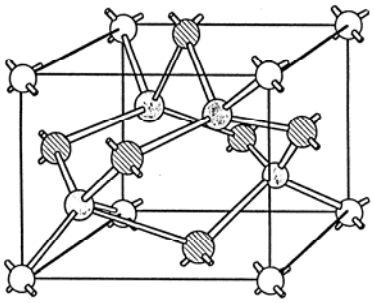

Fig. 1.1 Face-centred cubic structure of diamond. (ref.[DAV93])

The pure natural cubic diamond structure consists of sp^3 hybridised carbon. The sp^3 sites use their four valence electrons to form tetrahedral σ bonds with four adjacent atoms. The bond angles are 109.5°, the bond length is 0.154 nm and the lattice constant is 0.356 nm [FIE92]. The very strong covalent chemical bond of diamond is partially responsible for its unique properties.

Polycrystalline Chemical Vapour Deposited (CVD) diamond films mainly consist of sp^3 bonded carbon. Because CVD diamond is synthesised under metastable temperature and pressure conditions, in the region were graphite is the stable form of carbon (see Chapter

2, Fig. 2.1), graphite and amorphous carbon (a-C) defects are incorporated in the diamond structure during CVD growth. These a-C and graphite inclusions are probably located in the grain boundaries and at other defect sites in the film. Graphite consists of sp^2 bonded carbon. A sp^2 site forms trigonal σ bonds with three neighbouring atoms in plane (in plane six-membered rings, bond angle 120°). The weaker π bond (p_z orbitals) normal to this plane, realises the bonding between the layers. In the case of amorphous carbon, the four valence electrons occupy s, p_x, p_y, and p_z atomic orbitals.

1.1.2. Classification of diamond

Both, natural and synthetic diamond contain a lot of impurities, including nitrogen (N), boron (B), hydrogen (H) and oxygen (O). The presence of different defects and impurities yields different peaks and bands in IR absorption spectra. Based on these spectra diamond is divided into different classes [WAL79], [FIE92], [WOO94], [ENC94].

The main subdividing in type I and type II diamond is based on the presence of N. Type II diamonds are nitrogen-poor; N is present in only such a very small concentration, that it is not detectable by IR spectroscopy while type I diamond contains up till 0.5 % nitrogen.

The different sub-classes of **type I** diamond may be understood in terms of the aggregation of nitrogen. *Type Ia* diamonds are these where nitrogen (till 0.3 %) is present in non-paramagnetic sites in the shape of nitrogen aggregates: A-centres (2 N atoms aggregated), B-centres (4 N + vacancy) formed by migrated A-centres and platelets (all different N-aggregates: pairs, triplets, quartets and larger aggregates). Most of the natural diamonds (more than 90 %) belong to the type Ia group. The colouring of these diamonds varies widely. Diamond containing paramagnetic single substitutional nitrogen is classified as *type Ib*. Type Ib diamonds, which contain till 0.05 % substitutional N, are seldom found in nature, but most high pressure high temperature (HPHT) diamonds belong to this type. The colour of these diamonds is yellow.

Type II diamonds are relatively pure, without nitrogen. *Type IIa* diamonds are the most pure natural diamonds, in principle free of defects and are very rare in nature. Because of the lack of defects resulting in colourless and transparent crystals, these gem stone quality diamonds are very much wanted for the diamond cutting and jewel industries. *Type IIb* diamonds contain boron in greater amount than nitrogen, exhibit p-type semiconducting

properties and are blue coloured. Boron-containing diamonds are also rare in nature.

Concerning CVD diamonds, most films contain an important concentration of a-C and graphite inclusions [NES96]. Nevertheless, state of the art high quality undoped CVD diamond films approach the purity of type IIa diamonds. Furthermore, as will be shown in chapter 4, we detected for the first time the presence of single substitutional N in CVD diamond films, pointing to type Ib material [MEY96]. Often even in intentionally undoped diamond films, very small amounts of N, H and O can be found because of contaminations of the deposition system. Up till now, no reports about type Ia CVD diamond have been published, but by using boron-dopants, type IIb CVD diamonds can be relatively easily synthesised [FUJ86], [MOR89].

1.1.3. Diamond properties and applications

Diamond possesses a variety of excellent properties and by most it is 'the biggest and the best' (see Table 1.1). Therefore, it attracts a lot of attention, both from fundamental and from technological point of view and it is the perfect candidate for a lot of industrial applications in a wide range.

Diamond is the hardest material known with a value approximately double that of cBN, which in turn is twice as hard as the conventional abrasives [DEB00]. Because of this, CVD diamond is applied as abrasive and as coating on cutting tools, and as wear-resistant coating on other tools [MAY95].

Other remarkable properties of diamond are the outstanding thermal and optical properties such as the highest thermal conductivity at room temperature (RT). The RT thermal conductivity is more than five times that of gold, silver or copper - a property which can be used to considerable advantage in the design and operation of high-performance electronic circuitry (heatsinks in laser diodes, high power amplifiers and IC's [LU92]). Diamond can be transparent over a very broad range, from UV to infra-red and for certain types of laser radiation (highest transparency of all materials), and so it can be used as high-performance windows and sensors (e.g. IR windows, X-ray beam-position sensors).

In addition, in combination with its wide indirect bandgap (5.49eV) [CLA64], [DEA65] diamond has high carrier mobilities and a high breakdown voltage leading to electronic device applications. Because of the high speed of sound and high phase velocity of diamond, the use of diamond SAW devices allows to work at much higher frequencies

(above 2GHz) [GLA98] than the conventional SAW devices. The negative electron affinity is exploited in diamond-based field emitters [SHI98]. These field emitters based on the cold electron emission of diamond can be used in flat-panel displays, electron guns, etc.

Table 1.1 Some of the outstanding properties of diamond [SPE94].

Properties	
Broad optical transparency	From deep UV (225 nm) to the far IR region (with the exception of the region from 3 - 5 μm) of the electromagnetic spectrum
Highest known thermal conductivity at RT	2 x 10^3 W/mK
Superior insulator: RT resistivity	10^{14} Ωcm
By doping the resistivity can be changed	p-type: 0.1 Ωcm
High carrier mobility electron hole	 2200 cm^2/Vs 1600 cm^2/Vs
High breakdown voltage	10^7 V cm^{-1}
Extreme mechanical hardness	90 GPa
Chemically inert	except for oxygen at HT

Because of its chemical inertness the diamond applications can operate in harsh environments. Moreover, the radiation-hardness of diamond is one of the advantages of diamond over more conventional detector materials (sensors such as UV detectors, particle detectors) [MAI98], [MAR98].

However, in practice, several obstacles had to be overcome before applications could be realised. Because of its polycrystalline nature, CVD diamond films contain a lot of grain boundaries. Furthermore, various defects and impurities can be incorporated during synthesis, leading to minor quality diamond with properties weaker than the optimal values listed in Table 1.1. Chapter 6 is devoted to defects in CVD diamond.

Diamond windows for the laser industry demand high optical quality material with a high transparency at the appropriate laser wavelengths, which means films with a very low defect concentration. Therefore the ultimate goal is the fabrication of large-area CVD diamond windows with the optical properties of type IIa crystals (the purest natural crystals) which can be polished till the wanted curvatures. Further, when trying to use diamond's electronic potential major problems occur. Only p-type doping (with B) is possible [FUJ86], [GLA98]. Although the first reports of successful n-type doping have been made [KOI97], a high quality low resistance n-type material is not yet available.

The recent progress in the development of CVD diamond thin film technology resulted in intensive research activities because of the possible industrial applications in electronics and optics. At present the most promising applications are tools, heatsinks, optical windows and SAW devices [SHI98]. Still, there is a lot of work to be done both in optimisation of the growth process to prepare optical- and electronic-quality material with low density of defect states and in characterisation of the CVD diamond films.

1.2. Optimisation of diamond for applications

As already mentioned in section 1.1, the quality assessment of CVD diamond films forms a very important issue for technological improvements. CVD diamond films containing intrinsic and extrinsic defects (minor quality films) do not meet the requirements for optical and electronic applications. The defects and impurities lead to localised defect states in the forbidden bandgap. Moreover, the lack of a suitable n-dopant hinders the full exploration of the electronic potential of CVD diamond films. For the realisation of numerous industrial applications, one has a huge need for high quality large area diamond thin films, both undoped and n- or p-type doped films.

Therefore, one of the main tasks in CVD diamond research is the quantification and the reduction of the (gap) defect states which cause sub bandgap absorption in the diamond films. To reduce these defects and impurities, and to improve the quality of the CVD diamond films, a fundamental knowledge about the nature, the ionisation energy, the energy distribution, the concentration and the origin of the impurities is indispensable. Secondly, one has to continue the search for a suitable n-dopant. Besides the above noted properties, the electronic activity of the dopant has to be investigated too. Finally, feedback from the characterisation measurements to the deposition process (growth procedure) lead to adaptations of the diamond deposition conditions. On its turn, this will

lead to material optimisation, in such a way that the changes result in better quality CVD undoped and electronically active doped diamond films.

To study both the defect-induced subgap absorption in the ppm range or lower and the absorption caused by dopant atoms, very sensitive appropriate characterisation techniques must be developed. The results obtained from a combination of different characterisation techniques will lead to a better understanding of the defects present in CVD diamond. The main characterisation techniques are spectroscopic methods. An important role play the optical characterisation techniques. The measurement of the optical absorption coefficient as a function of the photon energy is a standard method for the determination of defect levels in a semiconductor. Optical absorption methods, such as transmission/reflection spectroscopy, photothermal deflection spectroscopy (PDS) and the opto-electronic methods including the photocurrent (PC) and the constant photocurrent method (CPM), have proven to be very powerful for studying the electronic structure in the tetrahedrally bonded semiconductors [TAU74], [VAN83], [COD84]. In this thesis we have focused on the photothermal deflection method to study the very low optical absorption in CVD diamond films.

Other characterisation techniques used to study the defects in CVD diamond films and their influence on the film properties are Electron Paramagnetic Resonance (EPR), Infrared spectroscopy (IR), Fourier Transform Infrared spectroscopy (FTIR), Raman spectroscopy, Deep Level Transient Spectroscopy (DLTS), Optically excited Deep Level Transient Spectroscopy (O)DLTS, Thermally Stimulated Currents (TSC), Space Charge Limitted Currents (SCLC), Laser Calorimetry (LC) etc.

1.3. Transverse and collinear photothermal deflection spectroscopy (PDS) techniques as new detection techniques for diamond

When looking for defect-induced subgap absorption in the ppm range and lower, very sensitive techniques must be used. For high quality CVD diamond films conventional transmission measurements are not sensitive enough. The precision of transmission measurements (~ 0.1-1%) is only sufficient to detect high optical absorption values ($\alpha d \sim 10^{-2}$). Furthermore, the problem is that light scattering of the CVD diamond films strongly influences transmission measurements.

When testing the optical quality of CVD diamond films, the optical absorption of the films is monitored. Laser calorimetry (LC) measurements are excellent to obtain absolute

absorption values of the whole sample but the drawback of this technique is that mapping of the optical absorption coefficient cannot simply be carried out. A first attempt of LC mapping was presented very recently by Müller-Sebert et al. [MUL99].

The PDS method offers for both problems a solution. This method allows to investigate the optical (optical absorption coefficient α) and thermal (thermal diffusivity) parameters of thin films. PDS suffers considerably less from light scattering effects (see Chapter 4). Besides, it allows to measure absorptances down to a 10^{-5} level (transverse PDS), giving the possibility to investigate deep defects on the ppm scale and below, even in 10 µm thick diamond films. Collinear PDS (c-PDS) is even a more sensitive technique ($\alpha d \sim 10^{-7}$) [BOC80] and because of the design of the c-PDS set-up, local (spatial resolution ~ 100 µm) testing of the absorption coefficient is possible. When using a focused illumination 'pump' beam and by scanning the sample by this beam, two dimensional mapping of the optical absorption coefficient α can be carried out.

Absorption spectroscopy is an important way to determine the defects and impurities present in the material because the optical absorption coefficient α is related to the density of gap states (DOS). In theory, both the energy and the concentration of the DOS of the (localised) defects and dopants can be obtained by deconvoluting the absorption spectra. Absorption spectra showing the energy dependence of the optical absorption coefficient allow the characterisation of material parameters such as the defect and dopant levels, the doping concentration and the film homogeneity.

PDS can detect all optical transitions possible between electronic states, independently whether the final states are localised (localised electrons) or extended (yielding free electrons). Therefore, t-PDS and photocurrent techniques yield complementary information. In contrast to the t-PDS method, quasi-steady state photocurrent (PC) and constant photocurrent methods (CPM) are only sensitive to absorption processes which generate mobile (free) carriers. Only the electronic active levels contribute to the photocurrent, and the final states involved in the detected transitions are all extended states (free carriers).

1.4. References

[BI90] X.X. Bi, P.C. Eklund, J.G. Zhang, A.M. Rao, T.A. Perry, C.P. Beetz, Jr., J. Mater. Res. **5** (1990) 811.

[BOC80] A.C. Boccara, D. Fournier, W. Jackson, N.M. Amer, Optics Lett., **5** (9) (1980), 377.

[CLA64] C.D. Clark, P.J. Dean, P.V. Harris, Proc. Roy. Soc. A **227** (1964) 312.

[COD84] G.D. Cody in Semiconductors and Semimetals, ed. J.I. Pankove, (1984), Chap. 2, Academic Press, 11-82.

[DAV93] R.F. Davis, '*Diamond Films and Coatings. Development, Properties and Applications'*, ed. R.F. Davis, Noyes Publications (1993).

[DEA65] P.J. Dean, E.C. Lightowlers, D.R. Wright, Phys. Rev. **140A** (1965) 352.

[DEB00] http:/www.debid.co.uk

[ENC94] W.J.P. van Enckevort, '*Synthetic diamond, Emerging CVD Science and Technology', ed.* K.E. Spear, J.P. Dismukes, John Wiley & Sons, Inc. (1994), Chapter 9.

[FIE92] J.E. Field, *'The properties of natural and synthetic diamond'* Academic Press, London (1992).

[FUJ86] N. Fujimori, T. Imai, and A. Doi, Vacuum **36** (1986) 99.

[GLA98] J.T. Glass, B.A. Fox, D.L. Dreifus and B.R. Stoner, MRS Bulletin **23** (1998) 49-55.

[KOI97] S. Koizumi, M. Kamo, and Y. Sato, H. Ozaki and T. Inuzuka, Appl. Phys. Lett. **71** (1997), 1065.

[LU92] G. Lu, L.K. Bigelow, Diamond Relat. Mater.**1** (1992) 34.

[MAI98] A. Mainwood, Diamond Relat. Mater. **7** (1998) 504-509

[MAR98] M. Marinelli, E. Milani, A. Paoletti, A. Tucciarone, G. Verona Rinati, N. Randazzo, R. Potenza, M. Pillon, M. Angelone, Diamond Relat. Mater. **7** (1998) 519-522.

[MAY95] P.W. May, Endeavour Mag. **19** (1995) 101-106.

[MEY96] K. Meykens, M. Nesladek, C. Quaeyhaegens, L.M. Stals, M. Vanecek, J. Rosa, J.J. Schermer, G.Janssen, Diamond Relat. Mater. **5** (1996) 958-963.

[MOR89] J. Mort, D. Kuhman, M. Machonkin, M. Morgan, F. Jansen, K. Okumura, Y. M. LeGrice and R.J. Nemanich, Appl. Phys. Lett. **55** (11) (1989), 1121-1123.

[MUL99] Müller-Sebert et al. presented at Diamond '99 in Prague, 12-19 September 1999.

[NES96] M. Nesladek, L.M. Stals, A. Stesman, K. Iakoubovskii, G. Adriaenssens, J. Rosa and M. Vanecek, Appl. Phys. Lett. **72** (1998) 3306.

[SHI98] S. Shikata, MRS Bulletin **23** (1998) 61-64.

[SPE94] K.E. Spear, J.P. Dismukes, *'Synthetic Diamond, Emerging CVD Sciences and Technology'*, John Wiley & Sons, Inc. (1994).

[TAU74] J. Tauc in Amorphous and Liquid Semiconductors, (1974) ed. J. Tauc, Chapter 4, Plenum, New York.

[VAN83] M. Vanecek, J. Kocka, J. Stuchlik, Z. Kozisek, O. Stika, A. Triska, Solar Energy Mater. **8** (1983) 411.

[WAL79] J. Walker, Rep. Prog. Phys. **42** (1979) 1605.

[WOO94] G.S. Woods, '*Properties and growth of Diamond'*, ed. G. Davies, INSPEC, IEE, London (1994).

2. Synthesis of CVD diamond thin films

2.1. Historical background

As very well known, natural diamond is one of the most rare and expensive materials. Therefore, the possibility to synthesise diamond on a large scale, expanding the industrial applications, has always been an important topic of the materials research area.

One had to wait till 1953 when the high-pressure high-temperature (HPHT) synthetic diamond growth was developed by Eversole et al. [EVE62] at General Electric (USA), and by Bundy [BUN55]. The successful synthesis of diamond by HPHT methods heralded a new era for synthetic diamond industrial applications. The wide majority of HPHT diamonds is type Ib and contains nitrogen and (other) metallic inclusions. They are mainly consumed by the industry and used almost exclusively as grit for mechanical applications such as grinding, milling and drilling. Moreover, at that time, only diamond grains/granules of a very small size could be grown by the HPHT technique and diamond thin films were still dreams for a far future.

Important research activities are still going on in the field of HPHT synthesis. Very pure crystals of a few carats (1crt = 0.2 g), and large plates of 2 cm in diameter can be prepared currently. Nevertheless, this method could not be used for the preparation of large-area diamond which would allow completely new applications in the field of optics, thermal management and, what is very interesting, in the electronics area. The significant activity of development and the search for new techniques allowing such preparation has been ongoing since the fifties.

The first successful chemical vapour deposition (CVD) of diamond took place in the early seventies by Russian scientists (Deryagin, Fedoseev and Spitsyn) [DER75] using the chemical transport technique (starting from C and hydrogen). A few years later, Matsumoto and co-workers at NIRIM[1] [MAT81], [KAM83] used plasma enhanced CVD techniques to grow diamonds. Both developments engendered great expectations of industrial utilisation. The plasma enhanced CVD technique allowed for the first time the deposition of diamond thin films. This gave the initial impetus to an intensified research on this matter and hence, considerable progress has been made on the preparation of

[1] National Institute for Research in Inorganic Materials, Japan

CVD diamond films during the past decades. Nevertheless, the realisation of commercial applications based on diamond-films (tool, optical and corrosion-resistant coatings, flat-panel displays, thermomanagement for electronic components, etc.) didn't show up the boom as expected in the excitement of the beginning days. A lot of scientific and technical problems had to be solved before one fully could exploit the potential of diamond films.

One of the most important obstacles was the large proportion of non-diamond (sp^2-bonded) carbon present in the diamond films of the early days. A major amount of the scientific diamond research has always been focussed on the optimisation of the diamond quality. Nowadays, optical quality material can be prepared and the commercialisation has begun. There are two main approaches in this area. The first, used for example by De Beers, is to prepare large grain size diamond windows [PIC99] with very clean grain boundaries. The second one is the study of the growth of heteroepitaxial oriented films on Si, which can be removed, yielding free-standing films suitable for optical applications. Recently, people started to grow on other materials such as Iridium [SCH99], [SAI98] or Platinum [TAC99], aiming to prepare single crystal diamond films on non-diamond substrates.

Parallel with this, another very important development is improving the purity and lowering the defect density in diamond films. This is necessary to prepare material suitable for future electronic applications and, eventually, to dope in-situ diamond films. p-Type doped diamond layers are already for a long-time available and a lot of reports about successful B-doping occurred in literature. For example, in 1986, Fujimori et al. used diborane (B_2H_6) to dope the diamond layers in a Microwave Plasma Enhanced MW PECVD system [FUJ86]. Later, Mort et al. [MOR89] added B_2H_6 to the precursor gas mixture to grow by the hot-filament technique boron doped CVD diamond layers. Okano and co-workers [OKA89] used the MW PECVD technique with boron trioxide (B_2O_3) powder diluted in methyl alcohol (CH_3OH) as the boron source. On the other hand, the search for an active n-dopant, indispensable in electronic components, was much more difficult. Theoretical studies indicated P, Li, Na, as possible n-dopants [KAJ91]. But the whole scientific world had to wait till the major breakthrough in 1997 when Koizumi et al. succeeded to grow electrical active n-type doped material by adding phosphine (PH_3) in the MW reactor [KOI97]. Very recently sulphur-doped (using H_2S) diamond layers yielding n-type diamonds are reported [SAK99] and new attempts to dope the CVD diamond films with Li are carried out [STE99].

2.2. Low-pressure synthesis

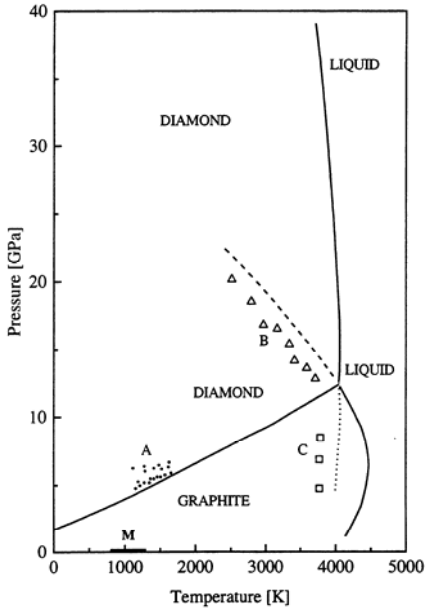

Fig. 2.1 Phase diagram of carbon. (A) Catalytic diamond synthesis. (B) Spontaneous transition to diamond. (C) Spontaneous transition to graphite.(M) Region of low pressure diamond synthesis (after ref.[BUN55])

The low-pressure synthesis of CVD diamond occurs at conditions where graphite is the stable form of carbon (see phase diagram Fig. 2.1). The trick to grow diamond is to generate atomic hydrogen during the deposition, which etches away to a more or lesser extent the graphitic (sp^2) bonded carbon, deposited simultaneously with the diamond. The presence of hydrogen has still additional functions such as the stabilisation of the diamond surface, participation in the surface C-addition reactions etc. [FOR96], [DAV94]. Although several groups have systematically studied this topic, there is no unanimous theory about the mechanism of CVD diamond growth. The relative concentration of atomic hydrogen, the substrate temperature (important for ongoing surface reactions) and the other CVD growth conditions, have an important influence on the diamond film morphology and the size of the grains on one hand, but also on the incorporation of non-diamond carbon and other impurities and on the generation of point defects and/or their complexes with impurities on the other hand. All this is very important for the preparation of diamond with controlled properties, which can be used

for example for optical applications.

Diamond growth can be performed by different types of methods. The most important and widely used techniques are plasma enhanced techniques such as MW deposition, plasma-jet (thermal plasma), dc glow discharge plasma and thermal decomposition methods (CVD) as hot filament, laser induced CVD and combustion flame deposition.

In the next paragraph the MW plasma deposition technique, which is used at IMO to grow thin CVD diamond films, is discussed briefly. The features necessary to understand the main characteristics of the prepared CVD diamond films are described. The samples studied in this thesis and coming from other origins (NIRIM - Japan, KUN - the Netherlands, and De Beers - UK) are also prepared by CVD techniques. The P-doped samples from NIRIM were homoepitaxially grown on natural diamond substrates in a MW system [KOI97]. The samples from the KUN were flame grown diamond layers, which contained nitrogen [SCH94]. At last, the deposition conditions of the optical quality samples of De Beers were not revealed. For more details and extended descriptions of the other CVD methods we refer to the literature [DIS98], [JAN92].

2.3. Main principles of microwave plasma enhanced deposition

A schematic picture of a commercial ASTeX PDS 17 MW deposition system used for preparing the diamond films for this thesis is shown in Fig. 2.2. The main components of the system are a microwave source, a rectangular waveguide with circular applicator, a vacuum vessel deposition chamber with a substrate holder, a gas inlet with mass flow meters, the vacuum pumps and the pressure control system.

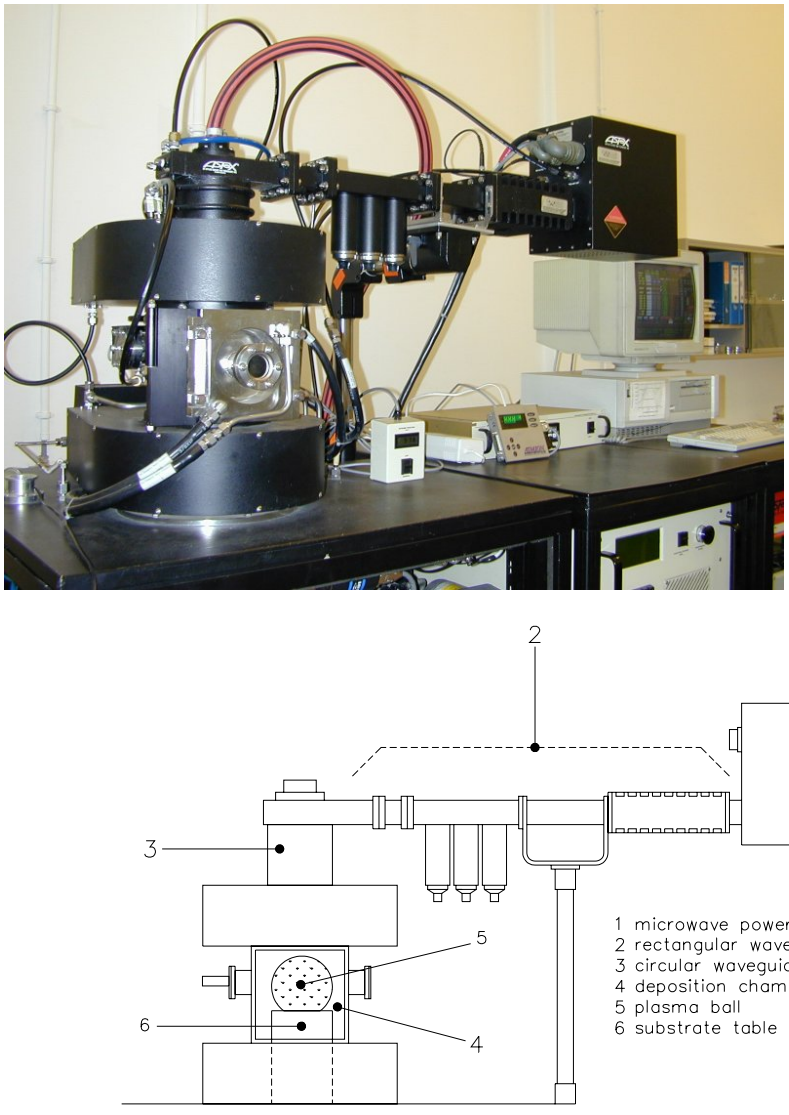

Fig. 2.2 (a) A photo of our commercial ASTeX PDS 17 MW deposition system, (b) a schematic picture of the MW deposition system.

Via a quartz window, the microwaves are coupled into the cavity in order to ionise the gas mixture and to initiate a gas discharge. A symmetrical ball-like plasma (TM_{01} mode) is thus generated in the cavity. Its size and the gas and plasma parameters (temperature,

spatial distribution of the gas species) can be controlled by precise tuning of the microwave power and the gas pressure [GHI93]. The microwave energy absorbed in the plasma activates chemical reactions in the gas phase. Dissociation of the gas species and creation of new species and/or radicals occur (e.g. H_2 produces atomic hydrogen). The generated plasma species are transported towards the growing surface. The exact description of the MW plasma has been a topic of many publications, see for example [SPE94], [GOO98].

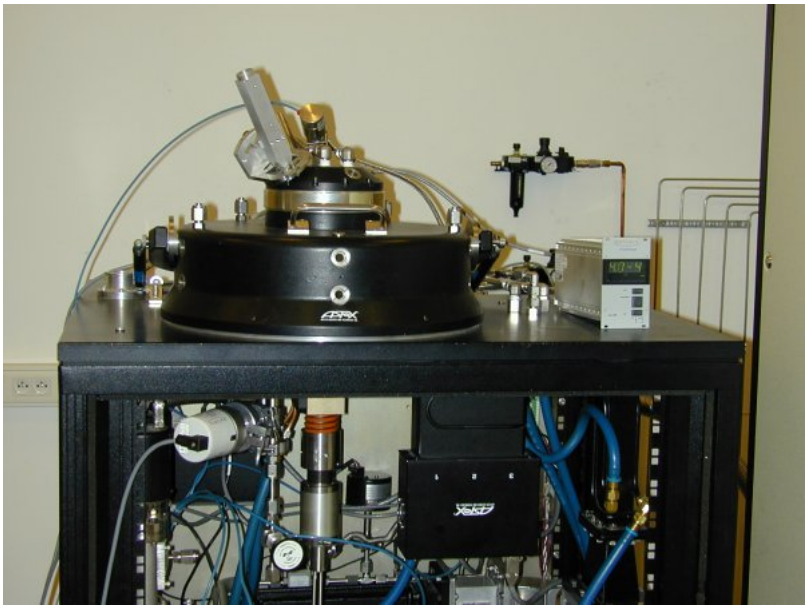

Fig. 2.3 A photo of our commercial ASTeX AX6500 MW deposition system

A mixture of process gases such as molecular hydrogen (H_2), carbon containing gas precursor typically methane (CH_4) and, eventually, oxygen (O_2) and various doping-sources (N_2, etc.), can be introduced in the vacuum reaction chamber of the diamond reactor.

Monocrystalline Si substrates with an {100}-oriented surface are often used as substrates on which the diamond films grow. The use of a Si substrate has the advantage that Si can be dissolved afterwards thus yielding free-standing CVD diamond films which can be measured with optical techniques such as PDS. The substrates are mounted on top of the substrate stage at the bottom of the deposition chamber.

2.4. Nucleation and diamond growth

It is known that the diamond nucleation density on an untreated surface is very low and that the nucleation density can be significantly enhanced by a nucleation pre-treatment such as scratching. The mechanism and the model for nucleation have been proposed in [DEM97], using a kinetic model for heterogeneous nucleation. The number density, the nucleation rate and the time delay for critical cluster formation were studied for the nucleation of diamond on untreated Si-wafers. Modelling revealed that the influence of scratches and microparticles at the surface were critical for diamond nucleation.

Bias enhanced nucleation (BEN) [WOL93], [STO92], [WIL94], [FLO98] is a well-known method used for heteroepitaxial CVD diamond growth resulting in a nucleation density enhanced by several orders of magnitude. Moreover, the growth of highly oriented films is promoted (see Fig. 2.7). A negative bias is applied to the substrate during the nucleation phase, i.e. during the first stage of CVD diamond growth. Afterwards, the diamond growth is performed under the normal process conditions. The BEN mechanism is not clear yet: different models have been proposed but the process is still subject of discussion [ROB95].

During the nucleation step, diamond seed crystals start growing from the nucleation sites generated by the pre-treatment. They grow out to larger columnar grains increasing in size from the substrate (nucleation surface) towards the growth surface. They coalesce to form a continuous film, whereby some of the grains are overgrown by their neighbours (see cross section drawing Fig. 2.5 and SEM photographs of the growth of a diamond film Fig. 2.6 and Fig. 2.7). The top surface of a diamond film is not completely flat but consists of truncated pyramids in the case of (111)-oriented crystals or rectangular grains in the case of (100)-oriented crystals. The top surface roughness is strongly related to the thickness of the diamond film (thicker films show higher roughness) and depends also on the orientation ((100)-oriented substrates are smoother than (111)-oriented ones).

The selection of the correct gas composition is necessary to obtain diamond growth. Bachmann et al. [BAC91] have summarised much experimental data for the diamond growth chemistry in a triangular C-H-O composition diagram. The conclusion from this diagram is that CVD diamond synthesis, no matter which type, only occurs within a small region of gas compositions (see Fig. 2.4).

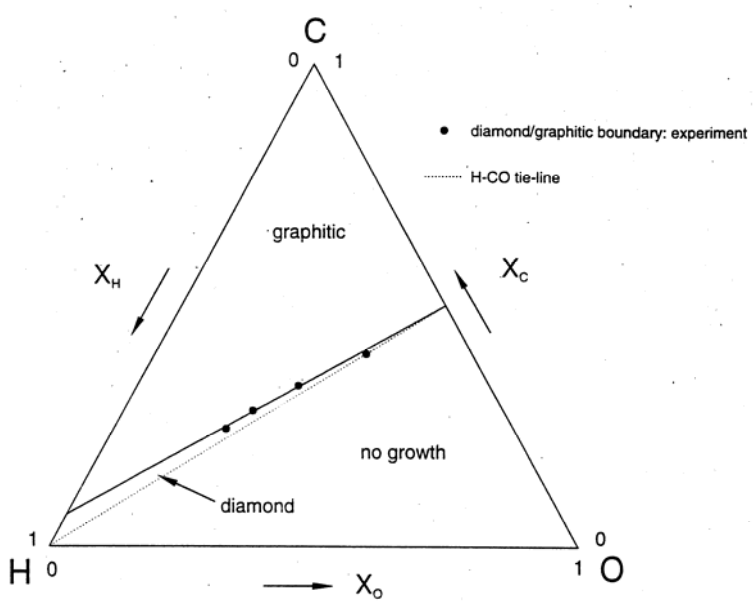

Fig. 2.4 Bachmann diagram showing diamond/graphitic region boundary as a function of the C-H-O ratios of the feed gas (after [FOR96]).

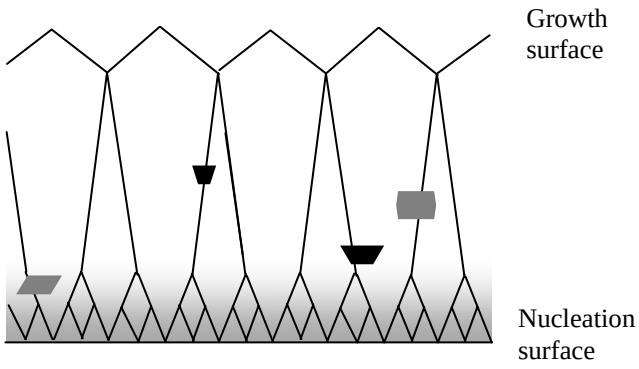

Fig. 2.5 Cross section drawing of a diamond film.

The size and the orientation of the grains, the concentration of non-diamond carbon at the grain boundaries, the stress and corresponding fractures in the film, etc., all depend not only on the selection of the correct gas composition but also on a correct surface/plasma temperature and chamber pressure in order to obtain optimal diamond growth and to

reduce the growth of a-C and graphite simultaneously. For example the grain boundaries in polycrystalline diamond films are assumed to be decorated by non-diamond carbon inclusions. This leads to black-brownish non-transparent films with deteriorated physical properties.

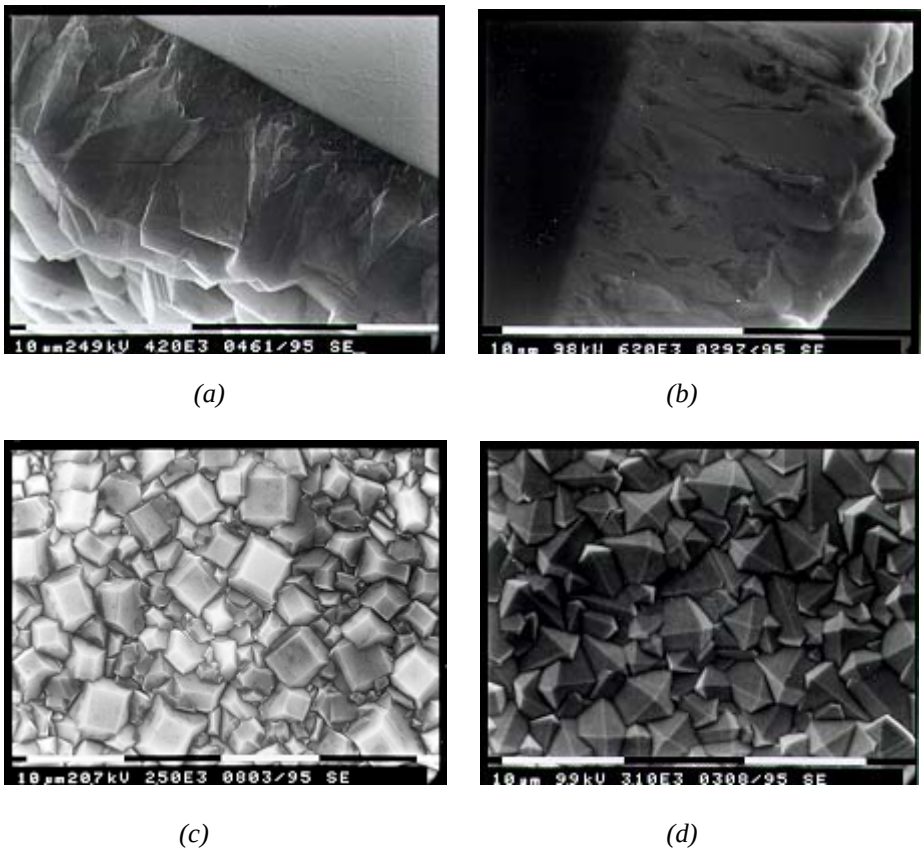

(a) *(b)*

(c) *(d)*

Fig. 2.6 Typical SEM photographs of different quality diamond films deposited on Si substrates with the MW technique: (a, b) cross sectional view, (c) top view of a (100)-oriented diamond film, (d) top view of a (111)-oriented diamond film.

The deposition parameters such as the gas concentration can be modified in a systematic way. In particular the hydrocarbon (HC) source (methane CH_4, hexane C_6H_{14}) and HC concentration, addition of other gases (for example oxygen causes an increased etching of the graphitic phase) or other dopants can be varied. The substrate temperature, the

substrate bias voltage, microwave power and chamber pressure can be varied. As a result of the changes in deposition parameters, the obtained films differ in their preferred orientation, morphology, colour, grain size and quality (sp^2/sp^3 ratio), see Fig. 2.6.

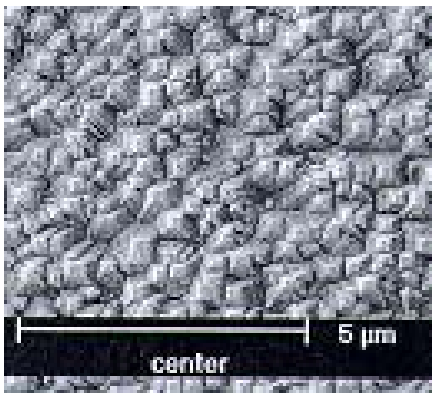

Fig. 2.7 Typical SEM photograph (100) highly oriented diamond film (according [FLO98]).

2.5. Experimental details

The samples investigated in this thesis can be divided into two categories. The first category consists of samples grown at our own institute (IMO). The goal was to obtain feedback from the optical characterisation of the samples to improve and optimise the growth conditions. The second category includes samples furnished by De Beers, NIRIM and KUN. The aim was the investigation of the optical quality of the diamond films and of the donor impurity energy levels present in the films. Most of the studied samples were CVD thin diamond films. For comparison also natural type IIa and synthetic HPHT diamonds are investigated.

The CVD diamond samples originating from IMO are prepared in the ASTeX PDS17, and AX6500 systems shown in Fig. 2.2 and Fig. 2.3. The two systems differ in MW power (5 kW - 15 kW), the MW feed (top - bottom), the allowed size of the substrates (2" - 4") and in a few technical details such as the cooling system of the substrate holder. The obtained diamond quality is slightly better for the films grown in the AX6500 system.

By means of cooling or heating the substrate holder, the substrate temperature is

adjustable in-between certain limits independently of the plasma conditions. To measure the temperature of the substrate an IR pyrometer[2] is used.

To reduce the incorporation of extrinsic impurities in the deposited films, first of all, a low background pressure was maintained in the vacuum chamber before starting the deposition. In the second place, care was taken about the cleanness of the reactor walls and the purity of the feed gases (see Table 2.1).

Table 2.1 Purities of the gases used for CVD diamond synthesis.

Gases[*]	**Purities** (%)
Hydrogen H_2	≥ 99.9997
Methane CH_4	≥ 99.995
Hexane C_6H_{14}	≥ 99.995
Nitrogen N_2 (mixture H_2-N_2/1%)	≥ 99.994
Oxygen O_2	≥ 99.9995

[*](Air Liquide)

Doping:

An advantage of CVD diamond growth is the possibility to dope the diamond films in-situ by adding well-selected precursor gases to the feed gas during the growth process. Thus, dopants can be incorporated in the diamond films during the deposition and n- or p-type diamond layers can be grown. To obtain nitrogen-, lithium- or phosphorus-doped diamond films, respectively nitrogen (N_2) or ammonia (NH_3) and butyllithium (C_4H_9Li) in hexane (C_6H_{14}) and phosphine (PH_3) in H_2 [KOI97] are used respectively.

Substrate preparation:

Monocrystalline (100)-oriented polished Si-wafers are used as substrate material to grow heteroepitaxial diamond layers. To generate a sufficient density of nucleation sites on the Si surface (typically 10^9 –10^{10} cm^{-2}), in our experiments the substrates are always pre-

[2] Minolta / Land / Cyclops 52/ Infrared thermometer with a close up lens No. 135 and No. 153.
Land infrared LTD England, Minolta camera co. LTD Japan

treated with the same optimised treatment. They are cleaned in norvanol and afterwards scratched with diamond powder (< 1 µm diameter) with a Vibromet (Buehler Ltd.) polishing apparatus (vibration table).

Growth conditions:

An overview of the key experimental parameters for all the samples studied in this thesis are given in Appendix A.1. In the case of MW PECVD deposition, important growth parameters are the pressure P, substrate temperature T_S, reactant composition, microwave power MWP, deposition time t_D and deposition rate r_D. The combustion flame method uses an acetylene – oxygen welding torch to produce atomic hydrogen and hydrogen radicals. Table A.8 shows the values of the major parameters of the flame deposition process: the deposition temperature, the distance d of the substrate from the inner flame cone, the absolute oxygen flow f_{ox} and the acetylene supersaturation S_{ac} and the deposition rate r_D [SCH94].

The diamond deposition rate depends on the deposition method and the growth parameters. The first CVD samples grown at IMO (MWPE) at the beginning of the nineties were of a poor to medium quality. Nowadays, the growth rate of optical quality diamond film, under optimal deposition conditions is ca. 5 – 10 µm/h. In the case of the combustion flame method rates up to 200 µm/h can be obtained [SNA91].

Undoped, N-doped and Li-doped polycrystalline CVD diamond was synthesised in an ASTeX PDS17 and AX6500 MW PECVD system at IMO. The incorporation of N atoms in the films was obtained by adding nitrogen (N_2) or nitromethane (NO_2-CH_3) to the feed gas. Further details about these samples are given in Table A.3, Table A.4 and in Chapter 6 (section 6.2).

Preparation of free-standing films:

After deposition the diamond samples have to be removed from the substrates to allow PDS measurements. Therefore, the Si-substrate is etched away in a 1:1 HNO_3/HF mixture and traces of surface graphitic carbon are removed in a H_2SO_4/CrO_3 solution. If desired, the diamond films can also be polished on one or both surfaces.

2.6. Polishing

Diamond films for window applications have to fulfill strict requirements considering flatness, parallellism and surface roughness. The roughness of the as grown surface,

mostly truncated pyramids, is in general rather high. The growth surface roughness depends on the deposition conditions and the thickness of the diamond film and causes light scattering. On the other hand, the substrate side surface roughness equals the roughness of the substrate, which is substantially lower. An appropriate way to reduces the surface roughness is polishing. This leads to a reduced scattering of incident light and an enhancement of the transparency of the film. A surface flatness of the order of 2λ to $\lambda/10$ is called optical finish. As mentioned before, for window applications the curvature of the diamond film is of great importance. The polished samples have to be either very flat or have to posses a carefully controlled shallow curvature [PIC99].

Because of the extreme hardness of diamond, polishing is a very time-consuming and delicate activity: to polish a diamond film to a final surface roughness[3] $R_a \sim 10$ nm it takes about 333 - 500 hours and care has to be taken not to stress the film to prevent cracks. Also, the polishing rate depends strongly on the crystallographic orientation of the films.

De Beers applied standard polishing techniques to their optical quality samples (see Chapter 4 and section 5.6). However, deposition conditions and details about the polishing process are proprietary knowledge of De Beers. Details cannot be given.

At IMO, a LP50 Autoprecision Lapping & Polishing Machine (Logitech) is used to polish CVD diamond windows. Before starting the lapping step, the surface of the diamond sample is smoothed by a laser treatment at Wetenschappelijk en Technisch Onderzoekscentrum Diamant (WTOCD Lier, Belgium). This substantially reduces the lapping and polishing times, because the start roughness and flatness of the surface are strongly improved. A roughness R_a of about 0.2 µm is obtained by lapping, using a slurry with 50 µm size diamond particles, while for the final polishing step 3 µm size particles are used.

2.7. Conclusions

The MWPE deposition method allows growing high quality CVD diamond films under metastable temperature and pressure conditions. In this region is graphite the stable form of carbon. Therefore, graphite (sp^2-bonded) and amorphous carbon (a-C) defects are easily incorporated in the diamond structure. The characteristics (morphology, thickness,

[3] R_a: arithmetical mean roughness (see also section 4.3)

purity, colour) and physical properties of the films depend on the deposition conditions such as the concentrations of the deposition gases, the microwave power, the pressure and the substrate temperature. By adding, in addition to the standard precursor gases H_2 and CH_4, dopant-sources, it is possible to synthesis p-type (boron-doped) as well as n-type (phosphorus-doped) CVD diamond films.

2.8. References

[BAC91] P.K. Bachmann, D. Leers, and H. Lydtin, Diamond Rel. Mater., **1** (1991) 1.

[BUN55] F.B. Bundy, H.T. Hall, H.M. Strong, R.H. Wentorf, Nature **176** (1955) 51.

[DAV94] R.F. Davis, '*Handbook on Semiconductors'*, ed. T.S. Moss, Vol.3, ed. S. Majahan, Chapter 2, 456.

[DEM97] P. Demo, Z. Kozisek, M. Vanecek, J. Rosa, K. Meykens, M. Nesladek, C. Quaeyhaegens, G. Knuyt and L.M. Stals, Diamond Relat. Mater., 6 (1997) 1092-1096.

[DER75] B.V. Deryagin and D.V. Fedoseev, Sci. Am. **233** (1975) 102.

[DIS98] B. Dishler, C. Wild (Eds.) '*Low-pressure Synthetic Diamond: Manufacturing and Applications*' Springer-Verlag, Heidelberg, (1998).

[EVE62] W.G. Eversole, US Patents 3 030 188 (1962).

[FLO98] A. Flöter, H. Güttler, G. Schulz and R. Zachai, Proceedings of ISAM'98, Tsukuba, Japan (1998) 85.

[FOR96] I.J. Ford, J. Appl. Phys. **78** (1995) 3106; J. Phys. D **29** (1996) 2229.

[FUJ86] N. Fujimori, T. Imai, and A. Doi, Vacuum **36** (1986), 99.

[GHI93] A. Ghicquel, E. Anger, C. Héau, *Microwave Discharges: Fundamentals and Applications*, Plenum, New York (1993).

[GOO98] D.G. Goodwin and J.E. Butler, '*Handbook of Industrial Diamonds and Diamond Films'*, ed. M.A. Prelas, G. Popovici and L.K. Bigelow, Chapter 21, Marcel Dekker, New York, (1998) 527.

[JAN92] G. Janssen, PhD thesis, 'Homoepitaxial diamond: synthesized by CVD processes', Universiteits Drukkerij Nijmegen (1992).

[KAJ91] S.A. Kajihara, A. Antonelli, J. Bernholc, Phys. Rev. Lett. **66** (1991) 2010.

[KAM83] M. Kamo, Y. Sato, S. Matsumoto, N. Setaka, J. Cryst. Growth **62** (1983) 642.

[KOI97] S. Koizumi, M. Kamo, and Y. Sato, H. Ozaki and T. Inuzuka, Appl. Phys. Lett. **71** (1997), 1065.

[MAT81] S. Matsumoto and N. Setaka, 8th Japan Carbon Soc. Fall Meeting (1981); S. Matsumoto,Y. Sato, M.T. Tsumi, and N. Setaka, J. Mater. Sci. **17** (1982) 3106.

[MOR89] J. Mort, D. Kuhman, M. Machonkin, M. Morgan, F. Jansen, K. Okumura, Y. M. LeGrice and R.J. Nemanich, Appl. Phys. Lett. **55** (11) (1989), 1121-1123.

[OKA89] K. Okano, H. Naruki, Y. Akiba, T. Kurosu, M. Iida, Y. Hirose, and T. Nakamura, Jpn. J. Appl. Phys., **28** (1989) 1066.

[PIC99] J.C.S. Pickles, T.D. Madgwick, C.J.H. Wort, R.S. Sussman, presented at Diamond'99 in Prague

[ROB95] J. Robertson, J. Gerber, S. Sattel, M. Weiler, K. Jung, and H. Ehrhardt, Appl. Phys. Lett. **66** (24) (1995) 3287.

[SAI98] T. Saito, S. Tsurunga, N. Ohya, K. Kusakabe, S. Morooka, H. Maeda, A. Sawabe, K. Suzuki, Diamond Rel. Mater. **7** (1998) 1381.

[SAK99] I. Sakaguchi, M. N-.-Gamo, Y. Kikuchi, E. Yasu, H. Haneda, T. Suzuki, T. Ando, Phys. Rev. B **60**(4) (1999) R2139.

[SCH94] J. J. Schermer, W. J. P. van Enckevort and L. J. Gilling, Diam. Relat. Mat. **3** (1994), 408.

[SCH99] M. Schreck, H. Roll, B. Stritzker, Appl. Phys. Lett. **74** (1999) 650.

[SNA91] K.A. Snail, L.M. Hanssen, J. Cryst. Growth **112**, (1991) 651.

[SPE94] K.E. Spear, J.P. Dismukes, '*Synthetic diamond: Emerging CVD Science and Technology'*, ed. K.E. Spear, J.P. Dismukes, Chapter 8, John Wiley & Sons New York (1994).

[STE99] H. Sternschulte, M. Schreck, B. Stritzker, A. Bergmaier, G. Dollinger, '*Li addittion during CVD diamond growth: influence on the optical emission of the plasma and properties of the film*', presented at Diamond'99.

[STO92] B.R. Stoner, G.H. Ma, S.D. Wolter, and J.T. Glass, Phys. Rev. B **45** (1992) 11067.

[TAC99] T. Tachibana, Y. Yokoya, K. Hayashi, K. Miyata, K. Kobashi, presented at Diamond'99 in Prague.

[WIL94]C. Wild, R.Kohl, N.Herres, W.Muller-Sebert and P. Koidl, Diamond Relat. Mater. **3** (1994), 373-381.

[WOL93] S.D. Wolter, B.R. Stoner, J.T. Glass, P.J. Ellis, D.S. Buhaenko, C.E. Jenkins, and P. Southworth, Appl. Phys. Lett. **62** (1993) 1215.

3. Experimental photothermal techniques

The following chapter is devoted to the Photothermal Deflection Spectroscopy (PDS) technique used in this thesis. After a short introduction about the evolution and usage of PDS in section 3.1, section 3.2 considers the physical principle lying at the basis of the PDS technique and the different possible configurations (transverse and collinear) are treated at length. In sections 3.3 and 3.4, the technical and computational details regarding the experimental transverse and collinear PDS set-ups used in this thesis are given. The normalisation and scaling problems considering the PDS measurements are discussed in section 3.5. Attention is devoted to the use of transmission and reflection measurements and laser calorimetry measurements for the scaling of transverse and collinear PDS measurements respectively.

3.1. Photothermal deflection (PDS) measurements: state of the art

The main objective of this thesis is to demonstrate the applicability of PDS to polycrystalline CVD diamond films. In the beginning of the eighties, the theory of the mirage effect or of the so called photothermal deflection (PDS) measurements has been developed for solids by Danièle Fournier [FOU79]. PDS is a contactless and non-destructive technique. It relies on a minute change of the index of refraction due to generated heat –optically induced– in the solid matter. PDS measurements were used to investigate thermal properties of materials (such as the diffusivity,…). Because of the very high sensitivity of this technique, temperature changes < mK can be easily detected, Jackson has put forward the idea to use this technique for absorption measurement in materials [JAC81], [BOC80a], [BOC80b].

Since its discovery, the transverse PDS technique (t-PDS) (see section 3.3) has been used for measuring the optical absorption in crystalline and amorphous semiconducting materials such as c-Si, a-Si:H, GaN,…[JAC83], [GRI90], [LOT91], [AMB96] as well as more recently in conducting polymers [SEA92], [MOS97]. This technique was preferable to classical transmission measurements because of its significantly higher sensitivity [AME84] and in addition because of the very low influence of light scattering [YAS82]. By means of this technique, densities of defects, at which absorption occurs, in the range of 10^{16} - 10^{17} cm^{-3} could be detected even in micron thick films. The bulk density of states (DOS) and surface DOS of undoped [LEB94] and doped a-Si:H [JAC82], [GAL93]

were investigated. The collinear PDS (c-PDS) technique (see section 3.4) [BOC80] has recently been successfully used for optical absorption measurements in very low absorbing optical window materials such as quartz, sapphire [BLA97], and ZnSe [KUB94].

The very high sensitivity of this method led to the idea to apply PDS on weak absorbing polycrystalline diamond thin films to evaluate the defect density in CVD diamond. This was done for the first time in the framework of this thesis. If it turned out successfully, it was expected that the PDS technique, similar as for Si, could be used as a dominant characterisation technique for the evaluation of the film quality. This would then allow optimisation of the deposition process for diamond films. Until our try-out, PDS was only applied to study the thermal conductivity of diamond single crystals [ANT90].

As compared to Si, a few important differences should be mentioned: diamond has the highest known thermal conductivity at room temperature (RT), it is transparent in a very wide range from IR till UV (wide indirect bandgap of 5.45 eV at RT) and in addition, the as grown diamonds have rough faceted surfaces which significantly scatter the light. Therefore the application of PDS on diamond films implies a detailed investigation of these facts both from the experimental and theoretical side.

The main aim of this thesis was the adaptation and the improvement of the PDS set up for CVD diamond films, more specifically to measure the optical absorption at RT over a very broad energy range on one hand, and to image the absorption in CVD diamond windows on the other hand (in our case at the CO_2 laser wavelength of 10.6 μm).

Parallel with our development of the PDS set-up for the measurement of the subgap optical absorption coefficient of diamond, other research groups adopted this technique to measure the thermal diffusivity and conductivity of polycrystalline CVD diamond films using an Ar^+ laser pump beam of constant wavelength λ = 514 nm, and changed the chopping frequency υ [BOU93], [BER94].

Nowadays, the PDS technique is also used as a characterisation tool for the subgap absorption in CVD diamond by other research groups. Gheeraert et al. applied t-PDS to investigate the effect of boron-implantation in CVD diamond and subsequent annealing [GHE95]. Rohrer et al. [ROH96] combined the constant photocurrent method (CPM), with t-PDS and electron paramagnetic resonance (EPR) measurements to investigate nitrogen related defect states in CVD diamond, while Zammit et al. studied undoped polycrystalline diamond thin films [ZAM98], [ZAM99].

3.2. Photothermal deflection (PDS) measurement of absorption: the principle

Photothermal methods used to study absorption are based upon heating of a sample by absorption of optical energy. An overview of the different photothermal methods is given in [TAM89] and [WU96].

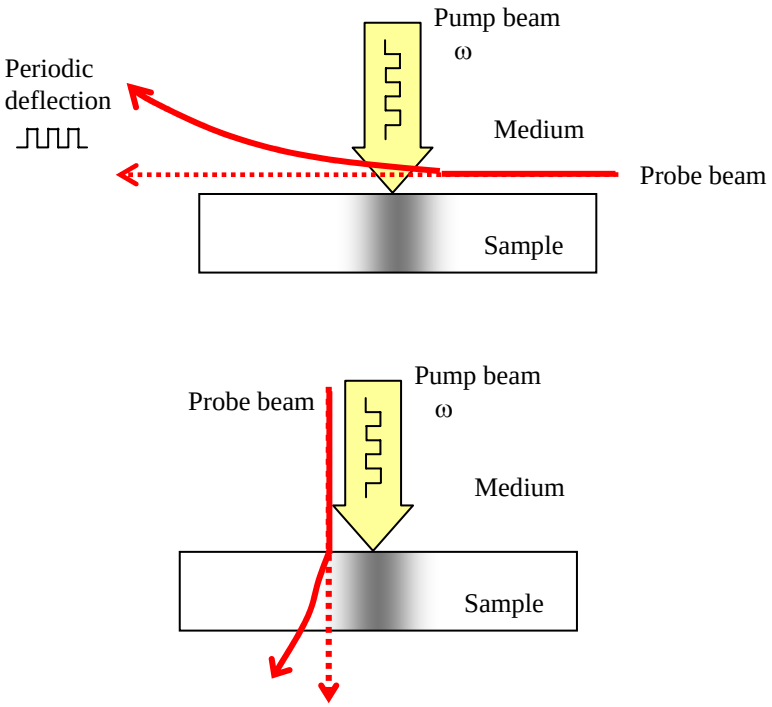

Fig. 3.1 Schematic presentation of the photothermal deflection method. (a) Transverse configuration, (b) collinear configuration. (deflections shown are exaggerated.)

In this thesis, the photothermal deflection (PDS) method has been applied to study absorption in CVD diamond films. The principle of PDS measurements is illustrated by Fig. 3.1. A periodically intensity modulated monochromatic light beam (the pump beam) is focused on the investigated sample. A part of the optical energy from the pump beam which is absorbed by the sample, is converted into heat via nonradiative deexcitation

processes.

The periodic heating generates thermal waves, which diffuse from the regions where the absorption takes place into neighbouring regions of the sample as well as into the surrounding medium. Thus, absorption leads to periodic temperature changes and temperature gradients in the sample and in its surrounding medium. Because the index of refraction of the sample as well as that of the surrounding medium is temperature dependent, the thermal gradients are accompanied by gradients of the index of refraction. These spatial gradients of the index of refraction can be probed by measuring the deflection of a laser beam (probe beam) upon traversing the refraction index gradients. From the deflection and from the geometry of the set-up, the absorption can be calculated, as described further in this chapter.

Depending on the direction of the probe laser beam with respect to the sample position and to the pump beam direction, two main PDS configurations can be distinguished. In the **transverse PDS** (t-PDS) method, the pump beam is perpendicular to the sample surface, while the probe laser beam is directed parallel to the sample just grazing its surface, as shown in Fig. 3.1 (a). In this case, it is the thermal gradient in the medium surrounding the sample that is probed [BOC80]. In the case of **collinear PDS** (c-PDS) measurements, the probe beam propagates perpendicular to the sample surface, quasi-parallel with the pump beam, as shown in Fig. 3.1 (b), and the thermal gradients in the sample itself are measured. Both configurations allow, in principle, a local testing of the absorption of a given sample. The collinear method, however, can only be used for samples, which neither absorb nor scatter the probe beam. Spatial resolution in the surface plane ((x,y)-plane) is, for both methods, determined by the width of the pump beam. In the z-direction, the resolution of the transverse method depends strongly on the thermal diffusion length inside the sample. E.g., for thermally thin samples t-PDS measures the total (surface and bulk) accumulated absorption over the whole thickness of the sample. For the collinear method, the resolution and the locality of the measurement are determined by the cross-sectional area of the pump beam and the probe beam. However, for thin samples and small angles between the probe beam and the pump beam, the collinear arrangement also measures the accumulated absorption over the whole thickness of the sample.

By changing the wavelength of the pump beam, the PDS technique yields the spectral dependence of the optical absorption $\alpha = \alpha(E) = \alpha(\lambda)$ of the material under investigation.

In order to determine the absorption from the probe beam deflection, the deflection angle must first be related to the refraction index field or, for that matter, to the thermal field and this, in turn must be linked to the absorption. The relation between the absorption of a pump beam in diamond thin films and the deflection of a probe beam is deduced in Appendix A.2.

3.3. Transverse PDS

3.3.1. Experimental set-up

In this section a transverse PDS set-up for measuring the spectral dependence of the optical absorption coefficient α of thin freestanding CVD diamond films, build at IMO for this specific application, is described and discussed in detail.

A schematic drawing of the set-up is shown in Fig. 3.2.

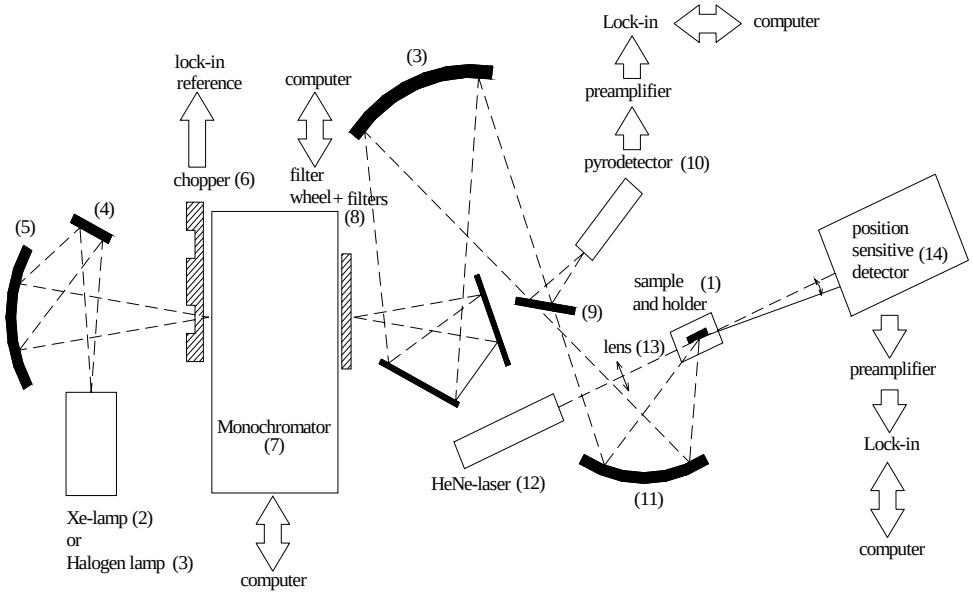

Fig. 3.2 Schematic picture of the transverse PDS set-up

Sample positioning

The central part of the set-up is the sample holder **(1**, see Fig. 3.2**)**. It is inserted in a quartz (suprasil, transparent from 210 nm to 2800 nm / 5.9 eV to 0.44 eV) optical cuvette filled with a liquid, which acts as the deflecting medium. This deflecting medium is one of the key parameters determining the sensitivity of PDS. The deflecting liquid is selected on the basis of two properties. It has to be highly transparent over the whole (or at least over a part of the) spectral range of the pump beam (225 nm to 2480 nm / 5.5 to 0.5 eV for diamond) and the change of its index of refraction with temperature has to be high.

Liquids satisfying these requirements are spectroscopically pure carbon tetrachloride (CCl_4) which is transparent from IR 0.4 eV / 3100 nm to about 4.4 eV / 281 nm and fluorinert (FC72) which is transparent from IR to UV (0.6 eV / 2066 nm to 5.9 eV / 210 eV). Their thermal properties are summarised in Table 3.1, [CUR88], [SPE94], [DIS98].

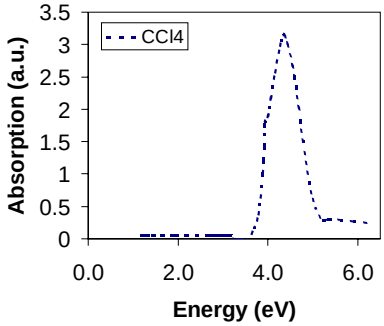

Fig. 3.3 Spectral dependence of the optical absorption in CCl_4..

CCl_4, which has the largest $|\partial n/\partial t|$, was used in the energy range 0.50 – 3.1 eV (2300 nm to 400 nm) where it shows an extremely low absorption. In the energy range above 3.1 eV, however, it was substituted by FC72, because CCl_4 has a prominent absorption peak around 4.4 eV. On the other hand, FC72 shows an absorption peak around 0.46 eV, masking the sample absorption [GHE95]. In the UV region, however, it is fully transparent.

The freestanding CVD diamond films **(1**, see Fig. 3.2**)** are glued (or, for thicker films, tightened) onto the holder and immersed in the deflecting liquid. The cuvette is mounted on translation and rotation stages[1], which allow a precise positioning of the sample with

[1] Melles Griot (07TSC503, 07TRT504, 17TFD001/D)

respect to the probe beam. The fine-tuning of the position, just a few microns from the diamond film surface, requires very precise movements.

Table 3.1 Thermal properties of deflecting media at 25°C.

Medium	Thermal conductivity κ (W/m K)	Specific mass ρ (kg/m^3)	Specific heat C_p (J/kg K)[1)]	Refraction index n	$\lvert \partial n/\partial T \rvert$ (K^{-1})
CCl_4	0.1	$1.6*10^3$	850	1.46	$8*10^{-4}$
FC72	0.057	$1.68*10^3$	1030	1.28	$4*10^{-4}$
Diamond	2000	$3.51*10^3$	516	2.4	$1.0*10^{-5}$

Pump beam

To cover the full spectral range of interest for our investigations, two interchangeable broadband light sources are used as pump beam: an UV enhanced Xenon lamp[2] **(2**, see Fig. 3.2**)** in the energy range [1.8 eV to 5.9 eV / 688 nm to 210 nm] and a quartz tungsten halogen lamp[3] **(3**, see Fig. 3.2**)** for the interval [0.4 eV to 4.5 eV / 3100 nm to 276 nm]. The UV-enhanced Xenon lamp allowed to measure the absorption spectrum up to 210 nm but in the IR region the Xe spectrum contains numerous intensity peaks (see Fig. 3.4). In the IR-VIS region it is, therefore, better to use a W-halogen lamp.

[2] USHIO Xenon short arc lamp UXL-151H (150W, 20V) mounted in a Photon Technology International PowerArc housing, equiped with an ellipsoidal suprasil coated mirror

[3] 6333 100W QTH (100W,12V) assembled in an Oriel Instruments series Q convective lamp housing model 60000

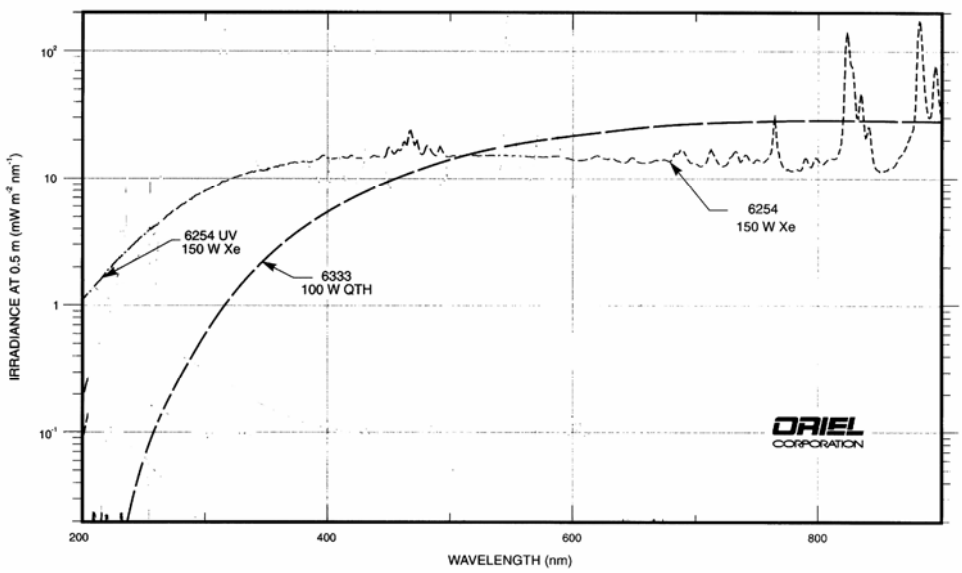

Fig. 3.4 Spectral dependence of the UV enhanced Xenon lamp (6254 UV 150 W Xe) and a quartz-tungsten halogen lamp (e.g. 6333 100W QTH).

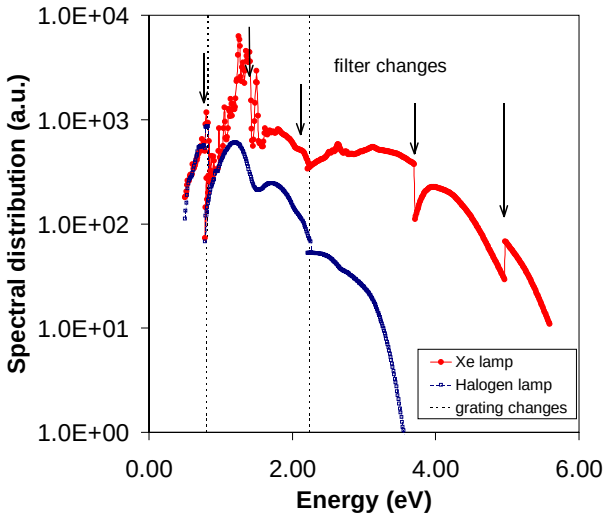

Fig. 3.5 Spectral intensity distribution of the light sources measured by the pyrodetector (for a 1 mm monochromator slit). Discontinuities indicated by dotted lines and arrows are due to change of gratings and filters respectively.

A flat and a concave mirror[4] **(4, 5**, see Fig. 3.2**)** focus the light on the monochromator entrance slit. Care is taken to match the f-number[5] of the imaging system to the 3.7 f-number of the monochromator, keeping simultaneously an almost 1:1 imaging of the filament (halogen lamp) / arc (Xe lamp) onto the monochromator entrance slit (1x3 mm^2) in order to minimise the light losses. The mirrors with Al-UV coating have the advantage of low spectral losses in the measured region and in addition no correction for spectral aberrations is necessary, as it would be for example for lenses.

Before it enters the monochromator **(7**, see Fig. 3.2**)**, the light is square wave intensity modulated by means of a mechanical chopper[6] **(6**, see Fig. 3.2**)**. Because the PDS signal (see Eq. 3.17) decreases very fast with increased chopping frequency via the thermal diffusion length μ_f (see section 3.3.2), a (low) chopping frequency υ ($\omega = 2\pi\upsilon$) between 3 – 30 Hz was used throughout the t-PDS measurements.

Table 3.2 Resolution of the monochromator for the different gratings.

Grating	Energy (eV)	ΔE (eV) (1mm slit)
300 lines/mm	0.65	0.007
	0.91	0.015
600 lines/mm	0.91	0.005
	2.76	0.072
1200 lines/mm	2.76	0.031
	5.39	0.137

The high light throughput monochromator is an automated triple grating monochromator[7] **(7**, see Fig. 3.2**)** with 300.0, 600.0, 1200.0 #lines/mm and blaze wavelengths 2.0 µm,

[4] borosilicate glass mirror coated with $AlMgF_2$
[5] f-number F/# is a concept which takes in account both the effect of the focal length f and the clear aperture D on the capture of radiation of an optical system. This allows a quick comparison and optimal matching of optics. For small angles the f-number can be approximated by $F/\# \approx f / D$.
[6] Stanford Research Systems Model SR540 Optical Chopper
[7] Acton Research Corporation SpectraPro® 275 with 3 diffraction gratings

1.0 µm and 300 nm respectively. These blaze wavelengths were chosen to allow a very wide wavelength span, necessary to measure CVD diamond over the broad energy range corresponding with the bandgap. In the present configuration the wavelength can be changed and measured from about 230 nm to 2480 nm (0.5 eV to 5.4 eV).

Undesired higher orders in the output beam are blocked by cut-off filters[8] placed in a filter wheel[9] **(8**, see Fig. 3.2**)**. The spectral dependency of the throughput of the light system (light sources, monochromator and filters) is shown in Fig. 3.5. The jumps in the curves, indicated by dotted lines and arrows, correspond to grating and filter changes at 0.82 eV and 2.25 eV, and 0.8 eV, 1.41 eV, 2.0 eV, 3.7 eV and 4.65 eV respectively.The spectral bandwidth of the output beam depends on the grating used and on the width of the exit slit. The spectral purity of the pump beam has to be traded off for intensity. The slit width used in our measurements was 1 mm. The corresponding resolution for the different gratings is shown in Table 3.2.

Behind the monochromator, a small fraction of the light is split off by means of a spectrally flat CaF_2 beamsplitter **(9**, see Fig. 3.2**)** and deviated to a spectrally independent pyroelectric detector[10] **(10**, see Fig. 3.2**)** for measuring the light intensity, necessary for the normalisation with respect to the spectral dependence of the light source. The flatness of the CaF_2 beam splitter and the pyrodetector has been carefully tested.

The transmitted beam is directed towards the sample where it is focused by means of a concave mirror **(11**, see Fig. 3.2**)**. The image of the mirrors is slightly defocused to obtain a homogenous 1.6 x 5 mm^2 image.

He-Ne laser probe beam

A high pointing stability (< 1 µrad) He-Ne laser[11] **(12**, see Fig. 3.2**)** is used as probe beam

[8] filters are selected out off: cutoff at 320nm (till ± 600nm), 590nm (till ± 1180nm), 665nm (till ± 1300nm), 715nm (till ± 1400nm), LWP-1310-25 (till ± 2600nm), LWP-2000-25 (till ± 4000nm), Oriel 51360 (cut on 830 till ± 1600), Oriel 51350 (cut on 750 till ± 1500, Fairlight IR-filter: TFLWP/173/97N (cut on 1.518µm)

[9] Acton Research Corporation FA-488-3 Six Position Filter Wheel with a IEEE interface option 488-03 for computer control

[10] Oriel Instruments Pyroelectric Detector Head Model 70123, spectra1independent in the range 50-9000 nm

[11] Oriel Instruments HeNe Laser System 79260, class IIIa, 1mW

to test the index of refraction gradient. The laser beam is directed parallel to the sample surface (see Fig. 3.7), and focused by means of a lens **(13**, see Fig. 3.2**)** with focal length 7 cm just in front of the sample. On focusing the laser beam, a compromise has to be made between the narrowness of the focal beam waist, which determines the spatial precision of probing, and an adequate Rayleigh range which should span the total sample width. The PDS signal S is of the following form (see further Eq. (3.17)):

$$S = cte\ L\ \exp(-z_0/\mu_f)$$

whereby L is the interaction length between the probe beam and the sample, which in practice for t-PDS measurements equals the sample width, z_0 is the minimal distance between the probe beam and the sample surface taking into account the widening of the laser. This widening is determined by the wavelength and the beam radius of the laser, the focal length of the focusing lens and the distances between the laser and the lens on the one hand and the lens and the sample on the other hand. To obtain the largest possible signal S, the focusing geometry must be optimised for a particular sample size. For a sample of 10 (5) mm width and an experimental set-up as described in this section, we have found an optimum (see Fig. 3.6) by focusing the beam by a lens with focal length f = 7 (5) cm to a waist of about 40 (30) µm with a corresponding Rayleigh range of about 10 (5) mm [YOU84], [END95].

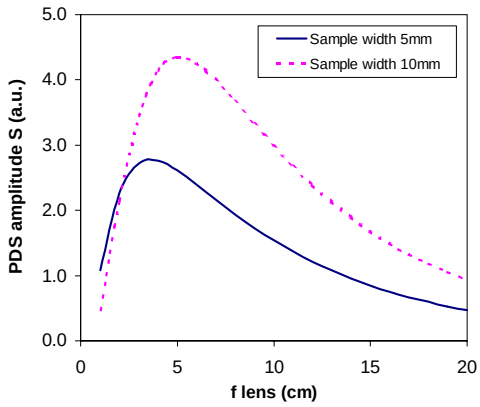

Fig. 3.6 Plot of the PDS signal amplitude as a function of the focussing distance for a sample width of 5 mm and 10mm and the experimental set-up as described in this section.

A pinhole and a narrow HeNe bandpass filter are introduced in the laser optical path to prevent scattered light of other wavelengths reaching the detector.

Position sensitive detector

The deflection of the He-Ne laser beam is monitored by a position sensitive Si photodiode[12] **(14**, see Fig. 3.2**)**. This PIN photodiode is working in the photovoltaic mode using the built-in potential of the diode. Compared to the photoconductive mode, this mode has the advantage of better NEP (noise equivalent power) at the used low frequencies. The total charge generated is independent of the position of the incident light. On the other hand the photocurrent itself does depend on this position via the resistance of the top layer. When the laser spot is displaced the resistivity of the circuit is changing because the generated carriers have to pass a longer distance in the top p+ layer. The spatial resolution is determined by the level of the dark-current noise (the selected model has a dark current of 0.5 nA) and the 1/f noise at the given chopping frequency. The spatial resolution is thus given by the precision of the detection. By using lock-in detection this can be significantly enhanced (S/N ratio can be improved).

By illuminating a fully absorbing CVD diamond plate (e.g. sample which reaches the saturation in the UV region) with white light, using the Xe lamp focused via the mirror imaging system and the monochromator with the 0-order diffraction, the total probe beam displacement is about 1 mm. For monochromatic light with typical incident power of 1 mW in the 0.02 eV energy interval focused on the sample, one can estimate the deviation of the probe beam depending on the optical absorption coefficient. Because the absorption coefficient span by going from 1.0 eV to the region of high absorption at 5.5 eV, is typically over 3-4 decades of magnitude, for the best quality CVD samples with the absorption coefficient at 0.5 eV about 0.1 cm^{-1}, one can estimate the minimum deviation of the probe beam to be less than 1 μm.

For a minimum detectable light spot displacement on the photodiode of about 1μm, the corresponding temperature increase can be estimated on the basis of Eq. (3.17) (see further):

$$T_{0s} = \theta\left(\frac{1}{n_0}\frac{\partial n}{\partial T}\right)^{-1} \frac{\mu_f}{\sqrt{2}\exp(-z_0/\mu_f)\,L}$$

Where in our experimental set-up the distance between the sample and the detector is approximately 0.5 m, a position resolution of 1 μm corresponds to an angular resolution of the order of $2.0*10^{-6}$ rad. In the case of a uniform rectangular illumination over a

[12] Hamamatsu Large area PSD series Pin-Cushion type S2044

distance L = 0.5 cm with the probe beam (υ = 8 Hz) passing at a distance z_0 = 50 µm in the deflecting liquid CCl_4 ($\mu_{CCl4,8Hz}$ = 54.1µm), one obtains surface temperature changes with an amplitude of $T_{0s,min} = 9*10^{-5}$ K.

Both the PDS signal from the position sensitive detector and the signal from the pyrodetector are preamplified[13] and applied to lock-in amplifiers[14]. The amplitudes of the PDS signal and of the pyrodetector signal are measured as well as their phase differences with the pump beam. The principle of lock-in detection allows to detect the periodically modulated deflection signal (modulation frequency $\upsilon = \omega/2\pi$), based on the FFT of the periodic changes of the position sensor and the pyrodetector signals. Such detection system has a much higher sensitivity (lock-in data) than DC detection, allowing to detect for example 20 fA AC-current modulated on background non-periodical noise.

Mechanical vibrations have been reduced by mounting the whole optical system on an optical anti-vibration top plate on an additionally absorbing heavy marble block (800 kg) and an anti-vibration table. Further, care was taken to avoid and reduce as much as possible probe laser beam scattering on dust particles (letting the HeNe laser pass through glass tubes) in the air and suspensions in the deflection medium (using additional filtering of the spectroscopically pure liquids) in his optical path.

Computer steering program and data acquisition

The outputs of the lock-ins (PDS signal, pyrodetector signal) are connected to a computer where the data processing takes place. A self-designed LabView program controls the whole measuring process and yields the spectral dependence of the PDS-signal. A schematic view of the link-up of the computer to the measuring apparatus is given in Fig. 3.2.

The computer controls the settings of the monochromator (wavelength, filter, grating, energy step) and the lock-ins (sensitivity, time constant, noise filters, modes, bandwidth etc). Typically, 300 readings of the lock-in amplifier were averaged under software control at each energy setting. If the read-out signal data ly within a specified precision range, the data are accepted by the computer and a next energy setting is chosen. If the signal exceeds the upper limit of the current lock-in sensitivity scale, a new one as well as

[13] Stanford Research Systems Transformer preamplifier model SR554
[14] Stanford Research Systems Lock-in model SR830

other detection parameters are automatically searched out. The program starts from the lowest energy and proceeds to the highest energy. This has the advantage that the occupation of the deep states does not change significantly during the measurement.

After each new energy setting a proper delay time is introduced before the lock-in outputs are being registered. After the measurement, the data are processed (outlying data points are rejected and the arithmetic average of the other data points is taken) and the signal is normalised automatically (see section 3.5). Finally, the PDS amplitude and phase are plotted as a function of the photon energy (in energy units eV). To obtain a plot of the spectral dependence of the optical absorption coefficient α, scaling is necessary. The used scaling procedures are described in section 3.5.

3.3.2. Theoretical considerations: Illumination, temperature field and deflection angle

In the transverse PDS set-up, shown in Fig. 3.7, the deflection of the probe beam takes place in the fluid surrounding the diamond sample. In order to calculate the deflection according to $\theta = \frac{1}{n_0}\frac{\partial n}{\partial T}\int_{path} \nabla_{\perp} T ds$ (Eq. (A.18) Appendix A.2) we now have to define the temperature field that causes the deflection and also the integration path along which the probe beam is deflected.

The integration path is determined by the focussing geometry and is supposed to be parallel to the sample front surface, at a distance z_0 from it. The integration limits in Eq. (A.18) may be restricted to the width L of the sample because of the small thermal diffusion length of the heat waves emerging from the sample into the surrounding fluid. Indeed, at the modulation frequency υ of 8 Hz, employed in our t- PDS measurements, the thermal diffusion length[15] $\mu = \sqrt{\frac{\kappa}{\pi \rho C \upsilon}}$ in the surrounding fluid is $\mu_{CCl4} \sim 54.1$ µm and $\mu_{FC72} \sim 36.2$ µm for CCl_4 and FC72 respectively. It is only within a few diffusion lengths from the sample surface that any noticeable thermal gradients are

[15] µ: thermal quantity that plays an important role in the theoretical model for heat transport in neighboring media. µ is the distance for which the amplitude of the thermal wave has decreased to 1/e or in other words a measure for how far the thermal wave diffuses in the material. At a distance $2\pi\mu$, the periodic temperature variation is completely damped out.

established. The thermal waves are heavily damped and consequently the probe beam has to be focused very finely and adjusted very closely to the sample surface to probe the gradients.

In stationary conditions with the illumination square wave modulated, for the frequency component ω of the Fourier series, the complex amplitude[16] of the temperature in the fluid near the sample surface relative to the ambient (room)temperature can be written as [JAC81], [MAN83]:

$$T_f(x,y,z) = T_s(x,y) \exp(-z/\mu_f) \exp(-i\, z/\mu_f) \qquad (3.1)$$

where $T_s(x,y)$ is the sample surface temperature ($z = 0$), and μ_f is the thermal diffusion length in the fluid.

The only quantity, which still has to be determined, is the sample surface temperature $T_s(x,y)$. It is this quantity which is directly influenced by the absorption of the light energy in the diamond film. The optical absorption via the thermalisation of the optical transitions causes local sample heating. The surface temperature is determined by the heat diffusion, depending on the thermal diffusivities and the thermal diffusion lengths of the sample and the surrounding liquid.

Before establishing the exact relationship between the surface temperature and the absorption, we first reduce the temperature field Eq. (3.1) to an one-dimensional field. An idealised one-dimensional configuration, only dependent on the z-component, is used to determine the t-PDS amplitude.

In our transverse PDS set-up the pump beam is focused by a mirror to form approximately a 1.6 x 5 mm² image of the monochromator exit slit on the sample front surface. This image is much wider than the probe beam waist (40 µm) (see Fig. 3.7). As the probe beam travels very close to the surface and right in the middle of the illuminated area, it is only the central strip with temperature $T_s(x,0)$, with $y = 0$ for the y-position of the centre of the pump beam, that is important. Furthermore, the sample is uniformly illuminated over its full width. This makes the temperature field x-independent.

[16] In this section, to work with complex quantities the complex amplitude notation is used.

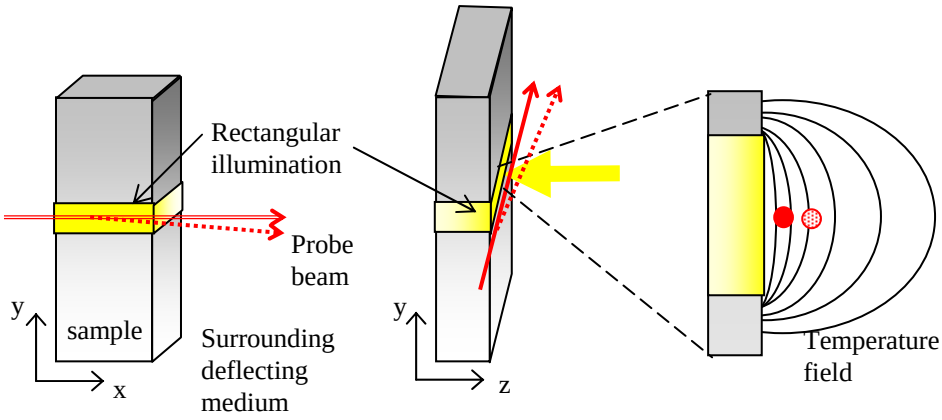

Fig. 3.7 Front view and side view of the pump-probe geometry. The pump beam is perpendicular to the sample surface, which is parallel to the (x,y)-plane (deviations are shown exaggerated).

To determine the sample surface temperature we consider the samples to be linear heat conductive systems surrounded by an infinite fluid. All along the length of a sample, heat may leak in the fluid.

The complex amplitude of the heat Q(z) deposited per unit length along the z-axis (depth) and per unit time in the sample can be written as [JAC81]

$$Q(z) = I_0 S_0 \eta \alpha(z) \exp\left(-\int_0^z \alpha(z')dz' \right) \qquad (3.\ 2)$$

where I_0 is the intensity of the pump beam in the focus spot (actually $I_0 = I_{0,inc}.(1-R)$ when taking into account the total reflectivity R), S_0 the illuminated surface area of the sample, η the quantum efficiency for conversion of absorbed light into heat by nonradiative deexcitation processes, $\alpha(z)$ the absorption coefficient at depth z inside the sample. In the following will be assumed that $\eta = 1$. This is true for most solids at room temperature [ROS76]. The photoluminescent processes, which constitute a parallel (radiative) recombination mode and thus reduce η, do usually not exceed a few percent and are not taken into account here [RIE96].

At the modulation frequency of 8 Hz the thermal diffusion length μ in diamond is 6.6 mm, which is much larger than the thickness of the investigated samples. The latter is of the order of 0.5 mm or less (see sample descriptions in Appendix A.1). The thermal

thinness of the diamond sample assures very fast levelling of the temperature inside the sample over its whole thickness. It thereby reduces the depth resolution of the transverse measurements (at the used frequency) to almost zero and the heat generated over the whole depth of the sample influences the surface temperature T_s. For low absorption values, $\alpha d < 1$, the light is absorbed homogeneously over the whole thickness of the sample. Therefore, the absorption coefficient α obtained from these measurements will be an average value over the illuminated volume of the sample. In the incoherent limit, the influx of heat, Q(z) can accordingly more adequately be expressed as:

$$Q(z) = I_0 S_0 \alpha \exp(-\alpha z) \tag{3. 3}$$

with α the average value of the optical absorption coefficient.

The total influx of heat in a sample with thickness d becomes:

$$Q = I_0 S_0 [1 - \exp(-\alpha d)] \tag{3. 4}$$

From the illuminated area, the heat diffuses into the other parts of the sample and, from any point of the sample surface into the surrounding medium.

The temperature of the illuminated area of a sample is determined by the balance of heat influx in and efflux out of the corresponding volume $S_0 d$ of the sample according to:

$$i\omega \rho_s C_s S_0 dT_s(0) = Q_{in} - Q_{out} \tag{3. 5}$$

where $T_s(0)$ stands for the complex amplitude of sample temperature at y = 0, i.e. at the illuminated area. (In general, T_i is the temperature rise above the ambient temperature in medium i, with i = s, f for respectively the sample and fluid.)

Q_{in} is given by expression (3.4), and Q_{out} is the rate at which heat diffuses out of the illuminated volume. The latter is given by:

$$Q_{out} = -2bd\kappa_s \left.\frac{\partial T_s(y)}{\partial y}\right|_{y=0} - 2S_0 \kappa_f \left.\frac{\partial T_f(y,z)}{\partial z}\right|_{\substack{z=0 \\ y=0}} \tag{3. 6}$$

where the first term in the right hand side corresponds to the heat diffusion into the neighbouring sample areas (b is the width and κ_s is the thermal conductivity of the sample), and the second term to the diffusion into the surrounding fluid (κ_f is the thermal conductivity of the surrounding fluid). In the second term, the surface from which heat diffuses into the fluid has been approximated to $2S_0$, neglecting the two side surfaces of the illuminated segment of the sample.

When reflections at the sample borders are neglected, Eq. (3.5) becomes:

$$i\omega\rho_s C_s S_0 dT_s(0) = I_0 S_0\left[1-\exp(-\alpha d)\right] + 2bd\kappa_s \left.\frac{\partial T_s(y)}{\partial y}\right|_{y=0} + 2S_0\kappa_f \left.\frac{\partial T_f(y,z)}{\partial z}\right|_{\substack{z=0\\y=0}} \quad (3.7)$$

Further we make the assumption that the y-dependence of the temperature of the diamond sample is given by:

$$T_s(y) = T_s(0)\exp(-y/\mu)\exp\left(-i\,y/\mu\right) \quad (3.8)$$

The thermal diffusion length μ in the above equation is the 'corrected' thermal diffusion length of the sample whereby heat leakages to the fluidum via non-illuminated sample surfaces are included. The effect of heat losses to the surrounding fluid corresponds to a smaller thermal diffusion length. In the case of diamond this effect is minimal and for a modulation frequency υ = 8 Hz $\mu_{corrected}$ can be approximated by the theoretical thermal diffusion length μ of diamond.

According to the above assumption we obtain:

$$\left.\frac{\partial T_s(y)}{\partial y}\right|_{y=0} = -\frac{(1+i)}{\mu} T_s(0) \quad (3.9)$$

While, for the fluid, where the temperature decreases exponentially with z, the temperature gradient at the sample surface equals (according to Eq. (3.1)):

$$\left.\frac{\partial T_f(y,z)}{\partial z}\right|_{\substack{z=0\\y=0}} = -\frac{(1+i)}{\mu_f} T_s(0) \quad (3.10)$$

Inserting Eqs. (3.8), (3.9) and (3.10) into Eq. (3.7) the latter becomes:

$$i\omega\rho_s C_s S_0 dT_s(0) = I_0 S_0\left[1-\exp(-\alpha d)\right] - \frac{2bd\kappa_s(1+i)}{\mu} T_s(0) - \frac{2S_0\kappa_f(1+i)}{\mu_f} T_s(0)$$

After some rearrangements we obtain for the complex amplitude of the surface temperature $T_s(0)$:

$$T_s(0) = T_{so}\exp\left(i.bgtg\Psi\right) \quad (3.11)$$

where

$$T_{so} = \frac{I_0 S_0 \left[1 - \exp(-\alpha d)\right]}{\sqrt{\left(\frac{2bd\kappa_s}{\mu} + \frac{2S_0\kappa_f}{\mu_f}\right)^2 + \left[\omega\rho_s C_s S_0 d + \frac{2bd\kappa_s}{\mu} + \frac{2S_0\kappa_f}{\mu_f}\right]^2}} \qquad (3.\ 12)$$

and

$$\Psi = \left(\frac{\left(\frac{2bd\kappa_s}{\mu} + \frac{2S_0\kappa_f}{\mu_f}\right)}{\left[\omega\rho_s C_s S_0 d + \frac{2bd\kappa_s}{\mu} + \frac{2S_0\kappa_f}{\mu_f}\right]} \right) \qquad (3.\ 13)$$

Finally, the temperature profile in the fluid becomes:

$$T_f(z) = T_s(0) \exp\left[-(1+i)\, z/\mu_f\right] \qquad (3.\ 14)$$

The temperature gradient in the fluid at distance z_0 to the sample surface can be written as:

$$\left.\frac{\partial T_f}{\partial z}\right|_{z_0} = -\frac{1+i}{\mu_f} T_s(0) \exp\left[-(1+i) z_0/\mu_f\right] \qquad (3.\ 15)$$

The complex amplitude of the temperature at the sample surface $T_s(0)$ (see Eq. (3.12)) is proportional to the amount of energy I_0S_0 deposited in the sample, to the optical absorption coefficient α and the thickness d via (1-exp(-αd)), and depends on the thermal conductivity κ_s, the specific heat C_s and the density ρ_s of the sample and the thermal conductivity κ_f, the specific heat C_f and the density ρ_f of the surrounding fluid.

For the transverse configuration with uniform illumination the deflection signal is then given by Eq. (A.18) and Eq. (3.15):

$$\theta = \frac{1}{n_0}\frac{\partial n}{\partial T}\int_0^L \left.\frac{\partial T_f(z)}{\partial z}\right|_{z_0} dx$$

$$\theta = -\frac{1}{n_0}\frac{\partial n}{\partial T}\int_0^L \frac{1}{\mu_f}(1+i) T_f(z_0) dx$$

$$\theta = -\frac{1}{n_0}\frac{\partial n}{\partial T}\frac{1}{\mu_f}(1+i)T_f(z_0)L$$

$$\theta = -\frac{1}{n_0}\frac{\partial n}{\partial T}\frac{1}{\mu_f}(1+i)T_{so}\exp(-z_0/\mu_f)\exp(-iz_0/\mu_f)L\exp(ibgtg\Psi) \qquad (3.16)$$

with amplitude

$$\theta_A = \frac{1}{n_0}\frac{\partial n}{\partial T}\frac{\sqrt{2}}{\mu_f}T_{os}\exp(-z_0/\mu_f)L \qquad (3.17)$$

It follows from this formula that the amplitude of the deflection θ_A is determined by the amplitude of the sample surface temperature T_{so}, the relative distance z_0 of the probe beam to the sample surface, and the thermal properties of both the sample (via T_{so}) and the deflecting medium. Because the temperature decays exponentially with z_0, a skimming positioning of the probe beam close to the sample surface is necessary to obtaining large PDS-signals. The thermal diffusion length of the deflection fluid is very short compared to the sample width b, therefore in a good approximation the integration path L equals b. Because the distance of the probe beam from the sample surface depends on the focus of the probe beam, the optimisation of the focus for the given sample length b determines the optimum signal (see 3.3.1 experimental set-up)

As T_{so} is proportional to $I_0S_0[1-\exp(-\alpha d)]$, the angular deflection θ_A in turn is, for fixed z_0, proportional to:

$$\theta_A \propto \frac{1}{n_0}\frac{\partial n}{\partial T}I_0S_0[1-\exp(-\alpha d)] \qquad (3.18)$$

3.4. Collinear PDS

3.4.1. Experimental set-up

Our t-PDS set-up (see section 3.3) has been changed into a collinear PDS arrangement. c-PDS was applied using a configuration similar to this described by Jackson et al. [JAC81], [BOC80]. In our case we worked at a fixed wavelength: the CO_2 laser wavelength of 10.6 µm. It should be noted that t-PDS could not be used at 10.6 µm, because there is no liquid which is sufficiently transparent at this wavelength. A photograph of the set-up is shown in Fig. 3.8. The set-up had to be optimised for

relatively thick diamond windows typically 1 mm thick, taking into consideration the specific material properties of diamond ($\partial n/\partial T$, high thermal conductivity implying the use of high chopping frequencies etc.).

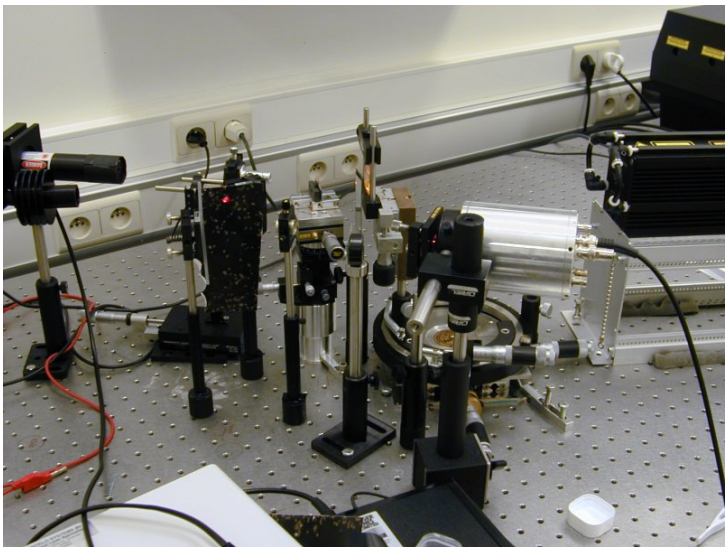

Fig. 3.8 Photograph of the collinear PDS set-up.

As already mentioned, the sample requirements for c-PDS measurements are much stronger than for t-PDS measurements. To start, at the probe beam wavelength, the optically thin samples have to be non-absorbing because absoption could distort the heat profile in the test material as created by the pump beam. Furthermore, the optical quality of the sample is more demanding. The samples have to be polished so that reflections and scattering on the truncated pyramids at the surface of as grown polycrystalline diamond samples are strongly limited.

The freestanding diamond window under investigation is mounted on top of a micrometer precision (xyzϕ - adjustable) positioning stage. In contradiction to the transverse configuration, no deflecting liquid is used, but the gradients in the diamond sample itself are used to deflect the probe beam.

The intensity of a 10.6 µm CO_2 laser[17] (the pump laser) is periodically modulated with frequency υ (10 Hz – 20 kHz) via an external trigger input connected to a function

[17] Synrad laser 48-1-28(W),10.6 µm, power: 10 Watt, long time instability 10%

generator[18]. A ZnSe lens (f = 5 cm) is focusing the laser to a spot with radius a_p of about 100 µm with a corresponding Rayleigh length of about 2.2 mm. Optical absorption of the pump beam in the sample causes local heating (see Fig. 3.10) and consequently a temperature gradient in the sample is generated. The accompanying periodic spatial changes of the index of refraction in the diamond sample are monitored by a He-Ne laser probe beam crossing at a small angle the area heated by the pump beam at the maximum gradient. The He-Ne laser is focused on the sample with a laser lens of f = 7 cm to a spotsize radius a_s of the order of 40 µm and the Rayleigh length of about 9.4 mm.

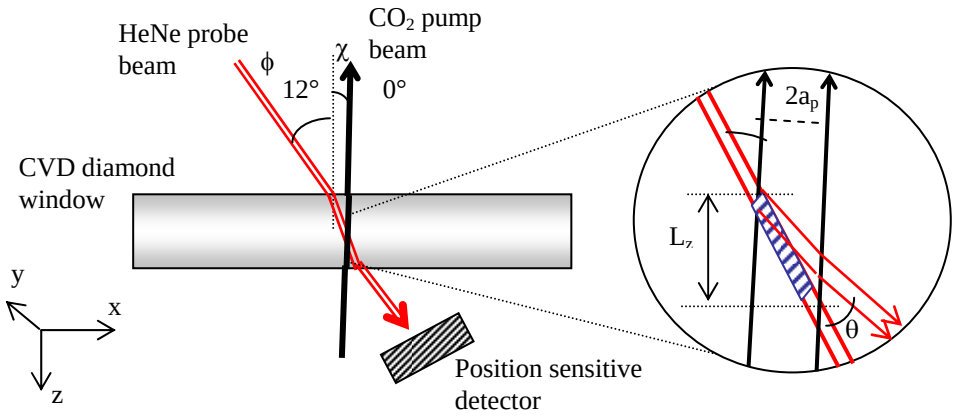

Fig. 3.9 Focusing geometry for the crossing collinear PDS arrangement. The shaded part in the zoomed view indicates the interaction length of the probe and pump beam (deviations are shown exaggerated).

At last, a position sensitive Si-detector is monitoring the periodic changes in the angular deflection of the probe beam, proportional to the absorbed power. The preamplified PDS-signal is measured by a lock-in amplifier. Optical components are mounted on position stages, which allow micron resolution movements in the x-, y- and z-direction.

The complete optical system is mounted on an anti-vibration table.

It is worth noting that for samples containing a large number of defects, scattering of the HeNe laser beam can be quite important. In such cases, to minimise the influence of the light scattering effect on the c-PDS signal (important only for the lowest quality samples)

[18] function generator HP 3324 A

the scattered laser light has been collected and refocused to a small spot on the position sensor.

At variance with the transverse set-up, a laser is used as pump beam because in this collinear configuration it is necessary to focus the pump beam to very small dimensions (< 100 μm). This in combination with its very high sensitivity, allows us to measure with collinear arrangement very low local optical absorptions (< 1 ppm/cm at 1 cm absorption length or $\alpha d \sim 10^{-6}$) of specified regions (e.g. with incorporated inclusions or defects) within the sample. Hence this technique is most convenient for imaging and spatial profiling of weakly absorbing inhomogeneities.

The c-PDS measurements can be spatially resolved as well in the (x, y) plane as in the depth, the z –direction. The dimensions of the investigated region and the resolution of the measurements depend on the beam geometry. The radius a_p and the position of the pump beam determine the region from which information is obtained. The radius a_p is inversely proportional to the optical resolution in the (x,y)-plane.

For our quasi-parallel set-up, the angle between the pump and probe beam ϕ is about 12° in air and 5° in diamond ($n_{diamond} = 2.4$). The CO_2-laser beam is quasi-perpendicular to the sample surface, while the HeNe-laser beam makes an angle of 12° with the surface normal as shown in Fig. 3.9.

The interaction length L of the two laser beams determines the resolution in the z-direction (see Fig. 3.9). The interaction length L is given by:

$$L = 2a_p / \sin \phi \qquad (3.\ 19)$$

and the corresponding resolution in the z-direction is:

$$L_z = 2a_p \cos (\phi-\chi) / \sin \phi \qquad (3.\ 20)$$

with χ the angle between the pump beam and the surface normal.

Consequently, the smaller the pump beam waist and the larger the intersection angle between the pump and probe beam (0° – 90°) the better the z-resolution.

For our particular situation, the corresponding interaction length (in the diamond sample), $L \sim L_z \sim 1951$ μm, is smaller than twice the Rayleigh length of the pump and probe beams. This means the waist of the laser beam can be assumed constant over the interaction region. Moreover, the interaction region is larger than the sample thickness. Therefore, the advantage of such a c-PDS arrangement is that an integrated absorption

over the full sample thickness (in the z-direction) will be measured. In the opposite case when L is much smaller than the thickness of the sample, a resolution corresponding to L_z can be obtained in the z-direction.

3.4.2. Theoretical considerations

In the collinear arrangement a direct measurement of the heat generated in the sample takes place. A focused gaussian laser beam is illuminating the sample. Because the absorption $\alpha(z)$ in the sample is very small, the intensity of the pump beam can be considered to be constant over the full depth of the sample:

$$I(z) = I_0 \exp[-\alpha(z)d] \sim I_0[1-\alpha(z)d] \sim I_0$$

As discussed above, the Rayleigh length of the pump beam is larger than the sample thickness. Therefore, the heating profile corresponds actually to a cylinder and the theoretical calculation can be treated with cylinder symmetry. Care has to be taken that the radius of the probe beam (a_s) is smaller than the radius of the pump beam (a_p). In case of homogeneous, uniform absorption of the pump beam, a refractive index profile with cylinder symmetry is created. Because of its small dimensions compared to the pump beam, in the quasi-parallel arrangement the probe beam is then travelling through a well-defined index of refraction field, which can be considered constant over the dimensions of the probe beam.

A complete theoretical treatment of the PDS measurements can be found in [JAC81]. There are two important limiting cases for the collinear PDS arrangement [JAC81], [BOC80b], [ZIM97]:

For high modulation frequency, when the thermal diffusion length μ of the deflecting medium is much smaller than the pump beam radius $\mu << a_p$, the amplitude of the deflection, θ_A, is given by:

$$\theta_A = 2\frac{r}{a_p^2}\frac{1}{n_0}\frac{\partial n}{\partial T}\frac{P_0}{\omega\rho C\pi^2 a_p^2}\left(1-\exp(-\alpha l)\right)\exp\left(-\frac{r^2}{a_p^2}\right) \qquad (3.\ 21)$$

where L is the interaction length within the diamond sample, a_p is the radius of the pump beam, α is the optical absorption coefficient, l is the thickness of the sample, P_0 is the power of the pump beam, ω is the angular frequency ($\omega = 2\pi\upsilon$), υ is the modulation frequency, ρ is the density of the deflecting medium ($\rho_{diamond} = 3.51 \times 10^3$ kg/m^3), C is the

specific heat of the deflecting medium ($C_{diamond}$ = 6.195 J/mol.K), n_0 is the index of refraction and dn/dT is the refraction index gradient ($(1/n.dn/dT)_{diamond}$ = 4.04x10^{-6} K^{-1}, dn/dT = 1.6x10^{-5} K^{-1} at 10.6 µm [TRO98]). The deflection of the probe beam is at its greatest when the distance r between the probe beam and the pump beam is $a_p/\sqrt{2}$.

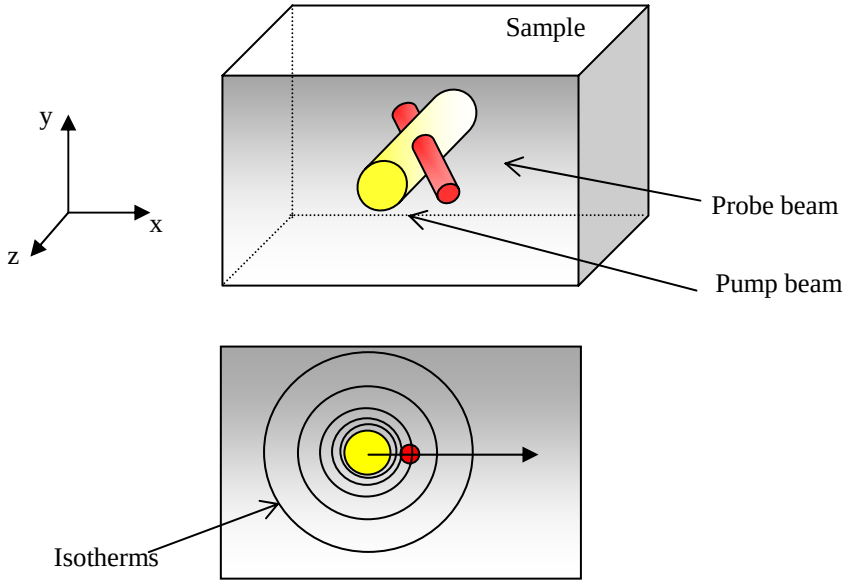

Fig. 3.10 Crossing collinear PDS: pump beam and corresponding temperature field (depicted by isotherms).

In the second case, for low modulation frequency, the thermal diffusion length is much larger than the pump beam radius µ >> a_p, and the PDS signal θ_A depends on the thermal diffusivity. The amplitude of the PDS signal θ_A is given by:

$$\theta_A = \frac{1}{n_0}\frac{\partial n}{\partial T}\frac{P_0}{\kappa\pi^2 r}(1-\exp(-\alpha l))\left(1-\exp\left(-\frac{r^2}{a_p^2}\right)\right) \qquad (3.\ 22)$$

with κ the thermal conductivity of the deflecting medium ($\kappa_{diamond}$ = 2000 W/m K). In this case, the deflection amplitude is at its greatest for r ~ 1.12a_p.

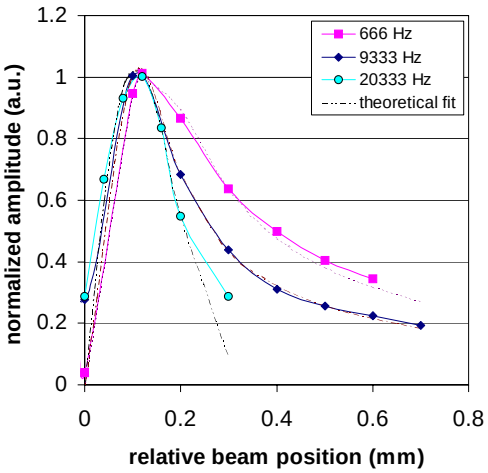

Fig. 3.11 Amplitude of the c-PDS signal as a function of the relative distance between the probe and the pump beam, measured for modulation frequency υ = 666 Hz, 9333 Hz and 20333 Hz. The experimental data are fitted with a combination of the theoretical expressions (3.21) and (3.22) (dashed lines).

By changing the position of the probe beam relative to the pump beam, the temperature field in the sample can be measured for the above two cases, allowing also an experimental verification of the pump beam radius and the determination of the thermal diffusivity. In Fig. 3.11, the c-PDS signal amplitude is shown for sample D2 (for sample description see Appendix A.1 and Chapter 5) as a function of the relative beam distance, measured at different frequencies (666 Hz – 9333 Hz – 20333 Hz). The theoretical fit of the experimental data is based on Equations (3.21) and (3.22), taking into account the sample thickness and the Rayleigh length of the pump beam. At low modulation frequencies (e.g. υ = 666 Hz), the thermal diffusion length μ in diamond is much larger (μ ~ 700 μm for υ = 666 Hz and a tabulated thermal diffusivity of the order of 12 cm^2s^{-1}) than the theoretical pump beam radius (≅ 100 μm) and the temperature profile extends beyond the gaussian pump laser-profile heated region. The experimental data for 666 Hz in Fig. 3.11 can be fitted with Eq. (3.21) yielding a pump beam radius of 130 μm, which is very close to the expected value of 100 μm. For higher frequencies (υ < 10 kHz), the pump beam radius is still smaller than μ. In this case, a good agreement between the predicted theoretical behaviour and the experimental data can be obtained by a fit using a combination of Equations (3.21) and (3.22). Again the same pump beam radius is found. At very high frequencies (υ = 20333 Hz) the experimental data can be fitted with quite

good agreement with Eq. (3.22).

3.5. Normalisation and scaling of the transverse and collinear PDS-signal

3.5.1. Normalisation of the transverse PDS-signal

Optical components such as light sources, used as pump beam to illuminate the sample, monochromator gratings and filters show a specific spectral dependence (see Fig. 3.5). Furthermore, as can be seen from Fig. 3.12, Fig. 3.13, Fig. 3.14 and Fig. 3.3, the transmittance and reflectance of the beamsplitter, the focusing mirror, the quartz cuvette and the deflecting liquid are also energy dependent.

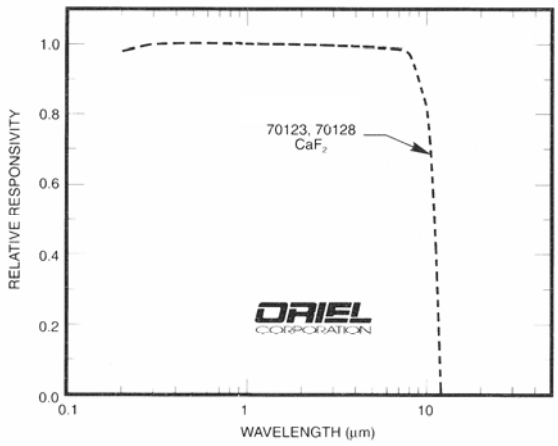

Fig. 3.12 Spectral dependence of the CaF_2 beamsplitter.

All these spectral dependencies have to be taken into account when evaluating the amplitude of the PDS-signals. The amplitude of the PDS-signal has indeed to be normalised to the incident light intensity. For the last series of optical components, the spectral dependencies varies by an amount of about 5% only. Therefore, the standard measured calibration curves shown in Fig. 3.12, Fig. 3.13, Fig. 3.14 and Fig. 3.3 are used to correct the PDS-signal for the spectral dependence of these optical components.

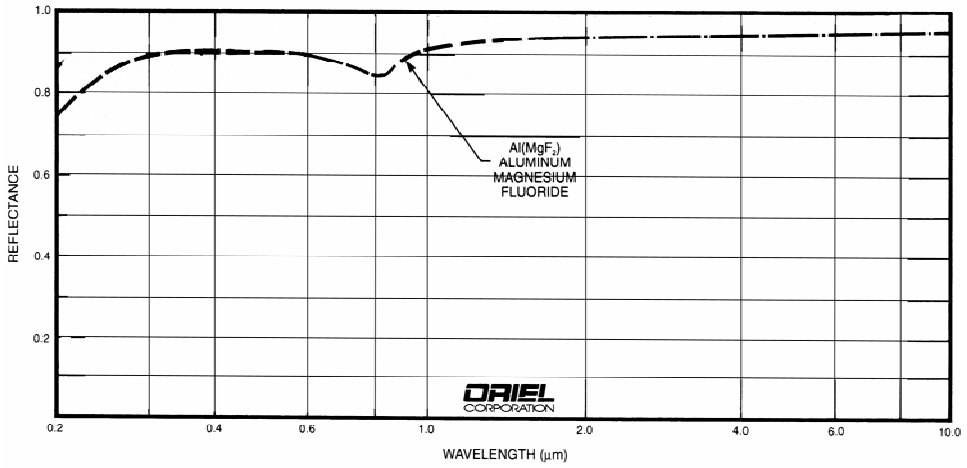

Fig. 3.13 Typical near normal incidence reflectance spectrum of Al(MgF_2).

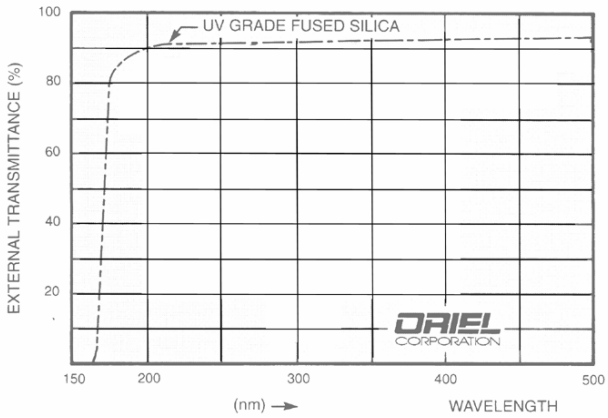

Fig. 3.14 Transmittance spectrum of UV grade fused silica.

To compensate for the spectral dependence of the illuminating system, the light intensity of the pump beam, originating from the light sources, after passing through the monochromator, filter and mirrors, is during each measurement monitored by a spectrally flat pyrodetector. The correction of the PDS-signal is done by dividing the PDS-signal by the corresponding pyrodetector signal. This procedure is automated and is performed during the data processing.

3.5.2. Normalisation of the collinear PDS-signal

During the c-PDS measurements, the optical absorption of CVD diamond was measured at the fixed CO_2 laser wavelength of 10.6 µm. Therefore, in this case, no corrections for the spectral dependence of the optical components are needed. Nevertheless, the SYNRAD CO_2 laser shows long term unstabilities such as wavelength shifts and intensity changes of about 10%. To compensate for this, these changes were recorded by a pyrodetector[19] and the ratio of the c-PDS signal to the pyrodetector signal was used.

3.5.3. Calculation of the optical absorption coefficient α - absolute values

In the incoherent limit and when scattering is negligible, the normalised PDS-signal S is proportional to the sample absorptance and is for both experimental arrangements - transverse and collinear PDS - (see Eqs. (3.18), (3.21) and (3.22)) given by:

$$S = S(E) = S_{sat}\left[1 - \exp\left(-\alpha(E)d\right)\right] \qquad (3.\ 23)$$

where d is the effective optical thickness of the sample (see Chapter 4) and S_{sat} stands for a proportionality constant called the saturation value. This constant includes the apparatus conversion and amplification factors (deflection-voltage/current), the distance of the probe beam to the sample surface z_0, the dimensions of the probe beam, the reflection coefficient, the width of the sample and the material parameters (thermal properties) of the sample and the deflecting liquid. It is difficult to determine exactly all these factors experimentally. The saturation signal S_{sat} is the PDS-signal when the incident power is completely absorbed in the film (strong absorption with $\alpha d > 1$).

When d is known and the PDS signal is saturating (S_{sat}), the absolute optical absorption $\alpha(E)$ can be calculate (for energies where no saturation occurs) from Eq. (3.23) in a very straightforward way:

$$\alpha\ (E) = -1/d\ \ln\ (1 - S(E)/S_{sat}) \qquad (3.\ 24)$$

In the energy region where the signal saturates, information about the absorption coefficient can not be obtained from PDS measurements.

In practice, this procedure is not so straightforward as it looks.

[19] ORPHIR laser power monitor 150 A series type 2176

3.5.4. S_{sat} - scaling procedure: absolute scaling of transverse PDS measurements using the saturation value S_{sat}

The calculation of absolute absorption values requires the knowledge of the saturation value S_{sat}. In the investigated energy range, the PDS-signal of most CVD diamond films does not saturate. Only those films which contained a large amount of sp^2 carbon showed saturation. To scale their PDS-spectra the S_{sat}-scaling procedure could be applied.

An example of this calibration procedure is shown in Fig. 3.15. Fig. 3.15 (a) shows the amplitude of the PDS-signal in arbitrary units as measured by the position sensitive detector. Above 4 eV, the PDS-signal is saturating with S_{sat} equal to $4x10^{-8}$. The energy dependence of the optical absorption coefficient α is calculated from Eq.(3.24), with the thickness of the sample d = 20 µm, and is presented in Fig. 3.15 (b).

For samples of the same deposition series with the same physical characteristics (morphology, thickness), but which did not reach the PDS saturation signal in the measured spectral range, the following procedure was applied: all parameters of the experimental set-up were kept the same (sample width and sample positioning towards the probe beam for maximum signal). Hence, the saturation value S_{sat} could be anticipated to be approximately the same for the measured specimen with a different defect concentration as for that one, showing the saturation. This assumes that the material parameters are the same, which is not necessary the case and therefore care has to be taken when applying this method.

The scaling procedure based on a saturation value has some drawbacks even when saturation of the deflection signal is reached. The physical thickness of the sample does not correspond to the effective optical thickness e.g. when the sample is ‘optically black’ and all the light is absorbed in a small surface layer or when the light is trapped in the bulk (see Chapter 4). For the S_{sat}-scaling procedure, the error on the absolute values is determined by the error on $d_{(eff)}$ in Eq. (3.24).

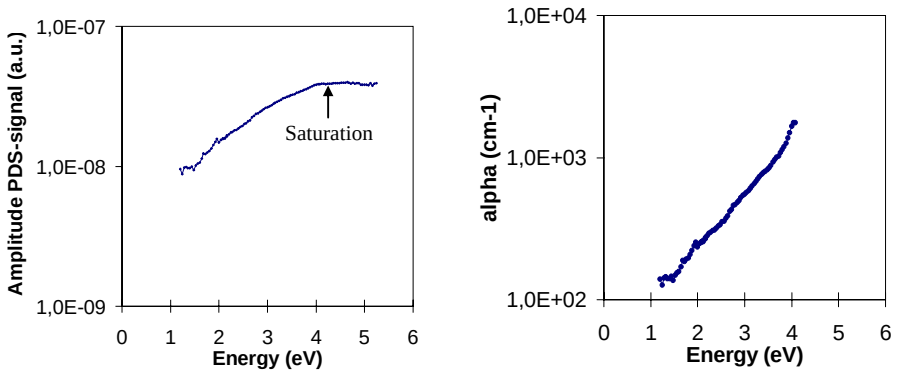

(a) (b)

Fig. 3.15 (a) The amplitude of the PDS-signal as measured by the position sensitive detector. (b) The energy dependence of the corresponding optical absorption coefficient of a CVD diamond sample in absolute units calculated from the normalised amplitude of the PDS-signal via the saturation value $S_{sat} = 4x10^{-8}$, for an effective thickness d=20 µm.

For our measurements on intermediate to high quality CVD diamond thin films, we did not reach the region of full absorption, also not in the UV region. The low absorption values of diamond at 5.45 eV (α = 10cm^{-1} for IIa diamond [COL93]) in combination with the low intensity of the Xe-lamp above 5.4 eV did not allow to detect a saturated PDS-signal. Therefore, the above described method could not be applied and another suited method had to be developed to obtain the absorption data on absolute scale.

3.5.5. T-scaling procedure: absolute scaling of transverse PDS measurements using transmission measurements

For optically polished samples, optical transmission and reflection measurements are the standard way to measure absolute absorption spectra. But, because of the low absorption and high scattering of polycrystalline CVD diamond films, T and R measurements are not sensitive enough in this case (see section 3.6.1). Only in the high-energy region near the bandgap where the optical absorption coefficient of diamond is sufficiently high, T and R measurements are usefull.

Therefore, to scale the PDS-spectra of diamond films we proceed as follows: in the high absorption region ($\alpha d > 1$), in addition to PDS, also T and R spectra are measured. For the PDS-spectrum, the spectral dependence of the optical absorption coefficient α is

calculated from Eq. (3.24) using an arbitrary value for S_{sat}. From T and R measurements the absolute optical absorption α is calculated[20] (see section 3.6.1).

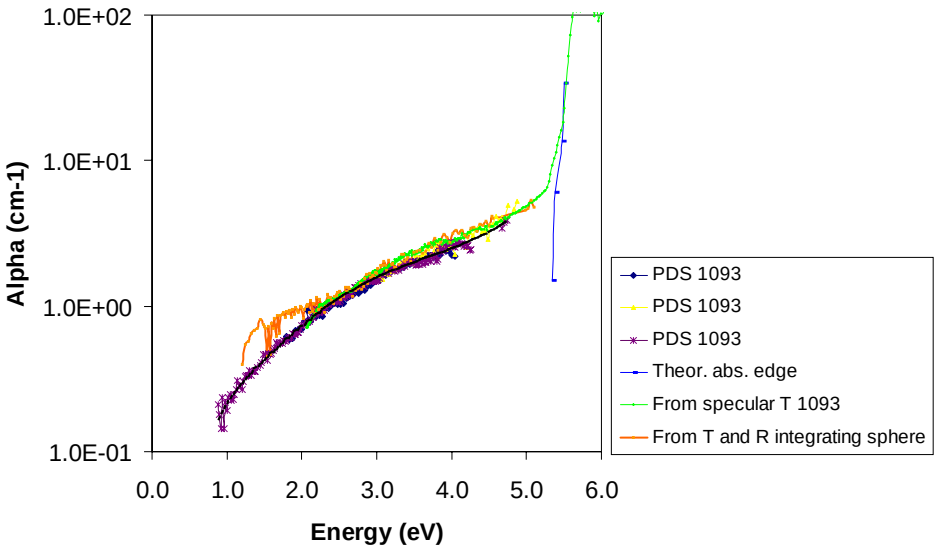

Fig. 3.16 Example of the scaling of an optical absorption spectrum recorded by t-PDS and matched with the corresponding integrating sphere and specular transmission measurements.

The calculated PDS absorption spectrum is then fitted to the UV-absorption coefficient (4.0 eV to 4.5 eV), obtained from the T and R measurement taking into account light scattering and light trapping. (An extended description of different types of scattering and the theoretical model of Filinski for surface scattering is given in Chapter 4.) Fig. 3.16 illustrates once more that, in the low energy range, T and R measurements are not precisely enough to calculate the optical absorption coefficient.

An advantage of this method is that knowledge of the parameter S_{sat} is not required. The saturation value S_{sat} which contains all the experimental parameters (see section 3.5.3) is

[20] Remark: For T and R measurements, the method to determine α depends on the used experimental configuration. When T and R measurements are performed using a spectrophotometer equipped with a light-integration sphere, α is calculated using Eq. (3.28). In the case of specular T and R measurements, α is calculated from Eq. (3.30). More information about the theoretical and experimental aspects of T and R measurements can be found in section 3.6.1)

determined by the fitting procedure. The same procedure is also used by Ambacher et al. [AMB96] to scale the PDS spectra of GaN samples.

The precision of the absolute T-scaling procedure is given by the precision of the T and R measurements. In the case of optically polished samples this is very precise but for samples showing light scattering, T must be corrected for scattering losses.

3.5.6. Absolute scaling of collinear PDS measurements using Laser Calorimetry measurements

To obtain absolute optical absorption values, the relative c-PDS values are calibrated using samples with known absorption. Standard LC measurements (see section 3.6.2) are performed firstly on a (high absorbing) reference sample and secondly on a IIa diamond. These measurements yield absolute absorption values of these samples ($\alpha_{I,\,LC}$ and $\alpha_{II,\,LC}$). From comparison with relative c-PDS absorption values from the same samples ($\alpha_{I,\,PDS}$ and $\alpha_{II,\,PDS}$), the proportionality constant C can be determined: $\alpha_{I,\,LC} = C\ \alpha_{I,\,PDS}$ and $\alpha_{II,\,LC} = C\ \alpha_{II,\,PDS}$). When the calibration constant C is known, absolute values of the total (surface and bulk) absorption coefficient of the other samples can be calculated from the relative c-PDS measurements by multiplying them by the factor C, taking into account multiple reflections at the surfaces.

When using a reference sample for the calibration of c-PDS measurements, it is vital that the beam geometry remains unaltered for measurements on all different samples. In our case, all the measurements were carried out in a fixed focusing geometry in a continuous set of experiments and the c-PDS signal on the reference sample was checked after the measurements.

In the case of c-PDS measurements, the alignment of the probe beam relative to the sample and the pump beam is very critical. Experimentally, it is difficult to put all the samples under investigation at exactly the same relative position, a prerequisite for working under exactly the same experimental conditions. Nevertheless, this method is rather commonly used to study the optical absorption in sapphire and ZnSe [BLA97], [KUB94]. The reproducibility of our measurements (c-PDS amplitude) comes to 5 - 10% as assessed from 10 measurements on one sample. The fluctuations are mainly due to the experimental complexity of the adjustments.

The precision of the PDS measurement is determined by the precision of the LC

measurements to which the PDS data are scaled.

Remark, when the c-PDS interaction length is smaller than the thickness of the sample one needs to sum or integrate the different contributions (c-PDS signals at subsequent depths) to be able to compare the c-PDS results with calorimetric measurements [WIL98]. For our collinear set-up, the interaction length was the sample thickness and therefore, we can use the normalised c-PDS values without performing some integration.

3.6. Additional experimental techniques

3.6.1. Transmission measurements

As already mentioned, the conventional straightforward way to obtain optical absorption spectra is measuring the transmittance and reflectance of the sample. When scattering is neglected, the absorptance A(E) and the absorption coefficient $\alpha(E)$ can be calculated from [BAS 95]:

$$1 = T + R + A \tag{3. 25}$$

where the transmittance and absorptance are given by:

$$T = (1 - R) \exp(-\alpha d) \tag{3. 26}$$

$$A = (1 - R) (1- \exp(-\alpha d)) \tag{3. 27}$$

As a result, the optical absorption coefficient α can be calculated according to:

$$\alpha = -\frac{1}{d}\ln\left(\frac{T}{1-R}\right) = -\frac{1}{d}\ln\left(1-\frac{A}{1-R}\right) \tag{3. 28}$$

When multiple reflections at the sample boundaries are taken into account, the total transmittance of the sample (for normal incidence) is given by summing up the intensities of all the individual transmitted beams:

$$T = (1-R_p)^2 x(1+R_p{}^2 x^2 + ...) = \frac{(1-R_p)^2 x}{1-R_p{}^2 x^2} \tag{3. 29}$$

with R_p the reflectance at the air/sample surface and $x = \exp(-\alpha d)$.

For known thickness, the optical absorption can be calculated from Eq. (3.29) [ESS93]:

$$\exp(-\alpha d) = \frac{\sqrt{(1-R_p)^4 + 4T^2R_p{}^2} - (1-R_p)^2}{2TR_p{}^2} \qquad (3.30)$$

When reflection measurements are unavailable, the theoretical expression for the reflection coefficient R_p at the air/sample interface (normal incidence) can be used in Eq. (3.30):

$$R_p = \left(\frac{n_2 - n_1}{n_2 + n_1}\right)^2 \qquad (3.31)$$

with n_1 and n_2 respectively the index of refraction of air (medium1) and of the sample under investigation (medium2).

Due to the low precision of the T and R measurements, absorptances calculated from these measurements, A = 1 - (T + R), have a limited accuracy. In the case of optically polished surfaces and homogeneous layers, the uncertainty on transmission and reflection measurements is in the range of 0.1-1%. In commercial spectrophotometers absorptance values down to only 10^{-2} can be measured. When the sample surface shows a substantial roughness, e.g. for pyramidal shaped surfaces, or when the sample is polycrystalline and contains grain boundaries, the precision becomes worse and scattering losses have to be taken into account. In that case, an extra scattering term S has to be added in Eq. (3.25):

$$1 = T + R + A + S.$$

To evaluate the scattering term S, the type of light scattering (surface scattering, bulk scattering, etc.) must be known. In general, the situation can be very complex and only a limited theoretical background is accessible in literature [BEC63], [BOR80]. If the surface profile is known for all (x,y) positions, detailed calculations are possible with Maxwell equations. Nevertheless, in practice, this is not possible (see Chapter 4).

To collect the total (specular and diffuse) transmitted and reflected light, an integration sphere has to be used (see Fig. 3.17). The light integration method can only be used if all the light is collected. If the light is partially directed out of the sample via side paths, using this method becomes significantly limited.

A consequence of the above is that T and R measurements are not suitable to study very low absorbing materials, such as polycrystalline CVD diamond. Light scattering due to bulk inclusions and grain boundaries hinders standard transmission measurements (see also Chapter 4) even when using an integrating sphere.

Experimental set-up integrated sphere transmission measurements

A schematic drawing of the experimental set-up used for the integrating sphere T and R measurements is shown in Fig. 3.17. This T and R arrangement uses the illumination beam of our PDS set-up as described in section 3.3.1. Monochromatic radiation illuminates the sample mounted on an integrating sphere[21]. In the case of T measurements the sample is fixed at the front port (see Fig. 3.17 a). For R measurements, the sample is attatched under a small angle[22] at the rear port (see Fig. 3.17 b). Finally, a calibrated Si-photodiode measures the transmittance and reflectance respectively.

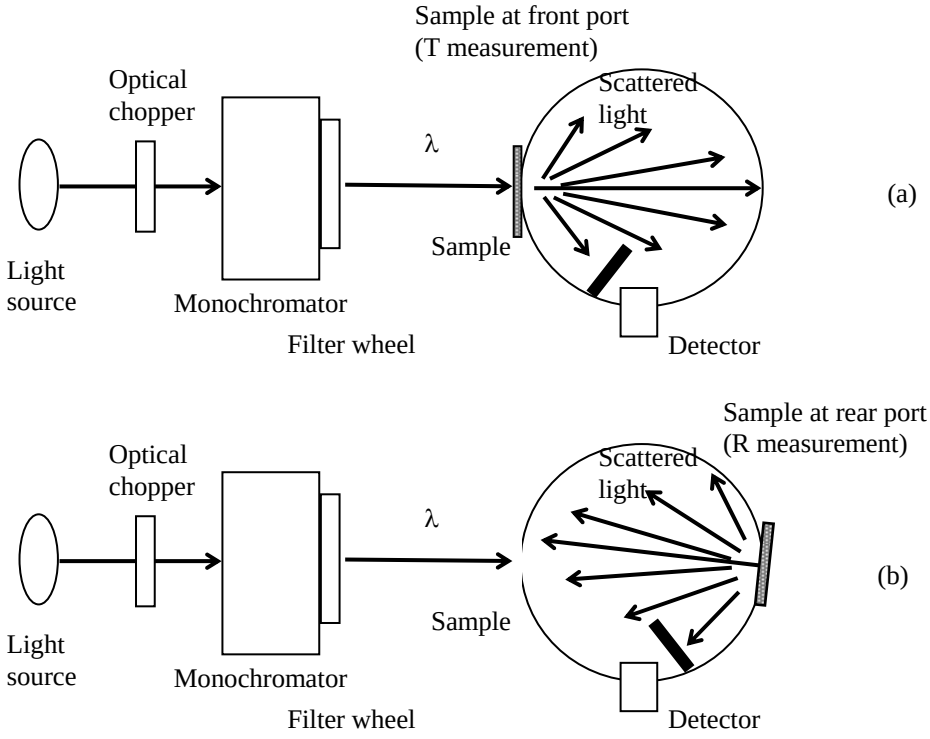

Fig. 3.17 Schematic drawing of an integrated sphere transmission (a) and reflection (b) measurement set-up.

[21] Labsphere Integrating Sphere, Model IS040, Spectraflect coating
[22] small angle: to measure both the specular and diffuse reflection

To rule out the spectral dependencies of lamp, monochromator and detection system, the ratio of the signal obtained with a sample relative to the reference measurement without a sample is taken. For the reference measurement, a rescan without altering the beam geometry but with the sample removed is carried out.

Specular transmission and reflection measurements were performed using a Perkin-Elmer Spectrophotometer.

3.6.2. Laser calorimetry measurements

Standard laser calorimetry (LC) with direct detection of the substrate temperature has been the predominant method for absolute absorptance measurements in the past. Since 1997, it has become the international standard for testing the absorptance of optical laser components [ISO97]. An advantage of LC in comparison with c-PDS is that absolute scaling is relatively simple and moreover, the technical and experimental aspects of the LC set-up are less complicated. LC measures the absolute total absorptance value while c-PDS performs a detailed spatially resolved analysis (see section 3.4). Whenever both absolute and spatial absorption properties must be studied, a combination of the two methods renders the most reliable results.

Experimental set-up

The LC measurements presented in this thesis are performed at Laser Power Europe (Gent). The absorptance is determined from the surface temperature profiles of the sample as recorded during heating (caused by a laser pulse) and subsequent cooling of the sample. The sample, mounted in a thermally isolating holder, is illuminated by a focused CO_2 laser beam in the centre of the sample with calibrated power P (± 30 Watt). The surface temperature as function of the time is measured by a Ni-Cr thermocouple. This thermocouple is fixed perpendicularly on the sample side surface. Thermal paste is used to ensure a good thermal contact between the thermocouple and the sample. Furthermore, care is taken to prevent heating of the thermocouple directly by the pump laser.

The irradiation time is computer controlled and depends on the instantaneous heating profile (rise time, temperature increase ΔT_1) of the sample under investigation. The slopes of the heating and cooling sequences of the measured temperature profile are determined from a fit. The absorptance A is calculated from [WIL98]:

$$A = \frac{mC}{P}\left(\left|\frac{\Delta T_1}{\Delta t}\right| + \left|\frac{\Delta T_2}{\Delta t}\right|\right) \qquad (3.\ 32)$$

with m the mass of the sample, C the specific heat, P the incident laser power (corrected for the reflectance of the investigated film), ΔT_1 and ΔT_2 the temperature increase and decrease of the sample corresponding to the heating and cooling sequences respectively.

For $\alpha d << 1$, the optical absorption coefficient α is given by:

$$\alpha \sim A / d \qquad (3.\ 33)$$

with d the thickness of the film.

A disadvantage of LC measurements is that strong efforts have to be made to minimise the heat transferred to the environment. Furthermore, LC relies on temperature measurements by a thermocouple, whose contact with the diamond sample depends on the surface, the applied pressure, etc. Moreover, care has to be taken not to illuminate directly the thermocouple. An additional disadvantage of LC is the necessity for data correction for the sample geometry, because this determines the kinetics of the heat propagation in the sample.

The advantage of c-PDS as compared to LC is that c-PDS is a noncontact method, relying on optical beams. Additionally, as already mentioned, focussing of the pump beam allows spatial profiling.

3.7. Conclusions

PDS is a very sensitive characterisation technique which allows to determine the optical absorption coefficient α of semiconducting films. The characteristic properties of CVD diamond films, such as its wide band gap, the rough surfaces of the as-grown films, the presence of possible light scattering centres in the films and the high thermal conductivity demanded special adaptions of the experimental set-up.

PDS measurements under two different configurations have been discussed. In the transverse arrangement, the pump beam and probe beam are perpendicular to each other and the index of refraction gradients in the deflection medium surrounding the sample are probed. In the case of the collinear set-up, the pump and probe beams are quasi-parallel and the index of refraction gradients in the sample itself are measured. The transverse set-up can be used in spectroscopic mode to determine the energy dependence of the optical

absorption coefficient, while the collinear arrangement is adapted to measure the local optical absorption at a fixed wavelength of 10.6 μm.

Theoretical considerations indicated that, for both arrangements, the optical absorption coefficient α can be calculated from the recorded photothermal deflection signal according to $\alpha(E) = -1/d \ln(1 - S(E)/S_{sat})$. This equation is valid in the incoherent limit and when scattering is negligible.

Different scaling procedures to obtain the absorption coefficient α in absolute units were compared. The S_{sat}-scaling procedure is only applicable to CVD diamond films which contain a large amount of sp^2 carbon and show saturation in the investigated spectral range. This method can not be applied on intermediate to high quality CVD diamond thin films, because full absorption is not reached. Absolute calibration of t-PDS measurements using the T-scaling procedure relies on fitting of the PDS absorption spectra to the absolute absorption values determined from transmission spectra. Because integrated sphere T measurements suffer much less from scattering, they are used to scale the PDS measurements. Collinear PDS measurements are calibrated using laser calorimetry measurements.

3.8. References

[AMB96] O. Ambacher, W. Rieger, H. Angerer, T.D. Moustakas, M. Stutzmann, Sol. State Comm. **97** (5) (1996) 365-370.

[AME84] N.M. Amer, W.B. Jackson, '*Semiconductors and Semimetals'* Academic Press, Inc. Vol.**21** (B) (1984) Chapter 3, 83-112.

[ANT90] T.R. Anthony, W.F. Banholzer, J.F. Fleischer, L. Wei, P.K. Kuo, R.L. Thomas, R.W. Pyor, Phys. Rev. B **42** (1990) 1104-1111.

[BAS95] M. Bass ed., E.W. Van Stryland, D.R. Williams, W.L. Wolfe, *'Handbook of optics'*, sec. ed., Vol. II (1995) 25.9.

[BEC63] P. Beckmann, A. Spizzichino, *'The Scattering of Electromagnetic Waves from Rough Surfaces'*, Pergamon Press NY (1963).

[BER94] M. Bertoletti, G.L. Liakhou, A. Ferrari, V.G. Ralchenko, A.A. Smolin, E. Obraztosova, K.G. Korotoushenko, S.M. Pimenov, V.I. Konov, J. Appl. Phys. **75** (1994) 7795-7798.

[BLA97] D. Blair, F. Cleva, C. N. Man, Opt. Mater. **8** (1997) 233- 236.

[BOC80a] A.C. Boccara, D. Fournier, W. Jackson, N.M. Amer, Optics Lett., **5** (9) (1980), 377.

[BOC80b] A.C. Boccara, D. Fournier and J. Badoz, Appl. Phys. Lett., **36** (1980) 130.

[BOR80] M. Born, E. Wolf, *'Principles of Optics, Electromagnetic theory of propagation interference and diffraction of light'*, 6th edition, Cambridge University Press (1980).

[BOU93] A. Boudina, E. Fitzer, U. Netzelmann, H. Reiss, Diamond Relat. Mater. **2** (1993) 852-858.

[COL93] A.T. Collins, Physica B **185** (1993) 284-296.

[CUR88] H. Curtins, M. Favre, *'Amorphous Si and related materials'*, ed. H. Fritzsche, (1988), 329-363.

[DIS98] B. Dishler, C. Wild (Eds.) '*Low-pressure Synthetic Diamond: Manufacturing and Applications*' Springer-Verlag, Heidelberg, (1998).

[END95] Endel UIGA, Optoelectronics, Prentice Hall, (1995)

[ESS93] J.M. Essick and R.T. Mather, Am. Journal of Phys. **61** (7) (1993) 646-649.

[FOU79] D. Fournier, A.C. Boccara and J. Badoz, '*Digest of Topical Meeting on Photoacoustic Spectroscopy'* Optical Society of American, Washington DC (1979) paper ThA1.

[GAL93] R. Gallonin R. Rizzoli, C. Summonte, F. Zignani, Y. Xiao, J.I. Pankove, J. Non-Cryst. Solids **164-166** (1993) 635-638.

[GHE95] E. Gheeraert, A. Deneuville, E. Bustarret, F. Fontaine, Diamond Relat. Mater. 4 (1995) 684-687.

[GRI90] G. Grillo, L. De Angelis, J. Non-Cryst. Solids **114** (1989) 750.

[ISO97] *'ISO 11551: test method for absorptance of optical laser components'* International Organization for Standardization, Geneva, Switzerland (1997).

[JAC81] W.B. Jackson, N.M. Amer, A.C. Boccara, D. Fournier, Appl. Opt. **20**(8) (1981), 1333-1344.

[JAC82] W.B. Jackson, N.M. Amer, Phys. Rev. B, **25** (1982) 5559-5562.

[JAC83] W.B. Jackson, D.K. Biegelsen, R.J. Nemanich, J.C. Knights, Appl. Phys. Lett. **42** (1983) 105.

[KUB94] A.P. Kubyshkin, .P. Matrosov, A. A. Karabutov, Opt. Eng. **33** (10) (1994) 3214.

[LEB94] F. Leblanc, Y. Maeda, K. Onisawa, T. Minemura, Phys. Rev. B **50** (1994) 14613-14616.

[LOT91] B.E. Lotter, .B. Schubert, M. Heintze, G.H. Bauer, Mater. Res. Soc. Symp. Proc. **219** (1991) 229.

[MAN83] A. Mandelis, J. Appl. Phys. **54**(6) (1983) 3404-3409.

[MOS97] M. Moser, S. Tasch, G. Leising, Synthetic Metals **84** (1997) 651-652.

[RIE96] W. Rieger, R. Dimitrov, D. Brunner, E. Rohrer, O. Ambacher, and M. Stutzmann, Phys. Rev. B **54** (1996) 17596-17602.

[ROH96] E. Rohrer, C.F.O. Graeff, R. Janssen, C.E. Nebel and M. Stutzmann, Phys. Rev. B, **54** (1996) 7874.

[ROS76] A. Rosencwaig, A. Gersho, J. Appl. Phys. **47** (1976) 64-69.

[SEA92] C.H. Seager, M. Sinclair, D. McBranch, A.J. Heeger, Synthetic Metals **49-50** (1992) 91-97.

[SPE94] K.E. Spear, J.P. Dismukes, '*Synthetic diamond: Emerging CVD Science and Technology'*, ed. K.E. Spear, J.P. Dismukes, Chapter 8, John Wiley & Sons New York (1994).

[TAM89] A.C. Tam, '*Overview of photothermal spectroscopy*' in Photothermal Investigations of Solids and Fluids, ed by J.A. Sell (Academic, Boston, 1989) pp.1-33

[TRO98] W.J. Tropf, M.E. Thomas, M.J. Linevsky, '*IR refractive indices and thermooptic coefficients for several materials*' SPIE Vol. 3425, SPIE conference on Optical Diagnostic Methods for Inorganic Transmissive Materials, San Diego, California, July 1998.

[WIL98] U. Willamowski, D. Ristau, E. Welsch, Applied Optics, **37**(36) (1998) 8362.

[WU96] Z.L.Wu, M. Thomsen, P.K. Kuo, Y.S. Lu, C. Stolz, M. Kozlowski, '*Overview of photothermal characterization of optical thin films coatings'*, SPIE Vol. **2714**/ 465

[YAS82] Z.A. Yasa, W.B. Jackson, and N.M. Amer, Appl. Opt. **21**, (1982), 21.

[YOU84] M. Young, *'Optics and Lasers'*, sec. ed., Springer Series in Optical Sciences Volume 5, Springer-Verlag, (1984).

[ZAM98] U. Zammit, K.N. Madhusoodanan, M. Marinelli, F. Mercuri, and S. Foglietta, Phys. Rev. B, **57** (1998) 4518.

[ZAM99] U. Zammit, K.N. Madhusoodanan, M. Marinelli, F. Mercuri, and S. Foglietta, (1999) 4518.

[ZIM97] B.L. Zimmering, A. C. Boccara, Appl. Opt. **36** (15) (1997) 3188.

4. Comparison of photothermal deflection and transmission: effect of light scattering

4.1. Introduction

Generally, it is accepted that the PDS technique is much less influenced by light scattering in comparison to conventional transmission measurements. PDS is only sensitive to the heat deposited in the sample and only the light deflected in the direction of the probe beam influences the signal (see Chapter 3). Nevertheless, the influence of light scattering at the surface (surface scattering) and in the bulk of the sample (volume scattering) has to be investigated. (Elastic) volume light scattering can take place at heterogeneities in the refractive index e.g. at bulk inclusions, voids, defects or grain boundaries in polycrystalline films. In that case, the total attenuation coefficient α_e can be written as $\alpha_e = \alpha_a + \alpha_s$, whereby α_a is the optical absorption coefficient and α_s is the volume scattering coefficient [VAN91]. Light scattering is related to the material quality (presence of crystalline defects and impurities, and size of the grains).

Polycrystalline CVD diamond films contain a lot of potential scattering centres. Moreover, their surface roughnesses are not negligible and certainly influence surface light scattering. Besides, light trapping in the diamond film can occur. Because of the large difference between the refractive index of diamond and the surrounding medium (air or fluid), the light can be totally internally reflected when it is scattered under angles larger than the critical angle.

The following chapter is devoted to light scattering and multiple reflections in diamond films. We investigate the influence they have on t-PDS[1] and compare the results with the scattering effects on transmission measurements. We will check if light scattering forms an obstacle to apply PDS to CVD diamond films.

[1] In the case of c-PTD measurements the samples were polished from both sides and therefore we assume we can rule out surface scattering. Moreover the investigated samples are of extremely high quality and we expect only minor influence of volume scattering.

4.2. Theoretical scattering models

4.2.1. Volume scattering

Strong internal light scattering (volume scattering) can affect the magnitude of the PDS signal, because light scattering can modify the optical path of the incident light in the sample [TAM89] (see Fig. 4.1 for a qualitative explanation).

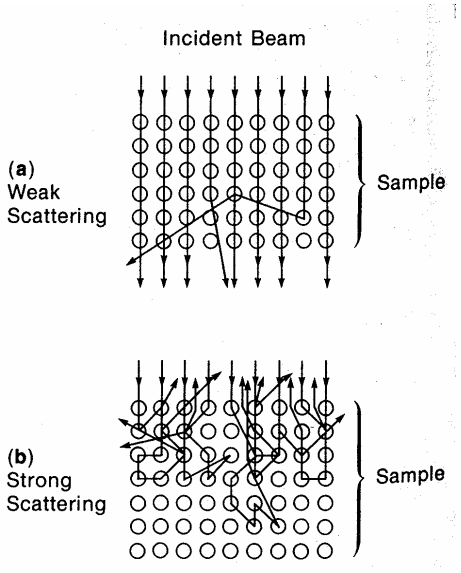

Fig. 4.1 Effect of weak (a) and strong (b) light scattering on the PDS signal, after [TAM89].

In terms of PDS measurements, this means that one has to take into account an effective sample thickness d_{eff} equal to the optical path length of the light beam in the film. This effective thickness can be equal to or larger than the physical thickness d of the sample. In the case of Fig. 4.1(b) the strong light scattering results in a longer optical path. Consequently more optical energy is absorbed in a thin layer at the sample surface. The effect of the corresponding enhanced absorption on the PDS signal is the largest for thermally thick samples (thermal diffusion length $\mu <$ optical attenuation length) where only a small skin layer is probed.

In the case of diamond, under the applied conditions ($\nu \sim 8$ Hz), the investigated samples

are thermally thin. Therefore we can assume that the influence of this type of scattering on the PDS signal is rather small.

4.2.2. Surface scattering

Already for decades, scattering of electromagnetic waves at rough surfaces of thin films has been subject of several studies. A general and exact solution is still unknown, but in literature, few models describing a specific type of light scattering can be found [BEC63], [FIL72], [YIN96], [REM99].

Beckmann et al. [BEC63] developed general models for scattering from rough surfaces. But in practice they only can be used for special types of surfaces such as periodically rough surfaces and purely randomly rough surfaces, because in these cases the geometry of the surface can be well described. Beckmann et al. [BEC63] define a correlation distance τ of the surface to represent the density of the inhomogeneities and irregularities. Because, not only the surface roughness value R_a is important but also whether the hills and valleys of the surface are crowded close together or far apart and whether there is some correlation over a certain distance. Both these factors R_a and τ play an important role in scattering theories. For random rough surfaces, τ is almost zero and typically much smaller than λ. For an uncorrelated surface ($\tau = 0$), the light is scattered with equal probability into all directions. The angular distribution of the intensity of the scattered light then satisfies the Lambert's (cosine) law. For periodical surfaces the correlation length has a certain value (infinite for an ideal periodical surface) and these surfaces start behaving as a diffraction grating. For more complicated surfaces only an approximation of the distribution of the scattering field can be obtained. To be able to apply one of the theoretical models one needs to know exactly the profile of the illuminated surface. This is, however, in practice for our diamond thin films rather impossible. An unpolished as grown top surface of polycrystalline CVD diamond can adopt different morphologies e.g. {100}, {111}. A SEM photograph of a typical surface, consisting of truncated pyramids tilted over different angles, is shown in Fig. 4.3.

Scattering at thin diamond films is studied by Yin et al. [YIN96]. They proposed a theoretical model to describe the specular transmittance and reflectance for thin films. The model incorporates the effects of surface scattering at one rough surface (the other surface is assumed to be smooth) whereby the rms surface roughness σ is small compared to the wavelength of the incident light and randomly distributed (uncorrelated surface). This can be true just for thin diamond films. Light scattering at a random rough growth

surface of the film is implemented by modifying the Fresnel transmission and reflection coefficients by scattering correction factors S_{ext}, S_{int}, S_t as introduced by Filinski [FIL72]. The reductions of the intensities of the transmitted and reflected beams are expressed in terms of these scattering factors. For a surface with rms surface roughness σ (or R_q) of the growth surface, the scattering factors are given by:

$$S_{ext} = \exp\left[-\left(\frac{4\pi n_0 \sigma}{\lambda}\right)^2\right] \tag{4. 1}$$

$$S_{int} = \exp\left[-\left(\frac{4\pi n_1 \sigma}{\lambda}\right)^2\right] \tag{4. 2}$$

$$S_t = \exp\left[-\left(\frac{2\pi (n_1 - n_0) \sigma}{\lambda}\right)^2\right] \tag{4. 3}$$

whereby λ is the wavelength of the incident light, n_1 is the index of refraction of the film and n_0 is the index of refraction of air (or, more general, of the surrounding medium).

For freestanding (thick) CVD diamond films (thickness is that large that interference effects between subsequent transmitted beams can be omitted), the following model can be proposed. Assuming multiple incoherent reflections in the film with two rough surfaces (front surface I and back surface II), Eq. (3.29) is modified by Eq. (4.1), Eq. (4.2) and Eq. (4.3) and the transmittance T is given by:

$$T = (1-R)^2 S_t^I S_t^{II} x (1 + R^2 S_{int}^I S_{int}^{II} x^2 + ...) = \frac{(1-R)^2 S_t^I S_t^{II} x}{1 - R^2 S_{int}^I S_{int}^{II} x^2} \tag{4. 4}$$

The reflectance R^I of the rough layer (light incident on surface I, back surface II) is given as follows:

$$R^I = R S_{ext}^I + (1-R)^2 R (S_t^I)^2 S_{int}^{II} x^2 (1 + R^2 S_{int}^I S_{int}^{II} x^2 + ...)$$

$$R^I = R S_{ext}^I + \frac{(1-R)^2 R \left(S_t^I\right)^2 S_{int}^{II} x^2}{1 - R^2 S_{int}^I S_{int}^{II} x^2} \tag{4. 5}$$

4.2.3. Light trapping

Light trapping can enhance light absorption [TUR97]. The fraction of the incident light energy flux that is entering the (diamond) sample can be enhanced by means of optical structures (diffractive optics) on the surface. Structures such as pyramids and inverted pyramids can enhance, depending on the entrance angle, the surface reflection by directing light into the sample and help to trap the light. Light trapping can also be due to a strong light scattering and a high index of refraction of the layer.

A critical angle of incidence θ_k (see Fig. 4.2 (b)) determined by the index of refraction of the layer n, is defined as θ_k = arcsin (1/n). For light incident on the back surface under angles θ larger than θ_k the light will be internally reflected (trapped in the layer). In the case of diamond θ_k = 25° (n = 2.4) and only a small fraction (~ $1/n^2$) of the light can escape [TUR97].

An example of light trapping by scattering at the front surface and total internal reflection at the back surface is given in Fig. 4.2 (a). Consequently the absorption in the material can increase significantly due to an increased optical path in the sample. The efficiency of light trapping can be quantified as an increase of the effective optical thickness of the film.

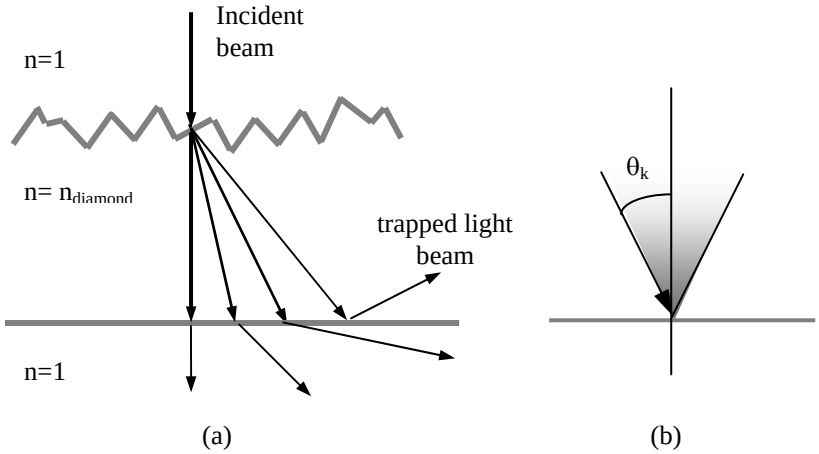

Fig. 4.2 (a) illustration of light trapping in a layer with a rough surface, (b) critical angle of incidence.

Snail et al. [SNA91] mention that the effect of total internal reflection at interfaces may decrease the transmittance in polycrystalline CVD diamond films. Besides surface and volume scattering, the effect of light trapping can be expected in polycrystalline diamond samples too, because of the combination of scattering and the high difference between the index of refraction of diamond and air (leading to a small critical angle).

The morphology of the diamond surface (e.g. truncated pyramids) and the scattering centres in the bulk both effect the light scattering and light trapping, which on their turn influence the transmission, reflection and PDS measurements. Therefore, we have to define an effective sample thickness (d_{eff}) which will account for the influence for all different types of scattering. This is a complicated problem because d_{eff} will be different in high and low absorption regions [POR00]. Yasa et al. proved that optically thin samples (low absorption) are independent of light scattering when $\alpha_s d < 0.1$ with α_s the optical scattering coefficient [YAS82].

4.3. Sample description

To study the effect of light scattering on t-PDS and transmission spectra, a set of four samples (see Table 4.1), specially deposited for this goal, is examined by the two optical characterisation techniques in a comparative way. A series of polycrystalline CVD diamond films with different surface roughnesses has been supplied by De Beers Industrial Diamond Division, (UK) Ltd[2]. A natural type IIa diamond is also measured for comparison.

The series consists of four samples prepared from one larger diamond film. Therefore a 1 cm^2 film of commercially available (standard) optical material is cut into four equally sized pieces. The original sample is deposited in a MWPE CVD system but the appropriate deposition conditions have not been disclosed and consequently are not mentioned here.

Hence, all four samples consist of the same bulk material, but they have been subjected to different surface treatments. After laser cutting, the first sample (1090) was left as grown. The top surface of this sample consists of truncated pyramids (see Fig. 4.3), while the surface at the substrate side has the substrate roughness.

[2] DeBeers Industrial Diamond Division, (UK) Ltd, Berkshire, SL59DX, U.K.

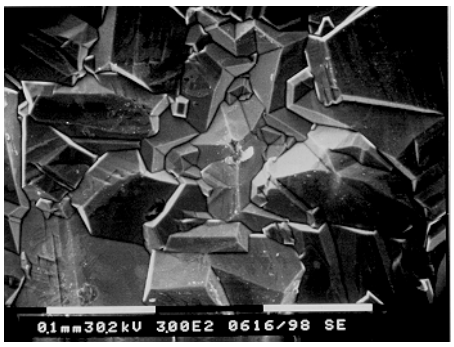

Fig. 4.3 SEM photograph of the as grown top surface of a CVD diamond with truncated pyramids (sample 1090).

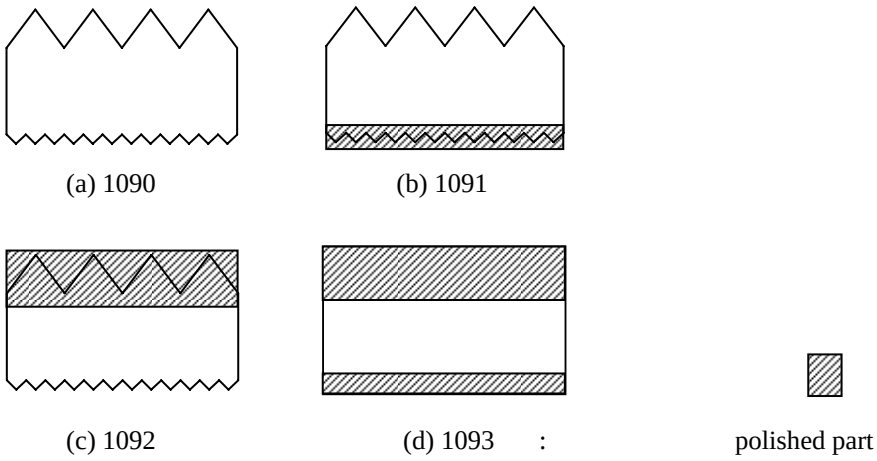

Fig. 4.4 Depiction of the different surface treatments performed on the four samples originating from the same as grown sample: (a) as grown sample 1090, (b) sample 1091 with a polished substrate surface, (c) sample 1092 with a polished top surface, (d) sample 1093 with both surfaces polished.

For sample 1091 and sample 1092, respectively the substrate surface and top surface were optically polished. Finally, sample 1093 was polished on both sides. An overview of the different samples is given in Fig. 4.4. Their respective surface treatments and roughnesses are summarised in Table 4.1. The thickness of the samples varied between 550 – 635 µm.

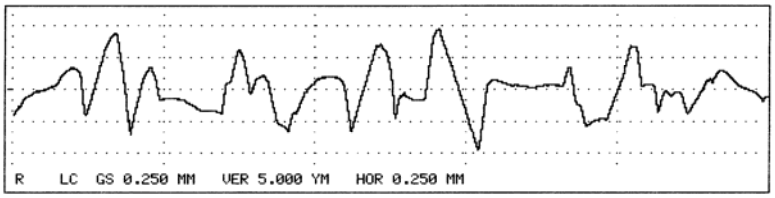

(a)

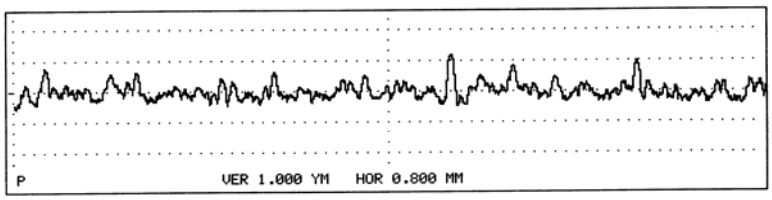

(b)

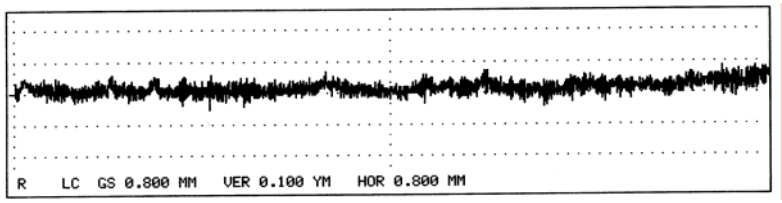

(c)

Fig. 4.5 (a) The as-grown top surface profile of sample 1090, (b) the substrate surface profile of sample 1092, (c) the polished surface of sample 1093.(attention has to be paid to the different vertical scales)

The four samples differ only as regards the surface roughness and the eventually larger amount of a-C polished away from the substrate surface side. At the substrate side there are more a-C regions expected because of the larger amount of grain boundaries, due to smaller sizes of the crystallites when they start to grow. Nevertheless, Pickles et al. [PIC99] have found that there is no enhanced absorption layer deeper than 5μm and no significant surface layer effect.

A quantitative parameter for the surface characterisation profile evaluation is R_a, the

arithmetical mean roughness[3]. The R_a values of the top- and substrate surfaces of the samples are measured by a Phertometer S8P 6.22. A surface profile of the as grown top surface, of the substrate surface and of a polished surface are shown in Fig. 4.5. The R_a values of the optical quality polished surfaces (see Fig. 4.5 (c)) are of the order of 10 nm, the experimental polishing limit. This surface can be considered as a random uncorrelated surface. The rms surface roughness value R_q[4] ($\equiv \sigma$), used in theoretical models, is only slightly larger than the R_a value.

Table 4.1 R_a values of the samples.

Sample	Substrate side	R_a substrate (μm)	Top side	R_a top (μm)
1090	as grown	0.20 ± 0.06	as grown	2.79 ± 0.73
1091	Polished	0.008 ± 0.001	as grown	2.42 ± 0.20
1092	as grown	0.19 ±0.01	Polished	0.010 ± 0.004
1093	Polished	0.006 ± 0.001 (R_q 0.007± 0.001)	Polished	0.008 ± 0.004 (R_q 0.010 ± 0.004)

4.4. Transmission, reflection and PDS measurements

4.4.1. Transmission measurements

Fig. 4.6 shows the transmission spectra in the 1 - 6 eV energy range for the four CVD diamond samples (1090-1091-1092-1093). The spectra are recorded in a Perkin Elmer spectrometer. For comparison, the transmission spectrum of a type IIa natural single crystal diamond is also measured. Because of light scattering, standard transmission measurements became difficult and gave only sufficient precision for the optically

[3] Arithmetical mean roughness R_a: arithmetic average deviation from the centre line defined as $R_a = \frac{1}{L}\int_{x=0}^{x=L} |y| dx$

[4] Root Mean Square (rms) surface roughness R_q: defined as $R_q = \left(\frac{1}{L}\int_{x=0}^{x=L} y^2 dx\right)^{1/2}$

polished sample 1093. The transmission of sample 1093 is very close to that of type IIa diamond. At 2 eV and lower, the transmission of the IIa diamond and sample 1093 rises to reach values close to the theoretical values of approximately 71% (limited by the inherent reflectance of the sample surfaces) [SAV97].

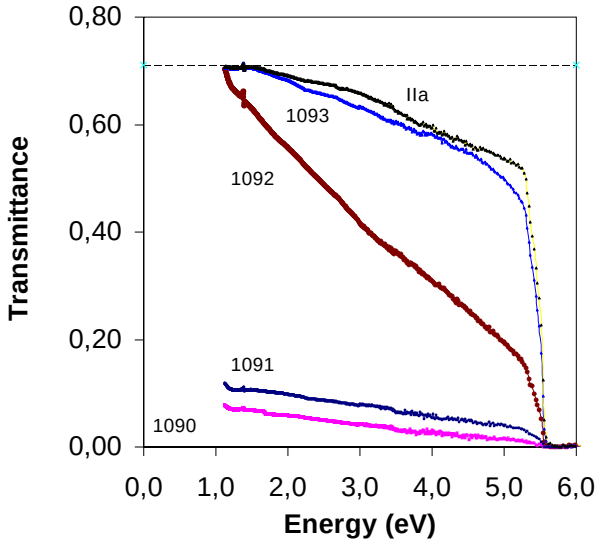

Fig. 4.6 Specular transmission spectra of polycrystalline CVD diamond films with different surface roughnesses (1090-1091-1092-1093) compared with IIa.

On the other hand, the transmission in samples 1092, 1091 and 1090 is to an increasing extent attenuated due to the roughness of the sample, which causes scattering losses, and not to higher absorption in these samples. This becomes more evident when we examine the results shown in Fig. 4.7, where we have plotted the transmittance at 2 eV versus the surface roughness for the different CVD diamond samples. Sample 1092 has only a rough substrate surface (R_a ~ 0.19 µm), sample 1091 has a rough top surface (R_a ~ 2.42 µm) while sample 1090 has two unpolished rough surfaces (R_a ~ 0.20 µm, R_a ~ 2.79 µm). When comparing the specular transmission spectra of samples 1091 and 1092, it is clear that the pyramidal top surface of sample 1091 has a much stronger influence on the scattering than the much smoother substrate surface of sample 1092 (see Table 4.1). Since all samples are of the same bulk material, there is no reason to assume that these samples show a higher optical absorption than 1093. These transmission losses have to be

attributed to scattering at the rough sample surfaces. An other effect which may decrease the transmittance in polycrystalline films is light trapping of the incident radiation at the diamond-air interface. The group of Bi et al. [BI90] observed also a strong surface dependence of the optical transmission of very thin (~10 µm thick with a surface roughness of the order of 0.2 µm) diamond films and made use of phenomenological fits in order to correct the data for this loss of specular transmission when calculating the absorption coefficient. Similar transmission spectra were obtained by Feng [FEN93] and Sussmann et al. [SUS94].

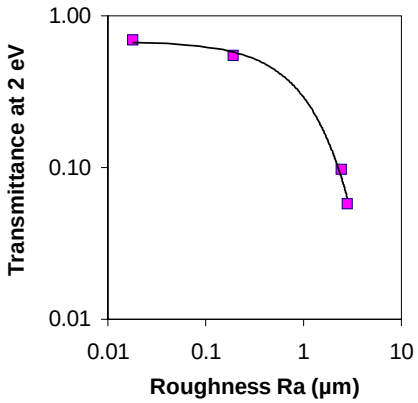

Fig. 4.7 Transmittance at 2 eV of the CVD diamond films as a function of the surface roughness (value of the most rough surface).

Fig. 4.8 shows the optical transmission spectra of samples 1091-1092-1093 measured with and without an integration sphere. The higher the surface roughness of the sample, the larger is the discrepancy between both spectra (see arrows). Nevertheless, as can be seen from Fig. 4.8, even the integrated sphere measurements suffer in a minor way from scattering. Because of the rough surface of the samples, incident light can be transmitted in different directions with corresponding optical paths longer than the physical thickness d of the sample. Consequently, the absorptance is higher and the transmittance decreases. Moreover, since the sample is larger than the entrance of the light integrating sphere, there is some possibility that scattered light is not completely collected by the integration sphere. This is for example the case when the scattered light is propagating along the sample and leaves the sample through its side edges.

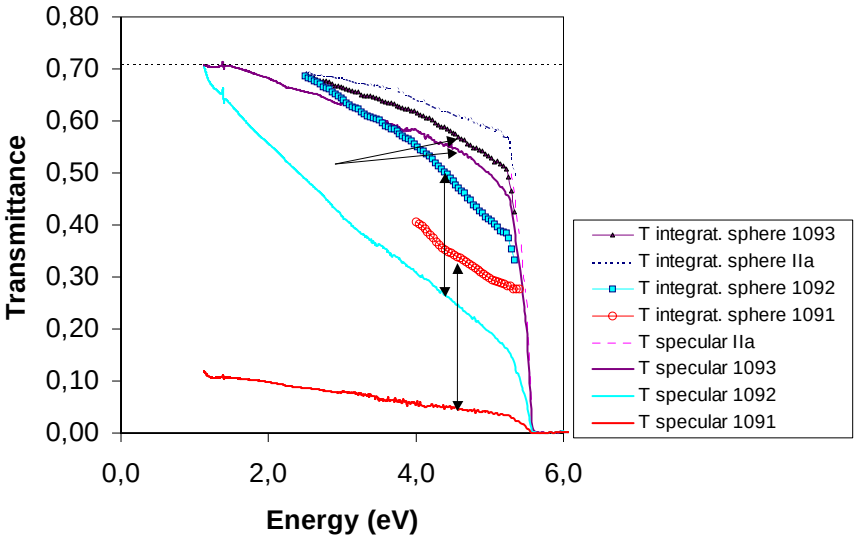

Fig. 4.8 Optical transmission spectra of CVD diamond samples 1091-1092-1093, measured with and without integrating sphere, illustrating the difference in scattering between the different samples.(arrows indicate corresponding specular and integrating sphere measurement for a particular sample.)

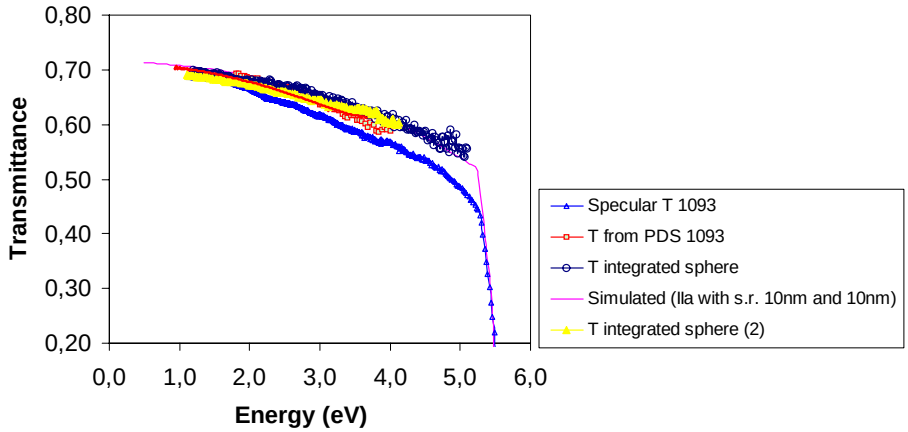

Fig. 4.9 Optical transmission spectra (obtained from specular and integrating sphere measurements) of the polished sample 1093 compared with the theoretical transmission spectrum of a diamond with top and substrate surface roughnesses of $\sigma 1$ 10 nm and $\sigma 2$ 10 nm respectively and with the transmission spectrum calculated from PDS data.

In Fig. 4.9 an overview is given of the transmission spectra of sample 1093 obtained via different methods: measured by specular and integrating sphere transmission measurements, and calculated from PDS measurements. The various curves are similar, only in the case of specular transmission measurements slight deviations can be observed.

As pointed out in section 4.2.3, we adopted the model of Filinski to take surface scattering in specular transmission and reflection measurements into account. The transmission of a IIa diamond is considered and corrected for rough substrate and top surfaces (see Eq. (4.4)). We applied this model to fit the transmission spectrum of sample 1093 (type IIa quality diamond) and the result is plotted in Fig. 4.9. A good fit could be obtained for top and substrate surface roughnesses of respectively $\sigma 1$ 10 nm and $\sigma 2$ 10 nm. No realistic roughness values could be fitted for the other samples (1090-1091-1092). The model of Filinski is not applicable for these samples because the surface roughness exceeds the wavelengths of the investigated energy region and moreover the surface roughness is not randomly distributed. As can be seen from simple observations the angular dependence of the reflectance is not a cosine distribution for the CVD diamond samples. This implies that our samples have a finite surface correlation length.

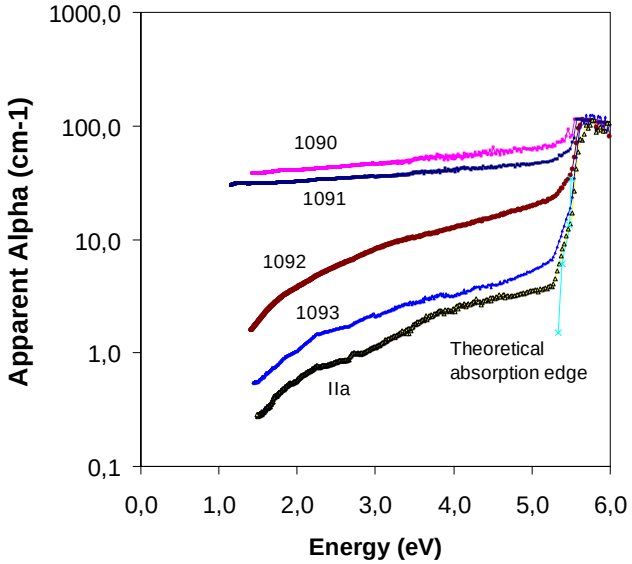

Fig. 4.10 The apparent optical absorption coefficient for CVD diamond samples 1090-1091-1092-1093 as calculated from the specular T measurements shown in Fig. 4.6.

Further, other theoretical models proposed by Beckmann could not be applied neither, because one needs to know the exact surface profile of the investigated samples, which is nearly impossible in practice.

The specular transmittance and reflectance are modified dramatically by the surface roughness of the diamond films. Fig. 4.10 shows the apparent optical absorption coefficient versus energy, as calculated according to Eq. (3.30) from specular transmission measurements in combination with theoretical reflectance values (Eq.(3.31)). Because all the four samples are originating from the same high quality diamond film, one should expect the same optical absorption for all of them. This is in great contrast with the results. Assuming Eq. (3.30) is valid for the experimental conditions, the differences between the apparent absorption coefficients for the four different samples have to be due to the differing surface roughnesses.

One can conclude from Fig. 4.10 that specular transmission measurements are failing as an instrument to characterise the optical absorption of as-grown CVD diamond films due to light scattering. Before making measurements, one first should polish the CVD films to make the surface as smooth as possible. In practice this seriously limits easy use of transmission measurements. Integrated sphere transmission measurements suffer much less from scattering, and therefore, are used to scale the PDS measurements.

4.4.2. Reflection measurements

The integrated sphere reflectance spectra of samples 1090, 1091, 1092 and 1093 are plotted in Fig. 4.11. All films were measured twice, illuminated from both the top and substrate surface sides because both surfaces show different roughnesses. The theoretical reflectance of a type IIa diamond is shown for comparison. In the low energy range (1.4 eV to 3.2 eV) the spectra were recorded with a halogen lamp while a Xe-lamp was used for the high energy range (2.5 eV to 5.4 eV).

From Fig. 4.11, it is clear that R is reduced for all polycrystalline CVD samples (1090-1091-1092-1093) compared to the theoretical reflection limit of IIa diamond of about 30%. These lower values can largely be attributed to losses of light (~ 5 %). Even with an integration sphere not all the diffuse scattered light is completely collected. A second minor contribution can come from a different index of refraction. For diamond films containing more a-C (as compared to type IIa diamond) the index of refraction can be smaller [YIN97], [REM99]. Yin et al. reported values for the index of refraction of

diamond ranging from 1.9 to 2.4 for different quality samples. Moreover, a wavelength dependence of the index of refraction was measured. Lower index of refraction values lead to smaller reflectances. Finally, because of the pronounced structured surface, reflected light can be reabsorbed which also can lower the reflection values.

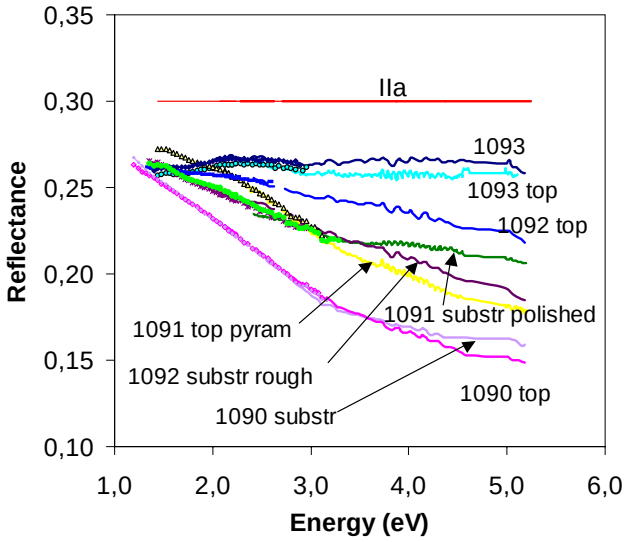

Fig. 4.11 Integrated sphere reflectance measurements on polycrystalline CVD diamond samples 1090-1091-1092-1093 compared with IIa diamond.

The reflectances (from the top and from the substrate side) of sample 1093 show no energy dependence. On the contrary, as can be seen from Fig. 4.11, the total reflectance of the other samples with a more pronounced structured surface (1090, 1091 and 1092) decreases at higher energies. Up till now, we do not have a theoretical model which is able to fit these results. The adapted model of Filinski predicts a stronger decrease of reflection at high energies.

4.4.3. Transverse PDS measurements

The PDS optical absorption data for samples 1090, 1091, 1092 and 1093 are shown in Fig. 4.12. Transverse PDS measurements were performed at room temperature. The spectral dependence of the optical absorption coefficient α of the samples was measured over the energy range 0.9 to 4.5 eV. To obtain absolute values, the absorption coefficient

was calculated from Eq. (3.24) with an arbitrary saturation value S_{sat} and matched, for all samples (1090, 1091, 1092 and 1093), to the transmission data from sample 1093 in the (low absorption) energy range of 4.0 eV to 4.5 eV (see section 3.6.6). We chose the transmission data of sample 1093 to scale the PDS data, because this sample experienced no surface scattering effects as follows from section 4.4.1 (transmission measurements).

The spectral dependence of the absorption coefficient is practically identical showing again the typical dependence (amorphous carbon inclusions) which we see generally in all CVD samples (see Chapter 5).

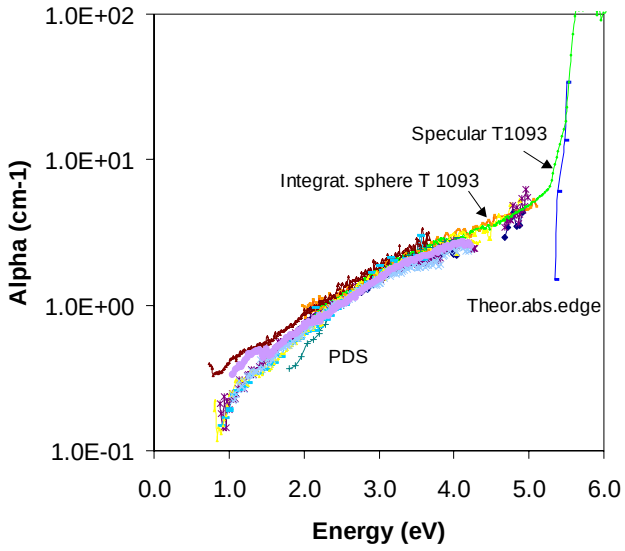

Fig. 4.12 The spectral dependence of the optical absorption coefficient α for CVD diamond samples 1090-1091-1092-1093.

Volume scattering can enhance the effective optical thickness of all CVD diamond films. In the case of unpolished samples, there is an extra enhancement of d_{eff} due to surface scattering and light trapping in the sample which causes an artificially higher absorption in the polycrystalline samples. Nevertheless, compared to transmission measurements, PDS is less sensitive to light scattering at the rough surface. This results from the fact that the sample is immersed in a liquid (n_{CCl4} = 1.48). If the liquid had the same index of refraction as diamond, the effect of the rough surface would be diminished. Because this is not so, it is just reduced.

The data in Fig. 4.12 show that all optical absorption curves for the four samples coincide after matching the PDS spectra. This is exactly what can be expected from the results of Poruba et al. [POR00]. In the low absorption region[5], where $\alpha d < 1$, the effective optical thickness enhancement and consequently the absorption enhancement is not energy-dependent. The shape of the spectrum is not distorted by scattering effects in this region, but the signal is enhanced by a constant factor (up till 10). This means that the sensitivity of the PDS measurement is even higher when scattering occurs. To get absolute absorption values the calibration has only to be performed with a constant d_{eff} (which can be different for each sample). Hence, it is possible to match the PDS spectra to the correct α values from the polished sample. In the high absorption region[5], on the other hand, the light is more quickly absorbed, quicker then it passes a distance d. Consequently the distance over which light is absorbed, d_{eff}, is energy dependent. The discrepancy between the spectrum corresponding to the true optical absorption coefficient α (α_a) and to the recorded apparent spectrum ($\alpha_a + \alpha_s$), where the scattering effects are included, decreases with increasing energy [POR00]. This indicates an energy-dependent scattering contribution. In our case, this forms no problem because the absorption spectra of the high absorption region were calculated from transmission measurements. As a consequence, the influence of scattering and light trapping is not visible in the final absorption spectra.

Fig. 4.13, Fig. 4.14, Fig. 4.15, and Fig. 4.16 show the optical absorption spectra of the different diamond samples obtained via t-PDS measurements (several measurements for each sample), specular transmission measurements, and integrated sphere transmission and reflection measurements. In addition, the theoretical absorption edge of diamond and the calibration transmission data of sample 1093 are also plotted. From these spectra can be concluded that the transmission measurements are strongly influenced by surface scattering, while t-PDS measurements of the different samples yield the same optical absorption coefficients.

[5] For CVD diamond: low absorption region - energies up till 4.5 eV, high absorption - energies above 4.5 eV

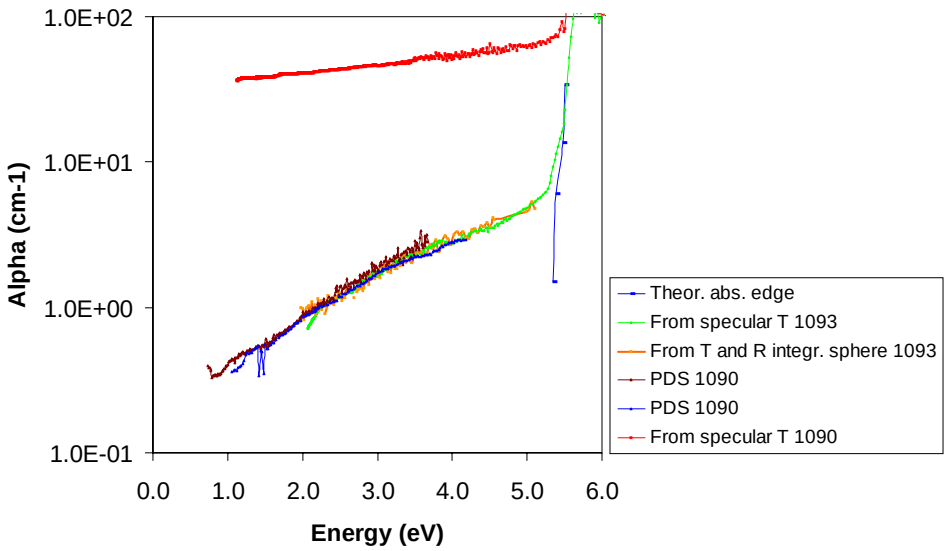

Fig. 4.13 The spectral dependence of the optical absorption coefficient α of sample 1090.

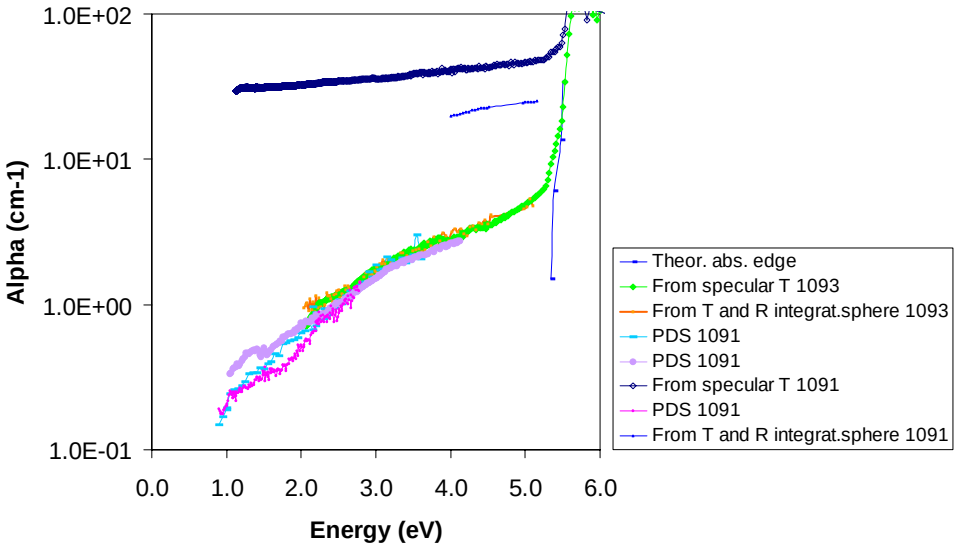

Fig. 4.14 The spectral dependence of the optical absorption coefficient α of sample 1091.

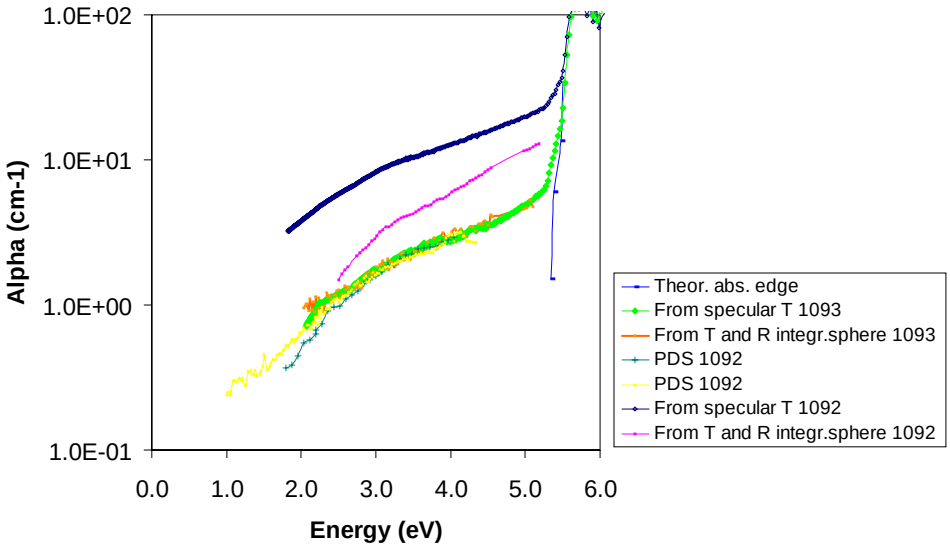

Fig. 4.15 The spectral dependence of the optical absorption coefficient α of sample 1092.

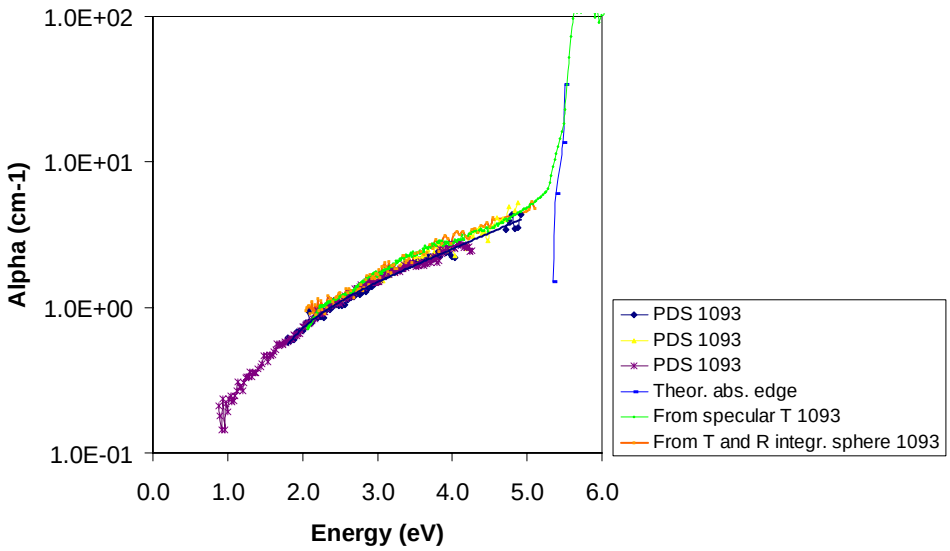

Fig. 4.16 The spectral dependence of the optical absorption coefficient α of sample 1093.

4.5. Conclusions

Surface scattering has a large influence on specular transmission measurements. Integrated sphere transmission measurements, on the other hand, are less influenced by scattering losses at a rough surface but still, differences between polished and unpolished samples are clearly visible. Theoretical simulations of IIa diamond transmittance spectra for different surface roughnesses are compared with the experimental transmittance curves. The theoretical model yields only good results for fits to the spectrum of the polished sample. On the other hand, the model of Filinski is not applicable on our samples with rough surfaces because the surface roughness exceeds the wavelengths of the investigated energy region and moreover the surface roughness is not randomly distributed.

Integrated sphere reflection measurements show lower reflection values for the CVD diamond films compared to type IIa diamond. The main reason is that even an integration sphere does not collect all the scattered light. Furthermore, to a lesser degree the lower values can be possibly attributed to a different index of refraction. When the surfaces of the sample possesses a more pronounced structure, the reflectance decreases, but up till now there is no explanation for this behaviour.

The PDS signal, finally, is artificially enhanced by an increase of the effective optical thickness because of both surface and volume scattering and light trapping in the CVD diamond films. In the low absorption region, $\alpha d < 1$, this enhancement is spectrally independent and the shape of the spectrum is not distorted. Actually, it comes down to an increased effective thickness d_{eff} and an enhancement of the sensitivity of PDS. Because of the spectral independence of d_{eff}, this allows to match the PDS data of the unpolished samples to the correct absorption values obtained from measurement of the polished sample or from transmission measurements. Obviously, in the final spectra (absolute units) the magnitude of the effective thickness has no importance anymore.

From this light scattering study we can conclude, that the roughness of the diamond surface is clearly of huge importance as far as measuring optical properties of CVD diamond films is concerned. For polished samples, both transmission and PDS measurements can be used and the precision of the optical measurements is of the order of a few percent.

For unpolished samples, the category to which most investigated samples belong, one has

to consider two cases. Firstly when the surface roughness is relatively small, the theoretical model of Yin et al. which takes into account the scattering losses can be used. Secondly, when surfaces with a substantial roughness (larger than the wavelength) are investigated, this model can not be used anymore. On the one hand, scattering strongly influences transmission measurements. The sensitivity of the transmission technique is not high enough to measure small absorptions. Consequently the low absorption values of high quality diamond are inaccessible. On the other hand, light scattering and light trapping do not influence the PDS spectra in the low energy region ($\alpha d < 1$). Therefore, in this region PDS is the most suitable technique to determine the spectral dependence of the optical absorption coefficient α of CVD diamond samples. The great advantage is that the samples do not have to undergo a time consuming polishing process, to obtain smooth surfaces, before they can be investigated, as is the case for transmission measurements. In the high absorption region transmission measurements yield correct absorption values. To get absolute values in the low energy region, the PDS data have to be scaled to integrated sphere transmission measurements in the boundary between the low and high absorption regions.

4.6. References

[BEC63] P. Beckmann, A. Spizzichino, *'The Scattering of Electromagnetic Waves from Rough Surfaces'*, Pergamon Press NY (1963).

[BI90] X.X. Bi, P.C. Eklund, J.G. Zhang, A.M. Rao, J. Mater. Res. **5** (1990) 811-817.

[FEN93] T. Feng, B.. Schwartz, J. Appl. Phys., **73**(3) (1993) 1415-1425.

[FIL72] I. Filinski, Phys. Stat. Sol.(b) **49** (1972) 577-588.

[PIC99] J.C.S. Pickles, T.D. Madgwick, C.J.H. Wort, R.S. Sussman, presented at Diamond'99 in Prague

[POR00] A. Poruba, accepted for publication in J. Non-Crystalline Solids in (2000).

[REM99] Z. Remes, *'Study of defects and microstructure of amorphous and microcrystalline silicon thin films and polycrystalline diamond using optical methods'*, PhD thesis (1999).

[SAV97] J.A. Savage, C.J.H. Wort, C.S.J. Pickles, R.S. Sussmann, C.G. Sweeney, M.R. McClymont, J.R. Brandon, C.N. Dodge, A.C. Beale, Proceedings of the SPIE Window and Dome Technologies and Materials Symposium, Orlando, Florida, (1997) SPIE **3060,** 144.

[SNA91] K.A. Snail, L.M. Hanssen, J. Cryst. Growth **112**, (1991) 651.

[SUS94] R.S. Sussmann, J.R. Brandon, G.A. Scarsbrook, C.G. Sweeney, T.J. Valentine, A.J. Whitehead, C.J. Wort, Diamond Relat. Mater., **3** (1994) 303-312.

[TAM89] A.C. Tam, '*Overview of photothermal spectroscopy' in Photothermal Investigations of Solids and Fluids'*, ed by J.A. Sell, Academic, Boston, (1989) 1-33

[TUR97] J. Turunen and W. Wyrowski, *Diffractive Optics for Industrial and Commercial Applications*, Akademie Verlag (1997) 361.

[VAN91] M. Vanecek, Holoubek, Shah, Appl. Phys. Lett. **59** (18) (1991).

[YAS82] Z.A. Yasa, W.B. Jackson, and N.M. Amer, Appl. Opt. **21**, (1982), 21.

[YIN96] Z. Yin, H.S. Tan, F.W. Smith, Diamond Relat. Mater. **5** (1996) 1490-1496.

[YIN97] Z. Yin, Z. Akkerman, B.X. Yang, F.W. Smith, Diamond Relat. Mater. **6** (1997) 153

5. PDS study of the optical absorption of undoped CVD diamond samples: results and discussion

5.1. Introduction

In this chapter, the optical absorption of undoped CVD diamond samples is investigated in the UV-VIS-NIR range as well as in the far infrared at 10.6 μm by means of PDS techniques. At the beginning of the diamond research at IMO, the main objective was to trace up the development of characteristic defects in CVD diamond upon changing the deposition conditions. Special interest was devoted to the investigation of diamond films, containing various amounts of sp^2-bonded carbon. The transverse PDS technique was used to study in detail the characteristic subgap continuum optical absorption in intentionally undoped CVD diamond films deposited under various conditions. The results will be discussed in terms of their variation with the deposition conditions resulting in the presence of different a-C concentrations (sp^2 bonded C) in CVD diamond films and thus diamond samples of different quality. Their absorption spectra were compared to known absorption spectra of natural diamond (type IIa) and HPHT synthetic (type Ib) diamond. A comparison with transmission data and with the results obtained from Raman measurements is included.

The characterisation of the optical absorption of the different CVD diamond films as a function of the deposition parameters allowed improving the quality of CVD diamonds. Nowadays, the state-of-the-art CVD diamonds almost reach the thermo-optical properties of the best natural type IIa diamonds [WIL98]. Moreover, thanks to a significant progress of the diamond synthesis methods, CVD diamond windows of 2 mm thick and several cm large (10 cm – 15 cm) can be produced. This development initiated the use of CVD diamond for high power laser applications. Diamond is highly attractive and is an excellent candidate to replace ZnSe as an output window material for CO_2 lasers. A breakthrough in laser performance could be realised, since the effect of thermal lensing is eliminated by the use of diamond [MUY99]. The collinear PDS technique is used for an accurate measurement of the optical absorption of freestanding CVD diamond windows at the CO_2 laser wavelength (10.6 μm). In the last section of this chapter, c-PDS scans showing the spatial dependence of the optical absorption coefficient for a set of CVD diamond windows are presented. The optical absorption coefficients of the diamond

windows, varying in optical quality, are determined by c-PDS and laser calorimetry.

5.2. Optical absorption in diamond: the sp^2 carbon model

We developed a theoretical model for the description of the defect induced optical absorption in CVD diamond. In the following sections it is shown that the optical absorption coefficient α can be fitted to the experimental data when considering optical transitions due to the presence of π-bonded carbon [NES96].

Various models of optical absorption, such as those based on theories of Tauc [TAU74], Abe and Toyoazawa [ABE81] and others were developed to describe the optical absorption in short range ordered σ-bonded materials such as amorphous silicon (a-Si) and amorphous hydrogenated silicon (a-Si:H). For amorphous carbon, the situation is more complex because of the mixed π - σ bonding environment. In the case of a-C and a-C:H the sp^3 sites form four σ bonds and the sp^2 sites form three σ bonds and one weaker π bond. The electronic structure of a-C and diamond-like carbon is reviewed by Robertson [ROB97]. The bonding and antibonding π states ly within the σ-σ^* gap and form a pseudogap. Theoretical considerations for possible optical transitions in a-C:H were discussed by Robertson [ROB92], based on Tauc's model of a virtual crystal. The virtual crystal is derived from the real crystal into which positional disorder is introduced. Tauc's model describes the optical transitions between two parabolic σ-bands (the valence and conduction band) in amorphous semiconductors and defines an optical Tauc gap E_g. The optical matrix element T_{ij} is assumed to be energy independent. If the localised wavefunctions can be constructed as linear combinations of the extended (Bloch) functions in the same band of the corresponding crystal then T_{ij} has the same (constant) value as in the crystal [TAU65]. If the initial and final wavefunctions are weakly localised we can consider transitions between wavefunctions which are not too much different from the Bloch functions, for which, however, the k-vector is not conserved. These transitions are indicated as non-direct transitions [SPI70], [TAU74].

In summary, in Tauc's model only the conservation of energy and no conservation of momentum is assumed. The momentum matrix elements T_{ij} are then replaced by their average value T_o [COD84]. Upon assuming the Velicky summation rule [COD84], the optical absorption coefficient α can be written as:

$$\alpha(E) = \frac{C}{E}\int g_i(\varepsilon) f(\varepsilon) g_f(\varepsilon + E)\left[1 - f(\varepsilon + E)\right] d\varepsilon , \qquad (5.1)$$

where g_i and g_f are the initial and final density of states respectively, f(E) and f(ε+E) the Fermi-Dirac occupation functions for the initial and final states and C a constant proportional to the square of the momentum matrix elements T_o^2. The assumed spectral independence of the matrix elements was experimentally confirmed for a-Si:H by Jackson et al. [JAC85]. By analogy, we used the same approximation for a-C defects in diamond and assumed constant matrix elements. We adopted the Tauc model of the virtual crystal to model the optical transitions in diamond.

5.3. Possible optical transitions in diamond

In this section, the most important optical transitions with the highest probability, occurring in diamond, are described and modelled. CVD diamond is a wide band gap semiconductor, which contains defect states in the gap. In the schematic model of the density of states in the gap, π and π* bands appear due to the presence of amorphous carbon (a-C) regions in CVD diamond. We explain now why those a-C regions are present in CVD diamond.

Specific for low-pressure CVD diamond is its synthesis in the pressure-temperature region, in which graphite is thermodynamically stable over diamond (see section 2.2). This fact may account for the differences observed between absorption spectra of CVD and natural or HPHT synthetic diamond [SPE94], [BI90]. One possibility to consider is the presence of π-bonded carbon. Thermodynamic growth models [DER77] [SPE94] [PIE92], based on the preferential etching of the non-diamond phase and/or diamond surface stabilisation by atomic hydrogen, always include a certain probability for the incorporation of sp^2 carbon in the diamond films. sp^2 sites play an essential role in hydrogenated amorphous carbon (a-C:H) or in higher ordered tetrahedrally bonded amorphous carbon (ta-C) films. It is widely accepted that in a-C:H π-bonded carbon atoms cause the formation of a π-π* pseudogap, emerging about midgap in between the σ-σ* bands and dominating the optical absorption [ROB87], [BRE85], [ROB92]. Similarly to a-C:H and ta-C, the D (disorder) and G (graphite) Raman scattering bands are present [SCH90], [KNI89] in lower-quality diamond films.

In-plane bonded six-membered hexagonal rings with 120° bonding angle between each C atom exist in pure graphite (sp^2 bonded carbon). Their incorporation into the diamond structure with 109.5° tetragonal bonded C leads to an enormous distortion. Much more probable is that amorphous carbon is located mainly in grain boundaries and at other

defects, such as cracks induced by stress in the material [PIC99]. It is interesting to note that already some time ago π-bonded carbon clusters were suggested as an explanation for the optical absorption induced by the radiation damage in IIa diamond [CLA56].

Based on the above presented arguments, it can be concluded that there is enough evidence to suggest that the main defect structure (dominating the defect-induced optical absorption in polycrystalline diamond films) is associated with π-bonded carbon. Our model of the subgap optical transitions is based on the currently accepted electronic picture of amorphous carbon [ROB92] and on recent molecular-dynamics simulations, showing the presence of π, π* states in the computed electronic density of states [MAR96], [STE94].

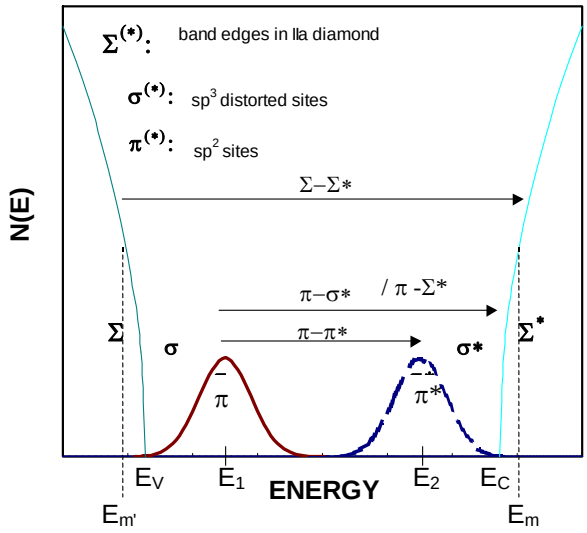

Fig. 5.1 Model of the density of states in the gap of CVD diamond. The π and π^* bands appear due to the presence of amorphous carbon regions. Shown are also two parabolic bands Σ, Σ^* for diamond and the exponentially broadened tails σ, σ^* (starting at energy E_m). Optical transitions are marked by arrows.

The proposed band structure model for CVD diamond is shown in Fig. 5.1. The conduction- and valence bands are modelled by two parabolic shape densities of states (DOS) with band edges E_C and E_V. In our model, both the valence and the conduction band edges are modified to include distorted sp^3 sites with differences in bond-angle,

bond-length, etc.. These modifications are implemented by introducing an exponential tail of localised σ-, σ*-states extending in the gap. The energies at which the parabolic bands transform into the localised exponential tails are noted by E_m and $E_{m'}$. Furthermore, a pseudogap is formed by the localised π- and π*- gaussian bands centred around E_1 and E_2.

From all the different possible optical transitions the one with the highest transition probabilities, indicated by arrows in Fig. 5.1, are considered:

1. π -π^* transitions in amorphous carbon regions,

2. π - σ^* and π - Σ^* transitions in amorphous carbon regions,

3. Σ - Σ^* indirect transitions between the valence and conduction bands of diamond.

5.3.1. π - π transitions*

The origin of the pseudogap in a-C and highly ordered materials, such as tetrahedrally bonded amorphous carbon (ta-C), is still subject of discussions [DRA94], [LEE94], [MAR96], [ROB95], [ROB97], [STE94], [VEE93], [WAN93]. The molecular dynamics study of Wang et al. [WAN93] suggests that graphitic clusters are arranged in planar sheets, containing mostly 6- but also some 5- or 7-membered rings. It has been proposed that in highly ordered structures the clustering of aromatic rings will not be energetically favourable. Stephan et al. [STE94] suggested that with increasing atomic density the number of fused rings decreases. For dense films, the existence either of single rings, pairs or single defects is favoured. This idea was supported by Drabold et al. [DRA94], who introduced the π-bonded defect pairs as the main defect. It was shown [ROB95] in the framework of the tight-binding Huckel Hamiltonian that a single, distorted aromatic ring, forming a boat or chair configuration and consequently causing the π-σ mixing, can produce states lying close to the midgap in ta-C.

In our model, the localised π-band is approximated by a gaussian distribution of the density of localised states, centred at E_i (i = 1, 2) and with a full width half maximum (FWHM) of 2w. Both π and π* bands are considered to be symmetrical around the midgap, as expected from recent molecular-dynamics simulations [MAR96]. The π (i =1) and π* (i =2) band density of states are:

$$g_{i(i=1,2)}(\varepsilon) = A'(2\pi w^2)^{-1/2} \exp\left[\frac{-(\varepsilon - E_i)^2}{2w^2}\right] \qquad (5.2)$$

The correlation integral Eq. (5.1) can then be solved analytically, leading to the following expression for the optical absorption coefficient $\alpha_{\pi\pi^*}$:

$$\alpha_{\pi\pi^*}(E) = A^2(2E\pi w^2)^{-1} \int \exp\left[\frac{-(\varepsilon - E_1)^2}{2w^2}\right] \exp\left[\frac{-(\varepsilon + E - E_2)^2}{2w^2}\right] d\varepsilon \qquad (5.3)$$

which, after the integration (A and B_1 are constants), becomes

$$\alpha_{\pi\pi^*}(E) = A^2(2Ew\sqrt{\pi})^{-1} \exp\left[\frac{-(E_{\pi\pi^*} - E)^2}{4w^2}\right]$$

$$\alpha_{\pi\pi^*}(E) = B_1 E^{-1} \exp\left[\frac{-(E_{\pi\pi^*} - E)^2}{4w^2}\right] \qquad (5.4)$$

with

$$B_1 = A^2(2w\sqrt{\pi})^{-1} \qquad (5.5)$$

The preintegration factor B_1 is proportional to the optical matrix elements and the concentration prefactors of the π and π^* distributions of states. Eq. (5.4) has a clear interpretation. The correlation integral reaches its maximum for a photon energy equal to the energy distance $E_{\pi\pi^*}$ between two symmetrical π-π^* DOS distributions. The final joint DOS is again a gaussian distribution but with a FWHM of 4w. In Fig. 5.2., the optical absorption coefficient, calculated according to Eq. (5.4) is plotted for various values of w and $E_{\pi\pi^*} = E_2 - E_1$. The similarity between specific curves in the spectra, and the experimental data, presented in Fig. 5.10 and the data measured by Bounough et al. [BOU93] and by Veerasamy et al. [VEE93] for a-C:H, suggests the validity of our model for π-π^* transitions.

It should be noted that the above approximation is different from the approach used frequently in the literature for a-C:H, where the Tauc plot, approximating the optical transitions between two parabolic bands in amorphous semiconductors, is used to fit the experimental data. Instead, in our model, two Gaussian bands forming a pseudogap are used.

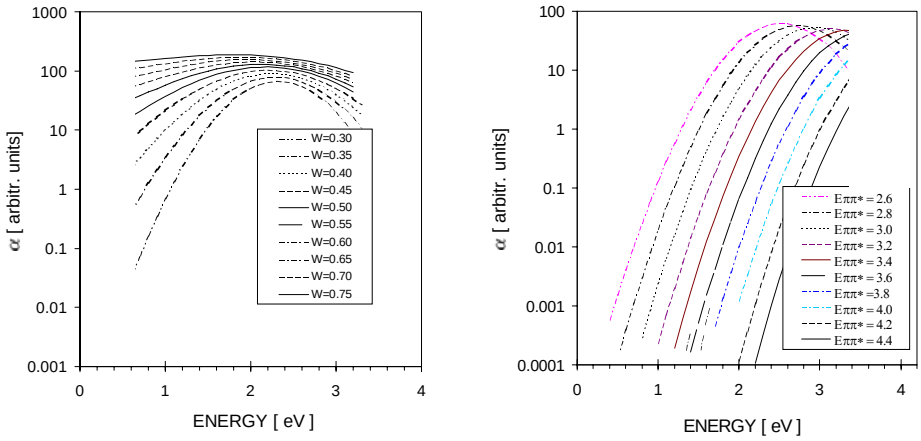

(a) (b)

Fig. 5.2 Numerical calculation of the optical absorption coefficient α according to Eq. (5.3) due to π-π transitions, described by the parameters w, $E_{\pi\pi^*}$, B_1. (a) Simulations are shown for different values (w); $E_{\pi\pi^*}$ is set to 2.4 eV in these calculations, and (b) simulations for various values of $E_{\pi\pi^*}$; w is set to 0.5 eV.*

5.3.2. π - σ and π - Σ* transitions*

It has been suggested that localised-localised state π - π* transitions are allowed, if they occur with the initial and final states localised on the same cluster [ROB92]. The π - σ* (and π - Σ*) transitions would be possible if π - σ bond mixing in amorphous carbon regions occurs. Bond-angle distortions due to immersing the sp^2 atoms in the sp^3 environment were suggested in recent molecular-dynamics work [MAR96], [STE94]. Because, the sp^2 sites are neighbouring the sp^3 sites, a sufficient bonding angle distortion could enhance the π - σ* optical transitions. This allows one to use the same approximation as in 5.3.1. for the calculation of the optical absorption coefficient α but with a different preintegration factor (B_2). This is in agreement with ref. [MAR96], where it has been suggested that the optical transitions in ta-C can be calculated by the convolution of the initial occupied and the final empty states.

Due to distorted bonds, potential fluctuations occur and because of that, the electron states become localised. The states within the band are only little displaced in energy and their wavefunctions remain approximately Bloch-like. To include this in our model, we

consider the σ* band density g_{σ^*} (the band tails) as an exponential, declining below the energy E = E_m from the parabolic g_{Σ^*}, which is expected for diamond as shown in Fig. 5.1. The π-band densities are taken as previously in Eq. (5.2).

So we have for (the conduction band edge) ε > E_m:

$$g_{\Sigma^*}(\varepsilon) = D(\varepsilon - E_{\Sigma^*})^{1/2} \qquad (5.6)$$

and for (the localised band tail) ε < E_m:

$$g_{\sigma^*}(\varepsilon) = \left\{ \frac{D(E_m - E_{\Sigma^*})^{1/2}}{\exp\left[\frac{E_m - E_{\Sigma^*}}{E_S}\right]} \right\} \exp\left[\frac{\varepsilon - E_{\Sigma^*}}{E_S}\right] \qquad (5.7)$$

where D is a constant, E_S is the slope of the exponential tail and E_{Σ^*} is the bottom of the Σ* diamond parabolic conduction band. The densities described by Eq. (5.6) and Eq. (5.7) are equal at E = E_m. This gives the pre-exponential factor in Eq. (5.7).

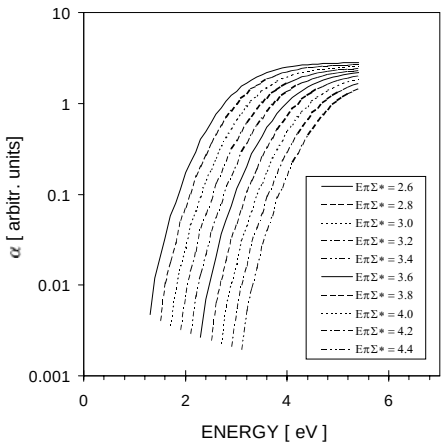

Fig. 5.3 Numerical calculation of the optical absorption coefficient α due to π-σ and π-Σ* transitions in amorphous carbon regions described by Eqs. (5.6) and (5.7). Simulations are shown for various energy distances of the π-Σ* density of states distributions, described by the parameter $E_{\pi\Sigma^*}$, the value for $E_{\pi\pi^*}$ is set to 3.2 eV and w is 0.55 eV in these calculations.*

In this case, the correlation integral Eq. (5.1) can only be solved numerically. The numerical solution of Eq. (5.1) for various values of $E_{\pi\Sigma^*}$, with $E_m = E_{\pi\Sigma^*} + 0.1$, $E_S = 0.1$, $E_{\pi\pi^*} = 3.2$ eV and w = 0.55 eV is shown in Fig. 5.3.

5.3.3. Σ - Σ^* indirect transitions in diamond

The indirect transitions in diamond are described by an $\alpha \sim (E - E_g \pm E_{ph})^2$ dependence [COD84], where E_{ph} is the phonon energy and E_g the width of the forbidden gap, assuming little change of the matrix elements around the band edges [JAC85]. Such transition corresponds to the fundamental absorption in type IIa diamond. As seen in Fig. 5.6 tailing of the optical absorption coefficient into the bandgap is present. Therefore it is expected that the optical absorption coefficient α is the sum of the indirect transitions between the valence and conduction parabolic bands and the transitions from the localised states in the broadened exponential tail to states above the band edges:

$$\alpha(E) = G(E - E_g \pm E_{ph})^2 + H\int g_\sigma(\varepsilon) g_{\Sigma^*}(\varepsilon + E)d\varepsilon \qquad (5.8)$$

where G and H are constants, E_g is the fundamental indirect gap, and g_σ is the initial density of states, which is approximated by Eq. (5.7)', assuming $E_{\Sigma\Sigma^*} = E_g$, and g_{Σ^*} is the density of final states above the band edge.

To test the validity of the above-described theoretical model for the optical absorption in CVD diamond, we have applied our model to the absorption spectra of undoped CVD diamond films obtained from t-PDS measurements. The presence of a-C in a series of polycrystalline undoped CVD diamond films with various contents of sp^2-bonded carbon is studied.

5.4. Optical characterisation of IMO undoped CVD diamond films

5.4.1. Introduction

The main defect structure in undoped CVD diamond films dominating the defect-induced optical absorption, is π-bonded carbon. The major experimental interest of this study was to find out how π-bonded carbon can be incorporated in CVD diamond films. There was particular interest in investigating films containing various amounts of sp^2 carbon. We

attempted to compare the optical absorption of the deposited films (see Appendix A.1, Table A.1) with our best film (D11), prepared at the optimised conditions.

5.4.2. Preparation and characterisation of the samples

The polycrystalline CVD diamond samples, studied and discussed in this section, have been grown in an ASTeX PDS17 MW PE deposition system at IMO (see section 2.3-2.5). The diamond films were deposited on (rectangular) mirror polished undoped Si substrates. After the Si substrates were etched away (see section 2.5), the self-supporting CVD diamond films of dimensions typically 2.5 x 5 mm^2 were used for the optical absorption measurements by means of t-PDS. Bulk type IIa (natural) and Ib (HPHT) De Beers monocrystalline diamond plates (250 μm thick) and also a {100}-oriented homoepitaxial diamond (sample D17) deposited on a IIa De Beers plate were used for comparison.

In the description below, the CVD diamond samples are subdivided into two categories based on their growth rate conditions.

Set I

The polycrystalline diamond films grown under *high-growth rate conditions,* which will be referred to as Set I, differ in quality concerning the concentration of non-diamond carbon. The characteristics of the deposited undoped films are summarised in Table A.1 (see Appendix 1.1). The highest purity films (e.g. D11) are white and optically translucent because of elastic light scattering at grain boundaries. Films containing non-diamond carbon, such as D12 and D13, are brownish and black respectively. Film D11 is randomly oriented, whilst the films D12 and D13 exhibit {111} and {100} morphology respectively (see Fig. 5.4). All films of set I were prepared under the following typical deposition conditions: pressure 10^4 Pa, MW power 5000 W, gas composition: 1-10 vol% CH_4 and 0.3 vol% O_2 in H_2 feed gas, and substrate temperature in the range 800-900 °C. Typical growth rates at these conditions are about 5 μm/hour. So, 100 μm thick samples can be prepared by deposition during 20 hours.

Set II

Polycrystalline samples grown at *low-growth rate conditions* (Set II) were prepared at lower pressures (typically 6 x 10^3 Pa) and at lower microwave power (typically 1000 W). For the films of Set II, the deposition process consisted of two consecutive steps: i) the

bias-enhanced nucleation step for creating a sufficiently high diamond nucleation density (10^{10} cm^{-2}) on a mirror polished Si substrate and ii) the diamond growth step (see section 2.4).

The deposition parameters of set **II.1** [samples d2.1, d2.2, d2.3, d2.4 and d2.6] (constant temperature) and set **II.2** [samples d2.7, d2.8 and d2.9] (constant methane concentration) are summarised in Table A.1. The substrate temperature and CH_4/H_2 ratio were varied in the range 700 – 900 °C and 0.65 - 3 % respectively. The deposition rate was about 1 - 1.5 µm/hour and films with thickness between 15 and 20 µm were deposited.

The Raman analysis of the best films, sample D11 and sample d2.1 revealed only the 1332cm^{-1} diamond peak and no characteristic broad feature (G peak) [SCH90], [KNI89], [BOU93] which occurs at about 1550 cm^{-1}. All other films of set I and II, deposited at different conditions exhibited a G component, suggesting the presence of sp^2 carbon in the film (see Table A.1). The G component of the spectra increased with deposition temperature.

As already mentioned, our main experimental interest was to trace the development of characteristic defects in CVD diamond while changing the deposition conditions. Because one possible site for a-C are grain boundaries [SCH90], [BUC89], [BER93], [BER94] and [FAL93], we attempted to change their area by changing the film morphology of the films of set II. By keeping the nucleation step constant and changing the growth-step deposition conditions various film morphologies were prepared, ranging from those showing well-defined crystals to those showing a finely grained morphology. The surface morphology of the investigated films of set I and set II (shown in Fig. 5.5) was strongly dependent on the deposition conditions (e.g. the relative ratio of the CH_4 to the H_2 concentration and the substrate temperature).

The films of set II, synthesised at low methane concentrations (samples d2.1, d2.2, d2.3), were white and/or translucent (light scattering) and non-textured. As the methane concentration increased, the films became very finely grained and they showed a brown to dark brown colour and were optically smooth. For the highest CH_4 concentrations, the films had a nanocrystalline-amorphous approaching character, with grain sizes below 0.1 µm. Surprisingly, reduction of the substrate temperature led again to the deposition of films with defined grain sizes, the films showed again diamond facets and at very sharp conditions a {100} textured film could be prepared. The development of the texture is summarised in Fig. 5.5.

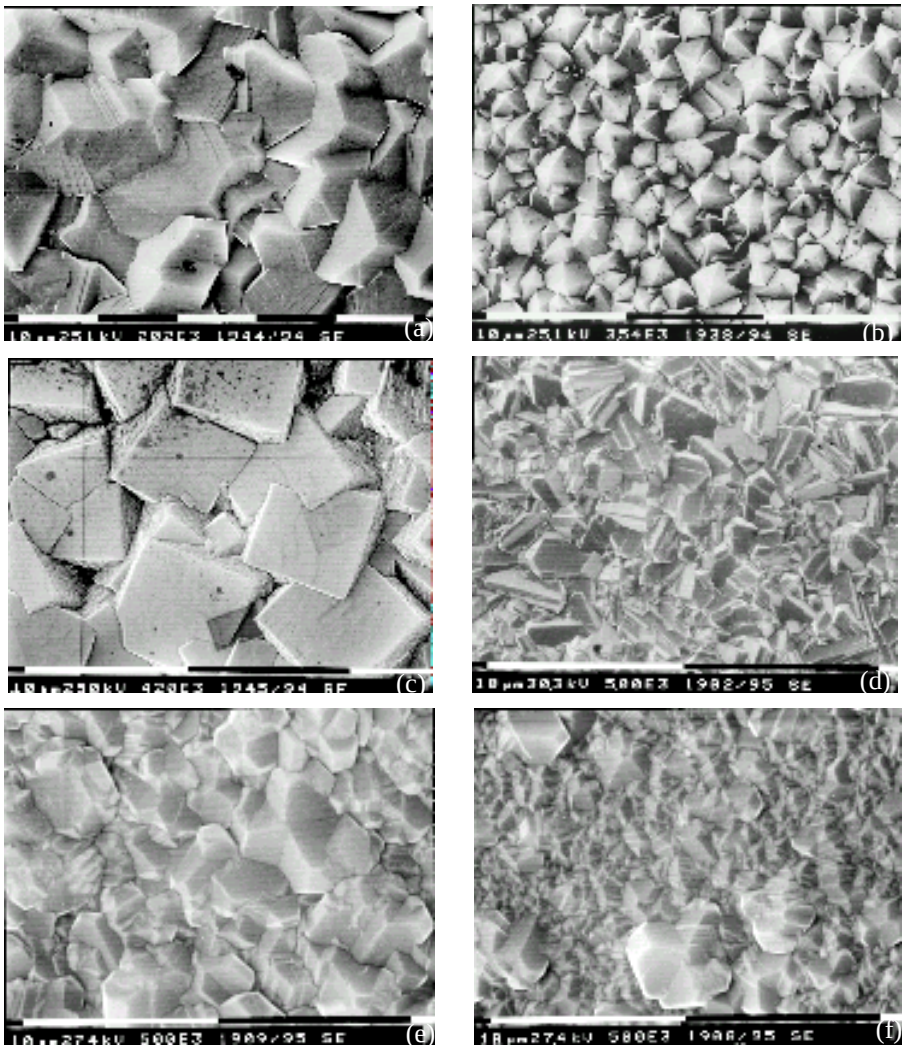

Fig. 5.4 Scanning electron micrographs of the surface morphology of the deposited films of set I and II, upon changing the CH_4/H_2 ratio.
Samples from set I: D11 (3% CH_4, 0.3% O_2) (a), D12 (6% CH_4, 0.3% O_2) (b), D13 (7% CH_4, 0.3% O_2) (c), Samples from set II d2.1 (0.6% CH_4, T_s 900 °C) (d), d2.3 (1% CH_4, T_s 900 °C) (e), d2.4 (2% CH_4, T_s 900 °C) (f).

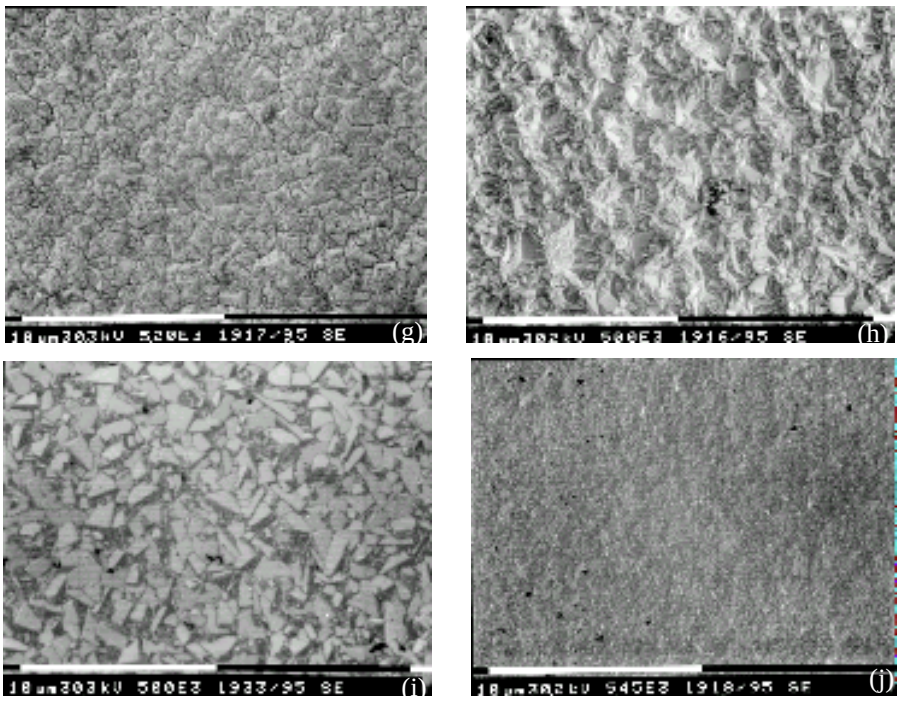

Fig. 5.5 Scanning electron micrographs of the surface morphology of the deposited films of set II, upon changing the CH_4/H_2 ratio or the surface temperature . Samples from set II, d2.6 (2.5 %CH_4, T_s 900 °C) (g), d2.7 (3% CH_4, T_s 820 °C)(h), d2.8 (3% CH_4, T_s 760 °C)(i) and d2.9 (3% CH_4, T_s 900 °C)(j).

Twinning [AGN92] must be at least partially responsible for the development of the observed finely grained film morphology (samples d2.4, d2.6, d2.7, d2.9). If only a drift from the diamond deposition domain (see Chapter 2, Fig. 2.2) [BAC91] causes the development of the finely grained morphology, a reduction of the deposition temperature would not restore regular crystal shapes (sample d2.8). Similar conclusions about the influence of the twinning on successively smaller areas were drawn by Tamor and Everson [TAM94].

Stacking or multiple stacking faults are very often found in diamond films [AGN92], [TAM94]. This is not surprising because the energy difference between the correct diamond and incorrect hexagonal ring stacking (staggered to eclipsed) is very small. On atomic scale, twinning means in-plane incorporation of boat type six-membered rings instead of an incorporation of the correct chair ring type. When the films grow, these two

cases differ only in the next-nearest neighbour environment [AGN92]. In case of a very small misorientation between crystallites, a bond-angle disorder will be induced to bond adjacent crystals. It appears likely that for crystallites with higher misorientations, amorphous carbon regions on grain boundaries can be produced to reduce the total energy of the system. The amorphous carbon on grain boundaries was experimentally confirmed by various techniques such as Raman spectroscopy, electron-energy-loss spectroscopy (EELS) and transmission electron microscopy (TEM) [BER93], [BER94], [STE99].

5.4.3. Transmission measurements

The results of the optical transmission measurements performed on the freestanding samples of set I and set II, the polycrystalline film D11, the homoepitaxially grown diamond D17 and the IIa and Ib diamond plates are summarised in Fig. 5.6 and Fig. 5.7.

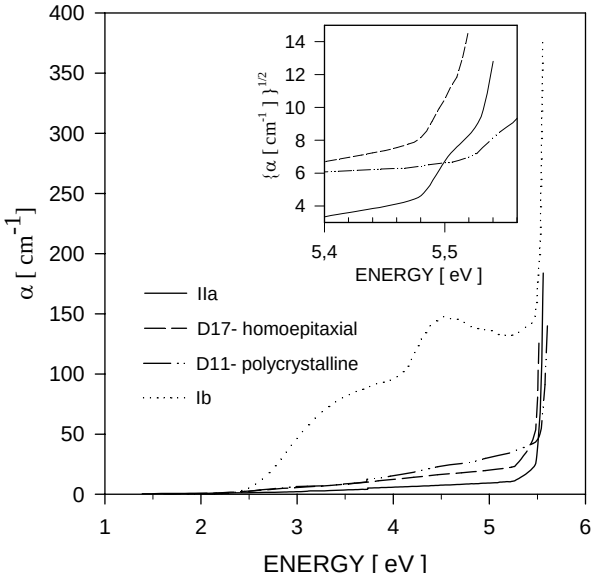

Fig. 5.6 The optical absorption coefficient α for a 100 µm thick high quality polycrystalline sample D11, for a 373 µm thick {100} oriented sample D17 and for type IIa (natural) diamond and type Ib HPHT diamond plates, calculated from optical transmission measurements. The inset shows the indirect optical transition at the fundamental absorption edge of diamond.

As mentioned in section 5.3.3. this absorption can be described by the $\alpha \sim (E - E_g \pm E_{ph})^2$ dependence for parabolic bands [COD84] (see the inset of Fig. 5.6). The homoepitaxially grown diamond (D17) and our best polycrystalline material (high-quality CVD diamond film D11) attain the character of the fundamental absorption edge. This is not the case for all CVD films. A broadening, especially for the polycrystalline material, can be clearly observed in Fig. 5.6.

In the high quality diamond sample D11, the optical transmission and reflection were measured using a Perkin-Elmer Spectrophotometer equipped with a light-integration sphere. The spectral dependence of the optical absorption coefficient α was calculated from Eq. (3.28). In Fig. 5.6 the spectral dependence of the optical absorption, obtained from transmission measurements, is shown for samples D11, D17, type IIa and Ib diamond. IIa natural diamond shows a typical indirect absorption edge at 5.45 eV.

Fig. 5.7 shows the optical transmission data for set II between two limiting cases: first (samples d2.1, d2.2), following the optical transmission of IIa diamond (measured without the integration sphere), but with much lower detected transmission because of the scattering losses and, secondly, a slowly decaying transmission from the energy corresponding to the expected band edge for diamond. Similar tailing of the optical absorption coefficient into the bandgap was also observed for a-C films [SAV85], [BOU93], [VEE93].

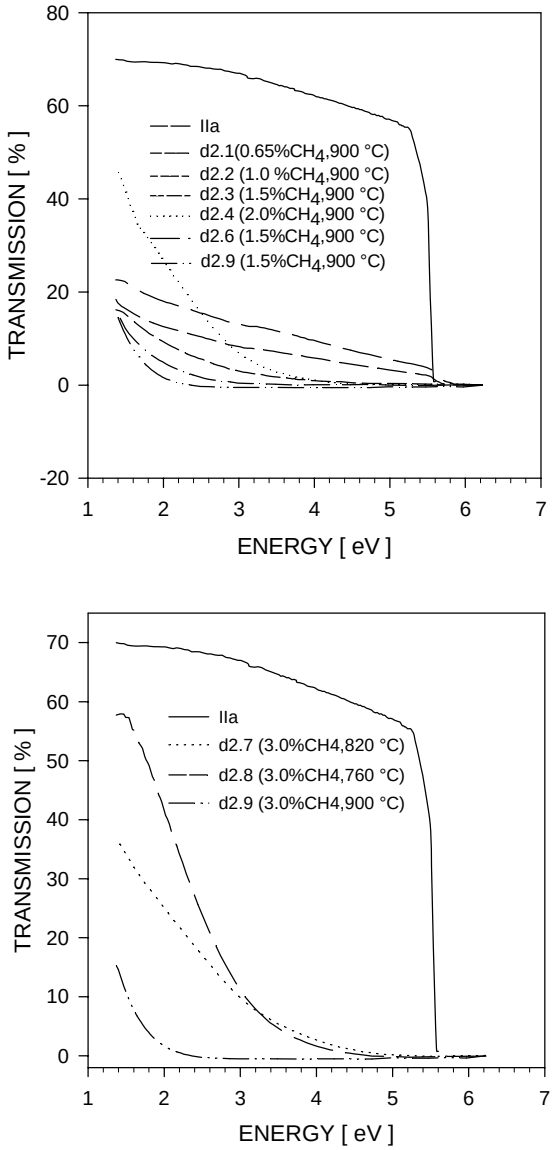

Fig. 5.7 The optical transmission spectra (without correction for the elastic light scattering) of (a) the samples prepared under various methane concentrations and at a substrate temperature of 900 °C (set II.1), (b) the samples prepared under a methane concentration of 3 % at various substrate temperatures (set II.2). Transmission of a IIa diamond plate is shown for comparison.

5.4.4. PDS measurements

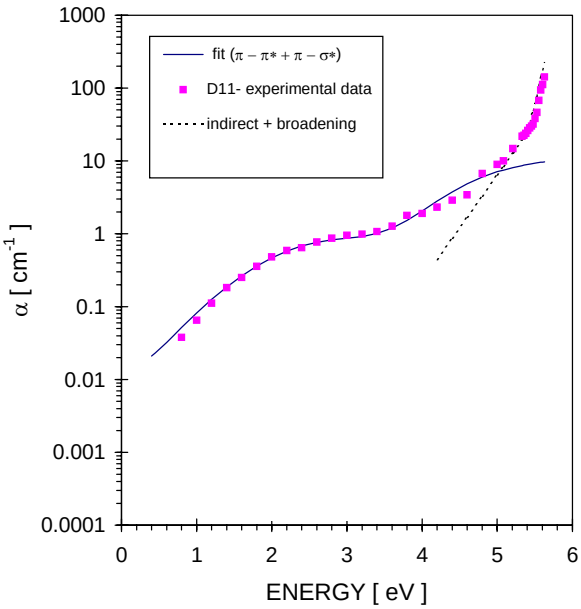

Fig. 5.8 The spectral dependence of the optical absorption coefficient α obtained from t-PDS measurements for the low defect density film D11. Plotted are also numerical fits to Eq. (5.4), Eq.(5.6) (π-π and π-σ*/π-Σ* transitions) and to Eq. (5.7) (indirect transitions and exponential broadening).*

As already mentioned, transmission measurements are strongly influenced by light scattering. To study the weak subgap absorption, t-PDS measurements, which are much less sensitive to light scattering, were performed. The t-PDS spectra were recorded at room temperature. The results of these t-PDS measurements on the unpolished freestanding IMO CVD diamond samples are shown in Fig. 5.8, Fig. 5.9 and Fig. 5.10.

In Fig. 5.8 the optical absorption coefficient α of our best polycrystalline material (D11) is plotted. For an absolute scaling of the absorption of sample D11, the t-PDS data are fitted to the UV-transmission data (corrected for the elastic light scattering). The polycrystalline diamond D11 shows a distinct optical absorption in the subgap region, which we call characteristic continuum subgap absorption.

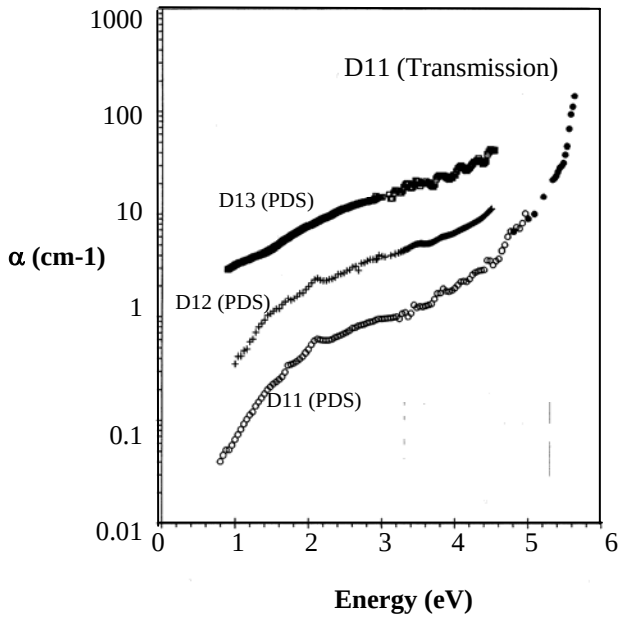

Fig. 5.9 The spectral dependence of the optical absorption coefficient α obtained from t-PDS measurements using Eq. (3.24) for samples D11, D12 and D13. The film D11 is fitted to transmission measurement (full symbols).

As already seen in the transmission measurements, D11 exhibits a fundamental absorption edge similar to natural IIa diamond. Similarly, it was found by Sussman et al. [SUS94] that the UV absorption spectra for polished high-quality CVD films approach those for IIa diamond.

In Fig. 5.10 the optical absorption coefficient α for samples of set II is plotted. These films are deposited at different CH_4 concentrations (d2.1, d2.3, d2.4, d2.6, d2.9) (Fig. 5.10 (a)) and at different substrate temperatures (d2.7, d2.8, d2.9) (Fig. 5.10 (b)). The worse quality films showed some saturated PDS-signal S_{sat} and the optical absorption coefficient α could be calculated in absolute units via Eq. (3.24) $\alpha = -1/d \ln(1-S/S_{sat})$ (see section 3.5). The absolute value of the optical absorption coefficient α(E) increases with the non-diamond carbon content (the closer to nanocrystalline films, see also Fig. 5.5, the higher the absorption) and the saturation of the PDS signal S occurs at lower photon energy, for the same sample thickness.

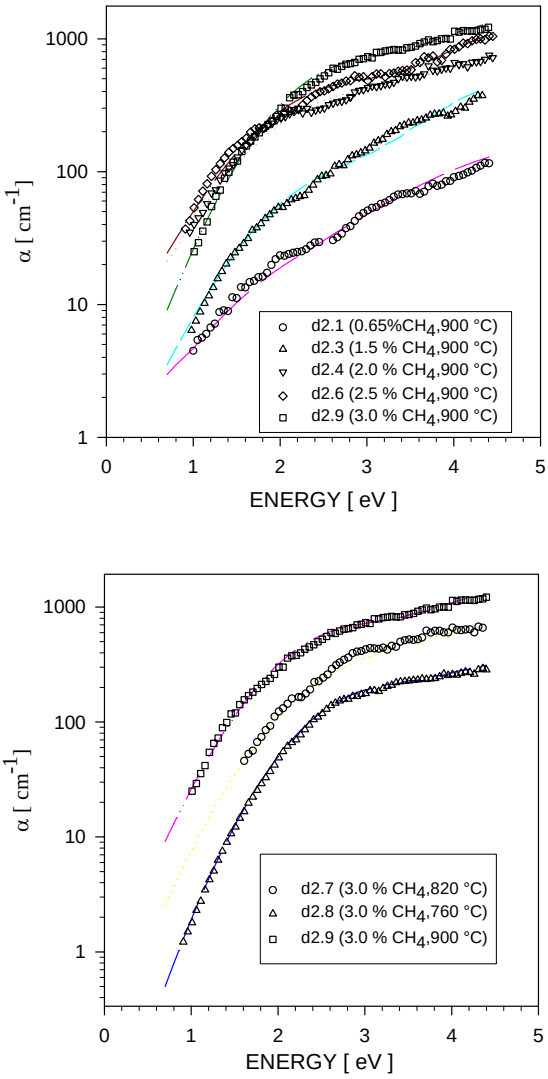

Fig. 5.10 The spectral dependence of the absorption coefficient α obtained from t-PDS measurement for films of set II (samples differ in CH_4 concentration in the H_2 gas during the deposition) and for films of set II (samples deposited at different substrate temperatures). Plotted are also numerical fits to Eq. (5.4).

For set II.2 (the concentration series), the quality of the films decreased with increasing methane concentration. For set II.1 (the temperature series), the quality of the films decreased and consequently the absorption values increased with increasing temperature

in contradiction with the results of Zammit et al. [ZAM98]. They observed a decrease of graphitic carbon content in the diamond films when the substrate temperature increased. The optical absorption of nanocrystalline films resembles that of a-C films [ROB92], [SAV85]. For the better quality samples (d2.1, d2.2, d2.3) with the regular crystal morphologies the subgap absorption is reduced. For sample d2.1 (and D11) the optical absorption coefficient continues to rise and at about 5.5 eV it shows the fundamental absorption edge of diamond.

From a comparison of the absorption spectra of the set I and set II samples, it can be seen that all the investigated samples show a very similar characteristic spectral dependence of the optical absorption coefficient α in the IR region, starting at an onset of about 0.9 eV [NES96]. This weak subgap absorption is also measured by means of t-PDS by Gheeraert et al. [GHE95]. The absorption spectra of the best quality CVD diamond films show some broad absorption bands superimposed on the continuum subgap absorption. For example, the absorption band at 2.1-2.3 eV could be due to N-defects present in low concentrations in nominally undoped CVD diamond films (see Chapter 6). A clear identification is not possible because the π-π^* transitions dominate the spectra and mask completely (for the low quality films) or partially (for the high quality films) other defects in the diamond films. Moreover, our low resolution room temperature measurements do not yield more information. It would be interesting to extend our PDS study to low temperatures. Up till now, this was impossible because of experimental constraints, such as precisely focussing the probe HeNe laser parallel with the sample mounted inside a cryostat, the use of liquid nitrogen as deflecting medium, etc. Nevertheless, the fine structure in the PDS spectra deserves some further examination. Photocurrent measurements performed on polycrystalline CVD diamond films [OKU92] showed a similar type of behaviour as the optical absorption measurements, presented above. It has been suggested that the optical transitions involved are due to the presence of an electronic level of 1 eV distance from the valence band edge. We too considered this as an explanation first [NES95], but we will show further in this section that this typical behaviour can be explained in terms of the π-π^* band type transitions as suggested for amorphous carbon [ROB87], [ROB92].

The typical characteristic subgap absorption in our films cannot be attributed to light scattering or the presence of N type defects, as will be explained below. On the other hand this absorption shows very similar spectral dependence in the IR region as the optical absorption coefficient for a-C:H films.

According to the development of the absorption spectra when continuously changing the deposition conditions (and correspondingly developing the finely grained morphology) and according to a close similarity of the measured absorption spectra with the absorption spectrum of a-C films [ROB87], [SUS94], [SAV85], we propose that the π - π^* band-type transitions are responsible for the observed absorption spectra. The model of π - π^* pseudogap was originally developed by Robertson et al. and Bredas et al. [ROB87] [BRE85] for amorphous carbon. Recently, photoluminescence studies in polycrystalline CVD diamond accompanied with micro-Raman measurements clearly attributed the observed broadband luminescence, centred about 2 eV, and the development of the G-Raman peak to amorphous carbon in grain boundaries [CRE93], [BER93], [BER94].

During diamond deposition, the presence of ultra low N concentrations (and other extrinsic impurities) in the deposition chamber and the incorporation in the deposited films is inevitable. Nevertheless, the typical optical absorption in our films cannot be due to nitrogen. Secondary-ion-mass spectroscopy (SIMS) analysis shows typically 30 ppm N, 500 ppm H and 100 ppm O in all measured films. The subgap absorption for dark brown films d2.9 and our best transparent film D11 varies at 2eV over 3 orders of magnitude. So it is difficult to explain the observed spectra by impurity absorption. Furthermore, we also investigated N-related absorption (see Chapter 6) [NES95], [MEY96]. A typical absorption spectrum related to N in substitutional position was found in N-doped films, similarly as in spectra of Ib diamond shown in Fig. 5.6. The investigated intentionally undoped films show a clearly different spectral dependence of the optical absorption coefficient α as compared to Ib diamond.

Hence, we can conclude that there is enough experimental evidence that the principal defect structure, seen in the optical absorption spectra of our polycrystalline CVD diamond films, is associated with amorphous (π-bonded) carbon, located mainly at the grain boundaries.

5.4.5. Deconvolution of experimental data.

A least squares fitting procedure was used to fit Eq. (5.1) to the experimental optical absorption spectra, as obtained from the t-PDS measurements. We took both π - π^* and π -σ^*/ π -Σ^* transitions into account resulting in a theoretical absorption coefficient of the form $\alpha = \alpha_{\pi\pi^*} + \alpha_{\pi\Sigma^*}$, whereby $\alpha_{\pi\pi^*} \equiv \alpha_{\pi\pi^*}$ (B_1, $E_{\pi\pi^*}$, w) and $\alpha_{\pi\Sigma^*} \equiv \alpha_{\pi\Sigma^*}$ (B_2, $E_{\pi\Sigma^*}$, w, E_m, E_S). with fit parameters: the preintegration factors B_1 and B_2, the energy distance $E_{\pi\pi^*}$ between the two maxima of the π and π^* state distributions and their FWHM of 2w, the energy distribution $E_{\pi\Sigma^*}$ between the maximum of the π state distribution and the bottom edge of the Σ^* band and the slope E_S of the exponential broadening of the parabolic band Σ, starting at the energy E_m. The preintegration factor B_2 is proportional to the optical matrix elements and the concentration prefactors of the π and σ^*/Σ^* distributions of states. The calculated optical absorption coefficient (line) is plotted together with the experimental data (symbols) in Fig. 5.8 and Fig. 5.10. The fit of the experimental subgap absorption spectra using the model based on Eq. (5.4) (π -π^* transitions) and Eqs. (5.6) and (5.7) (π -σ^*/ π -Σ^* transitions) yields a very good agreement for all films, ranging from nanocrystalline to well-faceted diamond films. It is interesting to note that the calculated absorption spectrum according to Eqs. (5.6) and (5.7) (π -σ^*/ π -Σ^* transitions) for film D11 (see Fig. 5.8) resembles the UV-continuum absorption, present in IIa diamond [CLA79].

The parameters of the fit are summarised in Table 5.1. The characteristic subgap absorption is dominated by the π - π^* transitions while the π - σ^*/π - Σ^* transitions play a minor role. Zammit et al. [ZAM98] applied our model to fit the absorption spectra on thin CVD diamond films measured by t-PDS. He obtained good fitting results with only taking into account the π - π^* transitions.

Table 5.1 Parameters of the least squares fitting procedure to Eq. (5.1) obtained by a numerical deconvolution of the experimental data (taking into account π - π^* and π -σ^*/ π -Σ^* transitions).

samples	W [eV]	$E_{\pi\text{-}\pi^*}$	$E_{\pi\text{-}\Sigma^*}$	E_m	B_1	B_2	E_S
D11	0.55	3.40	4.45	4.55	2	1.6	0.10
d2.1	0.65	3.50	3.89	4.00	95	0.8	0.10
d2.3	0.54	3.07	3.80	3.89	301	0.8	0.10
d2.4	0.57	3.06	3.70	3.80	1017	0.3	0.10
d2.6	0.54	3.00	3.80	3.88	1270	0.4	0.15
d2.7	0.52	3.08	3.70	3.78	1038	0.4	0.10
d2.8	0.47	3.24	3.80	3.89	444	0.2	0.11
d2.9	0.50	2.90	3.62	3.63	1440	0.2	0.20

The main difference between the fitting parameters is the value of constant B_1 in Eq. (5.4), which is proportional to the product of the optical matrix elements and the concentration prefactor of the π and π^* distributions of states (see Eq. (5.1) and Eq. (5.4)). Further, the fit yields typically 3.5 eV for the energy distance $E_{\pi\pi^*}$ between the two maxima of the π - π^* distributions for the investigated CVD diamond films of high quality (D11, d2.1). The molecular-dynamics simulations suggested a value between 4 eV and 5 eV for $E_{\pi\pi^*}$ in tetrahedrally bonded amorphous carbon [MAR96].

According to these results, by increasing the film quality, the absolute number of π - π^* transitions is decreasing (e.g. lower defect induced optical absorption) and the distance between the gaussian distributions (pseudogap) is widening. This is in agreement with the data obtained for a-C:H films [ROB97].

In Fig. 5.11, the relation between the numerically (least-square fitting procedure) obtained value (Eq.(5.4)) for the preintegration factor B_1 and the measured value of the optical absorption coefficient α at 3.5 eV is plotted. It can be seen that the $\alpha(B_1)$ dependence has a linear character as expected from Eq. (5.4) and this supports our model.

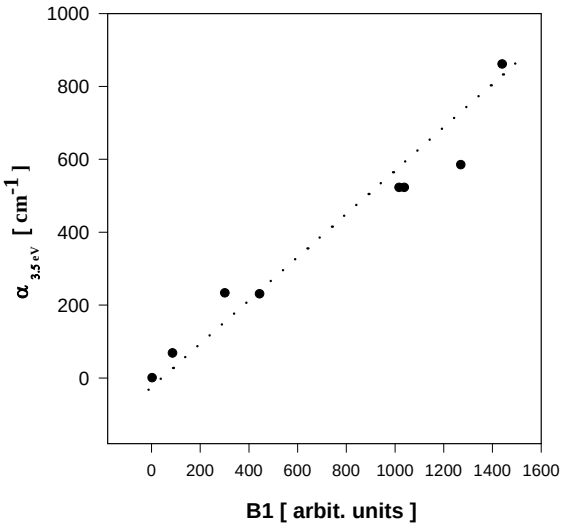

Fig. 5.11 The plot of the value of the experimentally measured optical absorption coefficient α at 3.5 eV as a function of the corresponding preintegration factor B_1 from Eq. (5.4), obtained by the numerical fitting procedure, for films from Fig. 5.8 and Fig. 5.10.

To summarise, the theoretical model describes the character of the characteristic continuum subgap optical absorption in CVD diamond films. The least square fitting is in very good agreement with experimental data of the optical absorption spectra for all investigated samples, starting from nanocrystalline films to high quality CVD diamond. Nevertheless, although our model has recently been used by other research groups [ZAM98] and [NEB99] to explain the subgap absorption, the origin of this continuum absorption has not yet been satisfactorily explained in literature. It has been suggested that it is connected with the presence of amorphous carbon clusters [CLA56], [ROB97].

5.5. Comparison of PDS absorption spectra with Raman spectra

Raman scattering has been widely used as a standard for the characterisation of CVD diamond quality in terms of detection of sp^3- and sp^2-bonded carbon [BAC92], [HUO91]. It allows the characterisation of the physical structure and the phase purity of the diamond films, i.e. crystalline or amorphous. Many studies have related Raman spectra to the deposition conditions and film morphology [KNI89], crystalline orientation

[STU93] and stress [VAN91]. On the other hand, as has been shown in the previous section, optical absorption spectroscopy is very powerful in detecting non-diamond carbon impurities, even at ppm level. In this section, the aim was to examine whether the features in Raman spectra were related to the sub gap absorption detected by t-PDS. Raman scattering was used to characterise the Raman quality (sp^2/sp^3 components) of the CVD diamond films, which were also studied by t-PDS (see section 3.6) to investigate the optical absorption of the samples. The PDS and Raman spectra obtained on identical samples were compared.

5.5.1. Sample description

A set of three freestanding diamond films (set III) was composed from the samples described in section 5.4.2. in such a way that the samples investigated differ widely in quality from the point of view of the content of sp^2 and sp^3 bonded carbon. Set III consist of the samples d2.1, d2.9 and K34.

Further, a set of three diamond films (set IV) was fabricated at ASTeX (Boston-USA). The samples were synthesised in a methane-hydrogen-oxygen mixture in an ASTeX AX6500 microwave plasma reactor and the sample deposition characteristics are given in Appendix A.1, Table A.3. This set of samples is of better quality than set III, as will be seen further. After the deposition, the silicon substrate was etched away. The sample 4i is 10 times thicker than the other ones.

5.5.2. Raman spectroscopy: experimental set-up

Room temperature Raman spectra, were measured in backscattering geometry. The exciting beam (the 514.5 nm line of an Ar^+ laser) was focused into a spot of about 30 µm. To avoid unwanted heating of the sample (checked by measuring Stokes/anti-Stokes ratio), the incident power density was kept below 5 kW/cm^2. The scattered light was analysed by a PC-controlled double spot spectrometer (SPEX-14018) followed by a standard photon-counting detection. The spectral resolution was better than 2 cm^{-1}.

When evaluating Raman spectra one has to keep in mind that sp^2 bonded carbon (graphite) has a much higher Raman scattering cross section than sp^3 bonded carbon (diamond). This ratio is depending on the excitation laser source wavelength and varies from 50 – 233 [SAI96].

5.5.3. Raman quality factor

A useful quantity for the film quality assessment (introduced as a Raman quality factor in [MOR95] and as a figure of merit in [SAI96] respectively) is the ratio of the integrated intensity of the sharp diamond peak (I_D), causing absorption at 1332 cm^{-1}, to that of the integrated intensity of both the non-diamond bands (I_N) and the diamond line [VOR97]:

$$\beta = (I_D)/ (I_D+I_N). \qquad (5.\ 9)$$

Taking into account that $I_{D(N)} \sim \sigma_{D(N)}.\phi_{D(N)}$, σ being the Raman scattering cross section and ϕ the volume fraction ($\phi_N + \phi_D = 1$) of the respective components, one can use β to determine the volume fraction (concentration) of the non-diamond component [MOR95]:

$$\phi_N = (1 - \beta)/(1+ K\beta), \qquad (5.\ 10)$$

where $K = [(\sigma_N/\sigma_D) – 1]$. The knowledge of σ_N/σ_D is crucial for such determination. The Raman cross-sections of diamond and non-diamond carbon are different indeed. It is well known that $(\sigma_N/\sigma_D) \sim 50$ for highly oriented pyrolytic graphite and diamond single crystals [ANA70], [WAD81]. However, neither the diamond nor the non-diamond component of diamond films may be regarded as single crystalline. Schröder et al. [SCH90] pointed out that in diamond films, the Raman signal sp^2-bonded components should ~ 100 times prevail that from diamond regions. On the other hand, Sails et al. [SAI96] found that the Raman cross section of amorphous carbon (a-C) is 233 times that of diamond when the Raman spectra are recorded with an Ar^+ 514.5nm laser line. The spectra obtained from laser Raman spectroscopy are very sensitive to the wavelength of the excitation source [WAG91]. The relative sensitivity to the G-band (graphite) and D-band (polycrystalline disordered graphite) increases with increasing wavelength [LEE98].

5.5.4. Raman measurements

Typical Raman spectra for the three samples of different quality (set III) are shown in Fig. 5.12. Each sample was measured several times on different locations. The sharp diamond peak at 1332 cm^{-1} becomes more clearly visible when going from sample d2.9 to K34. A standard fitting procedure was applied to analyse the spectra: luminescence background was fitted and subtracted. The diamond peak was fitted with a mixed Laurentzian – Gaussian lineshape whereas for the other features pure Gaussians (typical for amorphous materials) or Laurentzians (typical for crystalline materials) were used. All parameters, the width and the intensity of the peaks, were allowed to vary during the

fit.

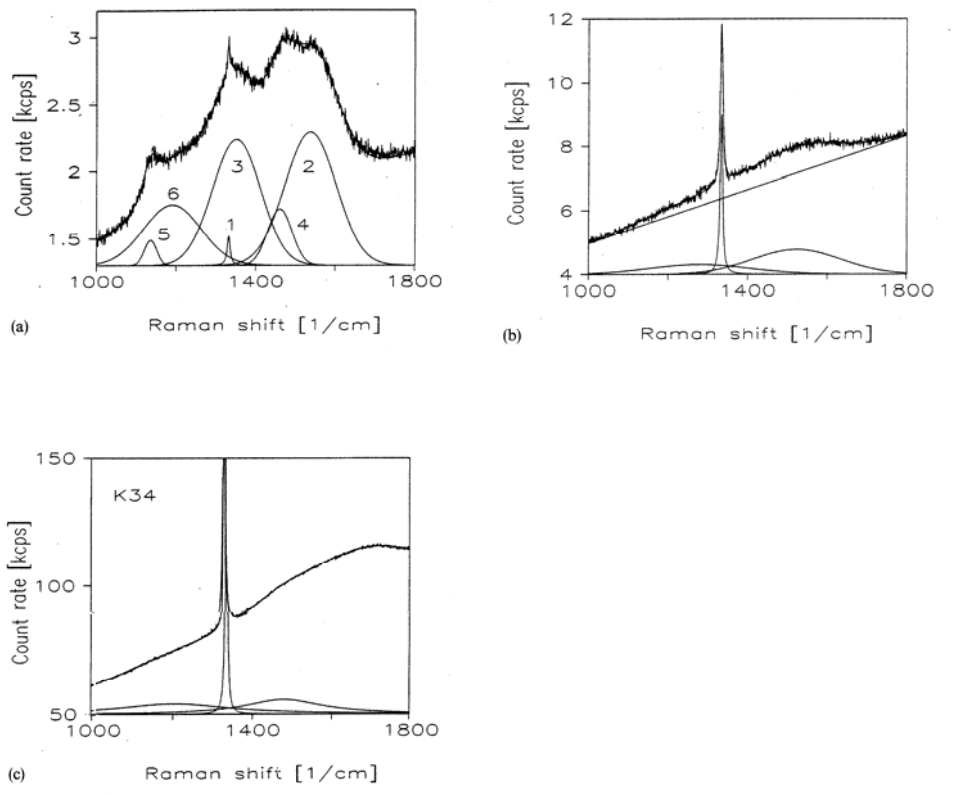

Fig. 5.12 Measured Raman spectra and their components determined by fit: (a) sample d2.9 (β = 0.007); (b) sample d2.1 (β = 0.164); (c) sample K34 (β = 0.332). Except for (b), the background lines (linear in most cases) are not shown.

The results of such decomposition are shown in the figures. Along with the sharp diamond peak (1), there are broad bands (2,3) characteristic for a-C and disordered graphite (1540 and 1350 cm^{-1}), diamond precursor band (4) (1460 cm^{-1}) and a band (5) related to nano- or microcrystalline diamond (1140 cm^{-1}) in the spectrum of sample d2.9 [KNI89], [YAR88], [BAC92], [HUO93], [MAR94] and [TAM94]. In addition, there is also a broad band (6) at about 1180 cm^{-1} in this sample. Its origin is not clear at present [MAR94], [BAC94]. As the quality of the sample improves, the number of (non-diamond) bands in the spectrum reduces: only the a-C bands (with the possible

unresolved precursor band) are seen in sample d2.1, the precursor and a broad low-frequency band are observed in the spectrum of K34. The broad maximum at 1700 cm^{-1} (in the spectrum of sample K34), well above all the one-phonon frequencies of diamond, graphite and a-C, belongs to the photoluminescence background which overlaps with the Raman spectrum. This background was substracted before fitting the Raman spectrum.

The frequencies quoted (for the diamond peak, D-band, G-band, etc.) for the different samples and for different locations on them varied within the limits consistent with other reports [BAC92],[TAM94].

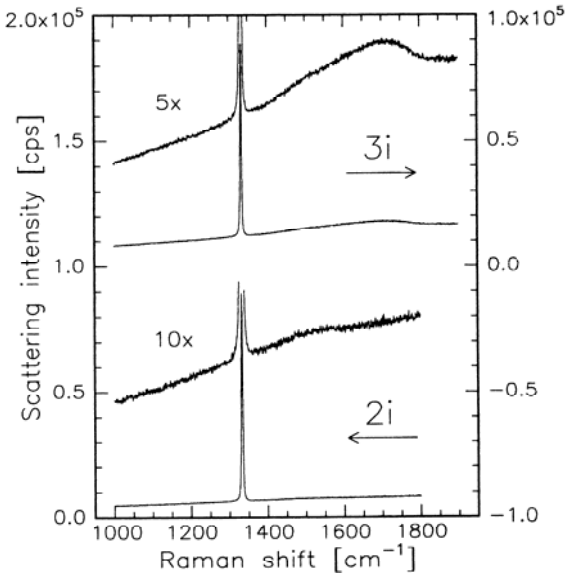

Fig. 5.13 Room temperature Raman spectra of samples 2i and 3i.

Raman spectra of the samples 2i and 3i (set IV) are shown in Fig. 5.13. The sharp diamond line dominates both spectra, the flat background (especially in sample 2i) indicates a very good sample quality. The diamond peak intensity is approximately the same in both samples, the photoluminescence background (at 1712 cm^{-1}) in the sample 3i is higher. A detailed study of the diamond peak shows that its position is, within the accuracy of the measurement, the same as that of the IIa single crystal diamond (1332 cm^{-1}). The measured width of this peak is very close to the measured width of the

single crystal (3.1 cm^{-1} for IIa, 3.6 cm^{-1} for sample 3i and 4.1 cm^{-1} for sample 2i). (Note that for decreasing slit width the measured FWHM converges to the reported value 1.8 cm^{-1} [BOR71]). The decomposition of the spectra into the individual components was performed in the same way as for the samples of set III described above. The interpretation of the components of the Raman spectra is rather straightforward for sample 3i. The features at 1300 and 1560 cm^{-1} may be identified with the well-known D and G bands of amorphous (graphitic) carbon. On the other hand, the proper assignment of the spectrum components of sample 2i (1230 and 1510 cm^{-1}) is still a subject of debate (see refs. [BAC92], [BER94]). The fact that only two non-diamond components (in addition to the sharp diamond line) are sufficient to model the experimental curves implies the good quality of the samples.

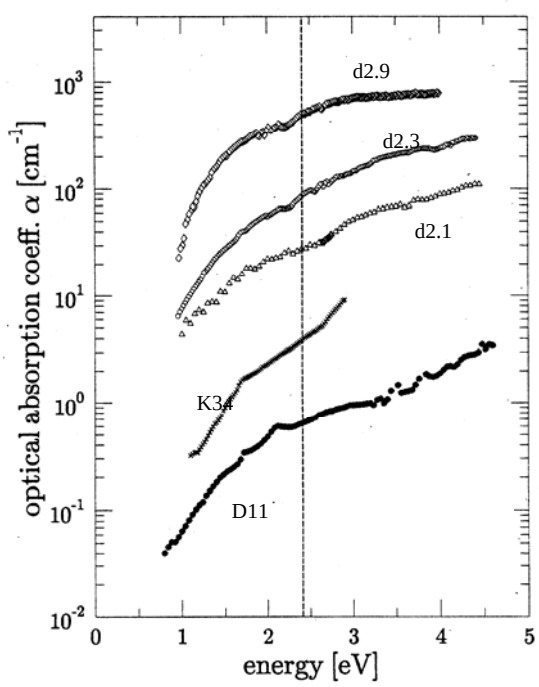

Fig. 5.14 Spectral dependence of the optical absorption coefficient α, measured by means of t-PDS, for CVD diamond films with a different fraction of sp^2 –bonded carbon. The Argon laser wavelength used in the Raman measurements is marked by the dashed line.

5.5.5. PDS measurements

A detailed discussion of the PDS spectra and the corresponding fitting with the π-π* model of the samples of set III is presented in section 5.4. For clarity, a typical spectrum of the optical absorption coefficient α in a sub-bandgap region is plotted in Fig. 5.14 for the samples of set III. The value of α at the photon energy of 2.41 eV (corresponding to the laser wavelength of 514.5 nm) ranges from 500 cm^{-1} to 3 cm^{-1}. For comparison, our best film D11 is also shown, α = 0.6 cm^{-1} at 2.41eV (see section 5.4). The value of α at the photon energy of 2.41 eV of the natural IIa diamond monocrystal is in the range of 0.1 cm^{-1}.

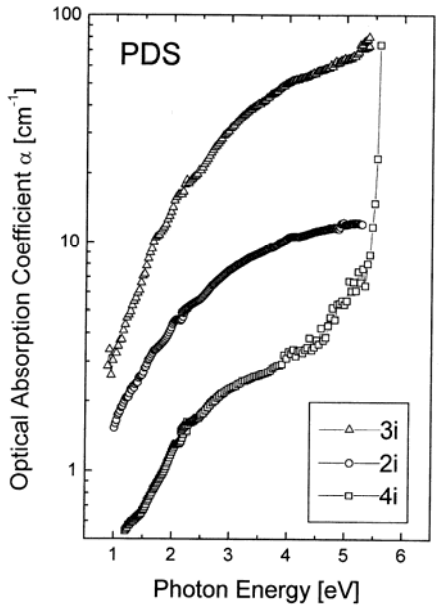

Fig. 5.15 Optical absorption coefficient, measured by means of t-PDS and transmittance measurements, of samples 2i, 3i and 4i.

Defect-induced optical absorption in samples 2i, 3i and 4i (set IV) can be seen in Fig. 5.15. The optical absorption coefficient α is plotted as a function of the photon energy E. We put them to the absolute scale by means of transmission measurements (see section 3.5). All spectra are featureless but show a different shape due to a-C as discussed in the previous section. Hence, the sample 2i is of better quality than 3i, as also follows from the Raman quality factor. Sample 4i is the most pure one. As already mentioned in

section 5.4, there are differences in the spectral shape of each sample which deserve further study.

5.5.6. Discussion

For each spectrum, we calculated β and, using Eq. (5.10) the volume fractions, ϕ_N. In the calculations, the intensity of the sharp diamond line was used for I_D, whereas all remaining components were included in I_N. This obviously results in some overestimation of ϕ_N, however, the contribution of the nanocrystalline component is not very substantial. In Fig. 5.16 the absorption coefficients α at 2.41 eV versus ϕ_N (calculated for $(\sigma_N / \sigma_D) = 233$ [SAI96], see section 5.5.3) are plotted for various measurements on the studied samples.

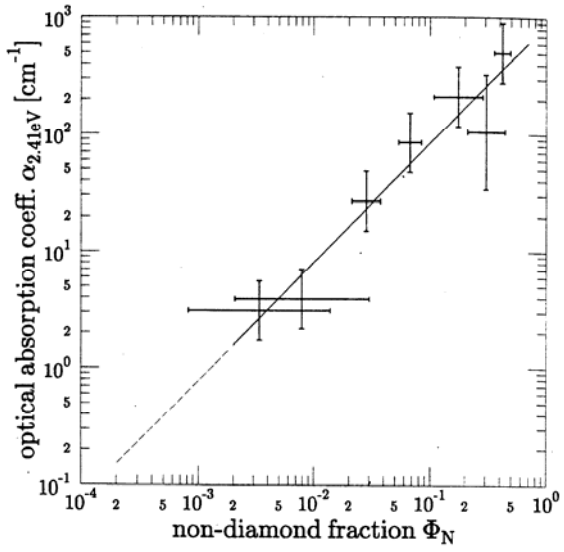

Fig. 5.16 Correlation between the non-diamond fraction ϕ_N, determined by Raman spectroscopy, and the optical absorption coefficient α at 2.41 eV, determined by means of t-PDS. A linear fit is used for the extrapolation towards the region where Raman spectroscopy reveals only the 1332 cm^{-1} diamond line. The error bars indicate the uncertainty in deconvolution of Raman spectra and in absolute precision of t-PDS measurements, together with the effect of sample inhomogeneity.

The error bars indicate the uncertainty in the deconvolution of Raman spectrum and in the absolute precision of the PDS measurements together with the effect of the sample

inhomogeneity. The straight line in this figure represents the least-squares fit to the data. Its dashed part indicates an extrapolation towards the region where Raman spectroscopy reveals only the 1332 cm^{-1} diamond line. The scatter in the data reflected by the error bars does not allow to go to more details. Nevertheless, it is evident that we find an almost linear dependence α on ϕ_N. The linear dependence can thus be explained by a linear relation between the concentration of a-C defects responsible for the observed absorption (and Raman scattering) and the observed magnitude of the PDS absorption.

The Raman quality factor β is 0.72 for sample 2i and 0.34 for sample 3i. The volume fraction of the non-diamond components, Φ_N, is then 1.6 x 10^{-3} and 8.1 x 10^{-3} , respectively. Based on the deconvolution of the Raman spectra (see section 5.5.4) the determination of Φ_N, performed above, appears plausible. On the other hand, the proper assignment of the spectrum components of sample 2i (1230 and 1510 cm^{-1}) is still a subject of debate (see refs. [BAC92], [BER94]).

5.6. Optical absorption in CVD diamond windows at λ = 10.6 µm

5.6.1. Introduction

The collinear photothermal deflection (c-PDS) technique was, for the first time, applied to the investigation of the optical absorption coefficient at the CO_2 laser wavelength (10.6 µm) for a set of CVD diamond samples of various optical qualities [MEY99]. The RT c-PDS measurements enabled absorption imaging to be performed (resolution ~ 100 µm) and thus the mechanism of optical absorption in CVD diamond to be studied. To obtain absolute values of the optical absorption, the relative c-PDS values were scaled by using a sample with known absorption (measured by LC) (see section 3.5).

5.6.2. Sample description

A set of polycrystalline CVD diamond plates, ranging from optical grade material to experimental grades containing a higher concentration of non-diamond inclusions, were provided by De Beers. The diamond plates were polished on both sides to an optical finish. The sample details are summarised in Table A.5 (see Appendix A.5). Black non-diamond inclusions, which are – to a greater or lesser extent depending on the material

grade – present in all CVD diamond films, could also be observed in the measured samples (see SEM photographs of section 5.6.3). The optical grade material contains just a few of these inclusions.

5.6.3. Optical imaging

The c-PDS technique can be used to measure the optical absorption in specified sample regions (microscopic analysis), for example regions with incorporated inclusions or other defects within the sample. Lateral position scans recorded over two different regions (lines) in a type IIa CVD diamond (sample D20) as indicated on the optical Leica MPS 32 –MZ12 micrograph in Fig. 5.17 (a), are shown in Fig. 5.17 (b). In direction 1, only very small fluctuations of the absorption coefficient can be observed. To ensure that the small changes in absorption coefficient are not due to some experimental artifacts, the c-PDS signal is measured twice: for a scan up and down over exactly the same region. The corresponding c-PDS amplitudes agree very well as can be seen from Fig. 5.17.

Nevertheless, in the high optical quality sample D20, in direction 2, a large absorption peak corresponding to the black spot in Fig. 5.17(a) is detected. As can be seen from Fig. 5.17 (a), even this very high quality CVD diamond contains regions of visible haziness and small black spots, be it in a very small amount.

The absorptance data of samples D20 and D21 obtained from regions of the order of 3.8 - 5 x 1 mm² are represented in contour maps (see Fig. 5.18). The distance in between two consecutive data points in the x- and y-direction was 250 µm and 50 µm respectively. From both maps follow that the absorptance in the diamond samples is homogeneous, as could be expected from optical micrographs (see Fig. 5.17). For the high optical quality sample D20 slight variations and small peaks could be detected while for sample D21 the absorbance shows more pronounced peaks. These peaks have been tought to arise from black spots present within the diamond films [PIC99].

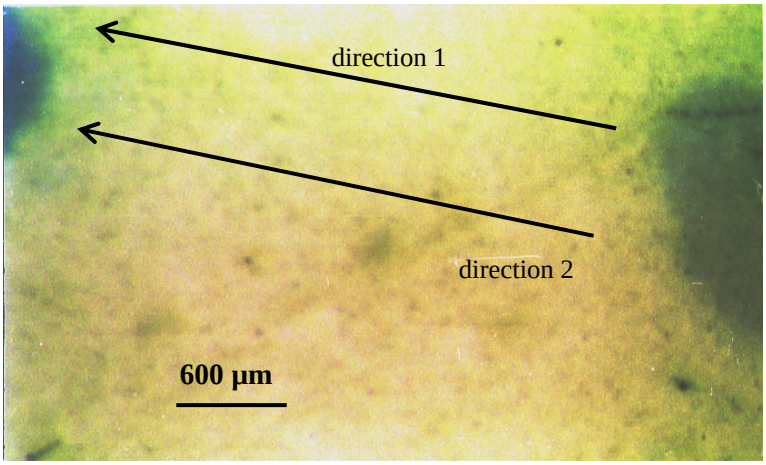

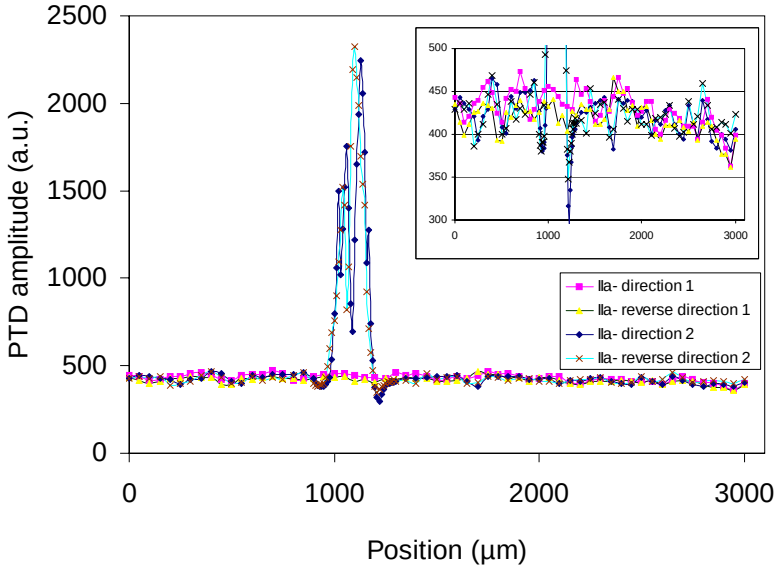

Fig. 5.17 Optical micrograph (a) of a scanned region of sample D20 (IIa diamond) . The lines on the micrograph indicate the scanned regions. The dark spots on the corners are ink drops used to identify the scanned region on the optical micrograph. The corresponding position scan is shown in (b). The inset shows a zoomed image.

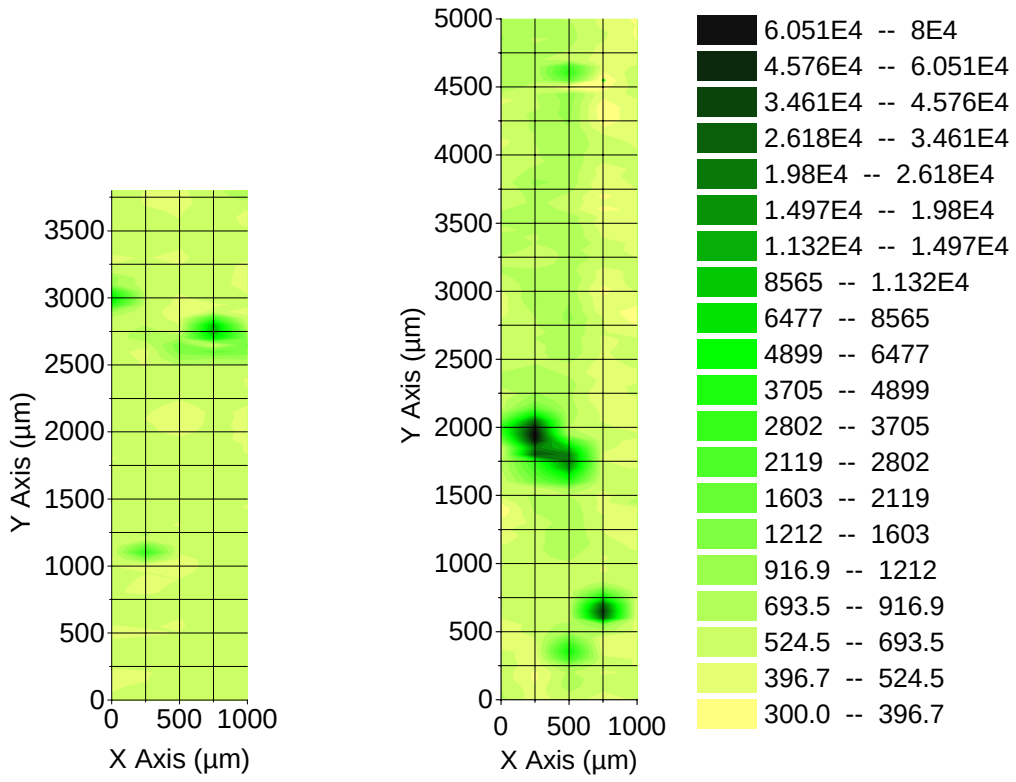

(a) *(b)*

Fig. 5.18 Contour maps showing the absorptance (a.u.) in CVD diamond optical windows (250 µm and 50 µm sampling interval in the x-and y-direction respectively). (a) Sample D20 and (b) sample D21.

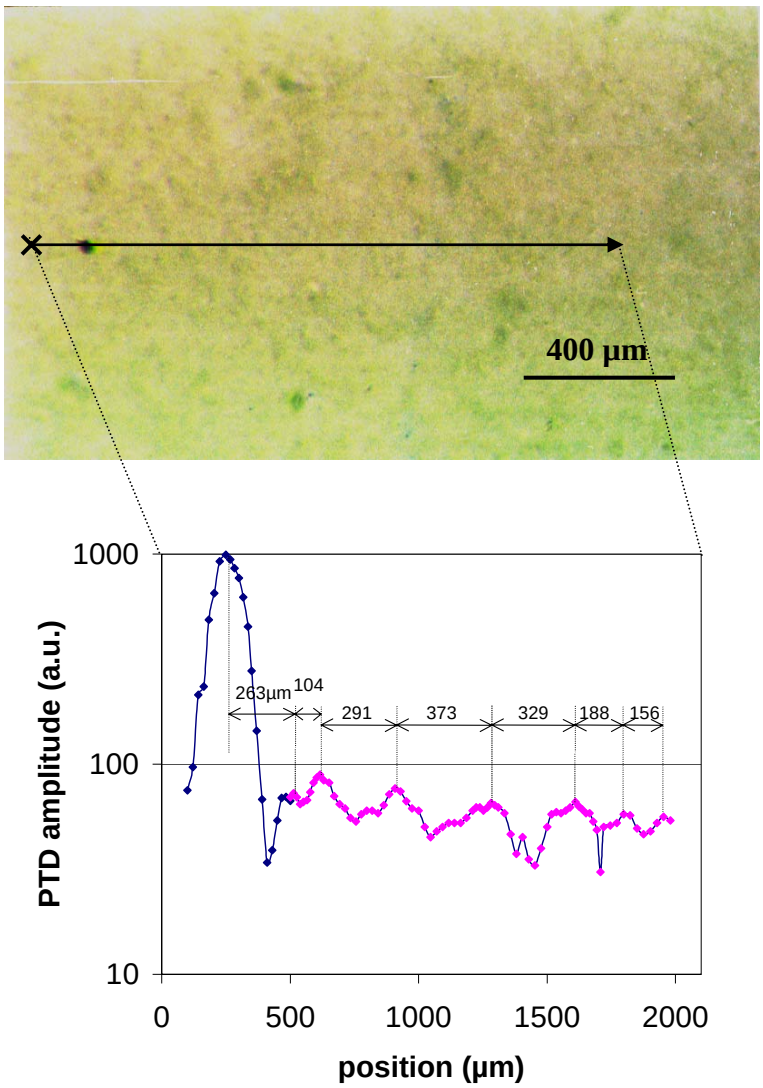

Fig. 5.19 Optical micrograph (a) of a scanned region of sample D1 with the corresponding position scan (b).

An optical micrograph and a c-PDS optical absorption image of a small region of the optical quality sample D1 are shown in Fig. 5.19. The homogeneity and the optical quality of this sample are very good and only a very few defects – 'black spots' are present. The large absorption peak in the c-PDS position scan corresponds to the small defect ("black spot") on the left side of the photo. The size of the defect, deduced from the optical micrograph, is about 40 µm. Because of the heat diffusion profile for the 666 Hz (large µ) modulated pump beam (see Eq. (3.21)), the full width of the measured peak corresponds to the diameter of the black inclusion plus twice a_p. Thus, indirectly, a PDS profile of a small isolated defect ($r<<a_p$) can be used to check the pump beam profile. A fine inspection of Fig. 5.19 (b) shows various maxima (indicated by the arrows in Fig. 5.19 (b)). One of the possible explanations for such maxima is the decoration of grain boundaries by non-diamond carbon [NES96] and/or the presence of other non-diamond inclusions or impurities. The size of the black spots can vary from a few micron to dimensions extending the grain boundaries (only a few micron thick defect layer [STE99]) and comparable with the grains itself (order of a few 100 µm) [PIC99].

Fig. 5.20 (a) shows an optical micrograph of a large planar defect in sample D2. Sample D2 contains more and larger black inclusions in comparison with sample D1. The c-PDS amplitude corresponding to a position scan over the planar defect is plotted for various frequencies (133 - 9333 Hz) in Fig. 5.20 (b). As predicted by the theory, the inset of Fig. 5.20 (b) shows that the amplitude of the c-PDS signal (for the two observed maxima) decreases with increasing modulating frequencies. Additionally, a fine inspection of the two PDS frequency- dependencies in the inset of Fig. 5.20 (b) indicates slightly different behaviour. The theoretical modelling of the c-PDS signal can explain such behaviour by considering the fact that the position scan was not carried out directly across the black spots but in their close vicinity. In such case, the temperature profile is determined not only by the modulation frequency but also by the local diffusivity value (inclusions / grain boundaries) yielding a small spatial variation in the temperature profile and resulting in a small deviation from equations (3.21) and (3.22).

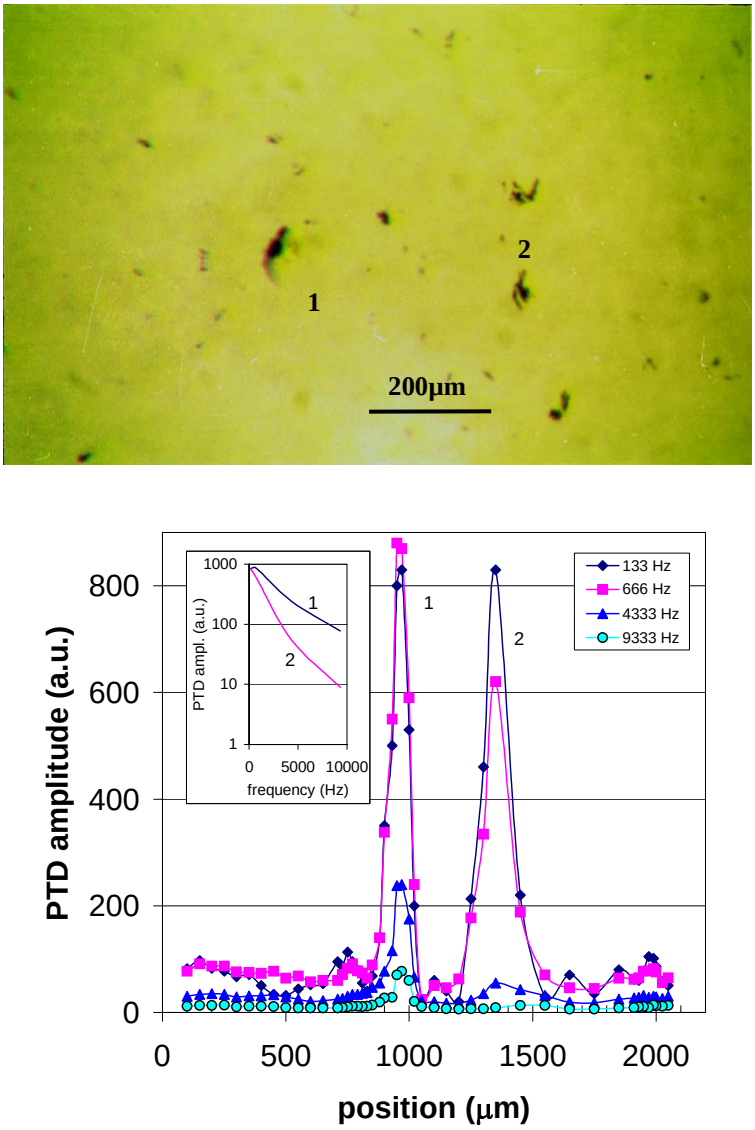

Fig. 5.20 Optical micrograph (a) of a scanned region of sample D2 with the corresponding position scan (b).

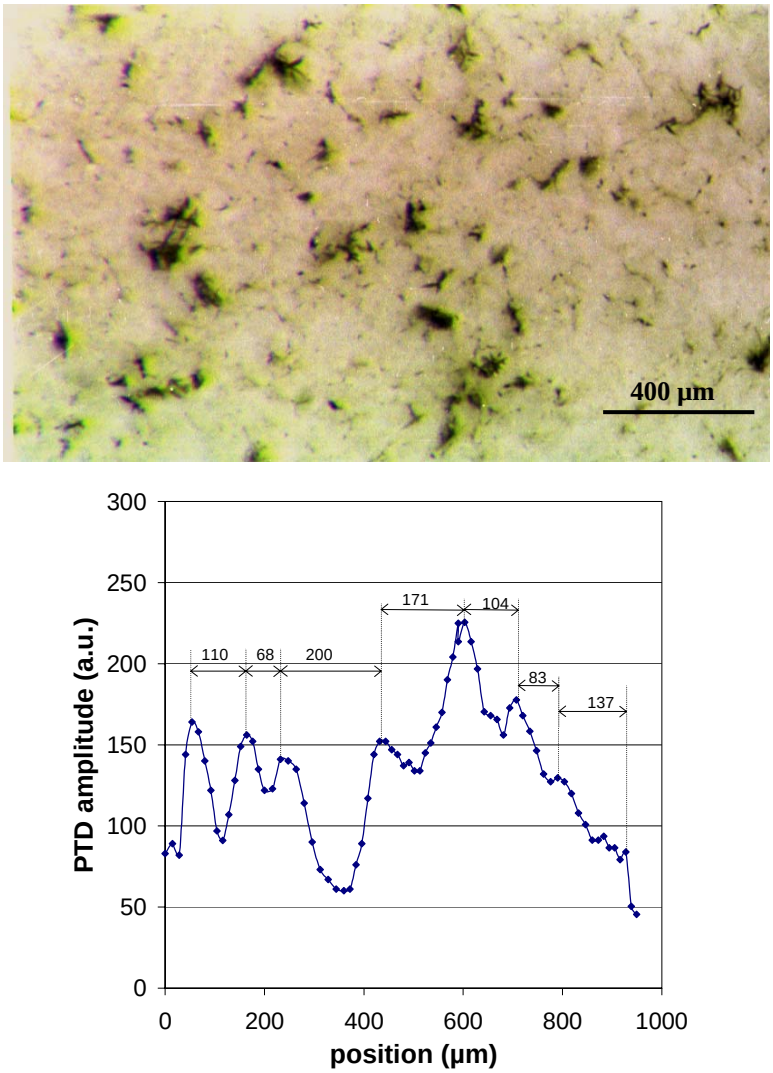

Fig. 5.21 Optical micrograph (a) of a scanned region of sample D6 with the corresponding position scans (b).

Finally Fig. 5.21 shows an optical micrograph and c-PDS scan of the non-optical grade sample D6. Although this sample has a very high thermal conductivity, the transparency of such a sample is lower and moreover the He-Ne probe beam is scattered. Comparison of the optical micrograph and the c-PDS scan for this sample with the optical grade

sample shows a significantly larger local variation of the optical absorption due to non-diamond inclusions.

5.6.4. Optical absorption values

The average optical absorption coefficient α for a given set of CVD diamond plates was investigated by the collinear PDS technique. Because the c-PDS method measures the absorption value locally, a 100 - points scan was randomly taken across the whole sample. With c-PDS, it is difficult to obtain absolute optical absorption values (see section 3.5). One of the problems is the exact determination of the angular deflection value from the c-PDS signal, detected by the position sensor, needed for the mathematical expressions (Eqs. (3.23), (3.21) (3.22)) to calculate α in absolute units. To avoid this problem, the majority of c-PDS measurements on quartz, sapphire, ZnSe and other optical material [BLA97], [MAS93] use a calibration sample of a known absorption value.

Table 5.2 Absorption data at 10.6 µm obtained from PDS and calorimetric measurements on CVD diamond samples.

Sample #number	Thickness (µm)	Absorption (%) Calorimetry	α (cm^{-1}) Calorimetry	Absorption (%) PDS	α (cm^{-1}) PDS
D1	660	0,45	0.057	0,38	0.048
D2	330	0,46	0.117	0,46	0.117
D3	1200	0,83	0.058	0,50	0.035
D4	760	0,7	0.077	0,70	0.077
D5	720	0,9	0.104	0,91	0.106
D6	660	1,2	0.152	1,15	0.146
D7	460	1,04	0.189	1,50	0.273
D8	700	1,67	0.200	1,78	0.214
D9	620	4,27	0.587	3,33	0.455

In our case, the c-PDS measurements are scaled relative to the reference sample D4, which was scaled via laser calorimetry at the Stuttgart University [GIE99] and Laser Power Europe (Gent). When using a reference sample, it is vital that the beam geometry remains unaltered for measurements on different samples. In our case all the measurements on different samples were carried out in a fixed focusing geometry in a continuous set of experiments and before and after the measurements the c-PDS signal on

the calibration sample was checked.

Table 5.2 summarises the results of the c-PDS measurements, the LC measurements and the optical characteristics of the CVD diamond windows. The absorption coefficient as measured by means of c-PDS ranges from 0.035 cm^{-1} for standard optical material to 0.5 cm^{-1} for non-quality material. Sample D3 which show practically no black spots/inclusions is of the highest optical quality of the measured samples and shows an optical absorption coefficient of 0.035 cm^{-1}. This value is in good agreement with absorption data for natural type IIa diamond, reported in literature [MAS95], [PIC99]. By comparing the absorption data measured by the different techniques, a quite good agreement is found. Some small deviation for samples D3, D7 and D9 can be caused by the sample homogeneity. Also, calorimetry measurements are done in the middle of the samples while c-PDS is averaged over 100 local points. The measured c-PDS absorption values are consistent with the optical micrographs.

5.7. Conclusions

In the first part of this Chapter, we have investigated in detail by means of t-PDS the subgap absorption in CVD diamond films upon changing the deposition conditions. The studied films ranged from high quality material to nanocrystalline films.

Experimental data showed that all investigated CVD diamond films exhibited a very characteristic shape of the subgap optical absorption in the IR and visible spectral regions. In nanocrystalline approaching films, an absorption spectrum resembling closely these of a-C films was observed. This absorption is believed to be due to the optical transition between π-π^* subgap states. The morphology study proved that the films with the highest subgap absorption were nanocrystalline with an increased surface of grain boundaries. Raman spectroscopy detected an increased amount of sp^2 carbon in these films. They were optically smooth (e.g. low scattering losses) and optical transmission measurement showed that characteristic indirect transition due to the long-range order of diamond structure was lost. On the other hand, the best quality CVD diamond attained the character of the fundamental absorption edge, but optical absorption in this region exhibited broadening. From comparison with synthetic Ib diamond, it has been shown that the characteristic absorption can not be explained by substitutional nitrogen or by other impurities. Therefore, the main defect structure in undoped CVD diamond films dominating the defect-induced optical absorption, is sp^2-bonded (π-bonded) carbon.

Based on these results we developed a mathematical model for the description of the optical absorption coefficient in the subgap region. A numerical deconvolution procedure was developed to fit the experimental data, according to our theoretical model. The fit yielded very good agreement with experimental data and the fitted parameters were very close to those expected from the current knowledge about the electronic structure of a-C.

We applied Raman and PDS measurements on the same CVD diamond films. We have demonstrated that there is an approximately one to one correlation between the non-diamond fraction (determined by Raman spectroscopy) and the value of the optical absorption coefficient α (determined by PDS) at a photon energy 2.41 eV. Hence, because of the high sensitivity of PDS, the graphitic inclusions (sp^2 bonded carbon) can be traced in CVD diamond films with a characteristic sub-bandgap absorption well below the ppm level. Measurements on a broader set of samples should help to increase the reliability of the inferred relationship and enable its more precise quantification. Further attempts to estimate the magnitude of Raman cross sections of all non-diamond components are needed. The wide dynamical range of absorption coefficients accessible by PDS (10^3-10^{-2} cm^{-1}) suggests that PDS offers a higher sensitivity for the detection of low values of ϕ_N than Raman spectroscopy. This is obviously true for Raman spectroscopy with visible excitation. However, the sensitivity of Raman scattering to non-diamond defects may be enhanced considerably when the wavelength of the exiting light is increased.

In the second part of this chapter, the collinear PDS method was successfully applied, for the first time, to measure the optical absorption of CVD diamond windows at the CO_2 laser wavelength. The measurements carried out on a set of samples of various optical qualities demonstrated the applicability of this technique for high quality CVD diamond windows. The c-PDS measurements were carried out with a spatial resolution of about 100 μm, determined by the focusing optics, yielding optical absorption images for different samples. It has been demonstrated that the optical absorption mechanism is greatly affected by the black features, which are – to a greater or lesser extent depending on the material grade – present in all CVD diamond films. The optical grade material contains mostly no such features. Finally, the apparent c-PDS values were scaled by using a sample with known absorption (obtained by calorimetry) and the c-PDS and calorimetric values were compared.

5.8. References

[ABE81] .S. Abe, Y. Toyazawa, J. Phys. Soc. Jpn. **50** (1981), 2185.

[AGN92] C. Agnus, M. Sunkara, S.R. Sahaida, and J.T. Glass, J. Mater. Res. **7** (1992) 3001.

[ANA70] E. Anastassakis, E. Burstein, Phys. Rev. B **2** (1970) 27.

[BAC91] P.A. Bachmann, D. Leers and H. Lydtin, Diamond Relat. Mater., **1**(1991), 1.

[BAC92] P.K. Bachmann and D.U. Wiechert, Diamond Relat. Mater., **1** (1992) 422-433.

[BAC94] P.K. Bachmann, H.D. Bausen, H. Lade, D. Leers, D.U. Wiechert, N. Herres, R. Kohl, P. Koidl, Diamond Relat. Mater. **3** (1994) 1308-1314.

[BER93] L. Bergmann, B.R. Stoner, K.F. Turner, J.T. Glass and R.J. Nemanich, J. Appl. Phys., **73** (1993), 3951-3957

[BER94] L. Bergmann, M.T. McClure, J.T. Glass, and R.J. Nemanich, J. Appl. Phys. **76** (1994), 3020-3027.

[BI90] X.X. Bi, P.C. Eklund, J.G. Zhang, A.M. Rao, T.A. Perry and C.P. Beetz, J. Mater. Res. **5**(4) (1990), 811- 817.

[BLA97] D. Blair, F. Cleva, C. N. Man, Opt. Mater. **8** (1997)233- 236.

[BOR71] W.J. Borer, S.S. Mitra, K.V. Namjoshi, Solid State Commun. **9** (1971) 1377

[BOU93] Y. Bounough and M.L. Theye, A. Dehbi-Alaoui and A. Matthews, J. Cernogora and J.L. Fave, C. Colliex, A. Gheorgiu and C. Senemaud, Diamond Relat. Materials, **2** (1993), 259-265.

[BRE85] J. L. Bredas and G.B. Street, J.Phys. C. **18** (1985), L651.

[BUC89] R.G. Buckley, T.D. Moustakas, Ling Ye and J. Varon, J. Appl. Phys. **66** (1989), 3595-3599.

[CLA56] C.D. Clark, R.W. Ditchburn and H.H. Dyer, Proc. R. Soc. Lond. **A237** (1956), 75-78.

[CLA79] C.D. Clark, E.W.J. Mitchel, and B.J. Parsons, in Properties of Diamond, edited by J.E.Field, Academic Press, (1979).22-78.

[COD84] G.D. Cody in Semiconductors and Semimetals, ed. J.I. Pankove, (1984), Chap.

2, Academic Press, 11-82.

[CRE93] A. Cremades, F. Dominguez-Adame and J. Piqueras, J. Appl. Phys., **74** (1993) 5726.

[DER77] B.V. Deryagin, D.V. Fedoseev, Growth of Diamond and Graphite from the Gas Phase, Nauka, Moscow (1977)

[DRA94] D.A.Drabold, P.A. Fedders, P. Stumm, Phys. Rev. B, **49** (1994), 16415-16422.

[FAL93] P.J. Fallon and L.M. Brown, Diamond Relat. Materials, **2** (1993), 1004-1011.

[GHE95] E. Gheeraert, A. Deneuville, E. Bustarret, F. Fontaine, Diamond Relat. Mater. **4** (1995) 684.

[GIE99] A. Giesen, Stuttgart University, Private communication (1999)

[HUO91] P.V. Huong, Diamond Relat. Mater. **1** (1991) 33-41.

[HUO93] P.V. Huong, J. Mol. Struct. **292** (1993) 81-87.

[JAC81] W.B. Jackson, N.M. Amer, A.C. Boccara and D. Fournier, Appl. Opt. **20** (8), (1981) 1333-1344.

[JAC85] W.B. Jackson, S.M. Kelso, C.C. Tsai, J.W.Allen and S.-J.Oh, Phys. Rev. B, **31** (1985), 5187-51198.

[KNI89] D.S. Knight and W.B. White, J. Mater. Res. **4** (1989) 385.

[LEE94] Ch.H.Lee, W.R.L. Lambrecht, B. Segall, P. C. Kelires, T. Frauenheim, U. Stephan, Phys. Rev.B, **49** (1994), 11448-11451.

[LEE98] S.M. Leeds, T.J. Davis, P.W. May, C.D.O. Pickard, M.N.R. Ashfold, Diamond Relat. Mater. **7** (1998) 233-237.

[MAR96] N.A. Marks, D.R. McKenzie, B.A. Pailthorpe, M. Bernasconi, and M. Parrinello, Phys. Rev. Lett. **76** (1996) 768.

[MAS93] E. Masetti, M. Montecchi, M.P. Da Silva, Thin Solid Films, **234** (1993) 557-560.

[MAS95] M. Massart, P. Union, G.A. Scarsbrook, R.S. Sussann, P. Muys, SPIE Vol. **2714** (1995) 177.

[MEY96] K. Meykens, M. Nesladek, C. Quaeyhaegens, L.M. Stals, M. Vanecek, J. Rosa,

J.J. Schermer, G.Janssen, Diamond Relat. Mater. **5** (1996) 958-963.

[MEY99] K. Meykens, K. Haenen, M. Nesladek, L.M. Stals, C.S.J. Pickles, R.S. Sussmann, presented at Diamond'99 Prague and Diamond Relat. Mater. (1999) in press.

[MOR95] P.W. Morrison, A. Somashekbar, J.T. Glass and J.T. Prater, J. Appl. Phys., **78** (1995) 4144.

[MUY99] P. Muys, *'CVD diamond laser window applications'*, presented at Diamond'99, Prague.

[NEB99] C. Nebel, A. Waltenspiel, M. Stutzmann, M. Paul, L. Schäfer, presented at Diamond '99, Prague

[NES95] Nesladek, M. Vanecek, J. Rosa, C. Quaeyhaegens, L.M. Stals, Diamond Relat. Mater. **4** (1995), 697-701

[NES96] M. Nesladek, K. Meykens, L.M. Stals, M. Vanecek and J. Rosa, Phys.Rev.B, **54** (1996),5552-5561.

[OKU92] K. Okumura, J. Mort and M.A.Machonkin, Philos. Mag. Lett, **65** (1992), 105.

[PIC99] J.C.S. Pickles, T.D. Madgwick, C.J.H. Wort, R.S. Sussman, presented at Diamond'99 in Prague

[PIE92] W. Piekarcyk, J. Crystal Growth **119** (1992), 345-362.

[ROB87] J. Robertson, E.P. O'Reilly, Physical Review B, **35** (1987), 2946-2957.

[ROB92] J. Robertson, Phil.Mag B, **66** (1992), 199-209.

[ROB95] J. Robertson, Diamond Relat. Materials **4** (1995), 297-301.

[ROB97] J. Robertson, Diamond Relat. Mater. **6** (1997) 212-218.

[SAI96] S.R. Sails, D.J. Gardiner, M. Bowden, J. Savage, D. Rodway, Diamond Relat. Mater. **5** (1996) 589-591.

[SAV85] N. Savvides, J. Appl. Phys. **58** (1985), 518-521.

[SCH90] R.E. Schroder, R.J. Nemanich, and J.T. Glass, Phys.Rev.B, **41** (1990), 3738.

[SPE94] K.E. Spear and M. Frenklach in Synthetic Diamond, Emerging CVD Science and Technology, edited by K.E. Spear, J.P. Dismukes, J. Willey &Sons, (1994).243-304.

[SPI70] W.E. Spicer, T.M. Donovan, Phys. Rev. Lett. **24** (1970).

[STE94] U. Stephan, Th. Frauenheim, P. Blaudeck, G. Jungnickel, Phys. Rev. B, **50** (1994), 1489-1501.

[STE99] J.W. Steeds, S. Charles, presented at Diamond'99 in Prague.

[STU93] S.A. Stuart, S. Prawer, P.S. Weiser, Appl. Phys. Lett., **62**(11) (1993) 1227.

[SUS94] R.S. Sussmann, J.R. Brandon, G.A. Scarsbrook, C.G. Sweeney, T.J. Valentine, A.J. Whithead and C.J. Wort, Diamond Related Materials, **3** (1994), 303.

[TAM94] M.A. Tamor and M.P. Everson, J. Mater. Res. **9** (1994), 1839-1848.

[TAU65] J. Tauc, A. Abraham, L. Pajasova, R. Grigorovici, A. Vancu, Proc. Int. Conference Physics of Non-Crystalline Solids, North Holland, Amsterdam (1965) 606.

[TAU74] J. Tauc in Amorphous and Liquid Semiconductors, (1974) ed. J. Tauc, Chapter 4, Plenum, New York.

[VAN57] H.C. Van De Hulst *'Light Scattering by Small Particles'*, Wiley, NY (1957).

[VAN91] N.S. Van Damme, D.C. Nagle, S.R. Winzer, Appl. Phys. Lett., **58** (25) (1991) 2919-2920.

[VEE93] V.S. Veersasamy, G.A.J. Armatunga, W.I. Milne, P. Hewitt, P.J. Fallon D.R.McKenzie and C.A.Davis, Diamond Relat. Materials, **2** (1993), 782-787.

[VOR97] V. Vorlicek, J. Rosa, M. Vanecek, M. Nesladek, L.M. Stals, Diamond Relat. Mater. **6** (1997) 704-707.

[WAD81] N. Wada, S.A. Solin, Physica B+C, **105** (1981) 353.

[WAG91] J. Wagner, C. Wild, P. Koidl, Appl. Phys. Lett. **59** (1991) 779.

[WAN93] C.Z. Wang, K.M. Ho and C.T. Chan, Phys. Rev. Lett, **70** (1993), 611.

[WIL98] C. Wild, 'CVD diamond for Optical Windows' in 'Low pressure Synthetic diamond', eds. B. Dischler, and C. Wild, Springer-Verlag, (1998).

[YAR88] W.A. Yarbrough and R. Roy in A. Badzian, M. Geis, G. Johnson (eds) '*Diamond and diamond-Like Materials*', Mat. Res. Soc. Pittsburgh, PA, Extended Abstracts Vol. **EA-15** (1988) 33.

[ZAM98] U. Zammit, K.N. Madhusoodanan, M. Marinelli, F. Mercuri, and S. Foglietta, Phys. Rev. B, **57** (1998) 4518.

6. Study of active impurities: substitutional nitrogen, lithium and phosphorus

6.1. Introduction - State of the art of n-type doping

6.1.1. Defects in diamond

An important issue of diamond research has always been that of defect characterisation. Defects have been thoroughly investigated in the past in natural and in HPHT synthetic diamond. They have been classified generally as N, GR, R, TR, H or others [WAL79]. Nowadays, more than 300 defects in diamond are known. The dominating impurities in natural as in synthetic diamond are nitrogen (N) and related defects (as A, B, P1, H2, H4, N3 defects, etc.) [WAL79], [DAV93], [MAI94]. Single substitutional nitrogen is detected by ESR measurements. Also optical detection of N via infrared absorption spectroscopy is possible. The IR spectra of diamond containing single substitutional nitrogen show a characteristic IR vibrational band at 1130 cm^{-1} [WOO90]. When nearest neighbour pairs of nitrogen are present these give rise to a peak at 1290 cm^{-1} [COL91]. Other common impurities and defects found in natural and synthetic diamond are carbon interstitials, hydrogen and boron [VEN94]. In HPHT diamond, nickel and cobalt complexes are observed as well. Irradiation can produce intrinsic defects namely vacancies and interstitials [DAV92]. The defects and their electronic models are discussed in detail in literature [WAL79], [CLA79], [BRI93], [DAV93], [MAI94], [MAI99].

Several of the defects detected in natural or HPHT synthetic diamond are encountered in CVD diamond films too e.g. nitrogen, boron and vacancies [MEY96], [MAI99]. Vacancies are incorporated in CVD diamond films during the deposition process, but they migrate and form complexes while the growth progresses. Nevertheless, there are also defects which are specific for CVD diamond films only, such as the a-C and graphite inclusions, discussed in Chapter 5, and silicon-vacancy defects [MAI99].

The defect-induced optical absorption in natural and synthetic diamond has been thoroughly investigated in the past. Nowadays the research is more focused on the defect characterisation of CVD material [MAI99]. Optical spectroscopy, such as UV-VIS and IR absorption spectroscopy, photoluminescence and cathodoluminescence, Raman

spectroscopy, have been used extensively to obtain information about all these defects in diamond. In addition, electron paramagnetic resonance (EPR) and photocurrent measurements are frequently used to provide complementary information. [DAV77], [WAL79], [COL92], [DAV94], [MAI94], [GRA96], [ROH96], [MAI99], [STE99a].

6.1.2. Doping

Doping of diamond forms a second important topic as far as the use of diamond as a semiconducting material for electronics is concerned. Many diamond-based semiconductor devices will require both p- and n-type conduction. p-Type conductivity is observed for both natural (type IIb) and HPHT synthetic boron-containing diamond [BRO55], [HUG62], [WAL79]. In 1971 Collins identified boron as the impurity responsible for the p-conductivity [COL71]. In 1973, this was confirmed by Chrenko [CHR73]. Moreover, p-conducting diamond can easily be made by CVD deposition with in-situ boron-doping [FUJ86] [MOR89] or by ion implantation followed by proper annealing [BRA83]. The activation energy of the acceptor was found to be 0.35 to 0.37 eV.

The development of diamond-based electronic devices is hindered mainly by the inability of growing n-type diamond. Although nitrogen is a possible doping element, in single substitutional position it forms a deep donor with an activation energy of 1.7 eV [FAR69]. Because of this high activation energy, nitrogen doped diamonds are not suitable for semiconductor applications. Optical ionisation of the substitutional N donor occurs at 2.2 eV and is ascribed to an electronic transition to the conduction band. Superimposed on this ionisation continuum in the optical absorption spectrum are 3 bands centred around 3.3 eV (A band), 3.9 eV (B band) and around 4.5 eV (C band) respectively.

Theoretical studies indicated phosphorus (P), lithium (Li) and sodium (Na), as possible n-dopants of diamond [JAC90], [KAJ91], [AND93]. The situation is however not very clear. The results of these theoretical calculations are not unambiguous: Jackson et al. [JAC90] found a P donor level of 1.09 eV, while Kajihara et al. [KAJ91] suggested an ionisation energy of 0.2 eV below the bottom of the conduction band for substitutional P. For Li and Na at interstitial positions, Kajihara et al. found energies of 0.1 eV and 0.3 eV respectively. But they expect very low concentrations of donor centres and thus a low n-conductivity. It is suggested by Anderson et al. [AND93] that interstitial Li should form a shallow donor, whilst Li on substitutional position would be a deep defect, probably with

acceptor character. Nevertheless, the theoretical predictions expect only very low solubillities of these donor atoms in the diamond lattice.

The first experimental results about doping of diamond films were also, just like the theoretical ones, inconsistent. It is well known that the calculated equilibrium concentration of P is very low in diamond [AND93], [KAJ93] because of the large atomic radius of P in comparison with the diamond lattice constant. The majority of n-doping trials using the in-situ doping or post-deposition diffusion were unsuccessful or only a low P incorporation was shown. Several studies about P as a n-type dopant for CVD diamond are published [OKA90], [KAM91], [ALE92], [BOH95] but the epitaxially P-doped diamond films were highly resistive. Okano et al. [OKA90], who used P_20_5 in the feed gas, reported an activation energy of the dark conductivity of about 0.3 eV. But there was no evidence presented of true n-type conduction. In 1995, Prins [PRI95] claimed a successful n-doping, making use of the ion implantation technique. Three years ago, researchers from NIRIM were the first to successfully prepare phosphorus doped CVD diamond films [KOI97]. Confirmation of the n-type conductivity was obtained by Hall effect measurements, pointing to an activation energy E_a of the charge carriers of about 0.55eV to 0.60 eV [KOI97], [KOI98], [KOI99]. The first direct optical confirmation of P optical activity has been done by our group at IMO [HAE99].

Parallel to phosphorus doping, other n-dopants as light elements have been studied. Successful lithium ion implantation of intrinsic diamond leading to n-type conductivity with an activation energy of 0.1 eV – 0.2 eV has been reported by Vavilov et al. [VAV80] and Prawer et al. [PRA93]. Thermally activated electrical conduction with an activation energy of 0.16 eV was measured in Li-doped homoepitaxially grown diamond films [BOR95]. A few groups have performed in situ Li-doping of diamond films during the CVD growth but up till now, no extended electrical characterisation took place [NES96]. Very recently Sternschulte et al. [STE99b] have grown Li-doped homoepitaxial CVD diamond films on synthetic type Ib (100) single crystal diamonds by addition of Li-t-butoxide ($LiOC_4H_9$) to the feed gas. Neither by doping nor by in-diffusion of Li in natural single crystal diamond n-type characteristics could be obtained [POP96], [NIJ97]. Despite al these attempts no prove of Li as the origin of n-type electrical activity has been found. The measured mobilities are very low.

Recently sulphur-doping leading to successful n-type doping of diamond is reported [SAK99]. Hall effect measurements indicated n-type conduction with a room temperature Hall mobility value of 597 $cm^2V^{-1}s^{-1}$. The activation energy was estimated to be 0.38 eV.

On the other hand, Kalish et al. [KAL00] doubt these results. They measured the Hall mobilities of exactly the same S-doped diamond films and found p-type conduction. Besides boron contamination was detected by means of SIMS measurements. Therefore they suggest the measured conductivity is p-type conduction due to B impurities instead of active S donors.

In spite of several studies, still little is known about the way P, Li and S are incorporated into the films, and about the electronic structure of the P-, Li- and S-related defects. Additionally, defects and impurities present in diamond can compensate (e.g. acceptor like defects) or neutralise (e.g. creating a complex with P) the active doping action in diamond.

6.2. Optical Absorption in nitrogen-doped CVD diamond films

In the framework of this thesis, several N-doped diamond films of different sources were investigated. The spectral dependence of homoepitaxially flame grown diamond layers is studied by means of t-PDS. For comparison, type Ib high-pressure high-temperature (HPHT) synthetic diamond (containing substitutional N) and type IIa natural diamond were investigated as well. The subgap optical absorption of the homoepitaxial diamond films is compared with cathodoluminescence (CL) measurements. Polycrystalline diamond films were doped by introducing nitrogen (N_2) and nitromethane to the gas mixture during MWPE CVD diamond growth. Raman spectra and t-PDS absorption data were recorded and are discussed below.

6.2.1. Sample description

In this section, an extended description of all N-doped samples is given. The key growth parameters are summarised in Appendix A.1, Table A.2 and Table A.8.

Flame grown diamond layers

The homoepitaxial diamond layers, examined in this study, were deposited by the flame deposition technique on top of type IIa natural diamond seed crystals [SCH94]. Nitrogen, incorporated in these specimens, entered the gas phase by in-diffusion from the ambient during the film growth. N-doped CVD diamond films were grown at the Katholieke Universiteit Nijmegen (KUN, Nijmegen, the Netherlands).

150 - 400 μm thick diamond layers were grown on {001} and {110} oriented type-IIa

natural diamond seed crystals, using an acetylene-oxygen combustion flame. The acetylene supersaturation was between 3.9 and 5.4 % and the substrate temperature was about 1200 ^{o}C. In order to control the substrate temperature, the seed crystals were soldered onto a water-cooled substrate holder. After the deposition, the backsides of the specimens were polished to remove both small residues of the solder and etch-pits, caused by a reaction of the solder with the diamond seed crystal. The experimental arrangement used for diamond growth is described in [SCH93].

The films deposited on the {001} substrate are fully transparent, whilst the films deposited on the {110} oriented substrate were greyish-brownish with small black inclusions.

The specimens were examined in detail by scanning electron microscopy (SEM), Raman and IR transmission spectroscopies [SCH94]. It was demonstrated that the spectroscopic characteristics and the surface morphology of the deposited diamond layers are determined by the crystallographic orientation of the substrates rather than by the small differences in growth conditions [SCH94].

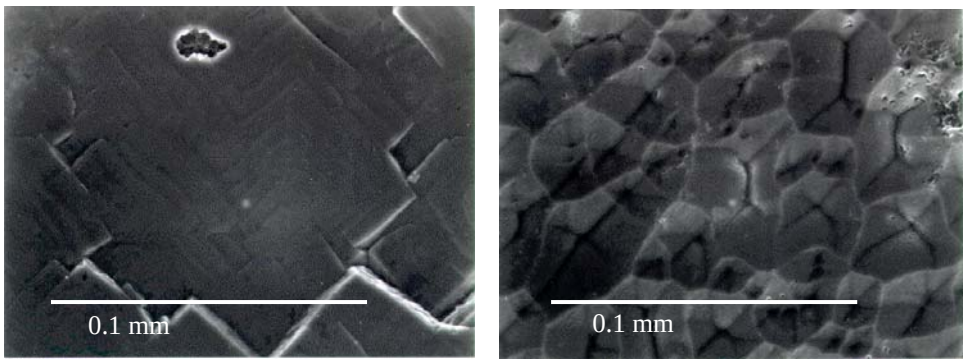

(a) (b)

Fig. 6.1 Scanning electron micrographs showing the surface morphology of the homoepitaxial diamond films, deposited by the acetylene-oxygen flame technique: sample C7 deposited on a {001} oriented substrate (a), sample C2 deposited on a {110} oriented substrate (b).

Summarised, the {001} layers can be generally classified as type IIa and they have a fairly smooth surface covered by macrosteps due to step bunching as well as by a limited

number of square growth-hillocks. However, most of the {110} layers contain bonded hydrogen which concentration can be determined from the IR C-H stretching bands of sp^3 hybridised CH_2 groups between 2800 and 3000 cm^{-1} (the amount of incorporated H was estimated to be 1200 ppm in the investigated sample). The {110} layers have a rough appearance due to the development of microfacets on the surface. Scanning electron micrographs, revealing the surface morphology of these samples, are shown in Fig. 6.1.

Natural and HPHT-synthetic diamond

Diamond, which contains virtually no (optically active) impurities, is generally classified as type IIa [DAV77] (see Chapter 1). Therefore type IIa diamond was selected as a reference sample for calibration of our PDS set-up. Natural IIa and yellow synthetic Ib De Beers bulk diamond plates (250 μm thick, 2mm x 2mm wide) were also measured. These diamond plates were polished on both sides.

Diamond containing single substitutional nitrogen is classified as type Ib [DAV77]. Type Ib diamond shows a characteristic IR absorption band at 1130 cm^{-1} [WOO90] and several UV-VIS absorption bands [KOP86], [NAZ87]. Type Ib HPHT-synthetic diamond (De Beers) was used to compare this characteristic UV-VIS optical absorption with the one measured for the CVD films. The Ib HPHT diamond plate, investigated here, shows a growth sector dependent concentration of substitutional nitrogen, which is typical for synthetic diamond [BUR90]. The nitrogen concentration ranges from 50 to 150 ppm, as determined by IR absorption spectroscopy and using the conversion factor of Woods et al. [WOO90].

N-doped polycrystalline MW PECVD diamond

N-doped polycrystalline CVD diamonds were synthesised in an ASTeX PDS17 MW PECVD system (as described in Chapter 2, section 2.1). The incorporation of N atoms in the films was studied by adding nitrogen (N_2) or nitromethane (NO_2-CH_3) to the hydrogen-methane feed gas in the ppm volume range. Further details about the samples are given in Appendix A.1 Table A.2.

The deposition conditions for set V (samples S1 and S2) corresponded approximately to the conditions used for the deposition of the highest quality diamond sample D11 (see Table A.1): 13600 Pa, 760 °C, 300 sccm H_2, 3 vol.% CH_4, 4000 W. The only difference

was the partial pressure of N_2 (100 ppm – 1 vol.% respectively).

For the deposition of samples of set VI (samples N1, N2, N3, N4 and NM1, NM2, NM3), the deposition conditions were changed: 11500 Pa, 830 - 930 °C, 2.88 – 4.76 vol.% CH_4, 3000 W. The concentration N_2 ranged from 95 to 714 ppm, while the amount NO_2-CH_3 varied between 17 and 173 ppm. To add the liquid NO_2-CH_3 (0.9 vol.%) it was diluted in isopropanol (C_3H_7OH). The ppm value and the number of atoms (N, C, O) fed into the gas phase per minute can be calculated using the theoretical partial pressure at 50 °C and the flow in sccm admitted by the mass flow controller (heated at a temperature of about 70°C to avoid vapour condensation) [VAN98]. The ppm value is listed in Table A.2 (Appendix A.1)

Influence of N_2 on the film morphology

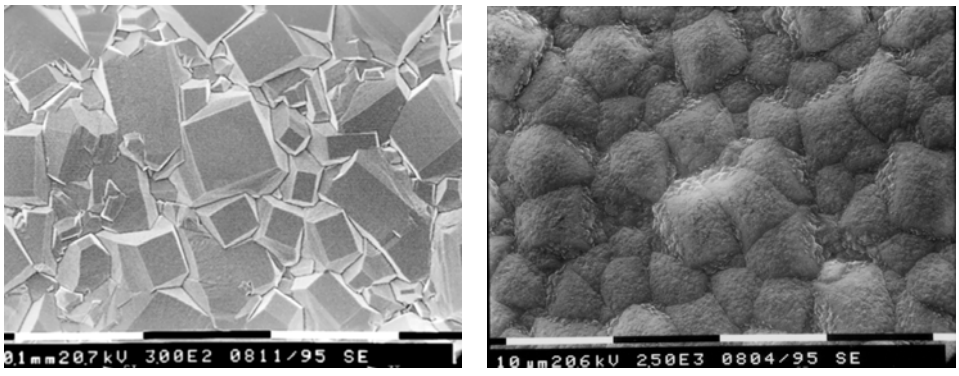

Fig. 6.2 Scanning electron micrographs of the surface morphology of in-situ nitrogen doped films S1, (a), S2 (b). Deposition conditions and N_2 concentration in the gas phase during diamond growth are specified in Table A.2.

The deposition conditions for set V (samples S1 and S2) were varied to find the optimal conditions for the preparation of white transparent films when hexane was used instead of methane as a hydrocarbon source. Upon changing deposition conditions (hexane vapour flow, substrate temperature), the film texture developed in agreement with the observation of Wild et al. [WIL94]. Films showing {111} or {100} morphology could be prepared. Because films are deposited at relatively high pressures, where the best film quality is obtained (films exhibit the lowest subgap optical absorption), we did not

attempt to use the bias-enhanced nucleation, which is performed at lower pressures and which is necessary for a heteroepitaxial "texture-oriented" growth [FOX94].

Under the deposition conditions for {100} textured growth (0.5% C_6H_{14} in H_2) it was difficult to obtain a homogeneous film morphology over a larger deposition area. A temperature gradient of about 20 °C caused a change in film morphology from {100} to the type containing both {100} and {111} facets and numerous twins. Under these conditions, a low N_2 concentration (100 ppm) in the feed gas had a beneficial influence on the film morphology resulting in a reduction of the multiple twinning and stabilisation of the {100} texture. This is in agreement with other investigations reported [CAO97]. Films with thickness of about 20 - 30 µm were white and transparent. If the N_2 concentration was increased from 100 ppm to 1 vol.% or higher (keeping the same conditions as for the best quality samples), the film quality deteriorated. The film morphology became irregular and films became dark brown. It suggests that the N involvement in the surface chemistry can lead to an increased incorporation of π-bonded carbon in the film. Similar conclusions were suggested by Bergmann et al. [BER94] (based on photoluminescence data) and by Jin and Moustakas [JIN94]. The morphology of the as- grown films was imaged by scanning electron microscopy (SEM). Scanning micrographs for samples S1 and S2 are shown in Fig. 6.2.

For the samples of set VI, the effect of nitrogen addition on the film morphology as a function of the nitrogen fraction in the feed gas was investigated by Vandevelde [VAN96]. At a substrate temperature of ± 830 °C, when nitrogen is added to a hydrogen-methane (4.8 %) plasma, the film morphology evolves from a polycrystalline texture without any preferential orientation to a polycrystalline film with a {100} preferential orientation. Nitromethane has a similar effect on the film morphology as nitrogen. At 930 °C (sample NM1), for a hydrogen-methane (3.8 %) with 17 ppm NO_2-CH_3, the films show a polycrystalline morphology with no preferential orientation. By increasing the nitromethane fraction to 86 ppm and to 172 ppm (sample NM2 and NM3), the film texture evolves to a {100} textured film with a strong {100} preferential orientation. The {100} crystals are still inclined with respect to the substrate surface for sample NM2 and are completely parallel to the substrate surface for sample NM3.

6.2.2. Optical absorption: experimental results and discussion

6.2.2.1. Optical absorption in homoepitaxially grown CVD diamond films.

Defect-induced optical absorption in homoepitaxially diamond layers is investigated by means of RT t-PDS (section 3.3). From the measured PDS signal, the optical absorption coefficient α is calculated, using the T-scaling procedure described in section 3.5. The measured spectral dependence of the optical absorption coefficient for these layers is compared with the optical absorption in type IIa natural and type Ib synthetic diamond.

Additionally, we performed transmission and reflection measurements using a Perkin-Elmer Spectrophotometer, equipped with an integrating sphere to determine light scattering losses. For polished IIa and Ib diamond plates the scattering losses were negligible. These losses were also very low for the homoepitaxial {001} diamond film C7. The microfacets developed on the surface of the {110} oriented sample C2 caused light scattering.

The cathodoluminescence measurements were performed at the KUN using a 8200 MK II system for CL topography equipped with a single monochromator system [SCH94].

Optical absorption in natural and HPHT-synthetic diamond

Fig. 6.3 shows a plot of the energy dependence of the optical absorption coefficient α, measured for type Ib HPHT-synthetic diamond and type IIa natural diamond plates.

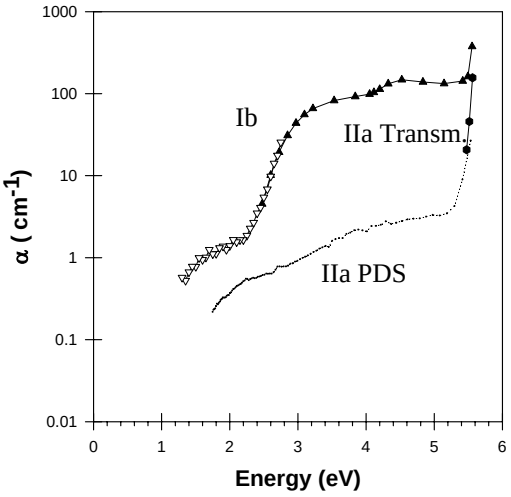

Fig. 6.3 Spectral dependence of the optical absorption coefficient α of type Ib and IIa diamond samples, determined from t-PDS and from optical transmission measurement.

The spectrum of the IIa diamond shows the typical fundamental absorption edge at 5.45 eV. In the case of the type Ib diamond, the observed absorption is higher. At an onset of about 2.2 eV the optical absorption coefficient α starts to rise. At higher energies, two broad bands centred about 3.3 and 4.5 eV are present. At 5.5 eV the fundamental absorption edge of diamond is observed. This spectrum agrees well with the known spectral dependence of the optical absorption coefficient α for type Ib diamond, which is due to the presence of single substitutional N [KOP86], [NAZ87].

The onset of the optical absorption at 2.2 eV was ascribed to the photoionisation of the substitutional N centre [WOO90]. Superimposed on the photoionisation continuum three bands, known as the A (3.3 eV), B (3.9 eV) and C (4.5 eV) bands, were described in literature [KOP86], [NAZ87].

The A and B features are overlapping and for the measurements at RT they are difficult to resolve. These features are probably caused by transitions from the ground state to excited levels of the nitrogen centre [KOP86]. The C band is currently attributed to a vibronic transition [NAZ87]. Low temperature measurements are necessary to resolve the fine structure.

From the value of the optical absorption coefficient at 4.5 eV the concentration of single substitutional nitrogen can be estimated using the conversion factor of Woods et al. and

the relation between the UV (4.5 eV) and IR (1130 cm^{-1}) absorption bands from work of Nazaré et al. [WOO90], [NAZ87]. An optical absorption coefficient α of 1 cm^{-1} at 1130 cm^{-1} corresponds to a N concentration of about 25 ppm and 44 ppm, according to refs. [KHA94] and [NAZ87] respectively. The UV and IR cross sections were compared, leading to the following relation: $\alpha(1130\ cm^{-1}) = 1/45\ \alpha(4.5\ eV)$.

For this Ib sample, the substitutional N concentration is estimated to be about 90 ± 30 ppm. This is in good agreement with the IR measurements using a focused light beam, where values in the range from 50 - 150 ppm were found for different locations at the sample.

A broad feature is observed in the low energy part of the absorption spectrum of type Ib diamond. A similar spectral dependence of α was observed for polycrystalline CVD films (see Chapter 5), where it was ascribed to π-π^* transitions in CVD films. To our knowledge, the presence of π-bonded carbon in Ib diamond was not reported before. The observed absorption feature seems more likely to be caused by the presence of Ni in Ib-HPHT diamond [ENC92].

N-related absorption in homoepitaxial CVD diamond layers

Fig. 6.4 shows the spectral dependence of the optical absorption coefficient α for the flame grown single-crystal diamond layers compared to the optical absorption coefficient for the type Ib diamond plate. The {001} sample C7 shows a continuously increasing subgap absorption, starting at the onset of the measurement at 1 eV and rising up to the fundamental absorption edge. This feature is discussed in section 5.4.

The {110} oriented diamond film C2 also shows the characteristic continuum absorption in the low-energy part of the absorption spectrum. Starting at an onset of 2.2 eV, broad features centred at about 3.3 eV and 4.5 eV are superimposed on the continuum absorption. The shape of the optical absorption coefficient in this spectral region is identical with the one measured for the Ib diamond. After subtraction of the characteristic subgap absorption, using a fitting procedure described in Chapter 5 (section 5.3), an optical absorption coefficient of about 30 cm^{-1} at 4.5 eV is obtained. Using the conversion factors [KOP86], [NAZ87], this coefficient corresponds to a N concentration of about 15 ppm.

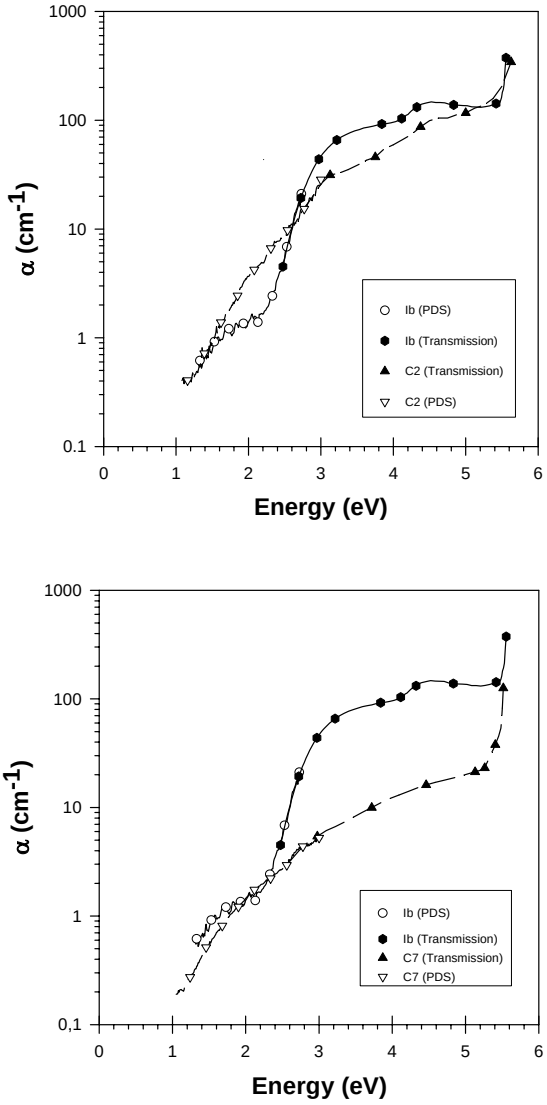

Fig. 6.4 Spectral dependence of the optical absorption coefficient α of the samples C2 (a), and C7 (b) compared with Ib diamond sample. The symbols in the plots correspond only to a fraction of the measured data points.

To our knowledge, this is the first confirmation of substitutional N, obtained from ultraviolet optical absorption measurements, in CVD diamond [MEY96]. Because of the

high mobilities of vacancies at the CVD deposition temperatures, one expected N to be present in CVD diamond in the form of a nitrogen- vacancy (N-V) complex. McNamara et al. [MCN94] demonstrated by IR absorption measurements that single substitutional N can be present in CVD diamond films. No N was found by IR spectroscopy neither in sample C2 nor C7 by Schermer et al. [SCH93]. It should be noted that a concentration of 15 ppm N would correspond to an absorption coefficient of about 0.7 cm^{-1} at 1130 cm^{-1} (absorptance value of $1x10^{-2}$). For the diamond film C2, which shows considerable light scattering in the IR part of the spectra, this value is very close to the IR-spectrophotometer detection limit.

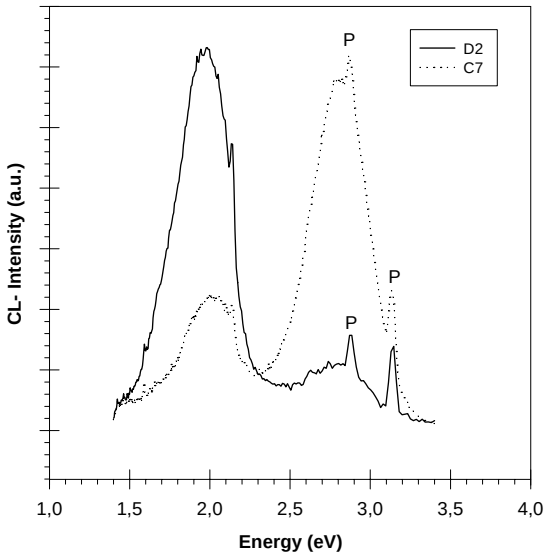

Fig. 6.5 Cathodoluminescence (CL) spectra of the top surfaces of the flame grown homoepitaxial diamond layers C2 and C7. The plasma peaks produced in the CL unit are denoted by P.

The observed differences in nitrogen incorporation in the homoepitaxial films grown on {001} and {110} oriented substrates are in agreement with the CL results, [SCH94], shown in Fig. 6.5. The CL spectrum of the top face of the {110} oriented film C2 revealed the well-known orange-red CL system with a zero phonon line (ZPL) at 2.145 eV, due to the presence of nitrogen-vacancy (N-V) pairs.

However, the top face of sample C7 showed a CL spectrum, dominated by blue band A luminescence which is characteristic for type IIa natural diamond. In addition, a relatively

small signal of the 2.145 eV system was observed for this sample. CL topography revealed that this orange-red system originates from an area with rough, partly curved step bunch patterns. Thus both, the PDS and CL techniques present clear evidence for the incorporation of nitrogen - albeit in different forms - only in the {110} grown film.

The orientation dependent nitrogen incorporation is most readily explained by a difference in the growth mechanism, which depends on the orientation of the seed crystals. The {001} oriented films grow by a layer mechanism via the incorporation of growth units at steps [ENC93]. In this way, the uptake of impurities (e.g. hydrogen or nitrogen) is generally quite low. On the other hand, the {110} surface is fully stepped (see Fig. 6.1(b)) and impurities are relatively easily trapped in the growing diamond film. The local incorporation of nitrogen in the area with rough step bunch patterns on the {001} oriented specimen, as observed by CL-topography [SCH94], is in full agreement with this explanation. In contrast with the smooth macrosteps on {001} aligned along the in-plane <110> directions (see Fig. 6.1(a)), the rough macrostep bunches are curved. Therefore, these macrosteps have a high density of kink sites and the incorporation of impurities becomes more likely than for the smooth step bunches [SCH95].

Continuum absorption in homoepitaxial films

In Chapter 5 has been demonstrated that for polycrystalline diamond samples a characteristic continuum absorption has been observed by means of t-PDS. This feature was ascribed to π-π^* transitions in amorphous carbon regions present in polycrystalline films at grain boundaries. In homoepitaxial diamond layers, the characteristic continuum absorption was expected to be significantly reduced. However, π-bonded carbon can readily occur at the surface of a crystal due to surface relaxations and reconstructions or even due to surface absorbates. Here, the surface roughness caused by step bunching on the surface of the {001} oriented layer and due to microfacets on the {100} oriented diamond layer might enhance these effects significantly.

6.2.2.2. Optical absorption in N-doped heteroepitaxially grown CVD diamond films at IMO.

The spectral dependence of the optical absorption coefficient α for sample S1 (100 ppm N_2 in the H_2 feed gas) measured by PDS in the range 1.0 - 3.3 eV and by optical

transmission in the range 3.0 – 6.0 eV, is plotted in Fig. 6.6. The optical absorption coefficient α for a polished type Ib De Beers diamond plate is shown for comparison (see Table A.8). The spectrum of this Ib diamond is already discussed in section 6.2.2.1.

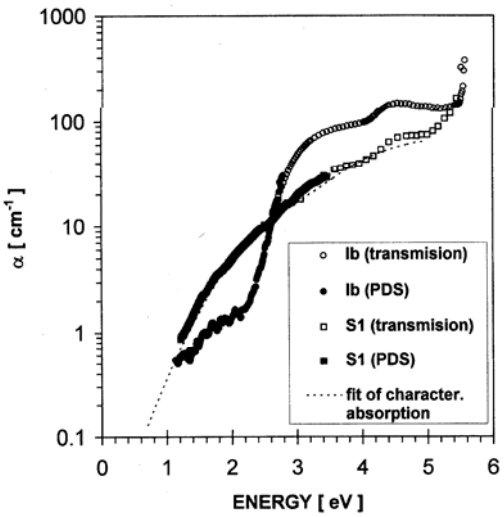

Fig. 6.6 The spectral dependence of the optical absorption coefficient α of the sample S1, doped with 100 ppm N_2 in the gas phase. For comparison, the optical absorption coefficient α of Ib diamond is also plotted.

It can be seen from Fig. 6.6 that α for sample S1 exhibits a spectral dependence similar to that for Ib diamond. This absorption is superimposed on the characteristic subgap absorption of CVD diamond films, due to the presence of π-bonded carbon. UV absorption due to single substitutional N has not been reported for CVD diamond films so far, but the presence of N in single substitutional position was found in CVD diamond by IR spectroscopy [MCN94]. Our accompanying PDS study of N in homoepitaxial diamonds shows the incorporation of N atoms on substitutional positions in the samples for which the 575 nm orange band cathodoluminescence associated with N-V pairs was measured.

From our PDS results, after subtraction of the characteristic CVD diamond subgap absorption (see Chapter 5), the value for the optical absorption coefficient at 4.5 eV is found to be about 10 ± 5 cm^{-1} (given by the precision of our fit of the background characteristic subgap absorption). The value of the absorption coefficient α at 4.5 eV

implies a concentration of about 10 ppm of N in substitutional position. SIMS analyses of sample S1 shows that about 80 ppm N (and 500 ppm H and 100 ppm O) is incorporated in the bulk of this film. This result is confirmed by EPR measurements. If all N atoms were on substitutional positions, this would correspond to a value of about 2 to 4 cm^{-1} for the optical absorption coefficient for the N-vibrational mode at 1130 cm^{-1} [KHA94], [NAZ87]. At such low active N concentrations, it was not possible to detect a N-related vibrational absorption band at 1130 cm^{-1} by FTIR measurements (masked by optical scattering).

When the N doping level was increased from 100 ppm to 1 vol.% in the H_2 feed gas, the PDS spectra showed a higher absorption coefficient in all spectral regions investigated (not shown here). The absorption spectra closely resembled our measurements for nanocrystalline diamond films containing a large amount of amorphous carbon (see Chapter 5). This points to a change in film quality, morphology and colour and to the earlier suggestion that N participates in the surface chemistry and its presence in higher concentrations can lead to an increased incorporation of π-bonded carbon in the film.

N-doping from nitromethane

The PDS optical absorption spectra for films prepared with N_2 and CH_3-NO_2 are given in Fig. 6.7 and Fig. 6.8. Because of high absorption causing already saturation at 2 eV in samples N3, N4 and NM3, only samples N1, N2, NM1 and NM2 are shown. The spectral dependence of the optical absorption coefficient α is calculated from Eq. (3.24) whereby the saturation values obtained for the respective samples are used for S_{sat}. The spectra are dominated by a-C absorption. Several bands and peaks are superimposed on this continuum absorption.

The films N1 and N2 show absorption spectra as expected for single substitutional N, with an absorption threshold at about 2.2 eV. EPR investigations confirmed that part of the N-atoms is in a single substitutional position, similar as in Ib diamond, with its characteristic resonance g = 2.0024 [REM97]. At about 1.68 eV a sharp peak, which probably can be dedicated to a Si-V centre feature, is present in sample N1 [MAI99]. The absorption at 2.145 eV can be caused by N-V complexes which have an absorption threshold at 2.145 eV [WAL79].

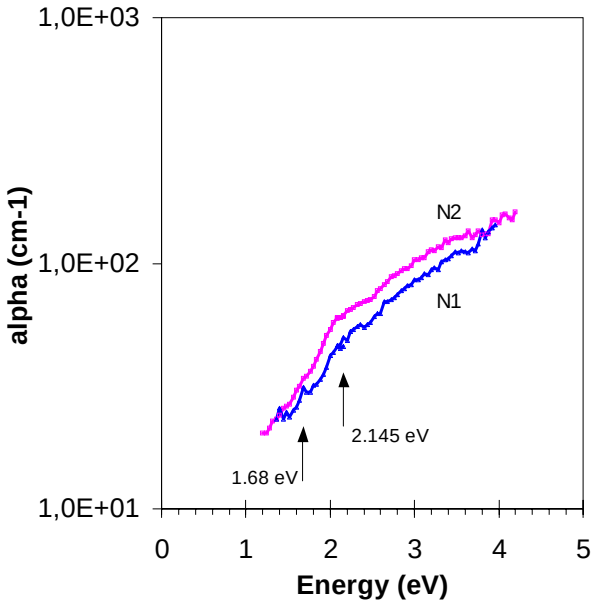

Fig. 6.7 Optical absorption spectra obtained by PDS of diamond films prepared with N2 addition. Arrows show the 1.68 eV and 2.145 eV features .

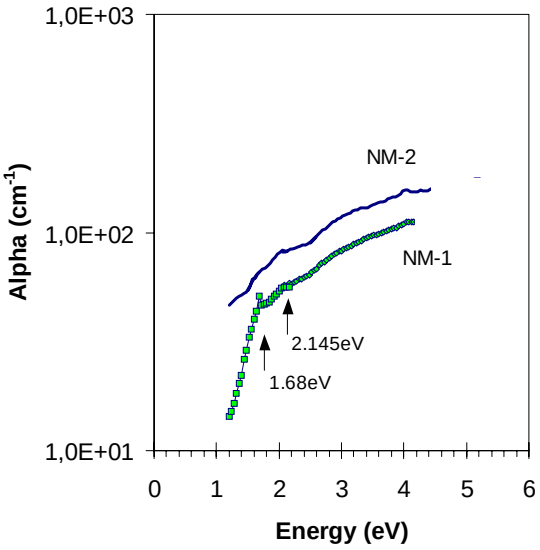

Fig. 6.8 Optical absorption spectra obtained by PDS of diamond films prepared with N_2-CH_3 addition. Arrows show the 1.68 eV defect and the 2.145 eV defect .

The nitromethane (NM) sample set indicates a similar type of absorption as the films prepared with nitrogen. The difference with N_2 is that a similar value of the optical absorption coefficient α is reached for much lower N atom concentrations in the plasma. Furthermore, sample NM1 shows a very steep increase in absorption below 1.6 eV. From Fig. 6.8, it can be established that at also for samples grown with nitromethane at about 1.68 eV a sharp feature is present [MAI99]. This feature appears systematically in all the samples prepared in similar conditions as sample NM1 and especially when O_2 is added to the plasma. A detailed optical absorption investigation of this feature is observed by various groups in photoluminescence (PL) [BER94], [GOR95] as well as in EPR.

A first start is made, but further investigations are necessary to explain all the observed absorption features in the spectra of the N-doped diamond films.

6.3. n-Type doping

6.3.1. Lithium doped CVD diamond films

Several attempts (in-diffusion, ion-implantation, in-situ doping) to dope diamond films did not lead to active Li-doping [VAV80], [PRA93], [BOR95], [POP96], [NIJ97]. In 1995, the group at IMO attempted to grow Li-doped CVD diamond films which should show some electrical activity. The preliminary results of these investigations are presented in this section. We demonstrated that Li is incorporated in the diamond films but no successful electrical properties were obtained. Recently, Sternschulte et al. used the MW PECVD technique to grow Li-doped diamond films on two types of substrates: on single crystal diamonds and on coplanar heteroepitaxial grown CVD diamond films on Si [STE99b].

6.3.1.1. Sample description

Polycrystalline Li-doped CVD diamond films were prepared at IMO in an ASTeX PDS17 MW deposition system, and are described in appendix A.1 (Table A.4). The diamond films were heteroepitaxially grown on Si substrates. The deposition conditions were as follows: pressure 10^4 Pa, microwave power 3500 W and substrate temperature 800 ± 15 °C.

In this thesis, we used hexane (C_6H_{14}) as the hydrocarbon source during the Li-doping

experiments. Hexane contains six times more carbon atoms per molecule than methane (CH_4), which has been used in the other deposition experiments. Therefore, a set of experiments was performed to optimise the film quality before starting the doping. C_6H_{14} was chosen because the Li-doping experiments are performed using a 2.5 mol l^{-1} solution of butyllithium (C_4H_9Li) in hexane. In the C_4H_9Li compound, Li is bonded to a carbon atom. Therefore, we expected Li to be incorporated easier in the deposited diamond films. The (undoped reference) sample, which was prepared using 0.5 vol. % C_6H_{14} in the H_2 feed gas, is further denoted as L1.

The C_4H_9Li + C_6H_{14} mixture (250 g) was enclosed under an Ar atmosphere in a stainless steel cylinder, which was connected to the deposition chamber via a MKS flow meter. The pressure in the deposition chamber was maintained at 10^4 Pa. The content of the Li precursor-containing vapour in the H_2 feed gas (250 sccm) was varied in the range of 0.25 to 2.5 vol.% (samples L2: 0.25 vol.%, L3: 0.5 vol.%, L4: 1 vol.%, L5: 2.5 vol.%, see Table A.4 Appendix A.1). The other conditions were kept the same. The amount of Li incorporated in the diamond film during the deposition was dependent on the deposition conditions and was measured by SIMS (see further 6.3.1.3).

The deposition rate was very weakly dependent on the relative vapour flow, changing from 1 µm/hour for sample L2 (0.25% of the vapour flow) to about 1.5 µm/hour for sample L5 (2.5% of the vapour flow). All samples had a thickness varying inbetween 17 µm and 23 µm.

To investigate the Li incorporation at lower substrate temperatures, the sample L6 was prepared at identical conditions as the sample L3 but the substrate temperature was reduced to 500 °C and 0.3 vol.% of O_2 was added to the H_2 feed gas to maintain the quality of the diamond. In this case, the deposition rate dropped to 0.5 µm/h.

6.3.1.2. Influence of Li on the film morphology

Films prepared from the 2.5 molar solution of C_4H_9Li in C_6H_{14}, using a vapour flow in the range from 0.25 to 1 vol.% in the H_2 feed gas (samples L2-L4), were all white and transparent. An increase in the concentration of the vapour flow to 2.5 vol.% in the H_2 feed gas led to the deposition of brownish films (sample L5). The morphologies of the deposited films are shown in Fig. 6.9. It is interesting to note that, despite the different carbon concentration in the gas phase, the film morphologies of all deposited Li-doped films were very similar, much multiple twinning with only the grain sizes differing.

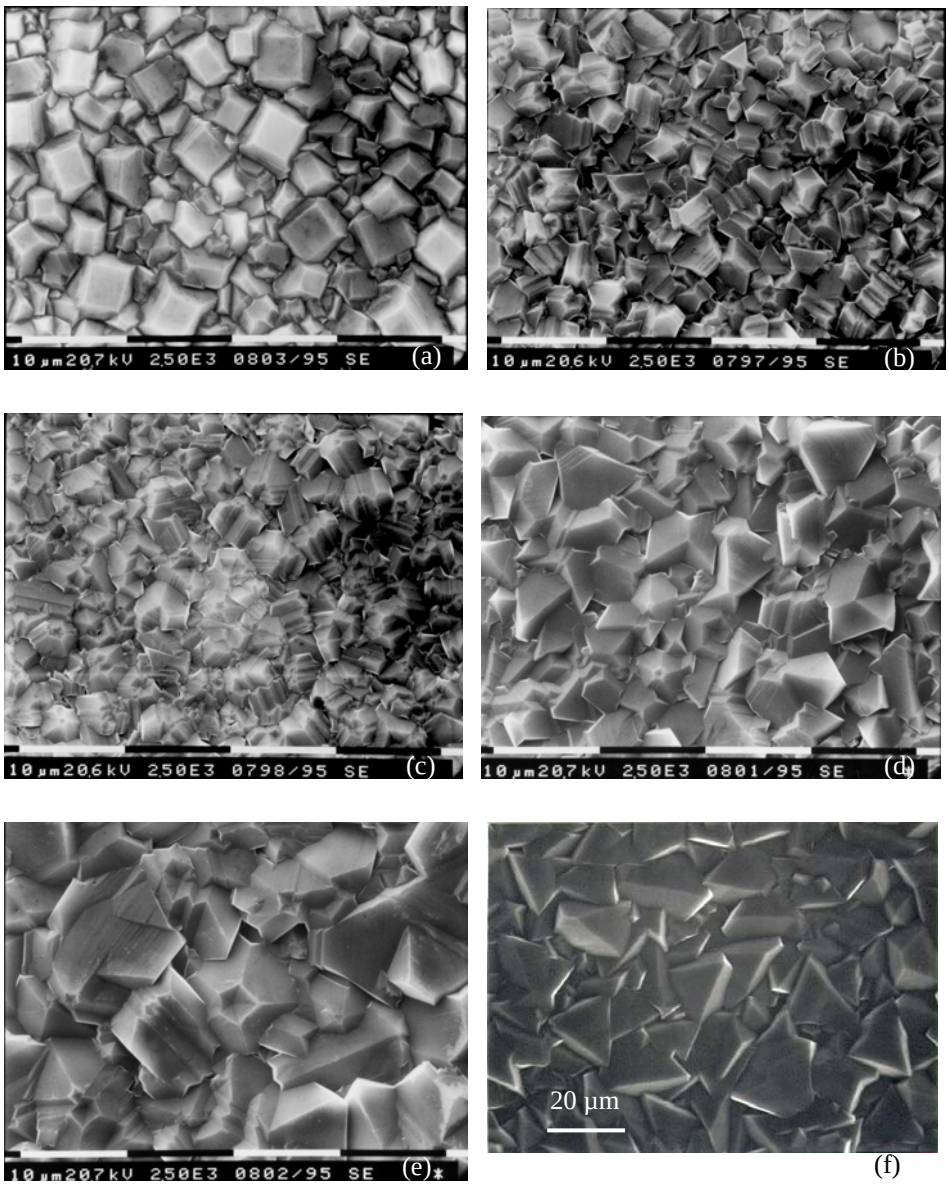

Fig. 6.9 Scanning electron micrographs of the surface morphology undoped (L1) and in-situ Li doped films (L2-L5) upon increasing the relative flow of hexane vapour with Li-containing organometallic precursor in the H_2 feed gas. L1: undoped (a), L2: 0.25 % (b), L3: 0.5 % (c), L4: 1 % (d), L5 2.5 % (e), L6 (f). Deposition conditions are specified in section 6.3.1.

The grain sizes slightly increase for increasing Li-precursor gas concentrations. Sample L6, prepared under the same Li concentrations as sample L3 but at a lower temperature, shows a slightly larger grain size. The morphology of the {100} film (sample L1), prepared using 0.5 vol.% pure hexane vapour in the H_2 feed gas, is shown in Fig. 6.9a.

6.3.1.3. Secundary Ion Mass Spectrometry (SIMS) measurements

SIMS depth profiling (from the top diamond surface) was carried out on diamond films before removing them from the Si substrates. The bottom sides of the free-standing diamond films were also investigated by means of SIMS.

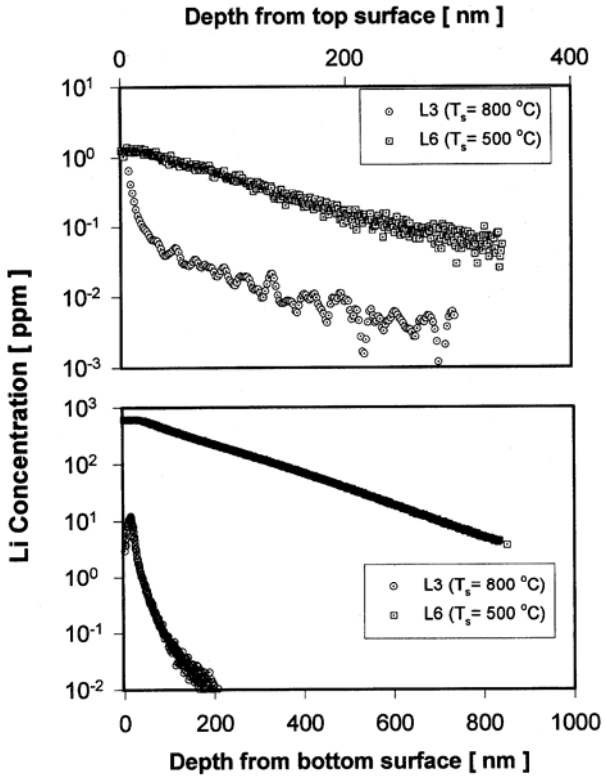

Fig. 6.10 SIMS depth profile of Li-doped film L3 and L6, using 10 kV O_2^+ beam for Li^+ detection (different depth-scales for bottom and top surface).

The concentrations of incorporated Li atoms were studied by SIMS, using a CAMECA ims5f instrument. The depth profiling (400 – 1000 nm) was performed using O_2^+ primary

beam for Li^+ detection. The initial energy of the primary beam was 10 keV. The sample was polarised at +4500 V for the detection of positive secondary ions. To prevent charging, the sample was coated with a thin Au layer. The SIMS measurements confirmed the presence of Li in the diamond films. The SIMS profiles for samples L3 and L6 are shown in Fig. 6.10. The absolute impurity concentrations were calculated by the procedure described in [WIL89], using the SIMS sensitivity factors from [SMI92].

SIMS depth profiles of sample L3 and L6 are shown in Fig. 6.10. The SIMS profiles confirm that Li is present in the film, but the concentration of Li decreases from the top diamond surface to a sub-ppm level at a depth of 250 nm. This decrease could be due to out-diffusion of Li. Theoretical studies predict 0.85 eV for the activation energy for Li diffusion and a high mobility of Li-atoms [KAJ93]. But up till now, no consensus exist about Li-diffusion in diamond. Some papers report about existing Li-diffusion and others claim there is no diffusion [OKU90], [NIJ97], [POP96], [POP95], [CYT94]. A reduction of the substrate temperature to 500 °C during the diamond deposition (sample L6) led to an increased concentration of Li in the film (keeping the same Li-doping level in the feed gas). If one assumes that Li diffuses in diamond, this can be explained by the fact that at elevated temperatures the Li diffusing process is faster and, consequently, a lower amount of Li is detected in the film. Similar results were obtained by Sternschulte et al. [STE99b]: reduction of the substrate temperature from 800 °C to 620 °C led to an increase of Li in the film from 8 ppm to 71 ppm as detected by elastic recoil detection (ERD).

Surprisingly, the SIMS depth profile study made from the bottom of our diamond films shows a significantly higher concentration. This could be an indication for a favourable incorporation of Li at the grain boundaries, which are present in higher amounts at the substrate side. To obtain more detailed information about the Li incorporation ratio and to clear out the fast decreases of the Li-concentration with depth, a more extended study of Li depth profiles in CVD diamond should be carried out.

6.3.1.4. Optical absorption in Li -doped films.

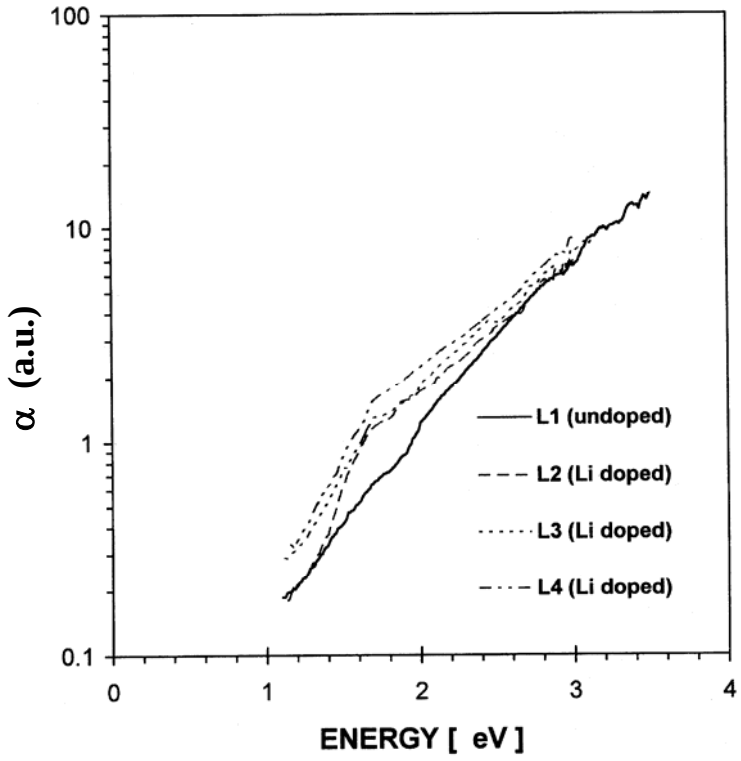

Fig. 6.11 The optical absorption of the undoped film L1 and Li doped films L2-L4. The inset shows the fit of the characteristic optical absorption for an undoped diamond film on which the calculated optical absorption coefficient α is plotted, using the dependence for the photoionisation cross section of deep impurities from ref. [INK81].

The t-PDS arrangement, described in section 3.3, was used to study the defect-induced optical absorption in the Li-doped films in the energy range of 1.0 eV to 3.6 eV. Room temperature t-PDS measurements were performed on free-standing Li-doped diamond samples with a halogen lamp as light source (pump beam), using CCl_4 as the deflection medium. Scaling of the absorption spectra was based on a comparison of the PDS spectrum of the undoped sample L1 with the PDS spectra of undoped CVD diamond films grown under similar conditions, measured over a broader energy range and scaled

with the saturation value S_{sat} (see section 3.5). The PDS measurements of the Li-doped diamond films were scaled relatively to sample L1. Nevertheless, the energy dependence and, consequently, the position of absorption features are not influenced by this procedure.

The energy dependencies of the optical absorption coefficients α of samples L1-L4 are plotted in Fig. 6.11 .

It is interesting to note that in the near-IR region, at about 1.5 – 1.6 eV, a new absorption structure starts to evolve when the concentration of the Li precursor in the feed gas is increased. The intensity of the absorption band at about 1.5 – 1.6 eV is proportional to the amount of Li added to the feed gas. Therefore, we expect this feature to be a Li-related defect, but a complete picture of the electronic structure of this defect is not clear yet. The defect level at an energy 1.5-1.6 eV does not agree with the theoretical predictions of Kajihara et al., which suggest a shallow donor level (0.1 eV [KAJ91]).

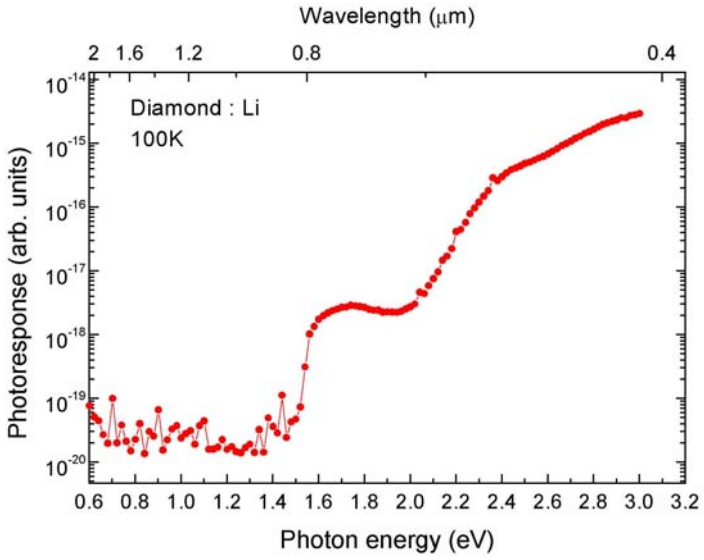

Fig. 6.12 Low temperature photocurrent measurement on a homoepitaxial Li-doped CVD diamond film (200 nm thick) (data taking from [ZEI99]).

Very recently, photocurrent spectra were recorded on homoepitaxially grown Li-doped CVD diamond samples [STE99b] by the group at TU Muenchen [ZEI99]. Fig. 6.12 shows a low temperature photocurrent measurement on a homoepitaxial Li-doped CVD

diamond film (200 nm thick, Ib substrate, total lithium content 25 ppm). The spectrum was recorded at 100K after annealing the sample at 400K. An absorption band at 1.5 eV is detected. At RT there is no difference in photoconductivity in the region around 1.5 eV. Zeisel et al. did not see a clear correlation between photoconductivity and lithium content [ZEI99]. However, a bare type Ib crystal does not show this photoconductivity at 1.5 eV. The results of Zeisel et al. [ZEI99] agree very well with the absorption spectra we measured by PDS. Up till now, it is not clear if this defect scales to the conduction band or valence band.

A close look to the absorption spectra shows that the small peak superimposed on the 1.5 - 1.6 eV band is probably the Si-V peak situated at 1.68 eV. A lot of work has to be done to discover the origin and structure of the defect responsible for the 1.5-1.6 eV absorption band. The possibility of the involvement of a vacancy in this defect centre has to be investigated. The influence of H on the Li-incorporation and on the presence of this defect has to be considered.

The successful incorporation of Li in the diamond film as follows from SIMS measurements together with a possibly Li-related absorption peak in the PDS absorption data, does not imply electrical active Li-related defect levels in the gap. Hall effect measurements should be performed to prove n-type conductivity. Samples were highly resistive.

6.3.2. Phosphorus doped diamond layers

As already mentioned, in 1997, researchers from NIRIM were the first to successfully prepare phosphorus doped CVD diamond films [KOI97]. Confirmation of the n-type conductivity was obtained by Hall effect measurements, giving an activation energy E_a of the charge carriers of about 0.55eV to 0.60 eV [KOI97], [KOI98], [KOI99]. However, still little is known about the way phosphorus is incorporated in the films and about the electronic structure of the P-related level. We studied the optical absorption and the electronic structure of this phosphorus-related level in P-doped CVD diamond films prepared at NIRIM. In this section we present preliminary RT t-PDS data.

6.3.2.1. Sample Description

The phosphorus doped diamond thin films were fabricated in NIRIM (Tsukuba, Japan), using MW PECVD. The used deposition system is described in detail in [KOI97]. The

CVD diamond films are homoepitaxially grown on type Ib {111} substrates. A phosphine source is used as dopant gas. Table A.7 (see Appendix A.1) summarises the deposition conditions and physical properties of the samples investigated by means of RT t-PDS. The thickness of the P-doped layers (P2 and P3) was limited to 1.5 µm. The P-doped samples were highly resistive and the mobilities were not measurable.

6.3.2.2. PDS measurements

The PDS spectra for samples P2 and P3 are presented in Fig. 6.13. The spectral dependence of the optical absorption coefficient shows several absorption bands. First of all, a broad absorption band, very pronounced for sample P2, arises at about 0.55 - 0.60 eV. A next band is located around 1.35 - 1.40 eV. Finally, above 2.0 eV, the typical type Ib (substrate-) absorption, due to substitutional N, dominates the optical absorption spectrum.

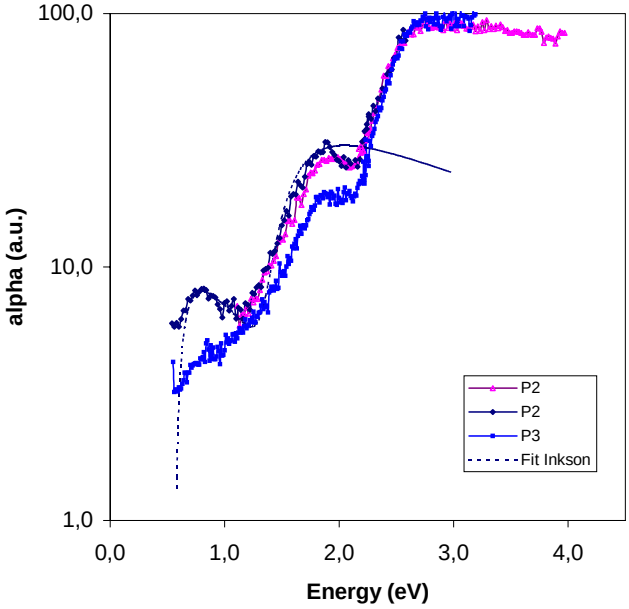

Fig. 6.13 Spectral dependence of the optical absorption coefficient of samples P2 and P3 as measured by means of t-PDS measurements.

We tried to fit the spectral dependence of the optical absorption coefficient α, using the Inkson model, a model of photoionisation cross section for deep impurities in crystalline

semiconductors [INK81]. The resulting fit is plotted in Fig. 6.13 (dotted line) and yields respectively ionisation energies of 0.56 ± 0.03 eV and 1.35 ± 0.03 eV for both defect related absorption bands. The level at 0.56 eV agrees very well with the activation energy for the phosphorus defect as measured by Hall-measurements. CPM measurements suggested an optical excitation energy of 0.56 ± 0.03 eV for the P-related level [HAE99]. Based on cathodoluminescence studies, Sternschulte et al. [STE99c] estimated an ionisation energy of 630 ± 50 meV for the phosphorus donor. The origin of the second band is still unclear. One of the possibilities is that this band is related to the 1.5 eV band also seen in the Li-doped samples.

Although PDS optical absorption spectra give a first indication about the position of the defect-level in the forbidden gap, additional information is necessary for an exact defect characterisation.

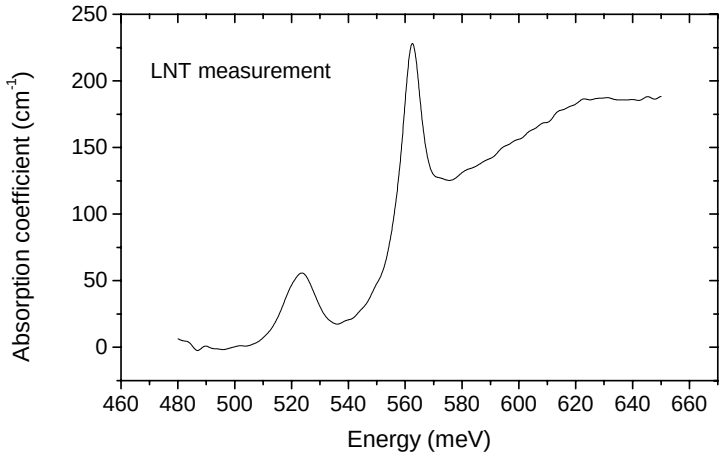

Fig. 6.14 Absorption coefficient α (cm^{-1}) from a typically P-doped sample measured with FTIR at LNT. Two peaks are clearly visible, one at 523 meV, the other at 562 meV (data taken from [GHE99]).

Independently, liquid nitrogen temperature (LNT) fourier transform infrared spectroscopy (FTIR) measurements were performed on the P-doped samples by Gheeraert [GHE99]. A typical optical absorption spectrum (α(E)) recorded at LNT representative for P-doped samples with 500-1000 ppm phosphine, is shown in Fig. 6.14. A continuum of absorption is observed together with two distinct peaks. The onset of the

photoionisation continuum is about the same level as in our measurements. The positions of these narrow peaks are 523 meV and 562 meV. As they are located on the rising edge of the photoionisation, the peaks are attributed to the electronic transitions from the bound electron ground level to the first and second excited states.

Therefore, it is very likely that several absorption peaks are involved in the broad band absorption as measured by t-PDS. To see the fine structure of the absorption spectra and to resolve the different optical transitions involved, low temperature t-PDS measurements should be performed yielding higher resolution (narrower bands) spectra.

Thus the results in Fig. 6.13 shows for the first time optical activity of P in CVD diamond films using the t-PDS technique.

6.4. Conclusions

This chapter presents the first PDS measurements of doped CVD diamond films.

Both homoepitaxial flame grown CVD diamond films and MWPE CVD diamond films have been studied by means of t-PDS. For the first time, the presence of substitutional nitrogen in CVD diamond films was clearly demonstrated. Substitutional nitrogen is a deep donor with an optical activation energy of 2.2 eV. Using the conversion factors from Woods et al. and Nazaré et al. the N concentrations present in the investigated samples could be estimated.

The spectral dependence of the optical absorption coefficient in homoepitaxial N-doped diamond films was investigated and compared to the spectra of type Ib and IIa diamond. The diamond film deposited on {110} oriented substrate exhibited a similar spectral behaviour of the optical absorption as type Ib diamond. For the layer deposited on {001} oriented substrate, no N-related absorption could be detected. The results on the orientation dependent nitrogen incorporation are in good agreement with the cathodoluminescence data. Further, all these N-doped CVD samples exhibited a characteristic continuum subgap absorption, which was absent in type IIa diamond. The continuum absorption was very similar to that observed for high quality polycrystalline diamond films, where it was attributed to π-π^* transitions due to the presence of a-C and graphite (Chapter 5). In the investigated homoepitaxial diamond single crystals, step bunches on the {001} oriented layer and microfacets on the {110} oriented layer might provide sites for an a-C phase at the surface.

N-doped polycrystalline CVD diamond films were in-situ doped by using nitrogen or nitromethane containing precursors. The N-doped sample, which was prepared with 100 ppm N_2 in the gas phase, showed the same spectral dependence of the optical absorption coefficient as Ib diamond, suggesting the presence of N in a substitutional position. The optical absorption spectra of N-doped diamond films by means of nitrogen and nitromethane were compared. PDS measurements suggested that the optical absorption spectra of such films are related to substitutional nitrogen.

Li-doped CVD diamond films were grown by adding C_9H_4Li in hexane to the precursor gases. SIMS measurements confirmed the presence of Li in the films. A new defect band at about 1.5-1.6 eV has been detected by t-PDS. The same band has independently been measured by PC on Li-doped samples of a different source. Nevertheless, up till now, the origin of this band is unclear. Further work is required to identify this defect band.

Finally, the first results of t-PDS measurements on P-doped diamond films, which were grown at NIRIM by using phosphine, are presented. The absorption spectra show three absorption bands. The defect structure at 0.56 eV is dedicated to the P-level. This value agrees very well with the results obtained by other characterisation methods. A second absorption band with a photoionisation energy of about 1.35 eV is observed but up till now, the origin of this band is unknown. The absorption band at higher energies is due to the substrate absorption. Still a lot of work has to been done to clarify the electronic structure of the phosphorus defect.

6.5. References

[ALE92] A.E. Alexenko and B.V. Spitsyn, Diamond Relat. Mater. **1** (1992) 705.

[AND93] .B. Anderson, S.P. Mehandru, Phys. Rev. B **48** (1993) 4423.

[BER94] L. Bergmann, M.T. McClure, J.T. Glass, and R.J. Nemanich, J. Appl. Phys. **76** (1994), 3020-3027.

[BOH95] S. Bohr, R. Haubner, B. Lux, Diamond Relat. Mater. **4** (1995) 133.

[BOR95] T.H. Borst, O. Weis, Diamond Relat. Mater. **4** (1995) 948.

[BRA83] G. Braunstein, R. Kalish, J. Appl. Phys. **54** (1983) 2106.

[BRI93] P.R. Briddon, R. Jones, Physica B **185** (1993) 179 -189.

[BRO55] J.J. Brophy, Phys. Rev. **99** (1955) 1336.

[BUR90] R. C. Burns, V. Cvetkovic, C. N. Dodge, D. J. F. Evans, M. -L. T. Rooney, P. M.Spear and C. M. Welbourn, J. Cryst. Growth, **104** (1990) 257.

[CAO97] G.Z.Cao, J.J. Schermer, W.J.P van Encenvort, W.W.L.M. Elst and L.J. Gilling, to be published in J.Cryst.Growth (1997).

[CHR73] R.M. Chrenko, Phys. Rev. B **7** (1973) 4560.

[CLA79] C.D. Clark, E.W.J. Mitchel, and B.J. Parsons, in Properties of Diamond, edited by J.E.Field, Academic Press, (1979) 22-78.

[COL71] A.T. Collins, A.W.S. Williams, J. Phys. C. Solid St. Phys. **4** (1971) 1789.

[COL91] A.T. Collins, MRS conference proceedings (1991) 659.

[COL92] A.T. Collins, Diamond Relat. Mater. **1** (1992) 457.

[CYT94] C. Cytermann et al. Diamond Relat. Mater. 3 (1994) 677

[DAV77] G. Davies, Chem. Phys. Carbon, **13** (1977) 1.

[DAV92] G. Davies, S.C. Lawson, A.T. Collins, A. Mainwood, S.J. Sharp, Phys. Rev. B, **46** (1992) 13157-13170.

[DAV93] G. Davies, A.T. Collins, Diamond Relat. Mater. **2** (1993) 80-86.

[DAV94] G. Davies, Materials Science Forum, **143-147** (1994) 21-28.

[ENC92] W.J.P. van Enckenvort, E.H. Versteegen, J. Phys. C: Sol. St. Phys, **4** (1992), 2361-2373, W. J. P. van Enckevort and E. H. Versteegen, J. Phys.: Condens. Matter, **4** (1992) 2361.

[ENC93]W. J. P. van Enckevort, G. Janssen, W. Vollenberg, J. J. Schermer and L. J. Gilling, Diamond Relat. Mat., **2** (1993) 997.

[FAR69] R.G. Farrer, Solid State Comm. **7** (1969) 685.

[FOX94] B.A. Fox, B.R. Stoner, D.M. Malta and P.J. Ellis, R.C. Glass, F.R. Sivazlian, Diamond Related Materials, **3** (1994), 382-387.

[FUJ86] N. Fujimori, T. Imai, and A. Doi, Vacuum **36** (1986), 99.

[GHE99] E. Gheeraert, S. Koizumi, T. Teraji, K. Kanda, M. Nesladek, presented at Diamond '99, 12-17 September 1999, Prague.

[GOR95] A.A. Gorokhovsky, A.V. Tutukhin, R.R. Alfano, W. Philips, Appl. Phys. Lett. **66** (1995) 43.

[GRA96] C.F.O. Graeff, E. Rohrer, C.E. Nebel, M. Stutzmann, H. Guttler, R. Zachai, J. Appl. Phys. **69** (1996) 3215.

[HAE99] K. Haenen, K. Meykens, M. Nesladek, G. Knuyt, C. Quaeyhaegens, L.M. Stals, S. Koizumi, E. Gheeraert, Phys. Stat. Sol.(a) **174** (3) (1999) 53-58.

[HUG62] C.M. Huggins, P. Cannon, Nature **194** (1962) 829.

[INK81] J.C. Inkson, J.Phys.C: Solid State Physics, **14** (1981), 10093-1101.

[JAC90] K. Jackson, M.R. Pederson, J.G. Harrison, Phys. Rev. B **41** (1990) 12641.

[JIN94] S. Jin and T.D. Moustakas, Appl. Phys. Lett **65** (1994), 403-405.

[KAJ91] S.A. Kajihara, A. Antonelli, J. Bernholc, R. Car, Phys. Rev. Lett. **66** (1991) 2010.

[KAJ93] S.A. Kajihara, A. Antonelli and J. Bernholc, Physica B 185(1993), 144-149.

[KAL00] R. Kalish, A. Reznik, C. Uzan-Saguy, C. Cytermann, Appl. Phys. Lett. **76** (2000) 757-759.

[KAM91] M. Kamo, H. Yurimoto, T. Ando, Y. Sato, Proc. 2nd Internat. Conf. New Diamond Science and Technology, Eds. R. Messier, J.T. Glass, J.E. Butler, and R. Roy, Materials Research Society, Pittsburgh (1991) 637.

[KHA94] I. Khawi. A.E. Mayer, P.M. Spear, J.A. Van Wyk, G.S. Woods, Phil. Mag. B, **69** (1994), 1141-1147.

[KOP86] J. Koppitz, O.F. Schirmer and M. Seal, J. Phys. C: Sol. St. Phys, **19** (1986), 1123-1133.

[KOI97] S. Koizumi, M. Kamo, and Y. Sato, H. Ozaki and T. Inuzuka, Appl. Phys. Lett. **71** (1997), 1065.

[KOI98] S. Koizumi, M. Kamo, Y. Sato, S. Mita, A Sawabe, A. Reznik, C. Uzan-Saguy, R. Kalish, Diamond Relat. Mater. **7** (1998) 540.

[KOI99] S. Koizumi, Phys. Stat. Sol. (a) **172** (1999) 71

[MAI94] A. Mainwood, Phys. Rev. B **49** (1994) 7934-7940.

[MAI99] A.Mainwood, Phys. Stat. Sol. (a) ***172*** **(**1999) 25-35

[MCN94] K.M. McNamara, B.E.Williams, K.K. Gleason and B.E.Scruggs, J. Appl. Phys., **76** (1994), 2466-2472.

[MEY96] K. Meykens, M. Nesladek, C. Quaeyhaegens, L.M. Stals, M. Vanecek, J. Rosa, J.J. Schermer, G.Janssen, Diamond Relat. Mater. **5** (1996) 958-963.

[MOR89] J. Mort, D. Kuhman, M. Machonkin, M. Morgan, F. Jansen, K. Okumura, Y. M. LeGrice and R.J. Nemanich, Appl. Phys. Lett. **55** (11) (1989), 1121-1123.

[NAZ87] M.H V. Nazare and A.J.T des Neves, J.Phys. C, **20** (1987), 2731-2722.

[NES96] M. Nesladek, K. Meykens, and L.M. Stals, M. Vanecek and J. Rosa, Phys. Rev. B 54 (1996) 5552.

[NIJ97] J. te Nijenhuis, G.Z. Cao, P.C.H.J. Smits, W.J.P. van Enckevort, L.J. Gilling, P.F.A. Alkemade, M. Nesladek, Z. Remes, Diamond Relat. Mater. **6** (1997) 1726-1732.

[OKA90] K. Okano, H. Kiyota, T. Iwasaki, Y. Nakamura, Y. Akiba, T. Kurosu, M. Iida and T. Nakamura, Appl. Phys. A **51** (1990) 334.

[OKU90]K. Okumura, J. Mort, M. Machonkin, Appl. Phys. Lett. **57** (1990) 1907.

[POP95] G. Popovici et al. J. Appl. Phys. 77 (1995) 5103

[POP96] G. Popovici et al. Thin Solid Films 279 (1996) 93

[PRI95] J.F. Prins, Diamond Relat. Mater. **4** (1995) 580-585.

[REM97] Z. Remes, V. Vorlicek, J. Pangrac, J. Rosa, M. Vanecek, M. Nesladek, K. Meykens, C. Quaeyhaegens, L.M. Stals, presented at the Diamond 1997 Conference, Edingburgh, Scotland.

[ROH96] E. Rohrer, C.F.O. Graeff, R. Janssen, C.E. Nebel and M. Stutzmann, Phys. Rev. B, **54** (1996) 7874.

[SCH93] J. J. Schermer, J. E. M. Hogenkamp, G. C. J. Otter, G. Janssen, W. J. P. van Enckevort and L. J. Giling, Diamond Relat. Mater., **2** (1993) 1149.

[SCH94] J. J. Schermer, W. J. P. van Enckevort and L. J. Gilling, Diamond Relat. Mater., **3** (1994) 408.

[SCH95] J. J. Schermer, F. K. de Theije and L.J. Giling, presented at the Diamond films

'95 conference, Barcelona, 10-15 september 1995.

[SMI92] S.P. Smith, M.I. Landstrass and R.G. Wilson, in SIMS VIII, ed. A. Benninghoven, K.T.F. Janssen, J. Tumpfner and H.M. Werner, Wiley, 1992, 159.

[STE99a] H. Sternschulte , *'Lumineszenzuntersuchungen an dotiertem Diamant'*, PhD thesis (1999).

[STE99b] H. Sternschulte, M. Schreck, B. Stritzker, A. Bergmaier, G. Dollinger, presented at Diamond 99, Prague, Czech Republic (1999).

[STE99c] H. Sternschulte, K. Thonke, R. Sauer, S. Koizumi, Phys. Rev. B **59**/20 (1999) 12924

[VAN98] T. Vandevelde, M. Nesladek, K. Meykens, C. Quaeyhaegens, L.M. Stals, I. Gouzmann, A. Hoffman, Diamond Relat. Mater. **7** (1998) 152.

[VAV80] V.S. Vavilov, A.A. Gippius, A.M. Zaitev, B.V. Deryagin, B.V. Spitsyn, A.E. Aleksenko, Sov. Phys. Semicond. **14** (1980) 1078.

[VEN94] W.J.P. van Enckevort, 'Synthetic Diamond: Emerging CVD Science and Technology' K.E. Spear, J.P. Dismukes, eds. John Wiley & Sons, Inc. (1994) Chapter 9.

[WAL79] J. Walker, Rep. Prog. Phys. **42** (1979) 1605.

[WIL89] R.C. Wilson, F.A. Stevie and C.W. Magee, *in Practical Handbook of Depth Profiling and Bulk Impurity Analysis*, Willey, New York, 1989, 31.

[WIL94] C. Wild, R. Kohl, N. Herres, W-Muller-Sebert and P. Koidl, Diamond Relaed Materials, **3** (1994), 373-381.

[WOO90] G. S. Woods, J.A. van Wyk, A. T. Collins, Phil. Mag. B, **62** (1990) 589.

[ZEI99] R. Zeisel, private communication

Conclusions and suggestions for further work

The main objective of this thesis was to investigate if Photothermal Deflection Spectroscopy (PDS) could be applied to study the defects present in undoped and doped polycrystalline CVD diamond films. Up till now, PDS was only used for the characterisation of semiconductors such as a-Si and a-Ge.

Photothermal Deflection Spectroscopy

PDS is a *very sensitive characterisation technique* which allows to determine the defect-induced optical absorption coefficient α of semiconducting films.

We have *adapted the PDS set-up* in such a way that it meets the specific requirements of *polycrystalline CVD diamond films* and moreover, we studied the validity of the PDS theory for diamond. This resulted in the construction of two different PDS configurations: the transverse and the collinear set-up.

(i) T*ransverse PDS* was used for the first time as a gap state spectroscopic tool to study the optical transitions due to the presence of defects in the bandgap of diamond. The spectral dependence of the optical absorption coefficient α in the energy range of 0.5 to 5.4 eV can be studied.

(ii) *Collinear PDS* was used to map the optical absorption (in our case at the CO_2 laser wavelength of 10.6 μm, with a spatial resolution of about 100 μm) in high quality CVD diamond windows.

In general, it is not straightforward to get *absolute optical absorption values* out of PDS measurements in arbitrary units.

(i) We compared different scaling procedures for transverse PDS measurements to calculate the absolute optical absorption coefficient.

- low quality CVD diamond films: S_{sat}*-scaling procedure* (transverse PDS + saturation value).
- intermediate to high quality CVD diamond films: *T-scaling procedure* (transverse PDS + transmission measurements)

(ii) In the case of collinear PDS, absorption values of high quality diamond films were calibrated by means of *laser calorimetry* on a reference sample. (Our collinear arrangement is not suitable to measure absorption in low quality diamond films.)

In particular, the *influence of light scattering* in diamond films on transverse PDS measurements has been studied thoroughly. In the low absorption range ($\alpha d < 1$), the effect of scattering and light trapping results in an artificially increased effective optical thickness. This enhancement is spectral independent and thus, the shape of the spectrum is not distorted. Actually, it comes down to an enhancement of the sensitivity of PDS. Since we measure PDS spectra in arbitrary units this influence is not relevant. In contrast with the transmission measurements, the PDS measurements are not hindered by scattering losses. Because specular transmission measurements suffer much more from scattering than integrated sphere transmission measurements, the latter are used to scale the PDS measurements.

Undoped CVD diamond films

It has been demonstrated that transverse PDS is very powerful to study the characteristic absorption in undoped CVD diamond films. The PDS spectra of the undoped films brought a first insight to the (intrinsic) defects in CVD diamond films and allowed the identification of the most important defect structure: all *CVD diamond films exhibit a very characteristic continuum subgap* optical absorption in the IR and visible spectral regions. On comparison with Raman measurement, this absorption was attributed to non-diamond carbon absorption, due to the optical transitions in the π-π^*sub gap states. We developed a theoretical model for the description of the optical absorption coefficient in the subgap region. Characterisation of this defect structure allowed the preparation of optical quality diamond films, approaching in the quality and purity the natural synthetic counterparts.

The collinear measurements carried out on a set of samples of various optical qualities demonstrated the applicability of this technique for high quality CVD diamond windows end yielded *1D and 2D optical absorption images*. It has been demonstrated that the optical absorption mechanism is greatly affected by the black features, which are – to a greater or lesser content depending on the material grade – present in all CVD diamond films.

Doped CVD diamond films

It has been demonstrated that transverse PDS can be used to study defect levels in nitrogen-, lithium- and phosphorus-doped CVD diamond films.

Substitutional nitrogen has been detected in a variety of *N-doped* CVD diamond samples for the first time by PDS. The characteristic nitrogen absorption, with a photoionisation at 2.2 eV, has been confirmed by comparison with Ib HPHT diamond. In addition N-V complexes have been observed by PDS.

The transverse PDS technique was applied to *Li-doped* CVD diamond samples to study the optical activity of Li in CVD diamond films. In such films, prepared by in-situ Li doping by adding butyllithium to the feed gas, a new defect structure around 1.5-1.6 eV has been observed.

Finally, the PDS technique has been applied to n-type *P-doped* CVD diamond samples, prepared at NIRIM in Japan. The photoionisation around 0.56 eV from the ground state of the P-defect to the conduction band has been demonstrated. This result agreed very well with complementary FTIR and CPM data and presents first optical confirmation of P in n-type diamond.

It is clear that much more work is necessary to understand n-type doping.

We have proven that PDS can be used as a spectroscopic characterisation tool to study the defect-induced subgap absorption in undoped and doped CVD diamond films. The strength of the PDS technique is its very high sensitivity, allowing to study defect levels below ppm, in combination with its immunity for light scattering. A minus of the technique is that transmission measurements are needed to scale the absorption spectra in absolute units. For a full characterisation of the extrinsic defects and dopants present in the CVD diamond films, additional characterisation techniques, such as photocurrent, FTIR, EPR, etc. are necessarily.

Challenges for the future

At this stage of our research, different challenging tracks can be followed:

i) the application of PDS as a ‘standard’ complementary optical characterisation tool for other semiconducting materials such as SiC, BN, GaN and conducting polymers.

ii) the extension of the transverse and collinear PDS set-ups itself.

It would be interesting to use a tunable laser as pump beam. In the case of transverse PDS, this would have the advantage that both the resolution and the incident power can be increased, resulting in an even higher precision of the absorption spectra. In combination with an extension to low temperatures, this would allow to observe fine structures in the absorption spectra. Considering the collinear PDS set-up, up till now used for optical imaging at the CO_2 laser wavelength, using a tunable laser which would allow to work in the spectroscopic mode (energy scans).

iii) the study in depth of doped CVD diamond films

The start is made to study doped CVD diamond films, nevertheless several absorption features remain unexplained up till now. Besides, the electronic transport properties, the trapping kinetics and the conductivity mechanism in CVD diamond films are not very well understood. Adapting PDS according to the extensions suggested under ii) could yield higher resolution spectra which could bring new insights about defect levels and concentrations. In addition to PDS, other characterisation techniques such as CPM and transient photocurrent techniques should be used to obtain a fundamental knowledge concerning the nature, the concentration and the energy distribution of the defect centres, just as the drift mobility and the lifetime of the charge carriers.

Appendix A.1 Overview of the samples studied in this thesis

Table A.1 Overview of the deposition conditions of the undoped CVD diamond samples grown at IMO (MW PECVD technique).

Sample	P (Pa)	T_S (°C)	CH_4 (vol%)	MWP (W)	t_D (min.)	Appearance	Morphology	Grain size (μm)	Thickness (μm)	I(D)/I(G) [d]
SET I										
D11	13200	760	3 [b]	4500	1440	White	Random	15	100	No G peak [a]
D12	13200	800	6 [b]	4500	1200	Brownish	{111}	3	100	G + D [*]
D13	13200	800	7 [b]	4500	1200	Black	{100}	10	100	G + D [*]
SET II.1										
d2.1	6600	900	0.65	800	720	White	Random	5	15 - 20	No G peak [a]
d2.2	6600	900	1	800	720	Grey	Random	3	15 - 20	~ 5
d2.3	6600	900	1.5	800	720	Grey	Random	3	15 - 20	~ 1
d2.4	6600	900	2	800	720	Brownish	Random	< 1	15 - 20	~ 0.2
d2.6	6600	900	2.5	800	720	Brownish	Random	< 0.1	15 - 20	Only G
SET II.2										
d2.7	6600	820	3	800	720	Grey	{100}	< 1	15 - 20	~ 0.2
d2.8	6600	760	3	800	720	Grey	{100}	~ 2	15 - 20	~ 0.5
d2.9	6600	900	3	800	720	Dark brown	Random, {100}	< 0.1	15 - 20	Only G

[a] 1332 cm^{-1} diamond peak only

[b] Also 1sccm O_2

[*] No ratio calculated

[d] At FWHM Raman peaks

Continuation Table A.1

Sample	P (Pa)	T_S (°C)	H_2 (sccm)	CH_4 (vol%)	MWP (W)	t_D (min)	Thickness (µm)
D17	Homoepitaxially grown on {100} oriented diamond seed crystal, no details available						373
K34	10000	800	300	3	4500	-	-

Table A.2 Nitrogen (N_2) or nitromethane (NO_2-CH_3) doped CVD diamond films grown at IMO (MW PECVD technique).

Sample	P (Pa)	T_S (°C)[a)]	H_2 (sccm)	CH_4 (vol.%)	N_2 (vol. ppm)	NO_2-CH_3 (vol. ppm)	MWP (W)	t_D (min)	Thickness (µm)
Set V									
S1	13200	760	300	3	100 ppm	-	4000	1440	250
S2	13200	760	300	3	1 vol.%	-	4000	1440	30
Set VI									
N1	11500	800	300	4.76	95	-	3000	-	18
N2	11500	800	300	4.76	190	-	3000	-	18
N3	11500	800	300	4.76	286	-	3000	-	19
N4	11500	800	300	4.76	714	-	3000	-	196
NM1	11500	900	300	3.88	-	17	3000	-	66
NM2	11500	900	300	2.88	-	86	3000	-	31
NM3	11500	900	300	3.88	-	173	3000	-	35

Table A.3 Overview of the deposition conditions of the N-doped CVD diamond samples grown at ASTeX (Boston, USA).

Sample	P (Pa)	T_S (°C)[a]	H_2 (sccm)	CH_4 (sccm)	O_2 (sccm)	MWP (W)	Thickness (µm)
2i	10660	920	500	18	5	5000	20
3i	10660	780	500	18	5	5000	20
4i	16000	780	1000	33	4	5000	200

Table A.4 Overview of the deposition conditions of the Li-doped CVD diamond samples grown at IMO (MW PECVD technique).

Sample	P (Pa)	T_S (°C)[a)]	H_2 (sccm)[c)]	CH_4 (vol %)	Li (vol %)	MWP (W)	t_D (min)	Thickness (µm)
L1	10000	800	250	[d)]	0	3500	1420	17 ± 3
L2	10000	800	250	[d)]	0.25	3500	1420	19 ± 3
L3	10000	800	250	[d)]	0.5	3500	1420	20 ± 3
L4	10000	800	250	[d)]	1	3500	1420	20 ± 3
L5	10000	800	250	[d)]	2.5	3500	1420	22 ± 3
L6	10000	500	250	[d)]	0.5 [e)]	3500	2440	23 ± 3

[c)] 0.3 vol.% O_2 was added to the H_2 feed gas to maintain the quality of the diamond sample.

[d)] For the Li-doping experiments, the standard carbon precursor methane has been replaced by hexane (C_6H_{14}). C_6H_{14} has been chosen because the Li source butyllithium C_4H_9Li is provided as a 2.5 mol l^{-1} solution of C_4H_9Li in C_6H_{14}.

[e)] The content of the Li precursor containing vapour in the H_2 feed gas.

Table A.5 Optical windows De Beers.

Sample	Thickness (µm)	Optical characteristics (optical microscope)	Light scattering
D1	660	Very good optical quality	NO
D2	330	Local defects (black spots), polishing defects	Locally
D3	1200	Local defects (black spots)	Locally
D4	760	Local defects (black spots)	Locally
D5	720	Inhomogeneous, (black spots)	Locally
D6	660	Partially inhomogeneous, large inclusions	YES
D7	460	Large inclusions	YES
D8	700	Large Inclusions	YES
D9	620	Large inclusions	YES
D20	1010	Very good optical quality	NO
D21	720	Very good optical quality	NO
D22	130	Local defects (black spots)	YES

Table A.6 Optical quality samples De Beers.

Sample	Substrate side	Top side
1090	as grown	as grown
1091	polished	as grown
1092	as grown	polished
1093	polished	polished

Table A.7 Basic characteristics of the P-doped samples from NIRIM.

Sample	Substrate $2mm^2$ Sumitomo	P (Pa)	T_S (°C)	Total flow (sccm)	CH_4/H_2 (vol.%)	PH_3/CH_4 (vol. ppm)	t_D (min)	MW P (Watt)	Thickness (µm) [1)]	N_D (cm^{-3}) [2)]
P2	Ib hexagonal shape	10640	950	400	0.075	1000	120	400	1.5	$5 .10^{18}$
P3	Ib hexagonal shape	10640	950	400	0.075	1000	120	420	1.5	5.10^{18} - 10^{19}

[1)] Thickness of doped layer

[2)] N_D measured by SIMS

Table A.8 Deposition conditions of the samples from the KUN (homoepitaxially flame grown: acetylene-oxygen combustion flame).

Sample	Substrate [h)] (orientation); (mm * µm) or (mm^3)	T_S (°C)	d (mm)	f_{ox} standard l min^{-1}	S_{ac} (%)[g)]	r_D ±5µm h^{-1}	Colour	Layer Thickness (µm)
C7	{001}; Ø 4 x 0.510	1200	0.7	3.4	5.4	111	yellow	370
C2	{110}; Ø 3 x 0.309	1200	1.5	3.4	3.9	76	white transparent	153
Ib	{110}; 4 x 2 x 0.250	natural diamond					light brown, less transparent	250
IIa	{001}; 2 x 2 x 0.250	natural diamond					brown opaque	250

[h)] Polished natural diamond substrates (surface roughness less than 20 nm) were used to grow homoepitaxially diamond layers. High purity source gases oxygen (99.999 %) and acetylene (99.6 %).

Appendix A.2 Theoretical description of the probe beam deflection

The probe beam changes its direction of propagation when it encounters a transverse gradient of the refractive index of the medium. To derive the deflection we look at the situation of the transverse PDS configuration of Fig 3.1 (a) (see Chapter 3) which is shown more in detail in Fig. A.1 [IIZ87][1]. The derivation below can also be applied for the collinear PDS configuration. The only difference is that for the latter the index of refraction gradients established in the diamond itself are probed.

The change $d\theta$ in the direction of propagation of the probe beam is, for any point **R** of the beam path, given by the curvature of the path in **R** :

$$d\theta = \frac{ds}{\rho} \qquad \text{(A. 1)}$$

where ρ is the radius of curvature and ds the length of the infinitesimal propagation measured along the path.

The deflection $d\theta$ can, alternatively, be written as

$$d\theta = \left| d\mathbf{s} \right| \qquad \text{(A. 2)}$$

where d**s** is the change of the unit tangent vector **s** along the beam path. The unit tangent vector can, in its turn, be expressed as:

$$\mathbf{s} = \frac{d\mathbf{R}}{ds} \qquad \text{(A. 3)}$$

Differentiating the last expression (A.2) with respect to s gives:

$$\frac{d\theta}{ds} = \left| \frac{d\mathbf{s}}{ds} \right| = \left| \frac{d^2\mathbf{R}}{ds^2} \right| \qquad \text{(A. 4)}$$

Now, we must relate the deflection to the gradient of the refractive index. This can be done by considering the complex amplitude of the wave expression of the probe beam,

---

[1] [IIZ87] K. Iizuka, 'Engineering Optics', sec. ed., Springer Series in Optical Sciences Volume 35, Springer-Verlag, (1987).

$$E(x,y,z) = E_0(x,y,z).\ \exp[ik.L(x,y,z)] \qquad \text{(A. 5)}$$

Where L(x,y,z) = cte represents an equi-phase surface of the beam.

The complex amplitude must satisfy the wave equation:

$$\left[\nabla^2 + k^2 n^2(x,y,z)\right] E(x,y,z) = 0 \qquad \text{(A. 6)}$$

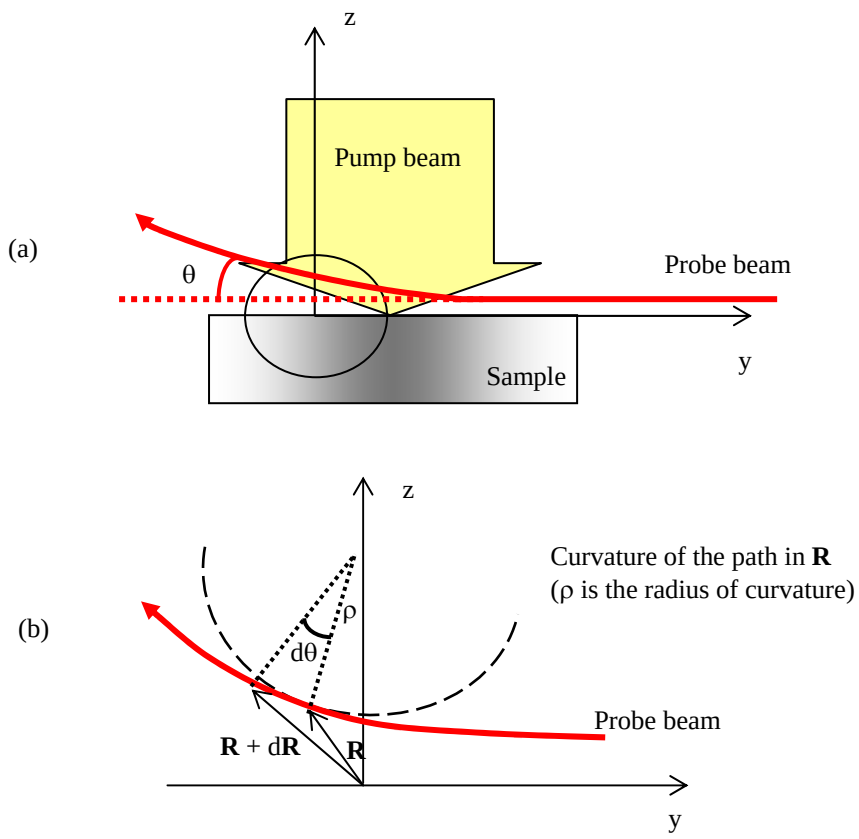

Fig. A.1 Geometry to derive the deflection of the probe beam: (a) general view, (b) enlargement of the encircled part of (a).

Inserting the complex amplitude (A.5) into this wave equation it follows that, if no abrupt spatial changes of the index of refraction n occur,

$$|\nabla L| = n. \qquad \text{(A. 7)}$$

From this result, together with the fact that the direction of light propagation is the direction normal to the equi-phase surfaces, follows that:

$$\frac{dL}{ds} = n \qquad \text{(A. 8)}$$

Taking the gradient of both sides of (A.8) gives:

$$\frac{d}{ds}\nabla L = \nabla n \qquad \text{(A. 9)}$$

where the order of applying the gradient and the derivative on the left-hand side was interchanged.

The direction of propagation can alternatively be given either by the tangent unit vector (A.3), $\mathbf{s} = \frac{d\mathbf{R}}{ds}$, or by the unit vector **N** normal to the equi-phase surfaces, $\mathbf{N} = \frac{\nabla L}{|\nabla L|} = \frac{\nabla L}{n}$. Combining these two expressions, we obtain

$$\frac{\nabla L}{n} = \frac{d\mathbf{R}}{ds} \text{ or } \nabla L = n\frac{d\mathbf{R}}{ds} \qquad \text{(A. 10)}$$

Inserting the last expression into (A.9) gives:

$$\frac{d}{ds}\left(n\frac{d\mathbf{R}}{ds}\right) = \nabla n\ . \qquad \text{(A. 11)}$$

This formula is called the Euler-Lagrange formula. Performing the differentiation in the left hand-side of the Euler-Lagrange formula gives:

$$\frac{dn}{ds}\frac{d\mathbf{R}}{ds} + n\frac{d^2\mathbf{R}}{ds^2} = \nabla n \qquad \text{(A. 12)}$$

According to equation (A.3), the second derivative $\frac{d^2\mathbf{R}}{ds^2}$ points in the direction given by $\frac{d\mathbf{s}}{ds}$, i.e. normal to **s.** Using equation (A.4), ∇n can thus be expressed as

$$\frac{dn}{ds}\mathbf{s} + n\frac{d\theta}{ds}\mathbf{s}_\perp = \nabla n \qquad \text{(A. 13)}$$

where $\mathbf{s}_\perp$ stands for the unit vector normal to **s**. Taking the scalar product of both sides of

equation (A.13) with $\mathbf{s}_\perp$ yields

$$n\frac{d\theta}{ds} = \mathbf{s}_\perp \nabla n \qquad \text{(A. 14)}$$

The right-hand side corresponds to the component of ∇n normal to the direction of propagation **s**. Designating this normal component by $\nabla_\perp n$, equation (A.14) leads to the familiar expression:

$$d\theta = \frac{1}{n}\nabla_\perp n ds \qquad \text{(A. 15)}$$

This expression is commonly used for the analysis of PDS measurements. In a real experiment, however, the integrated deflection angle θ is measured. To link this latter to the gradient field $\nabla_\perp n(x,y,z)$ the integration of formula (A.15) has to be performed. However, the integration path is unknown as long as the deflection is not known.

For small deflection angles, as they usually are in PDS measurements, it is customary to perform the integral over the path the probe beam follows when there are no refractive index gradients. The integrated deflection angle then becomes:

$$\theta = \frac{1}{n}\int_{path} \nabla_\perp n ds \qquad \text{(A. 16)}$$

In order to express the deflection angle θ in terms of the temperature field, we write the index of refraction $n = n(T)$ as a Taylor series around the ambient temperature T_R (with T the temperature deviation of T_R). For simplicity we rescale the temperature and set T_R to zero.

$$n(T) = n_0 + \left.\frac{\partial n}{\partial T}\right|_0 T + ... \qquad \text{(A. 17)}$$

For small temperature changes one can approach the function n(T) by only the first two terms of the series, hence

$$\theta = \frac{1}{n_0}\frac{\partial n}{\partial T}\int_{path} \nabla_\perp T ds \qquad \text{(A. 18)}$$

The integration path and the temperature field both depend on the experimental set-up used to measure the absorption and will be discussed in the sections related to the particular set-ups employed in our measurements.

Appendix A.3 List of papers related to this thesis

1. *Origin of characteristic subgap optical absorption in CVD diamond films,* M. Nesladek, K. Meykens, L.M. Stals, M. Vanecek and J. Rosa, Phys. Rev. B, 54 (1996), 5552.

2. *Optical absorption and cathodoluminescence in homoepitaxially grown CVD diamond films*. K. Meykens, M. Nesladek, C. Quaeyhaegens, L.M. Stals, M.Vanecek, J. Rosa, G. Janssen, J.J. Schermer, Diamond Related Materials, 5 (1996), 958.

3. *Investigation of n-doping in CVD diamond films*, M. Nesladek, K. Meykens,L.M. Stals, C. Quaeyhaegens M.D'Olieslaeger, T.D.Wu, M. Vanecek, J. Rosa, Diamond Relat. Mater., 5 (1996), 1006.

4. *Diamond films for electronic applications,* K. Meykens, M. Nesladek, C. Quaeyhaegens and L.M. Stals, Proceedings of the 5th Euromat, Maastricht, (1997), 421-424.

5. *On the development of CVD diamond film morphology due to the twinning on {111} surfaces.* G. Knuyt, M. Nesladek, K. Meykens, T. Vandevelde, C. Quaeyhaegens, L.M. Stals, Diamond Relat. Mater., 6 (1997), 435-439.

6. *On the {111} <111> penetration twin density in CVD diamond films,* G. Knuyt, M. Nesladek, T. Vandevelde, K. Meykens, C. Quaeyhaegens and L.M. Stals, Diamond Relat. Mater., 6 (1997) 1697-1706.

7. *Heterogeneous nucleation of diamond,* P. Demo, Z. Kozisek, K. Meykens and M. Nesladek, Czech J. Phys. 47, (1997) 385-388.

8. *Transient nucleation of diamond : theoretical and experimental study,* P. Demo, Z. Kozisek, M. Vanecek, J. Rosa, K. Meykens, M. Nesladek, C. Quaeyhaegens, G. Knuyt and L.M. Stals, Diamond Relat. Mater., 6 (1997) 1092-1096.

9. *On nitrogen incorporation during PE-CVD of diamond films,* T. Vandevelde, M. Nesladek, K. Meykens, C. Quaeyhaegens, L.M. Stals, I. Gouzman, A. Hoffman, Diamond Relat. Mater., 7 (1998) 152-157.

10. *Simultaneous characterisation of defect states in CVD diamond by PDS, EPR, Raman and photocurrent spectroscopies*, J. Rosa, J. Pangrac, M. Vanecek, V. Vorlicek, M. Nesladek, K. Meykens, C. Quaeyhaegens, L.M. Stals, Diamond Relat. Mater., 7 (1998) 1048-1053.

11. *Characteristic defects in CVD diamond: optical and electric paramagnetic resonance study*, M. Nesladek, K. Meykens, K. Haenen, J. Navratil, C. Quaeyhaegens, L.M. Stals, A. Stesmans, K. Iakoubovskij, G. Adriaenssens, J. Rosa, M. Vanecek, Diamond Relat. Mater. 8 (1999) 1480-1484.

12. *Study of defects in CVD and ultra dispersed diamond*, K. Iakoubovskij, G. Adriaenssens, K. Meykens, M. Nesladek, A. Ya.Vul, V. Yu Osipov, , Diamond Relat. Mater. 8 (1999) 1476-1479.

13. *Photocurrent and optical absorption spectroscopic study of n-type phosphorus-doped CVD diamond*, M. Nesladek, K. Meykens, K. Haenen, L.M. Stals, T. Teraji, S. Koizumi, Diamond Relat. Mater. 8, (1999) 882-885.

14. *Low-temperature spectroscopic study of n-type diamond*, M. Nesladek, K. Meykens, K. Haenen, L.M. Stals, T. Teraji, S. Koizumi, Phys. Rev. B 59 (23), (1999) 14582.

15. *Low Temperature Photoconductivity Detection of Phosphorus in Diamond*, K. Haenen, K. Meykens, M. Nesladek, G. Knuyt, C. Quaeyhaegens, L.M. Stals, S. Koizumi and E. Gheeraert, Phys. Stat. Sol. (a) 174, (1999) 53.

16. *Study of the Electronic Structure of the Phosphorus Level in n-type CVD diamond*, K. Haenen, K. Meykens, M. Nesladek, L.M. Stals, T. Teraji, S. Koizumi and E. Gheeraert, Phys. Stat. Sol. (a) 174, R1 (1999).

17. *Measurement and mapping of very low optical absorption in CVD diamond IR windows*,. K. Meykens, K. Haenen, M. Nesladek, L.M. Stals, C.S.J. Pickles, R.S. Sussmann, Diamond Relat. Mater. In press.

18. *Temperature dependent spectroscopic study of the electronic structure of phosphorus in n-type diamond films*, K. Haenen, K. Meykens, M. Nesladek, G. Knuyt, L.M. Stals, T. Teraji, S. Koizumi and E. Gheeraert, Diamond Relat. Mater. In press